Modeling of metal nanocluster growth on patterned substrates and surface pattern formation under ion bombardment

Dissertation

zur Erlangung des akademischen Grades
Doctor rerum naturalium
(Dr. rer. nat.)

vorgelegt

der Fakultät Mathematik und Naturwissenschaften

der Technischen Universität Dresden

von

Dipl.-Math. Satoshi Numazawa
geboren am 6 Juli 1977 in Tokyo, Japan

Reviewer:

1. Prof. Dr. Wolfhard Möller, Technical University of Dresden, Germany

2. Prof. Dr. Roger Smith, Loughborough University, UK

Abstract

This work addresses the metal nanocluster growth process on prepatterned substrates, the development of atomistic simulation method with respect to an acceleration of the atomistic transition states, and the continuum model of the ion-beam inducing semiconductor surface pattern formation mechanism.

Experimentally, highly ordered Ag nanocluster structures have been grown on pre-patterned amorphous SiO_2 surfaces by oblique angle physical vapor deposition at room temperature. Despite the small undulation of the rippled surface, the stripe-like Ag nanoclusters are very pronounced, reproducible and well-separated. The first topic is the investigation of this growth process with a continuum theoretical approach to the surface gas condensation as well as an atomistic cluster growth model. The atomistic simulation model is a lattice-based kinetic Monte-Carlo (KMC) method using a combination of a simplified inter-atomic potential and experimental transition barriers taken from the literature. An effective transition event classification method is introduced which allows a boost factor of several thousand compared to a traditional KMC approach, thus allowing experimental time scales to be modeled. The simulation predicts a low sticking probability for the arriving atoms, millisecond order lifetimes for single Ag monomers and ≈ 1 nm square surface migration ranges of Ag monomers. The simulations give excellent reproduction of the experimentally observed nanocluster growth patterns.

The second topic specifies the acceleration scheme utilized in the metallic cluster growth model. Concerning the atomistic movements, a classical harmonic transition state theory is considered and applied in discrete lattice cells with hierarchical transition levels. The model results in an effective reduction of KMC simulation steps by utilizing a classification scheme of transition levels for thermally activated atomistic diffusion processes. Thermally activated atomistic movements are considered as local transition events constrained in potential energy wells over certain local time periods. These processes are represented by Markov chains of multi-dimensional Boolean valued functions in three dimensional lattice space. Consequently, the fluctuating system evolution process is implemented as a Markov chain of equivalence class objects. It is shown that the process can be characterized by the acceptance of metastable local transitions. The method is applied to a problem of Au and Ag cluster growth on a rippled surface. The simulation predicts the existence of a morphology dependent transition time limit from a local metastable to stable state for subsequent cluster growth by accretion.

The third topic is the formation of ripple structures on ion bombarded semiconductor surfaces treated in the first topic as the prepatterned substrate of the metallic deposition. This intriguing phenomenon has been known since the 1960's and various theoretical approaches have been explored. These previous models are discussed and a new non-linear model is formulated, based on the local atomic flow and associated density change in the near surface region. Within this framework ripple structures are shown to form without the necessity to invoke surface diffusion or large sputtering as important mechanisms. The model can also be extended to the case where sputtering is important and it is shown that in this case, certain 'magic' angles can occur at which the ripple patterns are most clearly defined. The results including some analytic solutions of the nonlinear equation of motions are in very good agreement with experimental observation.

Contents

List of acronyms and symbols

Acronyms and symbols listed below are defined first in the consistent chapter and used through the context. Symbols used in multiple chapers are only listed here. Other symbols are defined in each chapter and utilized localy.

1D	One dimensional	
2D	Two dimensional	
3D	Three dimensional	
AL	Adatom lifetime	Chapter 2.2.3
BH	Bradley-Harper	Chapter 4.1
BKL	Bortz-Kalos-Lebowitz	Chapter 1.3.3
bcc	Body centered cubic	Chapter 1.3.3
ES	Erhlich-Schboebel	Chapter 2.1.2
DFT	Density functional theory	Chapter 1.1.2
DMC	Diffusion Monte Carlo	Chapter 1.3.4
fcc	Face centered cubic	Chapter 1.3.3
KMC	Kinetic Monte Carlo	Chapter 1.3.3
MD	Molecular dynamics	Chapter 1.2
MC	Monte Carlo	Chapter 1.3
ML	Mono-layer	Chapter 2.1.3
NC	Nanocluster	Chapter 2
NN	Nearest neighbor	Chapter 1.3.3
PBC	Periodic boundary conditions	Chapter 1.3.3
PVD	Physical vapor deposition	Chapter 2
PDE	Partial differential equation	Chapter 1.1.1
PW	Perdew-Wang	Chapter 1.1.2
RB-KMC	Rate-based KMC	Chapter 2.4.1
RGL	Rosato-Guillopé-Legrand	Chapter 2.3.1
RMS	Root mean square	Chapter 3.6.1
RT	Room Temperature	Chapter 2.1.3
sc	Simple cubic	Chapter 1.3.3
TAD	Temperature accelerated dynamics	Chapter 1.3.3
v-SiO$_2$	Vitreous silica	Chapter2
VW	Volmer-Weber	Chapter 2

k_B	Boltzmann constant	
D, D_*	Diffusion constant, $* = sc, fcc, bcc, diam, ..., etc$	
E, E_*	Energy, $* = b, bst, kin, pot, ..., etc$	
$\mathcal{F}$	Fourier transformation	Chapter 1.3.3
ω, ω_*	Frequency $* = Ag, ad, eff, ..., etc$	
Π	Gibbs distribution	Chapter 1.3.1
f_{loc}	Local flux	Chapter 2.2.1
$\mathbf{T}, \mathbf{S}, \mathbf{M}$	Markov kernel	Chapter 1.3.2
$\mathcal{H}$	Hamiltonian	Chapter 1.2.1
Z	Partition function	
T	Temperature	

Chapter 1

Introduction: Atomistic Models

"Imagination is more important than knowledge."
Albert Einstein, Physicist, 1879-1955.

Atomistic modeling of the growth of thin films, self assembled monolayers or surface pattern formations on the nano-scale has attracted much attention over recent years due to the large number of technological applications in the field of nanotechnology [30, 68, 104, 130, 137, 142]. The aim of this work is to propose some innovative atomistic models connecting elemental scale complexity to experimental observation. The author hopes that these methods contribute to the further development of basic research as well as industrial application of nano physics.

There are three main topics in this thesis. The first topic is an atomistic level understanding of the silver crystal growth mechanism observed in the experiments of Ag physical vapor deposition (PVD) on ripple like pre-patterned vitreous silica substrates described in chapter 2. An overview of the cluster growth mechanism on substrates and the experimental motivation are introduced. Then the behavior of adsorbed monomers on a ripple like pre-patterned substrate and the topography dependent local flux variation are discussed. Simple nucleation simulations are performed with the Monte Carlo (MC) method in order to explore the crucial binding energy between metal atoms and substrates. Concerning some problems about the simulation time scale the model is further extended and this modified model reproduces the cluster formation observed in experiment quite successfully. The second topic relates to this extended model discussed in chapter 3. A mathematical model describing the atomistic transition states is proposed and the acceleration of the simulation is considered in the framework of this abstract model. The concept is examined using a PVD model with some metals as well as a simple one-dimensional (1D) diffusion model. The modification of the fundamental algorithm is discussed in terms of the convergence limit of the probability distribution of atomic states. The third topic is the surface pattern formation induced by ion beams, especially ripple pattern formation. It is known that by ion beam irradiation some self-organized nano scale pattern formations appear on the surface of semiconductors such as Si, Ge, GaSb and that the pattern type is dependent on a large number of experimental parameters. There are long discussions about the main driving force of these intriguing phenomena in the literature. In chapter 4, a short overview of some recent theoretical discussions is given first. Then a fundamental observation of Si surface modification induced by low energy ion impact molecular dynamics (MD) simulations as well as some surface modification models performed by Kinetic Monte Carlo (KMC) simulations are introduced. From these considerations, a new kind of surface modification theory describing atomic flow induced by ion beam irradiation is proposed.

In the rest of this introductory chapter, three different scales of atomistic modeling approaches relating to this work, mainly the binding energy calculation, MD, and KMC, are introduced for the

fundamental overview of whole content of this thesis. The finest level approach is a self-consistent quantum theoretical model treating the electronic structure of small number of atoms. The second level approach allows to treat up to $\sim 10^7$ atoms and nanosecond order dynamics of systems by utilizing the classical Newton's theory with appropriate inter-atomic potential functions. The third level approach is the statistical approach for the dynamic evolution of systems. This approach is one of the main methods used in this thesis and discussed in more depth. Here, the time range can be up to some milliseconds. By adopting the basic algorithm to certain types of simulation, these atomistic models are able to treat systems over experimental timescales.

1.1 Density Functional Theory

Consideration of the electronic structure of small atomic systems is the starting point of the whole approach. In this section, an overview of density functional theory (DFT) is given in order to understand the basic concept of this approach appearing in some parts of this work. The details of the theory can be found in the review papers of Segall *et al* [200], Ziegler [260] and references therein.

1.1.1 Schrödinger equation

Wave-particle dualism

When a metal is exposed to incident light with short wavelength, electrons, called the photoelectrons, are emitted. This phenomenon is known as the photoelectric effect, or Hertz effect after the German physicist firstly reported it in 1887 [103]. In 1905, Einstein postulated that this effect is due to the particle character of light (photon). On the other hand, de Broglie considered a wave description in 1924 [56], i.e. the particle has the wave character in this case. The kinetic energy E and the momentum $\vec{p}$ of photon is then given by

$$E = \hbar\omega = \frac{|\vec{p}|^2}{2m}, \vec{p} = \hbar\vec{k}, \tag{1.1}$$

where $\hbar$ is the Planck constant with factor $1/2\pi$, m is the mass of the particle, ω is the angular frequency of the light, and $\vec{k}$ is the wave vector with $|\vec{k}|$ being the angular wavenumber. From the equation (1.1), one obtains the dispersion relation for the matter with the wave-particle dualism

$$\omega = \frac{\hbar}{2m}|\vec{k}|^2, \tag{1.2}$$

Due to the duality, this relation should hold for free particles. The relation (1.2) is generalized for the particle with the potential energy $V(\vec{r})$ at position $\vec{r}$. The dispersion relation in the energy dimension is then

$$\hbar\omega = \frac{\hbar^2}{2m}|\vec{k}|^2 + V(\vec{r}), \tag{1.3}$$

It is known that the special solution of the wave equation can be represented by the function being proportional to the complex traveling wave

$$\psi(t, \vec{r}) := e^{i(\vec{k}\cdot\vec{r} - \omega t)}. \tag{1.4}$$

The simplest linear partial differential equation (PDE) describing the dispersion relation (1.3) for the wave function (1.4) may be

$$i\hbar\frac{\partial}{\partial t}\psi(t, \vec{r}) = \left[-\frac{\hbar^2}{2m}\frac{\partial^2}{\partial\vec{r}^2} + V(\vec{r})\right]\psi(t, \vec{r}). \tag{1.5}$$

This equation is called the time-dependent *Schrödinger equation.* Another implementation of this equation will be discussed in chapter 1.3.4, the last section of this chapter.

Time-dependent Schrödinger equation

In 1926, Schrödinger proposed eq. (1.5) for the description of the probability distribution of matter with wave duality [197]. A solution ψ of eq. (1.5) is called a *wave function* and $\psi^*\psi$ describes the quantum state of a particle. Note that ψ is a complex valued function. As is shown above, the dispersion relation (1.3) is essential for the equation. For a N-body system, the right hand side of eq. (1.3) can be generalized to the Hamiltonian $\mathcal{H}$, i.e. the mean total energy of the system. The Hamilton operator $\hat{\mathcal{H}}$ is defined as the operator possessing $\mathcal{H}$ as the eigenvalue of the corresponding wave function Ψ of the system, i.e.,

$$\hat{\mathcal{H}}\psi = \mathcal{H}\psi.$$

Then this wave function Ψ of N particles satisfies

$$i\hbar\frac{\partial}{\partial t}\Psi(t, \mathbf{x}) = \hat{\mathcal{H}}\Psi(t, \mathbf{x}), \tag{1.6}$$

where $\mathbf{x} = (\vec{r}_1, ..., \vec{r}_N) = (x_1, ..., x_{3N})$ is the position vector of N particles. The modulus square of the wave function $|\Psi|^2 = \Psi^*\Psi$ indicates the probability distribution of particle and a physical quantity measured corresponds to the expectation value given by the consistent integration called the *probability amplitude.* For example, the total energy of system is given by

$$< \Psi|\hat{\mathcal{H}}\Psi >:= \int \Psi^*\hat{\mathcal{H}}\Psi d\mathbf{x}.$$

It can be shown that these wave functions construct a Hilbert space with the inner product $< \cdot >$.

DFT provides the interaction field between target atoms through the inter-atomic potential calculation based on the electronic structure obeying this Schrödinger equation (1.6). The usual formation is a single-particle expression for the most energetically stable (static) configuration called the *ground state* and the Schrödinger equation of interest is generally time-independent.

Time-independent Schrödinger equation

In a usual electronic structure calculation, the external potential V is assumed as being static since the nuclei of the related system are much heavier than electrons (the Born-Oppenheimer approximation). For such a stationary system with N electrons, the wave-function $\Psi(\mathbf{x}) = \Psi(x_1, ..., x_{3N}) = \Phi(\vec{r}_1, ..., \vec{r}_N)$ satisfies the time-independent Schrödinger equation

$$\mathcal{H}\Psi \equiv [\hat{T} + \hat{V} + \hat{U}]\Psi = E\Psi, \tag{1.7}$$

where $\hat{T}, \hat{V}$ and $\hat{U}$ are the kinetic, potential, and the electron-electron interaction energy, respectively, and E is the total energy of the system. They are represented as [105]

$$\hat{T}\Psi \equiv \quad \tfrac{1}{2}\int \nabla\Psi(\mathbf{x})^*\nabla\Psi(\mathbf{x})d\mathbf{x}, \tag{1.8}$$

$$\hat{V}\Psi \equiv \quad \int V(\mathbf{x})\Psi(\mathbf{x})^*\Psi(\mathbf{x})d\mathbf{x}, \tag{1.9}$$

$$\hat{U}\Psi \equiv \quad \tfrac{1}{2}\int \frac{1}{|\mathbf{x}-\mathbf{x}'|}\Psi(\mathbf{x})^*\Psi(\mathbf{x}')^*\Psi(\mathbf{x}')\Psi(\mathbf{x})d\mathbf{x}d\mathbf{x}', \tag{1.10}$$

with atomic units. The principle of least action may hold in the system and thus the static wave function corresponds to the ground state with the minimum energy. Thus such minimum energy as well as the ground state electron structure providing the configuration energy is to be investigated.

1.1.2 Density functional theory

Thomas-Fermi-Dirac theory

In order to avoid a complex many-body problem, Thomas and Fermi developed individually a statistical model to describe the electron density distribution $n(\vec{r})$ depending only on the space parameter $\vec{r}$ in an atom [77, 229]. The basic concept of DFT is the same as this approach, namely, to calculate the energy $E = E[n_0]$ as a functional of the ground state electron density $n_0(\vec{r})$ of the system. In the Thomas-Fermi (TF) model, electrons are uniformly distributed in phase space with the density $2/h^3$ where h is the Planck constant. Because of the lack of accurate mathematical expressions of the exchange energy and exclusion of the electron correlation, the kinetic energy functional of the TF theory for most applications is rather inaccurate even with the exchange energy functional correction by Dirac (Thomas-Fermi-Dirac theory) [60, 61]. Particularly, it was shown that the bond energy can not be described by this approach [227].

Hohenberg-Kohn equation

Hohenberg and Kohn showed in 1964 [105] the existence of a universal functional $F_u[n]$ independent from the external potential V with the property that the ground state energy E_0 can be represented as

$$E_0 = E[n_0] \equiv \int V(\vec{r})n_0(\vec{r})dr^3 + F_u[n_0]. \tag{1.11}$$

Consequently, the external potential V is uniquely determined by n within a constant. Since the wave function $\Psi(\mathbf{x})$ is also determined uniquely from (1.7)-(1.10) with V, the full many particle ground state is a functional of the ground state electron density n_0. This is a drastic extension of the TF theory and the theory was further developed by Kohn and Sham [125, 126]. They represented the electron density by a set of non-interacting single particle wave functions ψ_i obeying single particle Schrödinger equations (the Kohn-Sham equations)

$$n(\vec{r}) = \sum_{i=1}^{N} |\psi_i(\vec{r})|^2,$$

$$\{-\frac{1}{2}\nabla^2 + [\phi(\vec{r}) + \mu_{xc}(n(\vec{r}))]\}\psi_i(\vec{r}) \quad = \epsilon_i\psi_i(\vec{r}), \tag{1.12}$$

where ϵ_i is the orbital energy, $\phi(\vec{r})$ is the (external- and Coulomb) potential term given by

$$\phi(\vec{r}) = V(\vec{r}) + \int \frac{n(\vec{r}')}{|\vec{r} - \vec{r}'|}dr'^3, \tag{1.13}$$

and $\mu_{xc}(n)$ is the exchange and correlation functional. The equations have to be solved self-consistently. I.e., one assumes an initial density state $n^1(\vec{r})$, then ϕ^1 is obtained from eq. (1.13) and consequently n^2 is found from $\mu_{xc}(n^1)$ and the Kohn-Sham equations (1.12). Denote this process as a mapping $\Gamma_{KS} : n^1 \mapsto n^2$ from the set of density functions to itself, then the self-consistency implies that there exists a limit density which is invariant with the mapping Γ_{KS}. Due to the non-interacting condition there exists an error in the kinetic energy term of (1.12). This error is usually included as a correction term in the exchange-correlation term. Thus the accuracy of the DFT calculation depends on the exchange-correlation term μ_{xc} together with the potential ϕ.

The total electronic energy functional $E[n]$ is represented by [14]

$$E[n] = T[n] + \int V(\vec{r})n(\vec{r})dr^3 + \frac{1}{2}\int \frac{n(\vec{r'})n(\vec{r})}{|\vec{r} - \vec{r'}|}dr'^3 dr^3 + E_{xc}[n]. \tag{1.14}$$

A common ansatz for μ_{xc} is the local density approximation (LDA). In this method, the exchange-correlation energy $E_{xc}^{LDA}[n]$ is approximated by the value of E_{ex} calculated for a homogeneous electron gas of the same density as the one at the local coordinate $\vec{r}$, where the functional is evaluated. For slowly varying spin-densities $n\uparrow, n\downarrow$ with $n = n\uparrow +n\downarrow$, the LDA is extended as the local spin-density approximation (LSDA)

$$E_{xc}^{LSDA}[n\uparrow, n\downarrow] = \int (n\uparrow, n\downarrow)\epsilon_{xc}^{unif}(n\uparrow, n\downarrow)dr^3,$$

where ϵ_{xc}^{unif} is the exchange-correlation energy per particle of a uniform electron gas. LSDA gives excellent molecular geometries, vibrational frequencies, and single-particle properties, but bond energies are seriously overestimated.

Basis set superposition error

The error in the bond energy resulting from the superposition of the basis sets of two joined fragments is a well-known error in DFT calculations. A basis set is a set of functions of electrons describing the molecular orbitals. A certain linear combination of these functions provides a reliable representation of the electron density distribution $n(\vec{r})$ of the system. Typical wave functions for orbitals are Slater orbitals, decaying exponentially with the distance from the nuclei [206]. Boys showed that this type of orbitals could be approximated by a linear combination of Gaussian functions (Gaussian orbitals) [25]. An advantage of these Gaussian-type orbitals is saving computation time due to the simplicity of the integral calculation. Pople developed an effective simulation package for the electronic structure calculation using basis sets of the Gaussian orbitals called GAUSSIAN[1] in 1970 (GAUSSIAN70).

In a large system, the whole density state is sometimes described by the combination of multiple basis sets used for different molecule geometries. An overestimation of the electron density can be caused by the overlapping of small basis sets. The counterpoise method correcting the basis set superposition error (BSSE) proposed by Boys and Bernardi [26] is particularly suited for systems which do not undergo a strong geometrical relaxation after bond formation [143]. In some cases, the difference of the bond energies calculated with, and without BSSE correction are so large that a quite different interaction is expected. In chapter 2.2.3, such a case will be discussed. When the geometry of two interacting fragments changes due to the relaxation process, the BSSE is determined for the optimal final structure and added to the interaction energy calculated with respect to the separated fragments in their equilibrium geometry. In some cases, however, the geometry relaxation is so large that the counterpoise procedure does not provide a realistic estimation of the BSSE but only an upper bound [143]. Xantheas pointed out the importance of the fragment relaxation for the BEES correction [246]. The details of the counterpoise technique can be found in the review paper of Chałasiński [38] and references therein.

B3LYP exchange-correlation energy

In 1986, Becke introduced the spin-density gradient $\nabla n\uparrow\downarrow$ to correct bond energy calculations [12] and Ziegler and co-workers further developed the method [260] known as the generalized gradient

---

[1]www.gaussian.com

approximation (GGA). The exchange-correlation energy is approximated as a functional of the local spin-densities and their gradient distributions, i.e.

$$E_{xc}^{GGA}[n\uparrow, n\downarrow]] = \int f(n\uparrow, n\downarrow, \nabla n\uparrow, \nabla n\downarrow)dr^3,$$

where f is the representation of GGA to be determined in various models.

Another approach utilizing the Hartree-Fock (HF) theory, in which the wave function is assumed to be a Slater-determinant (HF approximation), provides the exact exchange energy calculation E_x^{HF} in terms of this approximation. Lee, Yang and Parr proposed a correlation energy formula stemming from the correlation energy density expression of Colle and Salvetti [51], derived from the electron density and a Laplacian of the second-order HF density matrix E_c^{LYP}. There are also many alternative methods to determine the exchange and correlation energy. A widely used approach is the hybrid functional method mixing these functionals with three compound parameters determined by an appropriate fit to experimental data, introduced by Becke in 1993 [16, 17]. This B3LYP (Becke, three parameters, Lee-Yang-Parr) exchange-correlation energy is proposed by Becke [16, 216] as

$$E_{xc}^{B3LYP} = E_{xc}^{LSDA} + a_0(E_x^{HF} - E_x^{LSDA}) + a_x\Delta E_x^{B88} + a_c\Delta E_c^{GGA}, \qquad (1.15)$$

where a_0, a_x, a_c are semiempirical coefficients, ΔE_x^{B88} and $\Delta E_c^{GGA} = \Delta E_c^{PW91}$ are Becke's gradient correction to the LSDA for exchange [13] and the Perdew-Wang (PW) 1991 gradient correction [180] respectively. Here $a_0 = 0.20, a_x = 0.72$ and $a_c = 0.81$ are suggested by Becke based on fitting to heats of formation of small molecules [17]. The leading term E_{xc}^{LSDA} is assumed as separable, i.e., $E_{xc}^{LSDA} = E_x^{LSDA} + E_c^{LSDA}$, and the correlation component E_c^{LSDA} is the electron gas parametrization E_c^{LYP} [179]. The model was modified by Stephens [216] due to the difficulty of local separability of E_c^{LYP} and suggested as $\Delta E_c^{GGA} = E_c^{LYP} - E_c^{VWN}$ as well as $E_c^{LSDA} = E_c^{VWN}$ where E_c^{VWN} is the local correlation functional of Vosko, Wilk and Nusair [238].

Calculation example: Ag/MgO

Figure 1.1 shows an example of DFT calculations from the reference of Zhukovskii *et al* [256]. The differential electron density distribution for a silver adatom adsorbed on a regular O^{2-} surface ion of MgO(100) is illustrated. Atomic and electronic structures are calculated by the HF approximation (*ab initio* HF computer code CRYSTAL95 [64]) together with PW GGA *a posteriori* electron correlation corrections to the total energy [179]. Three basis sets used for Mg, O, and Ag are all-electron 8-61G, 8-51G, and a small core Hay-Wadt pseudopotential with a 311-31G for the $4s^24p^64d^{10}5s^1$ electrons, respectively. The adsorption energy of the Ag adatom is calculated as $E_{ad}^{Ag/MgO} = 0.23$ eV (over O^{2-}) as well as 0.22 eV (over Mg^{2+}).

1.2 Molecular Dynamics Simulation

As the second level approach, classical MD simulation is a well established method in order to investigate the dynamic interaction of atoms utilizing inter-atomic potentials often fitted to DFT calculations or empirical observations. The evolution of systems is performed through solving Newton's equations of motion describing atomistic dynamics induced through the exchange of the inter-atomic potential and kinetic energy. Alder and Wainwright proposed the method first in 1959 [2]. Their MD simulations could handle up to five hundred molecules with the best available computers at that time. Today, massively parallelized supercomputing enables us to simulate a system with millions of atoms [10, 124].
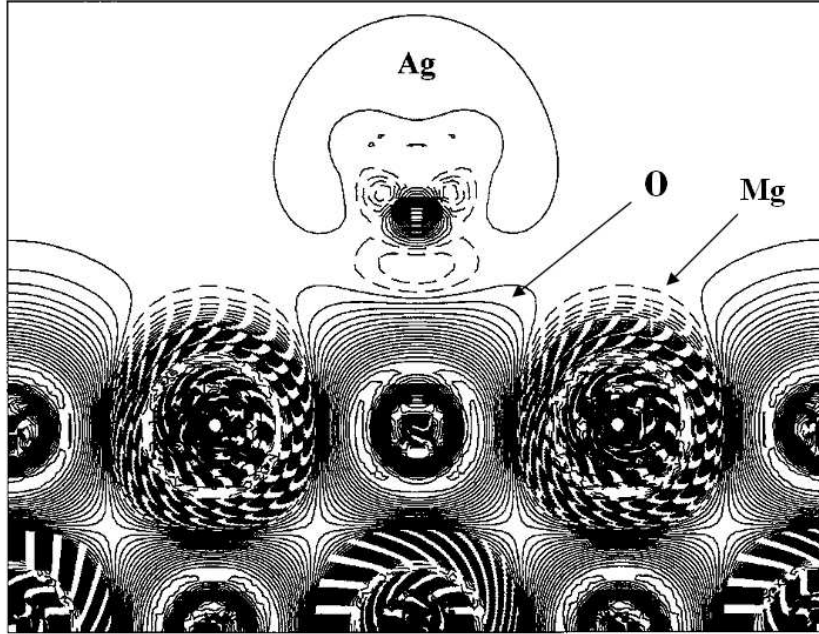
Figure 1.1: The differential electron density map (the total density minus superposition of atomic densities) for the cross section perpendicular to the MgO(100) surface plane for Ag monomer adsorption over a regular O^{2-} surface ion [256].

1.2.1 Lagrangian mechanics

A potential function represents the configuration energy induced by the formation energy of the electron density between atoms. Generally, the inter-atomic potential energy of the system E_{pot} with N atoms is represented as

$$E_{pot} = \sum_i V_1(\vec{r}_i) + \sum_{i<j} V_2(\vec{r}_i, \vec{r}_j) + \sum_{i<j<k} V_3(\vec{r}_i, \vec{r}_j, \vec{r}_k) + ..., \tag{1.16}$$

where the indices $i, j, k, ...$ range over all N particles, $V_m, m = 1, 2, 3, ...$ are m-body potential as functions of the position $\vec{r}_n$ of the nth particle. The *one*-body potential V_1 may correspond to an external potential, such as the gravity, electro-magnetic field, etc. The second term represents a pair potential energy which plays for many cases a crucial role in the interaction of the system. Especially, if the system favors having a close-packed structure, the simplest possible model can be constructed by the pair potential. The three body potential terms exhibit the formation energy often dependent on the angle subtended at one atom by two of the near neighbors located within the cutoff radius. In this work, the effect of the external potential is excluded and the models consider the pair potential term or at most the tree body potential terms. The Hamiltonian $\mathcal{H}$ of the simulation system, in physical sense[2], is defined as the total energy of the system

$$\mathcal{H}(\mathbf{q}, \mathbf{p}) = E_{pot}(\mathbf{q}) + E_{kin}(\mathbf{p}),$$

---

[2] In the mathematical sense, a Hamiltonian system is a system of differential equations that satisfy a special form $\dot{p} = -\frac{\partial \mathcal{H}}{\partial q}; \dot{q} = \frac{\partial \mathcal{H}}{\partial p}$, known as *Hamilton's equations*. These equations also hold for the Hamiltonian $\mathcal{H}$ defined above in the physical sense.

where $\mathbf{q}(t) = \{\vec{r}_1(t), ..., \vec{r}_N(t)\}$ is the atomic position vector, $\mathbf{p}(t) = \{\vec{p}_1(t), ..., \vec{p}_N(t)\}$ is the momentum vector, and E_{kin} is the total kinetic energy of all atoms. This is simply

$$E_{kin} = \sum_{i=1}^{N} \frac{\vec{p}_i^{\;2}}{2m_i},$$

where $\vec{p}_i$ and m_i are the momentum and the mass of atom i, respectively. The positions and momenta of all atoms are represented as a time dependent 6N-dimensional vector $(\mathbf{q}, \mathbf{p})$ for the three-dimensional system. In the Hamiltonian, the kinetic energy and the potential energy are the functions of two variables $\mathbf{q}$ and $\mathbf{p}$ separately. Such a Hamiltonian is called a *separable Hamiltonian*.

The correlation between these two energies follows the well-known Newton's law of motion

$$\vec{F}_i(t) = m_i\vec{a}_i(t) = \nabla E_{pot}^{(i)}, \qquad (1.17)$$

$$\vec{p}_i(t) = \int_0^t \vec{F}_i(t')dt', \qquad (1.18)$$

$$\vec{r}_i(t) = \int_0^t \frac{\vec{p}_i(t')}{m_i}dt', \qquad (1.19)$$

where $\vec{a}_i$ is the acceleration, $\vec{F}_i$ is the force and $E_{pot}^{(i)}$ is the potential energy with respect to the atom i. This $E_{pot}^{(i)}$ is a function of positions of atoms within the potential cutoff radius of the atom i. The time evolution of the system is determined by the iterative integration of these equations of motion.

These equations can be formalized with a functional with respect to the trajectory $\mathbf{q}(t)$ of particles, called the *Lagrangian*. In classical mechanics, the Lagrangian L is defined as the difference between the potential energy and the kinetic energy of the system, i.e.

$$L(\mathbf{q}, \dot{\mathbf{q}}, t) = E_{kin}(\dot{\mathbf{q}}(t)) - E_{pot}(\mathbf{q}(t)).$$

Then the *action* of the particles $\mathbf{q}(t')$ in the system during the time interval $[0, t]$ is given by the definite integral

$$S[\mathbf{q}] := \int_0^t L(\mathbf{q}(t'), \dot{\mathbf{q}}(t'), t')dt'. \qquad (1.20)$$

In nature, this action is minimized. This is known as the principle of least action, or the variational principle. In other words, the functional S is a minimum with the natural trajectory $\mathbf{q}_0(t')$ for $0 < t' < t$. This implies the functional derivative of S is 0 at $\mathbf{q}_0(t')$. Hence for any test function $\delta\mathbf{q}(t') \in (C_c^\infty[(0, t)])^{3N}$, it follows that

$$0 = \frac{d}{d\epsilon}S[\mathbf{q}_0 + \epsilon\delta\mathbf{q}]_{\epsilon_i=0} = \lim_{\epsilon \to 0} \frac{S[\mathbf{q}_0 + \epsilon\delta\mathbf{q}] - S[\mathbf{q}_0]}{\epsilon}. \qquad (1.21)$$

However,

$$S[\mathbf{q}_0 + \epsilon\delta\mathbf{q}] - S[\mathbf{q}_0] = \int_0^t \left[L(\mathbf{q}_0 + \epsilon\delta\mathbf{q}, \dot{\mathbf{q}}_0 + \epsilon\delta\dot{\mathbf{q}}_0, t') - L(\mathbf{q}_0, \dot{\mathbf{q}}_0, t') \right] dt' \qquad (1.22)$$

$$= \int_0^t \left[\sum_{i=1}^{3N} \left\{ \frac{\partial L}{\partial q_i}\epsilon\delta q_i + \frac{\partial L}{\partial \dot{q}_i}\epsilon\delta\dot{q}_i \right\} + O(\epsilon^2) \right] dt'$$

$$. = \int_0^t \left[\sum_{i=1}^{3N} \left\{ \frac{\partial L}{\partial q_i} - \frac{d}{dt}\left(\frac{\partial L}{\partial \dot{q}_i} \right) \right\} \epsilon\delta q_i + O(\epsilon^2) \right] dt'.$$

The derivation from the second line to the third line is due to integration by parts and the compactness of the test function. Dividing by ϵ and eq. (1.21) yields the Euler-Lagrange equations [3]

$$\frac{\partial L}{\partial q_i} - \frac{d}{dt}\left(\frac{\partial L}{\partial \dot{q}_i}\right) = 0$$

for $i = 1, ..., 3N$. These equations are essentially as same as eq. (1.17). The *symmetry* of the action, i.e. the invariance of the action (1.20) with respect to some transformation, is a quite important property of the Lagrangian since the equations of motion derived by the variation principle are also essentially conserved.

1.2.2   MD algorithms

In a potential based MD simulation, the time evolution of positions and momenta is calculated with these equations (1.17)-(1.19) step by step. The time integral is discretized using the time step δt which should be small enough to integrate the equations accurately. This δt can be a variable when the model considers an energetic, fast event such as an ion recoil process [166]. For an equilibrated system, this is usually a constant and order of 1 fs while the lattice vibrational period is $\sim 10^{-13}$ s in most cases. MD algorithms provide effective, i.e. fast and accurate, numerical calculation of the equation of motion. Basically, the methods aim for an effective representation of a Taylor expansion with respect to the time step δt for the position at the next time step. The Verlet algorithm [231, 232] and its extensions are well known methods. The algorithm computes the position of particle at the $k + 1$-th time step $\vec{r}_{k+1}$ from the current state $\vec{r}_k$, the previous state $\vec{r}_{k-1}$ and the acceleration for the current position $\vec{a}_k$ as

$$\vec{r}_{k+1} = 2\vec{r}_k - \vec{r}_{k-1} + \vec{a}_k \delta t^2.$$

For $t := k\delta t$, this form is obtained by subtracting the Taylor expansions of $\vec{r}(t + \delta t)$ and $\vec{r}(t - \delta t)$ with the notation of $\vec{r}(t - \delta t) = \vec{r}_{k-1}$ and ignoring the terms of $O(\delta t^4)$. This implies that the position at time $t + \delta t$ is predicted by the discretized data at time t and $t - \delta t$ whereas the real position is determined by the continuous accumulation of data during time range $[t, t + \delta t]$ as

$$\vec{r}(t + \delta t) = \vec{r}(t) + \int_t^{t+\delta t} \vec{v}(t)dt.$$

This local discretization error of $O(\delta t^4)$ can lead to a larger global error due to the cumulative mismatch with the exact solution. Indeed, if the magnitude of the error term at each step is assumed to be homogeneous, then the cumulative error at $t + 2\delta t$ is

$$\begin{aligned}
\vec{r}_{k+2} &= 2\vec{r}_{k+1} - \vec{r}_k + \vec{a}_{k+1}\delta t^2 + O(\delta t^4) \\
&= 3\vec{r}_k - 2\vec{r}_{k-1} + (2\vec{a}_k + \vec{a}_{k+1})\delta t^2 + 3O(\delta t^4).
\end{aligned}$$

Inductively it is shown easily that the cumulative error term from k-th iteration step to $k + k'$-th step is

$$\frac{k'(k'+1)}{2}O(\delta t^4).$$

---

[3] The definition of a Lagrangian $L = L(\phi, \partial\phi, x)$ can be generalized as a functional of the n-dimensional field with m variables $\phi(x) = (\phi_1(x), ..., \phi_n(x)), x = (x_1, ..., x_m)$ satisfying the correspondent Euler-Lagrange equations, i.e. $\frac{\partial L}{\partial \phi^{(i)}} - \sum_{j=1}^m \frac{\partial}{\partial x_j}\frac{\partial L}{\partial \phi_j^{(i)}} = 0$ with $\phi_j^{(i)} = \frac{\partial \phi^{(i)}}{\partial x_j}$ for $i = 1, ..., n$ in this case.

Thus for the cumulative global error for $t_{max} := k'\delta t$ is

$$\left(\frac{t_{max}^2}{2\delta t^2} + \frac{t_{max}}{2\delta t}\right) O(\delta t^4) \sim O(t_{max}^2 \delta t^2).$$

Hence the global error is at least order of $O(\delta t^2)$.

A more commonly used algorithm reducing the error is the *Velocity Verlet* algorithm [225] incorporating the velocity term $\vec{v}_{k+1}$ as

$$\begin{aligned}
\vec{r}_{k+1} &= \vec{r}_k + \vec{v}_k \delta t + \frac{1}{2}\vec{a}_k \delta t^2, \\
\vec{v}_{k+1} &= \vec{v}_k + \frac{\vec{a}_k + \vec{a}_{k+1}}{2}\delta t.
\end{aligned}$$

The mathematical accuracy of this method is as same as the Verlet algorithm, but it is superior on a computer of finite precision [54, 225]. For the reduction of the computation step, there is another type of approach called a *moving atom approximation* [95]. The equations of motion are integrated only for atoms that are moving or have had a sufficient force exerted on them by other atoms and thus the number of calculations is reduced significantly [212]. This type of approximation is useful if the system evolution is mainly resulting from an external event such as from ion bombardment, and thermal fluctuation does not play an important role.

In contrast, the Gear's predictor-corrector algorithm is mathematically more accurate but computationally expensive [88, 89][4]. The iteration step is as follows: the predicted position $\vec{r}_{pred,k+1}$ is calculated up to the third order from the current data, i.e. the polynomial function of δt with the coefficients $\vec{r}_k, \vec{v}_k, \vec{a}_k, \vec{b}_k$ as

$$\vec{r}_{pred,k+1}(\delta t) = \vec{r}_k + \vec{v}_k \delta t + \frac{1}{2}\vec{a}_k \delta t^2 + \frac{1}{6}\vec{b}_k \delta t^3.$$

and the other predicted values are simply set as the derivatives $\vec{v}_{pred,k+1}(\delta t) = \frac{d}{d\delta t}\vec{r}_{pred,k+1}(\delta t)$, and $\vec{a}_{pred,k+1}(\delta t) = \frac{d}{d\delta t}\vec{v}_{pred,k+1}(\delta t)$. Then this acceleration $\vec{a}_{pred,k+1}(\delta t)$ is compared with the analytical solution $\vec{a}_{an,k+1}$ obtained by the potential (1.17) for the predicted position $\vec{r}_{pred,k+1}$. The variation

$$\Delta\vec{a}_{k+1} := \vec{a}_{pred,k+1} - \vec{a}_{an,k+1}$$

is the correction parameter and the corrected values are set by

$$\begin{aligned}
\vec{r}_{corr,k+1} &:= \vec{r}_{pred,k+1} + c_0 \Delta\vec{a}_{k+1}, \\
\vec{v}_{corr,k+1} &:= \vec{v}_{pred,k+1} + c_1 \Delta\vec{a}_{k+1}, \\
\vec{a}_{corr,k+1} &:= \vec{a}_{pred,k+1} + c_2 \Delta\vec{a}_{k+1}, \\
\vec{b}_{corr,k+1} &:= \vec{b}_{pred,k+1} + c_3 \Delta\vec{a}_{k+1},
\end{aligned}$$

where c_0, c_1, c_2, c_3 are the fitting constant chosen to optimize the stability and accuracy of the trajectories [89]. The accuracy of the corrected trajectories allows to use a relatively large simulation time step δt.

The Hamiltonian of a simulation system is sometimes not conservative under the assumption that the system is contacting an ideal huge reservoir. For example, a well-known method controlling the temperature of the system is the Berendsen heat bath method [19] in which the Hamiltonian

---

[4]This method is sometimes not favored since it is not symplectic and this leads to enegy drift.

of the system is generally non conservative due to the stochastic coupling to an external bath. The damping force from the reservoir is accomplished by the responsible Langevin equation

$$m_i \dot{\vec{v}}_i = \vec{F}_i - m_i \gamma_i \vec{v}_i + \vec{R}_i(t),$$

where γ_i is the damping (friction) constant and $\vec{R}_i(t)$ is a Gaussian stochastic variable with zero mean with intensity $\int R_i^{(l)}(t) R_j^{(l)}(t+\tau) dt = 2m_i \gamma_i k_B \delta_{0\tau} \delta_{ij}$ for each component $l = x, y, z$. For a fixed reference external temperature T_0 and assuming homogeneous damping constant γ, the time derivation of the system temperature T is then [19]

$$\frac{dT}{dt} = 2\gamma(T_0 - T),$$

and the consistent equation of motion is given by

$$m_i \dot{\vec{v}}_i = \vec{F}_i + m_i \gamma \left(\frac{T_0}{T} - 1 \right) \vec{v}_i.$$

This corresponds to the velocity change $\vec{v}_i \to \lambda \vec{v}_i$ at each time step with

$$\lambda = \sqrt{1 + \frac{\delta t}{\tau} \left(\frac{T_0}{T} - 1 \right)},$$

where τ is the noncritical time constant of the coupling chosen typically of the same order as the vibrational period of the atoms [88]. Similarly, the hydrostatic pressure P of the system with the length of simulation system l_x, l_y, l_z is also controlled by the modified equation of motion

$$\dot{\vec{r}}_i = \vec{v}_i - \frac{\beta(P_0 - P)}{3\tau} \vec{r}_i,$$

where β is the isothermal compressibility which may not be accurately known, and P is the pressure given by

$$P = \frac{2}{3 l_x l_y l_z} (E_{kin} - \Xi)$$

with the *internal virial*

$$\Xi = -\frac{1}{2} \sum_{i<j} (\vec{r}_i - \vec{r}_j) \cdot \vec{F}_{ij}.$$

Here $\vec{F}_{ij}$ is the force on particle i due to particle j. The atomic position, or the length l_x, l_y, l_z is changed to $\mu l_x, \mu l_y, \mu l_z$, i.e. the volume is multiplied by μ^3, at each time step with

$$\mu = \left[1 - \frac{\delta t}{\tau} (P_0 - P) \right]^{1/3}.$$

This method is useful in order to avoid undesired temperature or pressure evolution of the small simulation system due to a relatively large external modification process as well as crystallization of amorphous materials, e.g. an ion impact [167, 224], and the annealing simulation such as solid phase recrystallization processes [187]. Figure 1.2 is an example of an MD simulation for the Ge recrystallization process from Ref. [187]. The model uses a three body Stillinger-Weber type potential [218] with parameters for germanium taken from Ding *et al* [59], Gear's predictor-corrector algorithm with the time step $\delta t \cong 1 fs$ [88] was used. The temperature and pressure are controlled by a Berendsen heat bath and the barostat method respectively. Under zero pressure, a single Ge crystalline amorphized at 2700 K for 100 ps is cooled down to 300 K at a cooling rate of 0.1 K ps^{-1} and equilibrated at 300 K for 100 ps. Then the system is annealed at 800 K for 5 ns.
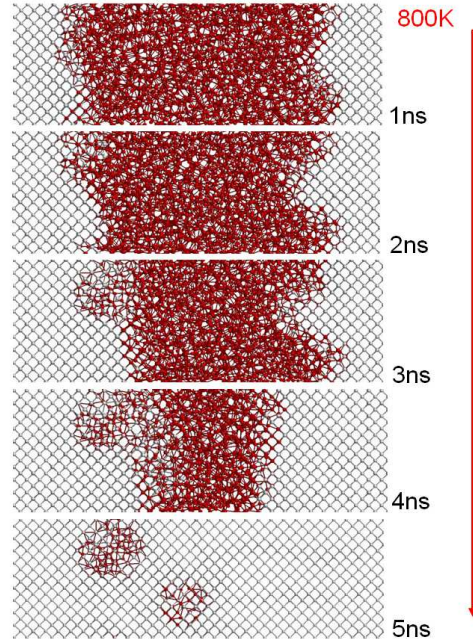
Figure 1.2: Recrystallization process of an amorphous Ge layer containing 3000 atoms. The atoms belonging to deformed sites are shown by red color [187].

1.3 Lattice Monte Carlo simulation

A third level atomistic approach discussed here is the lattice MC method. Instead of the continuum vector space, the atomic states are projected in lattice space based on the crystalline structure, or the system of interest. For example, the Einstein model considers that each atom in the crystalline lattice position is an independent 3D quantum harmonic oscillator and possesses the same frequency. The Debye Model is also a lattice approximation assuming the phonon contribution to the lattice vibration in contrast to the Einstein model [57].

By assuming thermo-dynamical equilibration of the system, the transition of the discrete atomic states can be performed with the MC method. The MC method is utilizing random numbers because the system propagates. In statistical physics, this method is a most important class of numerical solver. Metropolis proposed a calculation scheme of the thermo-dynamically equilibrated states of a physical system in 1953 [150]. The application of the MC method in statistical physics mainly results from such calculation algorithms integrating the equilibrated system.

This long section is laid out as follows. First, some important thermodynamic variables are introduced in section 1.3.1. In section 1.3.2, a limit theorem related to the Metropolis algorithm calculating the thermo-dynamic equilibration of the system is briefly described to see how such algorithms work. These topics will be also discussed in details for the acceleration of the simulation algorithm in chapter 3. KMC method and its application to an abstract particle diffusion in lattice systems are discussed in section 1.3.3. Section 1.3.4 describes another approach to the Schrödinger equation utilizing the MC method and an alternative interpretation of the dynamics of particles mentioned in the first section of this chapter is discussed.

12

1.3.1 Thermodynamic variables

Assume that the system is in thermal equilibrium with a reservoir at temperature T. In 1902, Gibbs showed that the probability $\Pi(\Omega)$ of the state Ω in such system is proportional to the Boltzmann factor of the Hamiltonian [90], i.e.,

$$\Pi(\Omega) \propto \exp(-\mathcal{H}(\Omega)/k_B T). \tag{1.23}$$

Set

$$Z := \sum_{\Omega} \exp(-\mathcal{H}(\Omega)/k_B T). \tag{1.24}$$

the sum of all these factors. The sum ranges over all possible atomic states Ω and we assume the summability, i.e. $Z < \infty$. From eq.(1.23) and (1.24), the probability distribution is

$$\Pi(\Omega) = \frac{\exp(-\mathcal{H}(\Omega)/k_B T)}{Z}. \tag{1.25}$$

This distribution is called the *Boltzmann distribution*, or the *canonical distribution*, or sometimes the *Gibbs field* as a measure of the probability space on the degenerate atomic states of the system. Since the temperature is constant, the kinetic energy of the Hamiltonian can be ignored in eq. (1.25). The sum Z is called the *partition function* which is a quite important quantity describing the statistical properties, such as the internal energy U, the specific heat C, the entropy S, and the Helmholtz free energy $\mathcal{F}$.

Internal energy

The internal energy U is defined as the expectation value of the Hamiltonian $\mathcal{H}$ of the system. Thus

$$U := < \mathcal{H}(\Omega) > = \frac{1}{Z} \sum_{\Omega} \mathcal{H}(\Omega) e^{-\mathcal{H}(\Omega)/k_B T} = -\frac{\partial \log Z}{\partial \beta}, \tag{1.26}$$

with $\beta := 1/k_B T$.

Specific heat

The specific heat C is the variation of the internal energy U with respect to the temperature T. From eq. (1.26), C is represented as

$$C := \frac{\partial U}{\partial T} = k_B \beta^2 \frac{\partial^2 \log Z}{\partial \beta^2}. \tag{1.27}$$

Entropy

The concept *entropy S* was defined first by Clausius during the study of reversible thermodynamic system (Carnot cycle). Clausius and Kelvin derived that the maximal work W efficiency of a Carnot cycle consisting of a hot reservoir A with temperature T_1 and a cold reservoir B with T_2 is given by

$$W = \left(1 - \frac{T_2}{T_1}\right) Q_1, \tag{1.28}$$

where Q_1 is the heat adsorbed isothermally from A. For the heat Q_2 given up isothermally to B, the work is $W = Q_1 - Q_2$. Thus

$$\frac{Q_1}{T_1} = \frac{Q_2}{T_2}$$

from eq. (1.28). Clausius called this conserved quantity *entropy* in his work in 1865. If the system is irreversible, the work W of eq. (1.28) is smaller than the maximal efficiency (*Clausius inequality*). Consequently, the entropy S increases ($S(A) := Q_1/T_1 < S(B) := Q_2/T_2$) during the process. This fact is known as the *second law of thermodynamics*.

Gibbs entropy

The entropy S of statistical physics is defined as follows

$$S := k_B < -\log \Pi(\Omega) >= -k_B \sum_{\Omega} \Pi(\Omega) \log \Pi(\Omega) = k_B \log Z - \frac{1}{T} \frac{\partial \log Z}{\partial \beta}. \tag{1.29}$$

This is the expectation value of logarithmic number of inverse probabilities with respect to all states. This entropy is often called the Gibbs entropy introduced by Gibbs in 1878 after the earlier work by Boltzmann. This quantity is consistent with the entropy of information theory, known as the Shannon entropy, associated with the Gibbs field and with the logarithmic base e except for the Boltzmann constant factor. The Shannon entropy $\mathcal{S}$ in this case is given by

$$\mathcal{S} = -\sum_{\Omega} \Pi(\Omega) \log \Pi(\Omega).$$

From eq. (1.26) and (1.27), one can see the relation

$$C = T \frac{\partial S}{\partial T}. \tag{1.30}$$

Boltzmann's entropy

If it is assumed that all major states possess the same magnitude of Hamiltonian $\mathcal{H}$ and that the other minor states with small contribution to the partition function Z can be ignored, then Z is approximately $Z \approx |[\tilde{\Omega}]| e^{-\mathcal{H}/k_B T}$ with $[\tilde{\Omega}]$ being the set of all such major states. In this case, the Gibbs entropy is simplified as

$$S \approx -k_B \sum_{\Omega \in [\tilde{\Omega}]} \frac{e^{-\mathcal{H}/k_B T}}{|[\tilde{\Omega}]| e^{-\mathcal{H}/k_B T}} \log \frac{e^{-\mathcal{H}/k_B T}}{|[\tilde{\Omega}]| e^{-\mathcal{H}/k_B T}} = k_B \log |[\tilde{\Omega}]|. \tag{1.31}$$

This coarse grained entropy is called Boltzmann's entropy. In 1872, Boltzmann derived this relation which was also formulated by Planck later [39]. This entropy will be again discussed in the equivalence class of the atomistic transition states in chapter 3.4.1.

Thermal fluctuation and canonical ensemble

The set of all degenerate states with the same energy $\mathcal{H}$, the same number of atoms, and the same volume are said to form a *microcanonical ensemble*. Because of the conservation of these quantities, this situation describes an isolated system. Generally, if the system is in contact with a huge thermal reservoir and thermally equilibrates, the energy of the system is fluctuating while the average energy is fixed. This thermal fluctuation plays an important role for the classification of the atomistic transition levels discussed in chapter 3.3. The set of all microstates belonging to some microcanonical ensemble within this fluctuation range is called a *canonical ensemble* in which the probability distribution of states follows the canonical distribution (1.25). The mean fluctuation range is relating to the specific heat, which will be shown below.

The Helmholtz free energy F of the canonical ensemble is defined as

$$F := U - TS. \tag{1.32}$$

From the relations (1.26) and (1.29), it follows

$$F = -k_B T \log Z. \tag{1.33}$$

The *chemical potential* $\mu_c^{(i)}$ of the component atom i is defined as

$$\mu_c^{(i)} = \left(\frac{\partial F}{\partial N_i} \right). \tag{1.34}$$

Specific heat and thermal fluctuation

From the definition (1.26) and (1.27), the specific heat C and the internal energy U satisfy the relation

$$C = k_B \beta^2 \frac{\partial^2 \log Z}{\partial \beta^2} = -k_B \beta^2 \frac{\partial U}{\partial \beta}. \tag{1.35}$$

On the other hand, the partial derivative of U with respect to β is

$$
\begin{aligned}
\frac{\partial U}{\partial \beta} &= -\frac{1}{Z^2} \frac{\partial Z}{\partial \beta} \sum_\Omega \mathcal{H}(\Omega) e^{-\mathcal{H}(\Omega)\beta} - \frac{1}{Z} \sum_\Omega^2 e^{-\mathcal{H}(\Omega)\beta} \\
&= \frac{1}{Z^2} \left(\sum_\Omega \mathcal{H}(\Omega) e^{-\mathcal{H}(\Omega)\beta} \right)^2 - <\mathcal{H}(\Omega)^2> \\
&= <\mathcal{H}(\Omega)>^2 - <\mathcal{H}(\Omega)^2>.
\end{aligned}
$$

Hence the specific heat C is proportional to the second moment of the Hamiltonian. This implies that C can be measured by the mean fluctuation of the canonical ensemble. In other words, the fluctuation range expected from the specific heat C is the *usual fluctuation* of the system. Such a relation is known as the *fluctuation-dissipation theorem* connecting the linear response relaxation of a system from a prepared non-equilibrium state to its statistical fluctuation properties in equilibrium.

Once the specific heat C is known, then the entropy S and the free energy F can be derived by integration of eq. (1.30) and by the definition (1.32), respectively. Since the specific heat can be measured experimentally, this quantity is useful for the quantitative, or qualitative comparison of simulations with experiments.

1.3.2 Metropolis Algorithm and limit theorem

In 1953, Metropolis and his co-workers introduced a novel algorithm for the computation of the canonical distribution of the system from the random sequence of microstates [150].

Let $\mathbb{L}$ be an equilibrated system and denote $\mathcal{O}(\mathbb{L})$ the set of all possible microstates in $\mathbb{L}$. From an arbitrary initial microstate $\Omega_0 \in \mathcal{O}(\mathbb{L})$, the *Metropolis algorithm* constructs a sequence of microstates as follows:
(1) chose a microstate $\Omega \in \mathcal{O}(\mathbb{L})$ randomly as a candidate of the next state Ω_1,
(2) accept the state Ω as the next state Ω_1 with the probability

$$P(\Omega_0, \Omega) = \begin{cases} 1 & (\ \mathcal{H}(\Omega_0) > \mathcal{H}(\Omega)) \\ \exp[-(\mathcal{H}(\Omega) - \mathcal{H}(\Omega_0))/k_B T] & (\ otherwise). \end{cases} \tag{1.36}$$

Here $\mathcal{H}(\Omega_0) > \mathcal{H}(\Omega)$ implies that the initial state Ω_0 is energetically more unstable than Ω. If Ω is rejected, then the current state Ω_0 remains as the next state Ω_1.

Iteration of these steps (1) and (2) yields a sequence of microstates. Since the successive state is only determined by the precursory state, this process is a Markov process. For a long enough sequence constructed by this algorithm, the probability that the state $\Omega \in \mathcal{O}(\mathbb{L})$ appears at an arbitrary t-th step follows the Boltzmann distribution $\Pi(\Omega)$. During a finite computation time, this probability distribution converges uniformly from any distribution of initial states. The *ergodicity* of the system is a postulation that all possible microstates are realized along the Boltzmann distribution during an enough long period. A MC simulation of canonical ensemble performing with the Metropolis algorithm exhibits this ergodicity due to the *detailed balance* of the transition probability and microstates. In order to see this situation more precisely, the limit theorem [244] is briefly introduced here.

For the simplicity of the convergence argument of every summation, microstates of a finitely discretized system $\mathbb{L}$ are considered whereas the argument is essentially similar in the case of infinite with an appropriate measure, e.g. Lebesgue measure in the probability space. Let ϕ denote an arbitrary probability distribution of $\mathcal{O}(\mathbb{L})$ represented by a vector with the dimension of $|\mathcal{O}(\mathbb{L})|$. The transitions of states with certain acceptance probabilities affect this distribution and let ϕ_k be the distribution after k-th transition step. Now consider the sequence $\phi = \phi_0, \phi_1, \phi_2, ...$ of distributions from the initial distribution ϕ with respect to the transition steps. This sequence is a Markov chain (Markovian), i.e., a random sequence with the property that the probability appearing an arbitrary state $\Omega \in \mathcal{O}(\mathbb{L})$ at $k+1$-th step $\phi_{k+1}(\Omega)$ is only depending on the precursor state distribution ϕ_k. Denote the array representation of these distributions ϕ_k with the same symbols. Then the Markovian satisfies the relation [48]

$$\phi_k = \phi \mathbf{T}^k, \tag{1.37}$$

where $\mathbf{T}$ is the transition probability matrix from $\mathcal{O}(\mathbb{L})$ to itself after one simulation time step. This relation is called the *Chapman-Kolmogorov* equation and the transition matrix $\mathbf{T}$ is called the *Markov kernel* on $\mathcal{O}(\mathbb{L})$. Each component of $\mathbf{T}$ represents the transition probability of corresponding microstates Ω to Ω'. This transition probability is denoted by $\mathbf{T}(\Omega', \Omega)$. Then clearly $0 \leq \mathbf{T}(\Omega', \Omega) \leq 1$ and

$$\sum_{\Omega' \in \mathcal{O}(\mathbb{L})} \mathbf{T}(\Omega', \Omega) = 1 \text{ for all } \Omega \in \mathcal{O}(\mathbb{L}). \tag{1.38}$$

A Markov kernel is *primitive* when there exist an integer k' such that $\mathbf{T}^{k'}(\Omega', \Omega) > 0$ for all $\Omega, \Omega' \in \mathcal{O}(\mathbb{L})$. A Markov kernel $\mathbf{T}$ and a distribution ϕ' fulfill the *detailed balance equation* if

$$\mathbf{T}(\Omega, \Omega')\phi'(\Omega') = \mathbf{T}(\Omega', \Omega)\phi'(\Omega) \text{ for all } \Omega, \Omega' \in \mathcal{O}(\mathbb{L}). \tag{1.39}$$

In this case $\mathbf{T}$ is called *reversible* with respect to ϕ'. An important property of such a Markov kernel is formulated as follows:

Limit theorem. *If the Markov kernel $\mathbf{T}$ is primitive and reversible with respect to ϕ', then the sequence of probability distributions from any initial distribution ϕ converges to ϕ' uniformly, i.e.*

$$\phi \mathbf{T}^k \to \phi' \text{ as } k \to \infty,$$

where, the convergence is with the total variation norm, i.e., $||\phi - \psi||$ for two probability distributions $\phi, \psi \in \mathcal{O}(\mathbb{L})$ is given by

$$||\phi - \psi|| := \sum_{\Omega \in \mathcal{O}(\mathbb{L})} |\phi(\Omega) - \psi(\Omega)|. \tag{1.40}$$

16

Proof. The proof is briefly introduced with some important lemmas and relevant notations. The most important quantity is the *contraction coefficient* $c(\mathbf{T})$ of a Markov kernel $\mathbf{T}$ which is defined as

$$c(\mathbf{T}) = (1/2) \max_{\Omega, \Omega' \in \mathcal{O}(\mathbb{L})} ||\mathbf{T}(\Omega, \cdot) - \mathbf{T}(\Omega', \cdot)||. \tag{1.41}$$

Note that from (1.38), the contraction coefficient is always $c(\mathbf{T}) \leq 1$. Two fundamental properties of the contraction coefficient are necessary.

Lemma 1. *Let* ψ, ψ' *be probability distributions and* $\mathbf{S}, \mathbf{S}'$ *be Markov kernels on* $\mathcal{O}(\mathbb{L})$. *Then*

$$||\psi \mathbf{S} - \psi' \mathbf{S}|| \leq c(\mathbf{S})||\psi - \psi'||, \text{ and } c(\mathbf{SS}') \leq \mathbf{c}(\mathbf{S})\mathbf{c}(\mathbf{S}'). \tag{1.42}$$

Lemma 2. *If* $\mathbf{T}$ *is primitive with* $\mathbf{T}^{k'}(\Omega', \Omega) > 0$ *for all* $\Omega, \Omega' \in \mathcal{O}(\mathbb{L})$, *then* $c(\mathbf{T}^{k'}) < 1$.

The following lemma is essential for the limit theorem and thus for the validity of the Metropolis Monte Carlo simulation applying to a canonical ensemble.

Lemma 3. *If* $\mathbf{T}$ *is reversible with respect to* ϕ', *then* $\phi'\mathbf{T} = \phi'$.

The proofs of these lemmas are omitted. For the reference, see e.g. [244], p.81-p.87. Now, it is easy to see the uniformly convergence as follows

$$||\phi_k - \phi'|| = ||\phi \mathbf{T}^k - \phi' \mathbf{T}^k|| \leq ||\phi - \phi'||c(\mathbf{T}^k) \leq 2 \cdot c(\mathbf{T}^{k'})^l,$$

where l is the maximum integer with $k'l \leq k$. The first and the second relations follow from lemma 3 and lemma 1, respectively. From lemma 2 it follows $c(\mathbf{T}^{k'})^l \to 0$ for $l \to \infty$.

$\square$

The uniqueness of the limit distribution for each Markov kernel follows from this theorem. For the Metropolis algorithm the limit distribution is clearly the Boltzmann distribution due to the detailed balance equation (1.39). The uniform convergence follows essentially from the fact that ϕ' is the left eigenvector of $\mathbf{T}$ with the eigenvalue 1. The ergodicity of the simulation system is exhibited through a certain number of iterations. In other words, iterations should continue until the probability distribution converges close enough to the limit distribution of the specified Markov kernel so that a steady state of the system is obtained.

The property can be extended to a quite general form with some additional assumptions.

Law of large number. *Let* $\mathbf{T}_k, k = 1, 2, ...$ *be the Markov kernels on* $\mathcal{O}(\mathbb{L})$. *Assume that each Markov kernel* $\mathbf{T}_i$ *is reversible with respect to* ϕ_k *with the conditions*

$$\sum_{k=1}^{\infty} ||\phi_k - \phi_{k+1}|| < \infty, \text{ and } \lim_{j \to \infty} c(\mathbf{T}_j...\mathbf{T}_{j+K(j)}) = 0$$

for some sequence $K(j) > 0$ *with* $\lim_{j \to \infty} \frac{K(j)}{j} = 0$. *Then there exists the limit distribution* $\phi_\infty = \lim_{k \to \infty} \phi_k$ *and for every arbitrary function* f *on* $\mathcal{O}(\mathbb{L})$, *every initial distribution* ψ *on* $\mathcal{O}(\mathbb{L})$, *every sequence* $\Omega_0, \Omega_1, ...$ *of the microstates in* $\mathcal{O}(\mathbb{L})$ *constructed by* ψ *and* $\mathbf{T}_k$ [5], *the means in time of* $f(\Omega_k)$ *converges to the* ϕ_∞- *expectation value of* f, *i.e.*

$$\frac{1}{k} \sum_{j=0}^{k} f(\Omega_j) \to \sum_{\Omega \in \mathcal{O}(\mathbb{L})} f(\Omega)\phi_\infty(\Omega) \tag{1.43}$$

---

[5]In the sequence, the probability of $\Omega_k = \Omega$ is $\hat{\psi}\mathbf{T}_1...\mathbf{T}_k(\Omega)$ for all $\Omega \in \mathcal{O}(\mathbb{L})$ and $k = 0, 1, 2, ...$, where $\mathbf{T}_0 \equiv \mathbf{1}$.

for $i \to \infty$ with $L^2(P_\psi)$ norm. Here, for two probability distributions $\phi, \phi' \in \mathcal{O}(\mathbb{L})$, $L^2(P_\psi)$ norm $||\phi - \phi'||_{L^2(P_\psi)}$ is given by

$$||\phi - \phi'||_{L^2(P_\psi)} := \sum_{\Omega \in \mathcal{O}(\mathbb{L})} \psi(\Omega)[\phi(\Omega) - \phi'(\Omega)]^2.$$

The proof is omitted (see Ref.[244], p.106-p.109). Note that if all Markov kernels are the same, then $\mathbf{T}_k = \mathbf{T}^k$ and $\phi_k = \phi_\infty = \phi'$ in the limit theorem and the mean of any physical value of microstates in time converges to the expectation value with respect to the canonical distribution as mentioned in section 1.3.1.

Such Markov chains and Markov kernels appearing in the theorem are called *inhomogeneous* Markov chains and kernels. The theorem guarantees the convergence of a system with time dependent transition probability such as an annealing process with temperature control under certain condition for the sequence of the responsible inhomogeneous Markov kernels.

Remarkably, the convergence of the system depends on the proper contraction coefficient of the Markov kernel resulting in the transitivity from any state to any state (lemma 2). By using such an algorithm, the probability distribution of the microstates converges to the limit distribution such that the Markov kernel is reversible with respect to it. Since every Markov kernel representing a probabilistic transition process possesses the right eigenvalue 1 with the right eigenvector $\mathbf{1}$, it possesses the left eigenvector consistent with the eigenvalue 1. This implies that every such Markov kernel possesses the unique limit distribution. The question is the stability of the system in the sense of the vicinity from the original evolution process under the modified transition probability which is discussed in chapter 3.

1.3.3 Kinetic Monte Carlo Simulation

Instead of the random choice of successive microstates, the candidates of possible transitions can be restricted on the kinetic pathways of the system evolution. The method considers local events randomly chosen and the accumulative evolution process of the target thermodynamical system. An important example is the evolution of the magnetism induced by the accumulation of spin-flips influenced by the local configuration. This system is known as the Ising spin system [110]. Bortz, Kalos and Lebowitz introduced the time scale into the MC simulation in order to investigate the equilibrium properties and the time evolution of the Ising spin system [24]. The Hamiltonian of this system is given by

$$\mathcal{H} = -J \sum_{<i,j>} s_i s_j - B \sum_i s_i,$$

where J and B are the constants relating to the material and external magnetic field respectively and the summation i as well as $<i, j>$ range over all lattice sites as well as all nearest neighbor spin pairs respectively. The model considers the iteration of simulation steps as follows [169]:

(0) Set the time $t = 0$.

(1) Form a list of all possible transitions, say N types of transitions (spin-flips), as well as the rate r_i with respect to the nearest neighbor configuration of each spin and calculate the cumulative function $R_j = \sum_{i=1}^{j} r_i$ for $j = 1, ..., , N$. Denote $R = R_N$.

(2) Get a uniform random number $u \in [0, 1]$.

(3) Find j such that $R_{j-1} < uR < R_j$ and carry out the event j.

(4) Get a new uniform random number $u' \in [0, 1]$ and update the time with $t = t + \Delta t$ where:

$$\Delta t = -\frac{\log u'}{R}.$$

(5) If the list should be reformed due to the transition, return to step (1). Otherwise return to step (2).

This algorithm is called the N-fold way, or the Bortz-Kalos-Lebowitz (BKL) algorithm, or the KMC algorithm, or residence-time algorithm. The time progression of step (4) implies that the transitions are Poisson processes. For a long time simulation with constant R, however, it is same as adding $1/R$ since the expectation rate is $-\int_0^1 \log u \, du = 1$ if the system has no periodical correlation with time step. From step (3), the attempt frequency of transitions is inhomogeneous and depends on the type of event. Moreover, the cumulative time R determined by step (1) is system dependent. In the original work, they considered a 10-fold way. All 6400 spins in the two-dimensional square lattice with periodic boundary conditions (PBC) are classified into 10 transition types (two spin types $\times$ 0-4 spin up NNs) with

$$R_{10} = \sum_{i=1}^{10} n_i P_i,$$

where n_i and P_i are the total number and the flip probability of spin with type i configuration. The probability P_i is determined by the Boltzmann factor with respect to the difference of the Hamiltonian ΔE before and after spin flip as $P_i = \min\{1, e^{-\Delta E/k_B T}\}$.

There are also various application examples of KMC. In addition to the spin model, atomic diffusion models including vacancy migration and epitaxy growth are also important applications of the KMC simulation. In each case, the attempt frequency and the acceptance ratio are crucial parameters for the simulation.

In this work, the KMC simulations have been performed for the surface diffusion of Ag/SiO$_2$ (chapter 2) and molecular beam epitaxy growth of Au/SiO$_2$ as well as Ag/SiO$_2$ (chapter 2, 3). The transition states are modelled by individual atomic hopping between the discrete lattice sites. The transition types are therefore restricted to movements in the underlying lattice structure. A typical algorithm employed in these models is as follows:

(0') Set the time $t = 0$ and form the list of all acceptance probabilities $\{P_i\}$ of jump events with respect to the possible nearest neighbor configurations.

(1') Set $R = Nr$, where N is the number of atoms listed as $\{1, ..., N\}$ and r is the number of jump directions depending on the responsible lattice structure.

(2') Get a uniform random integer $u \in [1, R]$.

(3') Find atom i such that $i = \lfloor u/r \rfloor$ and carry out the jump event with the direction $r^* = u \mod r$ with the probability P_{i*} corresponding to the local configuration of atom i.

(4') Update the time with $t = t + \Delta t$ where:

$$\Delta t = \frac{1}{N}.$$

(5') If another type of event is carried out, e.g. deposition, and the number of atoms N is changed, return to step (1'). Otherwise return to step (2').

The list formed in step (0') is called the *look up table*. The total number of atoms is conserved during the jump attempt in step (3'). Such an algorithm is called the *Kawasaki type algorithm* after the exchange spin flip model of Kawasaki [115, 116, 117]. A significant difference between the BKL algorithm and the algorithm described above is that the acceptance probability does not contribute to the simulation time. An advantage of this method is that the simulation time unit proceeds constantly, i.e. simply proportional to the real time. From the harmonic transition states theory of Vineyard [237], the transition frequency Γ can be represented as

$$\Gamma = \omega_* e^{-E_a/k_B T}, \tag{1.44}$$

where ω_* is the pre-factor relating to the lattice frequency of system and E_a is the activation energy of the transition. Thus by assuming the constant pre-factor (overall frequency), the transition rate follows the Arrhenius temperature dependence with respect to the activation barrier E_a. Hence if the probability P is chosen as

$$P = e^{-E_a/k_B T}, \tag{1.45}$$

then one iteration step of all atoms corresponds to one overall frequency which is usually in THz range ($10^{12} - 10^{13}$ s^{-1}). Together with the algorithm proceeding with the simulation time proportional to the real time, one can use the simulation time to determine real time. This will be discussed in chapter 3.

A disadvantage is that the acceptance ratio (1.45) is normally quite small at low temperature and many jump attempts are wasted. In order to reduce the computation time, a minimum activation barrier E_{min} of the system is subtracted from E_a, i.e.,

$$P = e^{-(E_a - E_{min})/k_B T}. \tag{1.46}$$

In this case, the correspondence between one simulation time unit (tu) and the real time is

$$1 \text{ [tu]} \cong \omega_*^{-1} e^{E_{min}/k_B T} \text{ [s]}. \tag{1.47}$$

However, if the system is large and complicated, then the minimum barrier can be quite small. Contrary, if a minimum migration barrier is chosen to be larger than the real minimum barrier, what happens? The interest of this question is one of the main motivations of this work. One obtains an acceleration of simulation time whereas the accuracy of the transition probability is lost. Further discussion about this acceleration approach will be handled in chapter 3.

Concerning the acceleration of simulation system using an MD approach, the temperature enhancement of the simulation system is known. Voter considered a general method for accelerating the of infrequent events in solid with a biased potential in 1997 [240, 241]. Another method is temperature accelerated dynamics (TAD) by Sørensen and Voter in 2000 [214]. In their method, the events are restricted on the events at original temperature with a kinetic energy basin and corresponding time is calculated from the transition states theory [8, 41].

Diffusion equation

For some specific atomistic KMC models, the diffusion coefficient of adatoms is to be investigated. Generally, the probability distribution $c(t, x, y, z)$ of atom in the three dimensional real space $\mathbb{R}^3$ follows the diffusion equation

$$\frac{\partial c}{\partial t} = D\nabla^2 c, \tag{1.48}$$

where D lu^{2}tu^{-1} represents the diffusion coefficient in lattice sites with lu denoting lattice unit of $\mathbb{R}^3$. Analytically, this type of linear partial differential equation can be solved by using the Fourier transformation

$$\mathcal{F}(c(t,\mathbf{x})) = \hat{c}(t,\mathbf{k}) = (2\pi)^{-3/2} \int_{\mathbb{R}^3} c(t,\mathbf{x}) e^{-i\mathbf{k}\cdot\mathbf{x}} d\mathbf{x}$$

where i is the imaginary number and $\mathbf{x}$ and $\mathbf{k}$ represent 3D vectors. This transform is reversible (the Fourier inversion theorem) and the inverse Fourier transform yields

$$c(t,\mathbf{x}) = \mathcal{F}^{-1}(\hat{c}(t,\mathbf{k})) = (2\pi)^{-3/2} \int_{\mathbb{R}^3} \hat{c}(t,\mathbf{k}) e^{i\mathbf{k}\cdot\mathbf{x}} d\mathbf{k}. \tag{1.49}$$

Set (*solution Ansatz*)
$$c_{\mathbf{k}}(t, \mathbf{x}) := \hat{c}_{\mathbf{k}}(t)e^{-i\mathbf{k}\cdot\mathbf{x}},$$

where $\hat{c}_{\mathbf{k}}(t)$ is the transformed distribution $\hat{c}(t, \mathbf{k})$. Then the time derivative is

$$\frac{\partial c_{\mathbf{k}}}{\partial t} = e^{-i\mathbf{k}\cdot\mathbf{x}}\frac{\partial \hat{c}_{\mathbf{k}}}{\partial t},$$

and the spatial derivative is

$$\nabla^2 c_{\mathbf{k}} = -\hat{c}_{\mathbf{k}}(t)(\mathbf{k}\cdot\mathbf{k})e^{-i\mathbf{k}\cdot\mathbf{x}}.$$

Thus if for all $\mathbf{k}$, $c_{\mathbf{k}}(t, \mathbf{x})$ satisfies

$$e^{-i\mathbf{k}\cdot\mathbf{x}}\left[\frac{\partial \hat{c}_{\mathbf{k}}}{\partial t} + D\hat{c}_{\mathbf{k}}(t)(\mathbf{k}\cdot\mathbf{k})\right] = 0, \tag{1.50}$$

then $c(t, \mathbf{x})$ satisfies the diffusion equation (1.48) from the representation form (1.49). Eq. (1.50) is reduced to an ordinary differential equation of order one and can be solved as

$$\hat{c}_{\mathbf{k}}(t) = \hat{c}_{\mathbf{k}}(0)e^{-D|\mathbf{k}|^2 t}.$$

Substituting into eq. (1.49), the solution $c(t, \mathbf{x})$ is represented as

$$c(t, \mathbf{x}) = (2\pi)^{-3/2}\int_{\mathbb{R}^3} \hat{c}_{\mathbf{k}}(0)e^{-D|\mathbf{k}|^2 t - i\mathbf{k}\cdot\mathbf{x}}d\mathbf{k}. \tag{1.51}$$

For the initial distribution $c(0, \mathbf{x})$, the inverse transformation yields the initial coefficients

$$\hat{c}_{\mathbf{k}}(0) = (2\pi)^{-3/2}\int_{\mathbb{R}^3} c(0, \mathbf{x})e^{i\mathbf{k}\cdot\mathbf{x}}d\mathbf{x}. \tag{1.52}$$

Especially, for the initial condition

$$c(0, \mathbf{x}) = \delta_{\mathbf{x}'\mathbf{x}} \tag{1.53}$$

with $\delta_{\mathbf{x}'\mathbf{x}}$ being the Dirac delta function, these initial coefficients (1.52) are

$$\hat{c}_{\mathbf{k}}(0) = (2\pi)^{-3/2}\int_{\mathbb{R}^3} \delta_{\mathbf{x}'\mathbf{x}}e^{i\mathbf{k}\cdot\mathbf{x}}d\mathbf{x} = (2\pi)^{-3/2}e^{i\mathbf{k}\cdot\mathbf{x}'}. \tag{1.54}$$

Substituting in (1.51) yields

$$\begin{aligned}
c(t, \mathbf{x}) &= (2\pi)^{-3}\int_{\mathbb{R}^3} e^{-D|\mathbf{k}|^2 t - i\mathbf{k}\cdot(\mathbf{x}-\mathbf{x}')}d\mathbf{k} \\
&= (2\pi)^{-3}\prod_{j=1}^{3}\int_{\mathbb{R}} e^{-Dk_j^2 t - ik_j(x_j - x_j')}dk_j \\
&= (2\pi)^{-3}\prod_{j=1}^{3}\int_{\mathbb{R}} e^{-Dt(k_j - i(x_j - x_j')/2Dt)^2 - (x_j - x_j')^2/4Dt}dk_j \\
&= (4\pi Dt)^{-3/2}e^{-\frac{|\mathbf{x}-\mathbf{x}'|^2}{4Dt}}.
\end{aligned}$$

This solution is for the special initial condition (1.53). It can be extended to more general cases. Let $G(t, \mathbf{x})$ be the *distribution* defined by

$$G(t, \mathbf{x}) := (4\pi Dt)^{-3/2}e^{-\frac{|\mathbf{x}|^2}{4Dt}}. \tag{1.55}$$

Then for the linear differential operator

$$\mathcal{L} := \frac{\partial}{\partial t} - D\nabla^2,$$

G satisfies

$$\begin{cases} \mathcal{L}G = 0 & \text{for } (t > 0) \\ G(0, \mathbf{x} - \mathbf{x}') = \delta_{\mathbf{x}'\mathbf{x}} & \text{for } (t = 0). \end{cases} \quad (1.56)$$

Now consider an inhomogeneous diffusion equation

$$\begin{cases} \mathcal{L}c(t, \mathbf{x}) = g(t, \mathbf{x}) & (t > 0) \\ c(0, \mathbf{x}) = f(\mathbf{x}) & (t = 0) \end{cases} \quad (1.57)$$

for arbitrary measurable functions $f \in L^1(\mathbb{R}^3), g \in L^1[(0, \infty) \times \mathbb{R}^3]$. Set $c(t, \mathbf{x})$ as

$$\begin{aligned} c(t, \mathbf{x}) &= G(t) * f + \int_0^t G(t - s) * g(s)ds \\ &= \int_{\mathbb{R}^3} G(t, \mathbf{x} - \mathbf{x}')f(\mathbf{x}')d\mathbf{x}' + \int_0^t \int_{\mathbb{R}^3} G(t - s, \mathbf{x} - \mathbf{x}')g(s, \mathbf{x}')d\mathbf{x}'ds, \quad (1.58) \end{aligned}$$

where $*$ implies the convolution with respect to the spatial variables. From the fundamental property of the convolution, it follows for $t > 0$

$$\begin{aligned} \mathcal{L}c &= \mathcal{L}(G)(t) * f + \int_0^t \mathcal{L}[G(t - s, \mathbf{x})] * g(s, \mathbf{x})ds \\ &= 0 + \int_0^t \delta(t - s, \mathbf{x}) * g(s, \mathbf{x})ds = g(t, \mathbf{x}) \end{aligned}$$

and

$$c(0, \mathbf{x}) = \delta_{\mathbf{x}'\mathbf{x}}f(\mathbf{x}')d\mathbf{x}' + 0 = f(\mathbf{x}).$$

Hence the function (1.58) satisfies the inhomogeneous diffusion equation with a generalized initial condition (1.57). Such a function G is called the *Green's function* or the *fundamental solution* for the linear differential operator $\mathcal{L}$. It can be easily seen that the fundamental solution G_n for n-dimensional diffusion is given by

$$G_n(t, \mathbf{x}) := (4\pi Dt)^{-n/2} e^{-\frac{|\mathbf{x}|^2}{4Dt}}. \quad (1.59)$$

Various relating methods and applications, e.g. to the boundary (Dirichlet) problem, Laplace equation, and Poisson equation, can be found in any comprehensive text book describing PDE problems (see e.g. [132]). For a rigorous description of the solution derivation of the inhomogeneous diffusion equation, Ref. [91] can be referred to.

Diffusion constants

As an example of the solution process of a physical problem using a KMC simulation, consider the Brownian motion of a single atom in some crystalline lattice gas system. This discrete diffusion process performed with the KMC algorithm mentioned above with nearest neighbor (NN) jumps can be described by the diffusion equation.

The diffusion coefficient D_{sc} for simple cubic (sc) lattice for NN jump diffusion process is calculated as

$$D_{sc} = \frac{1}{6}.$$

Thus for the initial condition

$$c(0, x, y, z) = \delta_{0x}\delta_{0y}\delta_{0z},$$

the statistics of the site occupation probability $c_{sc}(t, x, y, z)$ with sc lattice simulation is expected as the fundamental solution G_3 of the diffusion equation (1.48) with $D = \frac{1}{6}$, i.e.,

$$c_{sc}(t, x, y, z) \approx \frac{1}{\sqrt{2\pi t/3}^3} e^{-\frac{x^2+y^2+z^2}{2t/3}}.$$

For a face centered cubic (fcc) lattice grid represented by the linear combination of vectors

$$\vec{e}_x \pm \vec{e}_z = \begin{pmatrix} 1 \\ 0 \\ \pm 1 \end{pmatrix}, \vec{e}_x \pm \vec{e}_y = \begin{pmatrix} 1 \\ \pm 1 \\ 0 \end{pmatrix}, \pm\vec{e}_y + \vec{e}_z = \begin{pmatrix} 0 \\ \pm 1 \\ 1 \end{pmatrix},$$

the lattice constant is 2 lu and the number of NN sites is 12. Especially, the distance of two NN sites d^{fcc} is

$$d^{fcc} = \sqrt{2} \text{ [lu]}. \tag{1.60}$$

The diffusion coefficient is calculated as

$$D_{fcc} = \frac{1}{3}.$$

Similarly, the diffusion coefficient for the body centered cubic (bcc) case, and for the diamond lattice are given by

$$D_{bcc} = D_{diam} = \frac{1}{2}.$$

Some derivation details are given in appendix A. For crystal structures of bcc, fcc, and sc, this coefficient is represented as [185]

$$D_* = \frac{a_*^2}{\xi_*},$$

where a_* lu is the lattice constant for the crystal structure spanned by the NN jump directions, $1/\xi_*$ tu^{-1} is the frequency of the atom's hopping in the specific direction per simulation time unit, and $*$ indicates the type of crystal structure. This representation is however not valid for the diamond structure.

Figure 1.3 shows the density distribution $c(t, r)$ of the lattice diffusion process simulated by KMC simulations and theoretical prediction by the diffusion equation. The time proceeding in the simulation is considered as a Poisson process since the site occupation probability in a diamond lattice is correlated with the parity of total time steps. From eq. (1.55) and $r := \sqrt{x^2 + y^2 + z^2}$, the radial density $c(t, r)$ is

$$c(t, r) = \sqrt{4\pi Dt}^3 e^{-\frac{r^2}{4Dt}}.$$

The results of KMC simulation (symbols) agree with the theoretical prediction (solid curves) excellently.

If the diffusion is restricted by an annihilation rate of the particles to a short reaction diffusion time range, this kind of approximation is not accurate for the local density representation due to the overlapping area of random walks (see chapter 2.2.3).
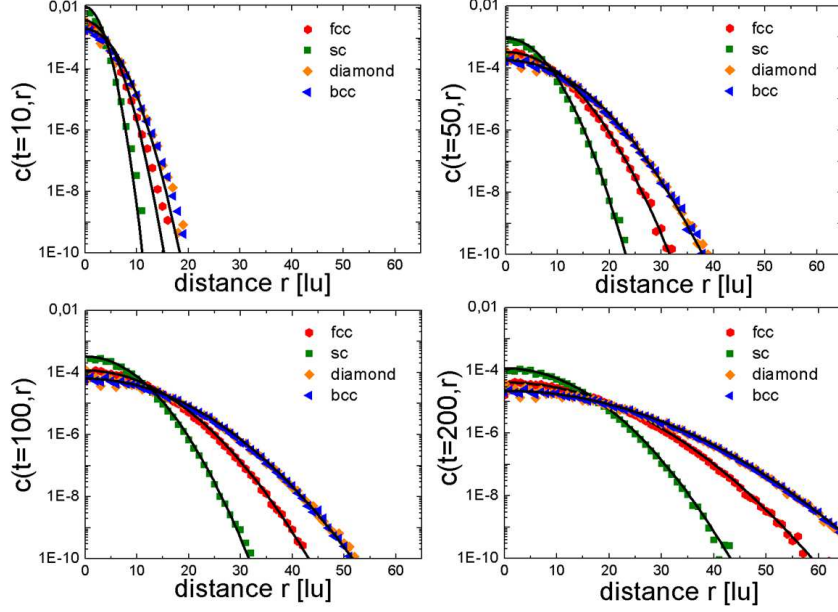
Figure 1.3: Density distribution $c(t, r)$ of free diffusion in fcc, sc, diamond, and bcc lattice cells. KMC simulation (symbols) and theoretical prediction by eq. (1.55) (solid curves) are shown.

1.3.4 Imaginary time reaction diffusion

Now consider the Schrödinger equation (1.5) again. The diffusion process in the discrete lattice cell follows the diffusion equation (1.48) as seen above. If one compares these two linear PDEs, there is some similarity. In fact, if ψ is assumed as a holomorphic function with respect to the complex time evolution $t = t_\Re + t_\Im$, since the complex conjunction of the wave function ψ^* should satisfy the Schrödinger eq. (1.5) as well, it follows that

$$
\begin{aligned}
i\hbar \frac{\partial}{\partial t_\Re} \psi^* &= \left[-\frac{\hbar^2}{2m} \nabla^2 + V(\vec{r}) \right] \psi^* \\
-\hbar \frac{\partial}{\partial t_\Im} \psi^* &= \left[-\frac{\hbar^2}{2m} \nabla^2 + V(\vec{r}) \right] \psi^* \\
\hbar \frac{\partial}{\partial t_\Im} \psi^* &= \left[\frac{\hbar^2}{2m} \nabla^2 - V(\vec{r}) \right] \psi^*.
\end{aligned}
\tag{1.61}
$$

Here, the derivation from the first equation to the second equation is due to the well-known Cauchy-Riemann equations. The interpretation of eq. (1.61) is that the particle diffuses with the imaginary time evolution and the potential field $V(\vec{r})$ is the annihilation rate of the particle. Where is the particle annihilated? It might be going to the next site along the real time axis. The intriguing aspect of this conversion is that the momentum operator in the real time is simply the gradient in the imaginary time, i.e.

$$
\hat{\vec{p}}_\Re = \frac{\hbar}{i} \frac{\partial}{\partial \vec{r}}, \hat{\vec{p}}_\Im = \hbar \frac{\partial}{\partial \vec{r}}.
$$

The imaginary time Schrödinger equation is thus

$$
\hbar \frac{\partial}{\partial t_\Im} \psi^* = \hat{\mathcal{L}} \psi^*,
\tag{1.62}
$$

24

where $\hat{\mathcal{L}}$ is the Lagrangian operator. This aspect of quantum mechanics can be easily incorporated into the path integral formalism of Feynman [82], if the annihilated particle appears at the same position at the next real time step. The possible pathways are restricted by weighting the range of imaginary lifetime at each discrete real time step. Since eq. (1.61) is essentially a reaction diffusion equation, this range is determined by the *diffusion coefficient*, i.e. the mass, and the *transition probability* from the imaginary time evolution to the real time evolution that is the potential energy. This imaginary diffusion coefficient $D_\Im$ has then the dimension of $lu^2 t_\Im^{-1}$. Since the diffusion coefficient is represented by

$$D_\Im = \frac{\hbar^2}{2m},$$

the dimension of imaginary time has the units of inverse energy. Note that these paths are homotopic relative to their start- and end points so long as the physical quantity is well-defined in the consistent region of the complex time plane. Hence the physical quantities arising from the integration with respect to the complex time is determined only by the both endpoints of paths and independent from the individual pathways in this case.

The method which involves solving the Schrödinger equation in the some way as the reaction diffusion equation is known as the *random-walk method* introduced by Anderson in 1975 firstly for calculating the optimal electron structure of molecules [5, 6, 7]. The real time $t_\Re$ is converted as imaginary time $it_\Re$ in his model. This diffusion aspect is often utilized in time dependent quantum Monte Carlo methods. These methods handle the time evolution of complex quantum-classical system of different kinds of particles, such as electrons and nuclei, beyond the Born-Oppenheimer approximation. As a recent application of this method, Christov calculated the time dependent ionization, correlated ground state energies, and the time dependent dipole moment under external electromagnetic field of para- and ortho-helium [49]. For the model of N-electron system, a definite i-th electron trajectory is chosen as the k-th Monte Carlo (random) walker and each trajectory $\vec{r}_i^{\;k}(t)$ follows the first order de Brogli-Bohm guidance equation

$$\frac{d}{dt}\vec{r}_i^{\;k}(t) = \frac{\hbar}{m}\mathrm{Im}\left[\frac{\nabla_i \Psi^k(\mathbf{x}, t)}{\Psi^k(\mathbf{x}, t)}\right]_{\mathbf{x}=\mathbf{x}^k},$$

where Ψ is an anti-symmetrised product

$$\Psi^k(\mathbf{x}, t) = A\prod_{i=1}^{N}\psi_i^k(\vec{r}_i, t)$$

with guide waves $\psi_i^k(\vec{r}_i, t)$, the antisymmetrization operator A including the spin states, and the position vector $\mathbf{x}^k = \mathbf{x}^k(t) = (\vec{r}_1^{\;k}(t), ..., \vec{r}_N^{\;k}(t))$. The guide wave follows the time-dependent Schrödinger equation for the electron i

$$i\hbar\frac{\partial}{\partial t}\psi_i^{\;k}(\vec{r}_i, t) = \hat{\mathcal{H}}(\vec{r}_i, \vec{r}_i^{\;k}(t))\psi_i^{\;k}(\vec{r}_i, t),$$

where the Hamiltonian operator $\hat{\mathcal{H}}$ consists of the operators for the kinetic energy $-\frac{\hbar^2}{2m}\nabla_i^2$, for the electron-nuclear interaction $V_{e-n}(\vec{r}_i)$ and for the electron-electron interaction

$$\sum_{j=1, j\neq i}^{N} V_{e-e}(\vec{r}_i - \vec{r}_i^{\;k}(t)).$$

From the initial set of guide waves, one obtains the evolution of trajectories and consistent guide waves through the computation of these equations mentioned above [50]. Especially, the guide waves relax to the ground state owing to the imaginary time evolution. Finally, from M Monte Carlo sample walkers, the squared modulus $|\psi_i(\vec{r}_i, t)|^2$ of the wave function representing i-th electron is approximated as the probability distribution of trajectories $\{\vec{r}_i{}^k(t)\}_k$, i.e.,

$$|\psi_i(\vec{r}_i, t)|^2 = \frac{1}{M} \sum_{k=1}^{M} \delta_{\vec{r}_i \vec{r}_i{}^k(t)}.$$

There is another application example for a larger system. Amera and co-workers reported a method for finding the global energy minimum of a many body system using this imaginary time converted Schrödinger equation evolution [4]. The method finding the global minimum was originally proposed by Kostrowicki *et al* as a deformation method of potential hypersurfaces using diffusion like evolution with respect to some *time* [127]. They realized that after some *time*, the local minima of the initial potential surface disappear and the global minimum remains. Amera *et al* pointed out that this *time* is the imaginary time in the Schrödinger equation. In both models, each atom is represented as a Gaussian wave packet and whole system is considered as a Hartree product, i.e. a simple multiplication, of single wave functions. For the inter atomic potential, a Lennard-Jones type potential is utilized and the global minimum configuration energies for small clusters are calculated as a function of the imaginary time [4]. A comprehensive review of these diffusion (quantum) Monte Carlo (DMC) methods can be found in Reference [87], for instance. Figure 1.4 illustrates an intuitive description of the DMC method taken from [87]. A single particle is confined by a potential well $V(x)$. The initial walker distribution Ψ_{init} is uniform and converges towards the ground state Ψ_0 as the imaginary-time propagation with $t_\Im$. τ is the single imaginary time step. The wave function Ψ_0 corresponds to the mean imaginary residential time and therefore this aspect coincides with the statistical quantum interpretation of de Broglie-Bohm theory [22, 23].
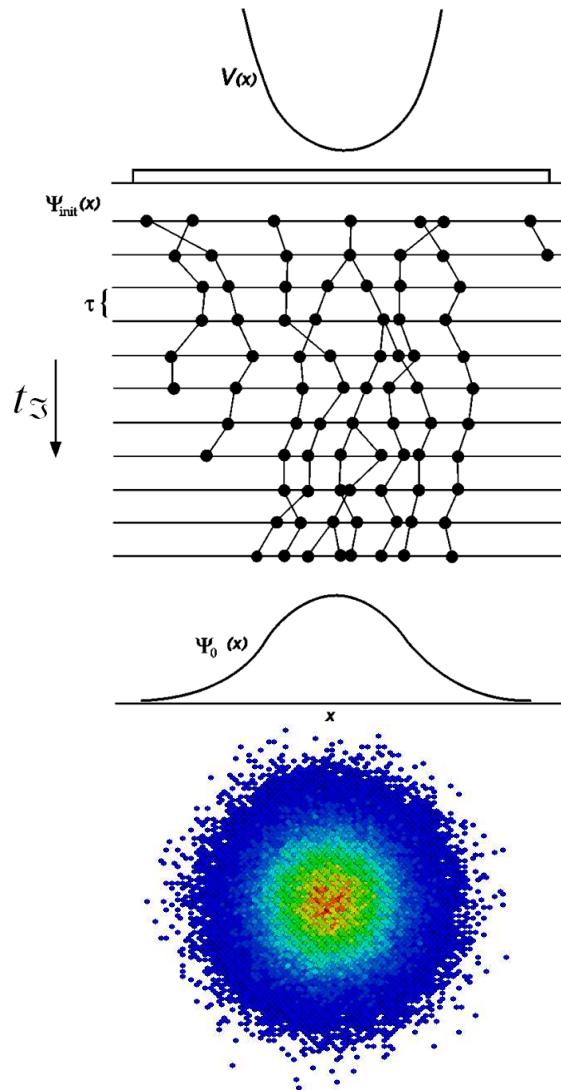
Figure 1.4: A schematic description of the DMC method from Ref. [87] and a cross section of the 3D particle distribution calculated by a lattice KMC simulation. Color indicates the site occupation probability through the imaginary time particle diffusion.

Chapter 2

Cluster Growth on Pre-patterned Surfaces

Functional nanostructures are explored by in both fundamental studies of materials science as well as in industrial applications. Nanoclusters (NCs) of noble metals have quite intriguing optical properties such as surface plasmon resonances [122] which can be utilized, e.g., for highly sensitive protein detection [104]. In particular, well-aligned metallic nanoparticles and nanowires provide novel electromagnetic, optical properties and are promising candidates for transparent conductive electrodes in advanced semiconductor devices [130, 137]. Some useful properties of NCs are strongly influenced by their shape and size [68, 122] and thus an accurate NC growth simulation is an attractive tool in order to understand the details of growth processes under various conditions. Traditionally, a fabrication of NCs, or nano colloid particles by chemical treatment is a common method since Faraday reported the first optical property of an Au nanocolloid in 1847 [75].

As a bottom-up technique for the manufacture of templates for functional metallic nanostructures, low energy (≤ 1 keV) ion bombardment is a well established method [118, 164, 175], which can be used to produce adjustable ripple structures with respect to height and wavelength. Oates *et al* [175] made self-organized arrays of Ag and Co nanoclusters by utilizing radio frequency magnetron sputtering on oxidized, rippled Si templates. Camelio *et al* [33] reported long-range ordered Ag nanoclusters produced by shadow deposition using ion-beam sputtering on BN (or Si_3N_4) doped, rippled Al_2O_3. Oxidized, amorphous substrates are often utilized as templates for such metal deposition since their weak interaction promotes Volmer-Weber (VW) type growth of nanoclusters (NCs) and the weak adsorption (physisorption) of metals on vitreous silica (v-SiO_2) results in an extremely low initial sticking probability [247].

Metals generally possess high adsorption energies at defect sites (chemisorption) [143] and therefore trigger heteronucleations which is considered as the dominant mechanism for metal nucleations on v-SiO_2. Energetic metal deposition using sputtering [33, 175] induces scattered heteronucleations since the energetic process itself can form surface defects. However, Xu and Goodman [247] established that the initial sticking probability of Cu by vapor deposition on v-SiO_2 depends on the surface temperature. They explained this observation with the precursor model of Singh-Boparai *et al* [204]. The model considers the restricted surface migration due to the difference the migration barrier to the vicinal physisorbed site and the adsorption energy. It would therefore be expected that a more accurate control of metal nucleation could be achieved if the surface were kept defect free so that such physisorbent species would dominate the nucleation process.

Recently, utilizing the electron (e-) beam evaporation instead of sputtering, where the deposition energy is much lower, Ni nanowire formation on rippled SiO_2 surface was reported [184]. With

even slower e-beam evaporation, (growth rate 2.6×10^{-4}nm/s compared to 0.1 nm/s reported in Ref.[184]) highly ordered Ag nanorod arrays grown on pre-patterned amorphous SiO_2 surfaces were successfully produced from self-organized Ag NC's of diameter $\sim$10 nm by Ranjan *et al* [190].

Despite of the small undulation of the rippled surface, the stripe-like Ag nanostructures are very pronounced, reproducible and well-separated. The structures are located on the slopes which point towards the evaporation source where a relatively high local flux rate is expected. However a difficulty of the reproduction process due to a sensitivity of setup conditions is reported experimentally[1]. In order to investigate the understanding at the atomistic level, a computer model of the growth process has been performed with a lattice-based KMC method using a combination of a simplified inter-atomic potential and experimental transition barriers taken from the literature.

In this chapter, the initial nucleation process of deposited metals on slightly pre-patterned substrates is discussed. By controlling the deposition angle, the local flux variation is strongly enhanced even by a slightly pre-patterned surface topography. Together with the idea of the precursor model, initial nucleation process simulations are performed. It is revealed that the sensitivity of the nucleation probability results from the local flux as well as from the restricted surface lifetime of metal monomers (2D gas).

2.1 Nanocluster growth

2.1.1 Classical nucleation theory

Classical Becker-Döring nucleation theory [18] describes the condensation of high concentrated gas materials in the sense of *droplet* formation. In this theory, a continuity equation for the time dependent concentration $\bar{n}_l(t)$ of l-clusters, that contain l atoms, and the cluster current J_l is considered as

$$\frac{\partial \bar{n}_l}{\partial t} + \frac{\partial J_l}{\partial l} = 0. \tag{2.1}$$

Here the cluster current J_l is given by

$$J_l = -R_l n_l \nabla(\bar{n}_l(t)/n_l), \tag{2.2}$$

where R_l is the reaction rate (e.g. droplet surface area times impinging rate), n_l is the number density of l-clusters represented as

$$n_l = n_1 \exp(F_l/k_B T). \tag{2.3}$$

F_l is the formation energy of an l-cluster which is an important quantity and which is also the matter of some disputes. Assuming each cluster to be spherical, the number density can be written

$$n_l = n_1 \exp(\Delta\mu l - Bl^{1-1/d}/k_B T), \tag{2.4}$$

with $\Delta\mu = (\mu^{liq} - \mu^{gas})/k_B T$, and $B = B(T)$ a normalized surface tension in d dimension. Here, μ^{liq} and μ^{gas} are the chemical potential of the liquid and metastable gas phase respectively. The nucleation rate J, i.e. the number of macroscopic droplets formed per unit time and volume from the metastable phase, is given by an Arrhenius formula

$$J = \nu_a \exp(-\Delta F/k_B T), \tag{2.5}$$

---

[1]Ranjan, M. private communication.

where ν_a is the attempt frequency, the energy barrier ΔF is the formation energy of a cluster with the critical size. The problem of the model is the accuracy of the formation energy which is represented by an extrapolation based on macroscopic bulk and surface free energy. This approach is developed by some extended theories, e.g. Lothe and Pound considered the additional degree of freedom accounting for the rotation and translation of the cluster [144]. The nucleation rate J changes typically by a factor of 10^{17} due to this correction because of the exponential dependency of the formation energy in eq.(2.5). Kiang et al suggested [123] an alternative treatment of the 'droplet' which originated from Fisher [83] as

$$n_l = q_0 l^{-(2+1/\delta)} \exp[-\Delta \mu l - b(1 - T/T_c)l^{1/\beta\delta}], \tag{2.6}$$

where q_0, b are constants, β and δ are the critical exponents of the coexistence curve and critical isotherm [84], and T_c is the critical temperature. By assuming the dense gas as a mixture of non-interacting droplets, the pressure can be represented as

$$p = k_B T \sum_{l=1}^{\infty} n_l. \tag{2.7}$$

It has been assumed that eq. (2.6) holds down to very small l. For example, for temperatures far below T_c and $l = 1, 2$, the constants of eq. (2.6) are chosen to fit the measured density and second virial coefficient of the gas [94]. The models of these classical theory work well while for many substances. However, a surprising disagreement with nucleation experiments arises in the region near T_c [96, 108, 109]. The critical nuclei are much larger than predicted. Concerning the free energy evaluation, the Cahn-Hilliard-Langer thory [31, 32, 133] introduces a coarse-grained continuous local order parameter (the density ρ) $f_{CG}(\rho)$. A free energy functional associated with this parameter is

$$F = \int [f_{CG}(\rho(\mathbf{r})) + C(\nabla \rho(\mathbf{r}))^2]d^3\mathbf{r}. \tag{2.8}$$

The constant C is to be found in order to fit F to the bulk macroscopic surface tension assumed normally as of a flat surface. The functional $f_{CG}(\rho)$ is called a *coarse grained free energy density* determined usually as a polynomial function of $\Delta \rho = \rho - \rho_c$ with ρ_c being the critical density. This f_{CG} can be defined in a meaningful way for $0.95 < T/T_c < 1.0$ [21] since the coarse graining is assumed to be done on a scale much larger than molecular distances, but not larger than the correlation length of density fluctuations. Thus for lower temperatures its accuracy is open to doubt. However, for the phenomenon near the critical temperature, such as a spinodal decomposition, the model agrees with the experiment nicely [198]. Further details of nucleation theory can be found in the comprehensive review of Binder and Stauffer [21], and the thesis of Müller [159] (chapter 2 and 5) in which the KMC simulation of spinodal decomposition is described.

2.1.2 Cluster growth on substrates

The study of crystal growth affected by the environment was firstly reported by Lehovec in 1964 [138] for the description of the band-bending in promoting selective adsorption of supersaturated, charged impurities at a semiconductor interface. In the late 1960s, Cho and Arthur developed a method of semiconductor crystal (GaAs) growth on substrates known as Molecular beam epitaxy [47] which is a quite common technique of thin film growth in vacuum today. E-beam evaporation is a useful method of providing molecules in MBE, utilizing an electron beam in order to evaporate the materials to be deposited. Figure 2.1 illustrates a schematic diagram and picture of an e-beam evaporator **a** and an example of the intensity of a molecular beam under Mo deposition with a 300
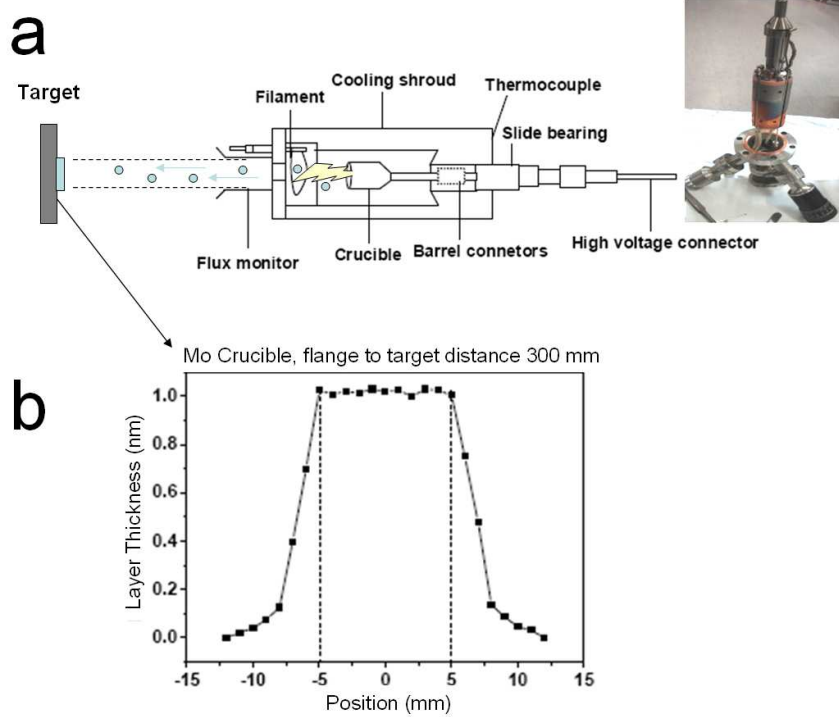
Figure 2.1: E-beam evaporation technique. Figures are cited from Ref. [191] and modified. **a** is a schematic diagram of the e-beam evaporator (**left**) and an actual evaporator is also shown (**right**). **b** shows a typical profile of thin film growth from a Mo crucible.

mm distance from the target **b** referenced from the thesis of Ranjan [191]. Note that if the aim of the evaporator is off, then the intensity of deposits decreases drastically [1]. Further details of the experiments are described in Ref.[191].

Once an evaporated atom arrives on the substrate, various behavior is expected as illustrated in figure 2.2 **a**. Especially, the cluster growth mode is categorized into three types with respect to the relative surface energies [151]. Let γ_D, γ_S and γ_* be the surface energy of the material deposited, of the substrate and the interfacial energy between them respectively. For the case

$$\gamma_D + \gamma_* > \gamma_S,$$

the energy balance of the system tries to minimize the area covered by the deposited material and consequently the deposit tends to grow in the form of three dimensional island called *Volmer-Weber growth* mode (figure 2.2 **b** i). Contrary, for

$$\gamma_D + \gamma_* < \gamma_S,$$

two dimensional island growth of the deposited material on the substrate is observed which is known as *Frank-van-der-Merwe*, or layer-by-layer growth mode (figure 2.2 **b** ii). There is another special case that is the inequality of the surface energies changes during the thin film growth process. This case happens if the elastic influence of the original substrate imposes a strained n-th layer and increases the interfacial energy γ_*. Then the cluster growth mode changes from layer-by-layer to Volmer-Weber. This type is called *Stranski-Krastanov growth* (figure 2.2 **b** iii).

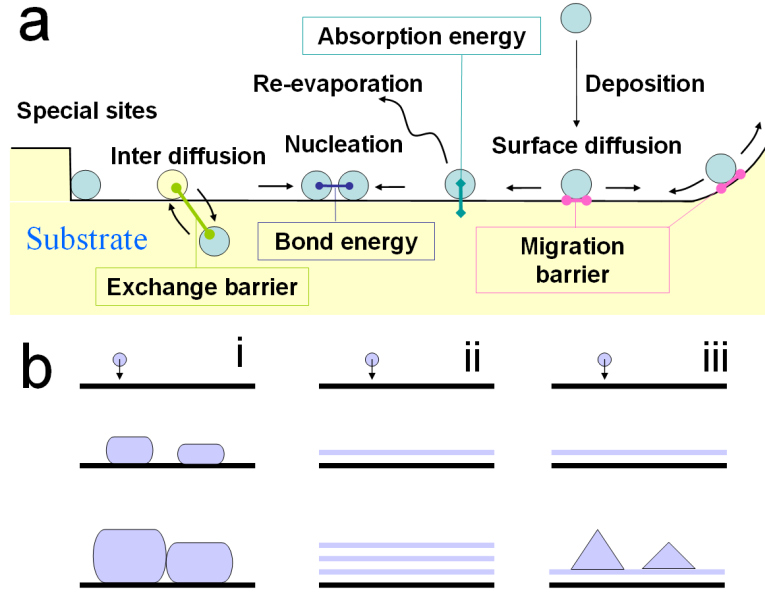[1]See also the discussion in chapter 3.5.3.

Figure 2.2: A schematic description of behavior of deposited atoms and growth modes. **a** Typical actions and characteristic energies. **b** Three cluster growth modes. i: Volmer-Weber growth mode; ii: Frank-van-der-Merwe (layer-by-layer) growth mode; iii: Stranski-Krastanov growth mode.

When an ad-monomer migrating on a metal surface arrives at the edge of the terrace, it preferentially diffuses backward and not to the down step. Ehrlich and Schböbel reported this phenomenon independently in 1966 [67, 199]. This downhill migration barrier at the edge is called the *step edge barrier* or the *Ehrlich-Schwoebel* (ES) *barrier*. For a 3D structure formation by cluster growth, this barrier plays a crucial role in distinct diffusion mechanisms [134, 151]. This barrier can be understood as the bond breaking resulting in the intermediate positioning of migration trace to the down step. Thus if the bond energy is reduced due to the strain field from the original substrate, this can be also reduced. Other intriguing phenomena that may be responsible for the instability towards the mound formation in epitaxial growth are ascending steps [3, 255], fast diffusion processes [186] at the edge as well as exchange jump processes beyond nearest neighbor (NN) position jumps (correlated jumps) [79, 121].

2.1.3 Experimental motivation

Our topic is Ag cluster growth on ripple-like pre-patterned vitreous silica substrate. Figure 2.3 shows a typical rippled template fabricated by 500 eV Ar^+ beam sputtering of Si(100) at an angle of 67° to the surface normal [118, 119, 190]. The wavelength is $\sim$ 35 nm and the ripple height is typically 2-3 nm. Thus the vertical topography variation is much smaller than that of the horizontal variation. An oxidized layer (vitreous (v-)SiO_2) $\sim$2 nm then forms immediately after exposure to the natural environment. The ripples are highly ordered and perpendicular to the ion beam. Then silver was deposited using an e-beam evaporator under ultra high vacuum condition (2.0×10^{-6} Pa) at room temperature (RT) with the source aligned at various deposition angles. Ag clusters observed were typically with Volmer-Weber growth mode preferentially aligned along the ripples. The adsorption energy of Ag and v-SiO_2 is thus expected to be smaller than the Ag-Ag interaction. Figure2.4 shows a typical evolution of Ag clusters by experiment. The number of clusters decreases with increasing mean cluster size [191]. An example of Ag cluster growth at the deposition angle
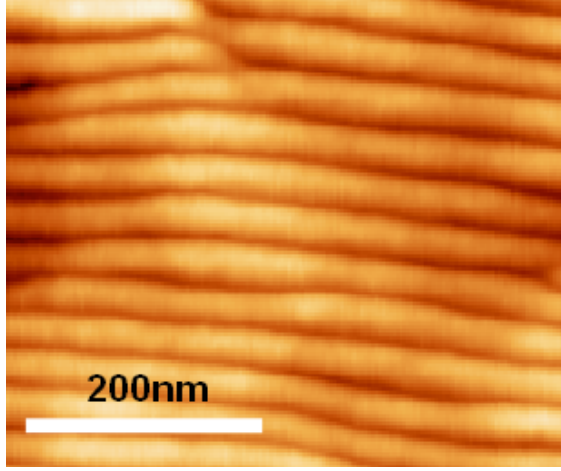
Figure 2.3: An atomic force micrograph image of a rippled, oxide Si surface cited after [172].

$-70°$ with respect to the mean surface normal (see also figure 2.8), the counter direction of the ion beam, is exhibited in figure 2.4. During the deposition the Ag islands grow preferentially along the ripple structure, especially in the late stage (75 min - 105 min). For the island diameter considered in the diagram is thus only the length of island along the ripples and the length perpendicular to the ripples is not taken into account. The number density $n = \sum_l n_l$ of clusters (see also eq. 2.7) in the sample SEM images agrees with the Campbell model [34, 254]

$$n = n_0 \exp(-a_{isl} n_0^{1/3} \bar{d}^{\,2/3}) \tag{2.9}$$

with the island density n_0 at the very beginning, with a constant a_{isl} determined by the shape of the islands [236], and with the average thickness $\bar{d}$ (figure2.4). The growth of mean thickness $\bar{d}$ is $d\bar{d}/dt = 0.1$ nm/min and the constant parameters are $n_0 \sim 8000$ and $a_{isl} \sim 0.036$. This indicates simply that the island density decreases with the growth of the thin film because of coalescence as shown in figure2.2 **b** i. The sample area is $\sim 2.8 \times 10^5$ nm^2 and thus the maximum island density n_0 is calculated to be 2.9×10^{12} cm^{-2} from eq. (2.9). This is around 10 times higher than the result of $Ag/ZnO(0001)$ by Zhang *et al* [254]. This fact suggests that the diffusion length of Ag on v-SiO$_2$ can be short [34]. I.e., the expected ad-monomer diffusion area can be small which is allowing a high maximum island density in the initial stage. A special feature of Ranjan's work is the manipulation of the island density by variation of the surface topography due to different sputtering conditions. By optimization of the deposition condition, one yields a well aligned metal nanowire along the ripples. Figure2.5 shows the scanning electron micrography image after Ag PVD. The deposition time was 75 minutes and the average Ag accumulation was 5.8 mono-layers (ML) calibrated by Rutherford Back Scattering. After deposition, silver nanorods with a mean length 20-120 nm, height and width $\sim$10 nm as well as small NCs with diameter up to 5 nm were obtained.

At the incidence angle of 70°, most of the rippled template was exposed to the incoming Ag vapor. Despite the non-shadowed deposition, the observed Ag NCs grow preferentially along the slope whose normal points towards the evaporation source and only a few small NCs in various growth stages are observed between the connecting Ag alignments. Why there is such a selective nucleation despite the exposure of the surface? Under oblique angle deposition, the cluster intensity is strongly influenced by the topographical condition of the amorphized v-SiO$_2$ substrate. In the following section, this situation is modeled at the atomic level.
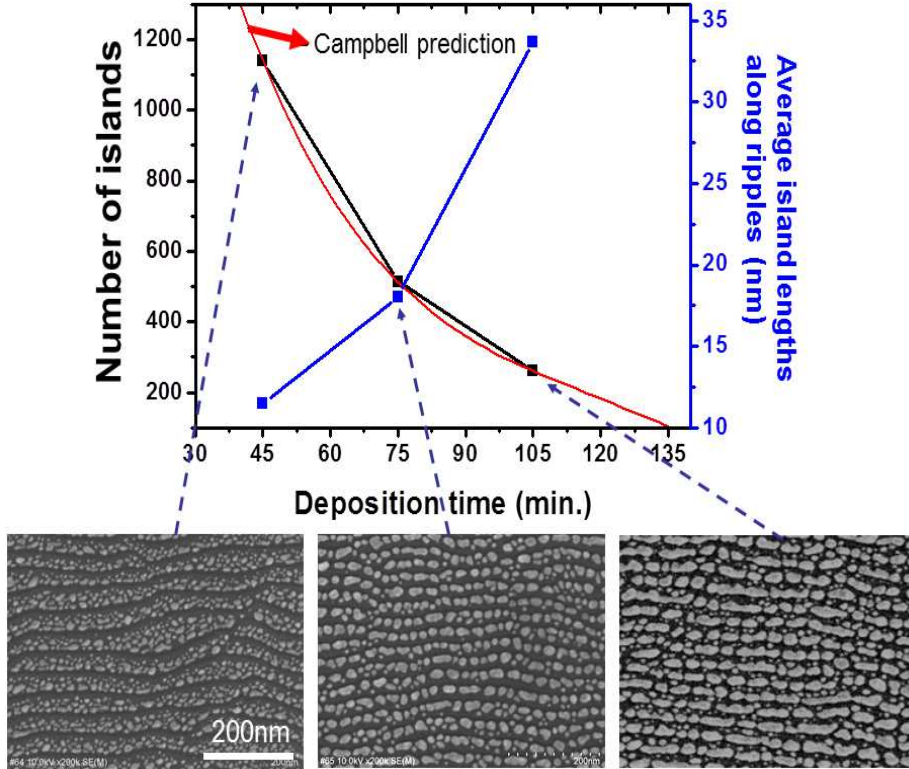
Figure 2.4: Number evolution of Ag islands and the mean island diameter *along the ripples* with deposition time cited after [191]. Three SEM images correspond to the growth stage of 45 min. (**left**), 75 min. (**middle**), and 105 min. (**right**).

2.2 Local flux and surface ad-monomer diffusion

The nucleation of the Ag cluster growth observed in the experiment (figure2.5) is highly ordered despite the small surface topography change. In this section, an ad-monomer diffusion process on the rippled surface modeling the experimental observation is considered. The local flux consistent with the topography together with the ad-monomer migration process affecting to inhomogeneous nucleation is discussed and a discrete reaction-diffusion equation will be derived.

The effect of a patterned substrate on island nucleation is studied by Nurminen *et al* [174] with KMC. Utilizing an Ising-like interaction potential the energy between metal-metal as well as metal-substrate, the thermodynamical behavior of the nucleation process is reported. Their model is motivated by metal deposition on another metal substrate, e.g. Ag/Pt(111). The deposits accumulate mainly at the special sites of a step edge (see figure2.2 **a**). Contrary to their model, the contribution of special sites are suppressed in the model considered here since the target substrate is an amorphized material and an averaged homogeneous interaction is to be investigated.

2.2.1 Surface topography and local flux

Figure 2.6 (a) shows a cross-sectional transmission electron microscopy (TEM) image of a ripple like pre-patterned, oxide Si template [172, 191]. An asymmetrical, saw-like ripple shape is typically observed on a Si surface bombarded [140, 257].

An analytical surface-height function has been found to fit nicely the observed surface topog-
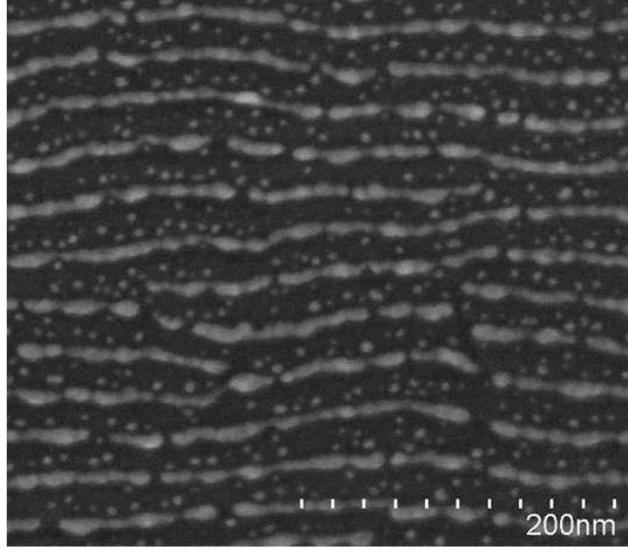
Figure 2.5: SEM image of the rippled surface after Ag deposition for 75 minutes at RT cited from [172]. The average thickness and width of the rods are ~10 nm estimated from the mean coverage 5.8 ML and Ag area fraction. The incidence angle is 70° from the mean surface normal and perpendicular to the ripples.

raphy (figure 2.6 (b)). The function is parametrically represented by

$$
\begin{aligned}
h(x) &= h_0 \sin p \\
x(p) &= l_0(p + \epsilon \sin p),
\end{aligned}
\tag{2.10}
$$

where h_0 and l_0 are typical wave amplitude as well as wavelength, ϵ controls the asymmetric shape of ripples, and p is an arbitrary parameter. While $dx/dp > 0$ there exists the inverse function $p(x)$ and hence the function $h(x)$ is well-defined for $|\epsilon| < 1$. For $\epsilon = 0$ the function is simply the sinusoidal function and for $0 < \epsilon < 1$ it exhibits the gentle slope and the steep slope of the asymmetric ripple.

The parameters used in figure 2.6 (b) are $(h_0, l_0, \epsilon) = (1.6, 7.4, 0.7)$ corresponding to the ripple with the amplitude $h_0 =$1.6 nm and the wavelength $2\pi l_0 \sim 47$ nm.

The amplitude, or ripple height is relatively small compared to its wavelength[2]. At an oblique angle deposition, the variation of the local flux is emphasized by this slightly undulated surface pattern.

The general form of the local flux f_{loc} is formulated as follows. Let $S := \{(x, y, z) \in \mathbb{R}^3 : z = h(x,y)\}$ be a static surface represented by the height function $z = h(x,y)$. Then the local flux $f_{loc}(x,y)$ at a point $(x, y, h(x,y)) \in S$ is given by

$$
f_{loc} = (\vec{i} \cdot \vec{n})f,
\tag{2.11}
$$

where f is the flux of atoms from the evaporation source, $\vec{i}$ and $\vec{n}$ are the unit vectors representing the reverse direction of incident atoms and the surface normal of S, respectively.

Figure 2.7 shows the correspondence between the local deposition rate and the surface topography with the ripple parameters for $(h_0, l_0, \epsilon) = (1.0, 5.5, 0.7)$ in eq. (2.10). The corresponding

---

[2]Intriguingly, a similar form of this parametric function satisfies a nonlinear ordinary differential equation derived by an equation of motion for the atomic flow surface modification model induced by ion beam with the traveling wave assumption (see chapter4).
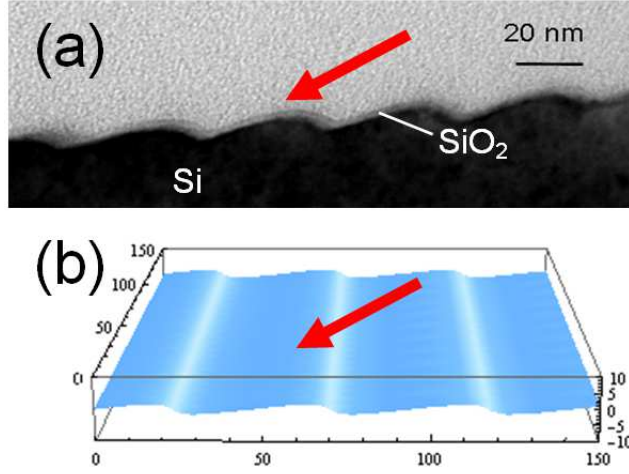
Figure 2.6: (a) A cross-sectional TEM image of a rippled Si surface covered by a thin SiO_2 layer. The surface layers ($\sim$2 nm) are oxidized by exposure to the natural environment [172]. (b) The analytical fitting function of the surface (a) indicated in nm. The wavelength and the height of the ripples are 47 nm and 3.2 nm respectively. Red arrows indicate the ion beam direction.

deposition angle θ	-80°	-70°	-60°	-50°	0°	50°	60°	70°	80°
minimum (%)	0	0	0	16.8	86.3	55.8	40.6	24.1	6.9
maximum (%)	27.7	44.0	58.8	80.0	99.4	94.1	86.9	76.9	64.7
max-min (%)	27.7	44.0	58.8	63.2	13.1	38.3	46.3	52.8	57.8

Table 2.1: List of relative flux rate variation on the sample surface in figure 2.7 with the incident deposition angle θ.

wavelength and ripple height are 35 nm and 2 nm respectively. The deposition angles shown are $\theta = \pm 80°, \pm 70°, \pm 60°, \pm 50°$, and $0°$.

The sharp peaks of the local flux variation for positive deposition angles are located on the slopes of the ripples oriented towards the evaporation source. On the other hand, the local flux peaks for negative deposition angles gradually varies on the slopes. The variation of the local flux ranges from 13.1% to 63.2%. For the positive deposition angle, the substrate surface is fully exposed to the incident flux. If the critical flux f_{crit} for the nucleation of surface ad-monomers is exceeded within this variation range, cluster growth is observed only in the high flux region. The variation increases with increasing deposition angle. In contrast, for the negative deposition angle, the steep slope located on the opposite side to deposition becomes the shadow region and the deposition is restricted in the gentle slope region. The local flux in this exposed region is almost homogeneous and thus relatively homogeneous cluster growth is expected.

2.2.2 Surface gas diffusion under inhomogeneous flux

Let $C(t, x, y)$ and r_d be the surface ad-monomer concentration and the desorption rate on the bare substrate S respectively. The substrate surface obtained experimentally is naturally oxide and amorphized. Consider the average interaction between amorphous surface and metal monomers and assume that adatoms diffuse homogeneously. Hence the diffusion coefficient and the adsorption energy are independent of the local topography of S.

As it is shown in figure 2.3, a pre-patterned surface S is varying approximately in an uniaxial direction. Thus the height function $z = h(x, y)$ can be simply set as $h = h(x)$. The local flux f_{loc}
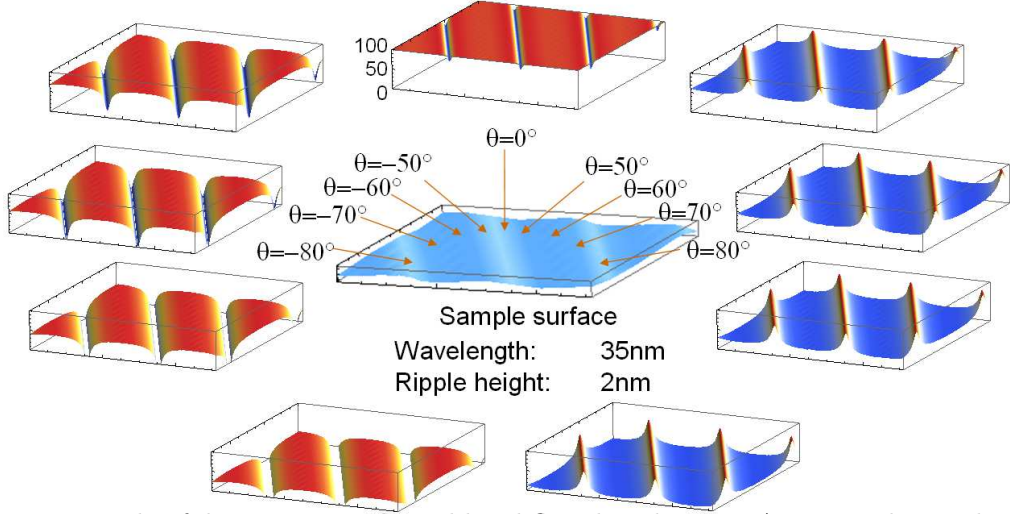
Figure 2.7: Example of deposition angle and local flux distribution. Arrows indicate the directions of depositing atoms. The local flux distributions $f_{loc}(x,y)$ on S with the incident angle $\theta = -80°$ to $\theta = 80°$ (upper right). are shown.

is now given by

$$f_{loc} = f \cos[\theta + \tan^{-1}(dh/dx)], \tag{2.12}$$

where θ is the angle between incident atoms and z-axis (see figure 2.8). The arctangent of the surface gradient is indicated by γ in figure 2.8.

Consider an area conserving mapping Φ from S onto the flat surface $\tilde{S}$ with the coordinate system (u, v). For instance, such a local mapping Φ is given by

$$\Phi : \begin{pmatrix} x \\ y \end{pmatrix} \mapsto \begin{pmatrix} u & = & \int_{x_0}^{x} \sqrt{1 + (dh/dx)^2}dx \\ v & = & y \end{pmatrix}, \tag{2.13}$$

where x_0 is an arbitrary constant. This Φ is an area conservation homeomorphism from the subspace $(x > x_0)$ of S to the subspace $(u > 0)$ of $\tilde{S}$ and even a C^{∞}-diffeomorphism as $h(x)$ is smooth. This mapping projects the rippled surface S onto an extended flat surface $\tilde{S}$ (see figure 2.9).

Let $\tilde{C}$ be the representation of C on $\tilde{S}$. Then the ad-monomer concentration $\tilde{C}$ may obey the diffusion equation

$$\frac{\partial \tilde{C}}{\partial t} - D \, \nabla_{uv}^2 \, \tilde{C} = \tilde{f}_{loc} - r_d \tilde{C}, \tag{2.14}$$

where $D = D(u, v)$ is the diffusion coefficient assumed as a constant on the surface $\tilde{S}$.

Now the transform of the partial derivative with respect to the coordinate system is represented by the Jacobian J with the following form

$$\begin{pmatrix} \tilde{C}_{uu} \\ \tilde{C}_{vv} \end{pmatrix} = J^2 \begin{pmatrix} C_{xx} \\ C_{yy} \end{pmatrix}. \tag{2.15}$$

Hence the square of the Jacobian of the mapping is

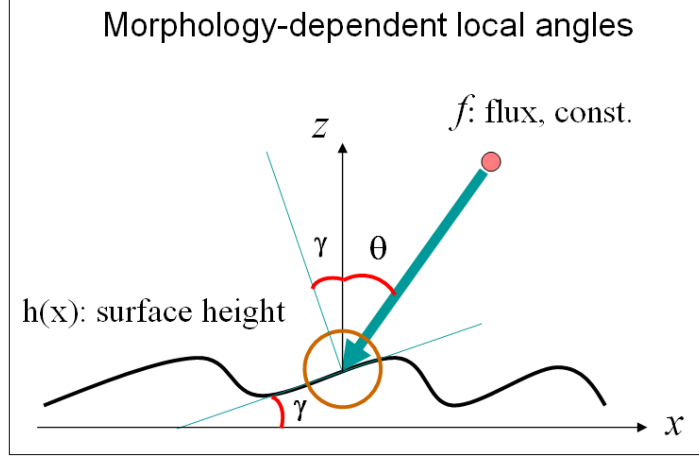$$J^2 = \begin{pmatrix} (\frac{dx}{du})^2 & 0 \\ 0 & 1 \end{pmatrix}, \tag{2.16}$$

Figure 2.8: Schematic description of local angles related to local flux. The angle γ is the arctangent of the surface gradient and θ is the angle between the incident atoms and the mean surface normal (z-axis). θ is positive when the incidence is the counter direction to the positive x-axis.

Together with (2.12), (2.14), (2.13), (2.15) and (2.16), the surface concentration $I(t, x, y)$ on S satisfies

$$\frac{\partial C}{\partial t} - D \left(\frac{1}{1 + h'^2} \frac{\partial^2 C}{\partial x^2} + \frac{\partial^2 C}{\partial y^2} \right) = f \cos[\theta + \tan^{-1}(dh/dx)] - r_d C. \tag{2.17}$$

With the first order approximation for dh/dx, i.e. $(dh/dx)^2, (dh/dx)(d^2h/dx^2), \dots \sim 0$, we have $u(x) \sim x$ in (2.13) and $\cos[\theta + \tan^{-1}(dh/dx)] \sim \cos[\theta + dh/dx]$ therefore the local flux on $\tilde{S}$ is $\tilde{f}_{loc}(u, v) \sim f_{loc}(u, v)$ (see figure 2.9). The average flux $\tilde{f}$ onto $\tilde{S}$ is

$$\tilde{f} = \frac{f \lambda \cos \theta}{\int_0^\lambda \sqrt{1 + h'(s)^2} ds} \sim f \cos \theta. \tag{2.18}$$
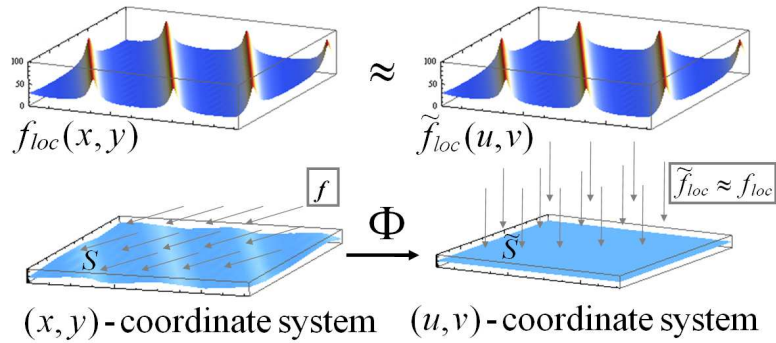
Figure 2.9: Schematic description of the coordination mapping Φ_a (2.13) and the local flux approximation. The local flux $\tilde{f}_{loc}$ of the flat surface $\tilde{S}$ (**right**) is approximated by the local flux f_{loc} of the original rippled surface S (**left**).

Now the equation (2.14) is

$$\frac{\partial \tilde{C}}{\partial t} - D \left(\frac{\partial^2 \tilde{C}}{\partial u^2} + \frac{\partial^2 \tilde{C}}{\partial v^2} \right) = f \; \cos(\theta + dh/dx) - r_d \tilde{C}. \tag{2.19}$$

39

The analytical solution of this equation (2.19) for the plane surface initial condition $\tilde{C}(0, u, v) = 0$ is

$$
\begin{aligned}
\tilde{C}(t, u, v) &= \frac{f}{4\pi D} \int_0^t \int_{\mathbb{R}^2} \frac{1}{s} \\
&\times \exp\left[-\frac{(u - u')^2 + (v - v')^2}{4Ds} - r_d s \right] \cos\left(\theta + \frac{dh(u')}{du'} \right) du' dv' ds.
\end{aligned}
\tag{2.20}
$$

The detail of the derivation is written in appendix B. The function (2.20) describes the ad-monomer concentration in the early stages on the flat surface $\tilde{S}$ under inhomogeneous, normal deposition induced by the oblique angle deposition on the rippled surface S. Obviously, the maximum concentration of the gas condensation at the slope region $u_1 < u < u_2$ is obtained at the deposition angle

$$
\theta = -\tan^{-1}(h'(u))
$$

from eq. (2.12). Since this local flux transformation does not consider the topography change due to the cluster growth itself, the model is valid as long as the surface is cluster free.

Let λ be the wavelength of ripples. Let m and M be the minimum and the maximum of $\cos[\theta + h'(x)]$ for $0 \le x \le \lambda$. Then the range of the ad-monomer concentration $\tilde{C}(t, u, v)$ can be derived from eq. (2.20) as

$$
\frac{mf}{r_d} \left(1 - e^{-r_d t}\right) \le \tilde{C}(t, u, v) \le \frac{Mf}{r_d} \left(1 - e^{-r_d t}\right).
\tag{2.21}
$$

Note that this relation holds for a general topography with a small variation when the first order approximation is valid. Since the range converges exponentially with time, the ad-monomer concentration is simply proportional to the reciprocal of the adsorption frequency which is the ad-monomer lifetime. Especially for metal deposition onto v-SiO$_2$, a high re-evaporation rate is expected due to the weak adhesive energy. This fact suggests the possibility of a strong localization of surface metal monomers concentration by variation of the topography and the deposition angle. The Campbell theory prediction suggests that the mean initial island density is $n_0 = 0.029$ nm^{-2}, i.e., one island per 34 nm^2 surface area. Accounting for the island intensity fluctuation due to the local flux variation 0.24-0.77 for $\theta = 70°$ (table 2.1), the upper limit of the intensity can be deduced from (2.21) as around one island per 10 nm^2.

2.2.3 Surface migration of ad-monomers

The mean migration area during the surface ad-monomer lifetime of monomers deposited on surfaces is characterized as a function of the energy variation between the adsorption- and migration energy. This atomistic model is based on the precursor theory of Singh-Boparai et al [204] considering diffusion and re-evaporation. A simple continuum model describing this reaction diffusion process is constructed and comparison with the simulation model will be discussed.

Adsorption energy and migration barrier

For the surface migration of deposited atoms, the precursor model [204] considers that each surface migration jump attempt possesses a risk of re-evaporation with respect to the difference between migration barrier and surface adsorption energy. This model restricts the mobility and the surface lifetime of deposited metals. The temperature dependency of initial sticking probability for Cu on v-SiO$_2$ was established by Xu and Goodman with this surface dynamics [247]. They reported that the

surface temperature dependent initial sticking probability S_0 follows a Fermi-Dirac distribution-like statistics

$$S_0 = \frac{\alpha}{1 + e^{\tilde{\nu} - \Delta E^{Cu/SiO_2}/k_B T}}$$

with constants $\alpha = 0.6$ and $\tilde{\nu} = 4.5 \pm 0.5$ from the initial sticking probability shown in figure 2.10. Here ΔE is the variation of the adsorption energy and migration energy of Cu ad-monomer on
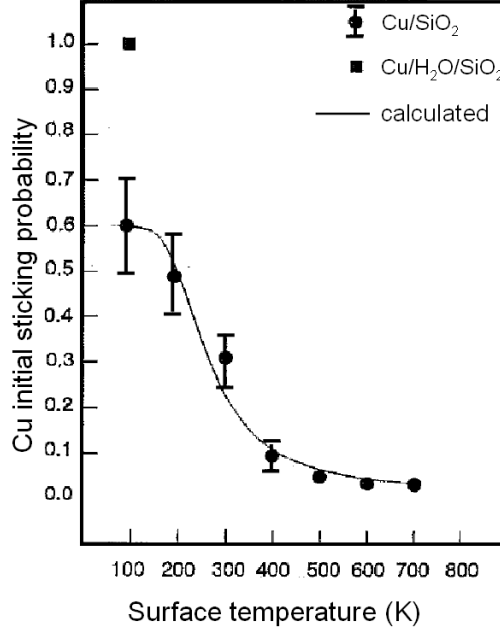

Figure 2.10: Initial sticking probability of Cu on SiO$_2$ with surface temperature [247].

v-SiO$_2$, i.e.

$$\Delta E^{Cu/SiO_2} := E_{ad}^{Cu/SiO_2} - E_m^{Cu/SiO_2},$$

and

$$\tilde{\nu} = \ln \left(\frac{\nu_{ad}}{\nu_m} \right)$$

with ν_{ad} and ν_m being the pre-exponential factors of jump frequency to the gas phase and to a neighboring physisorption site. The energy variation is $\Delta E^{Cu/SiO_2} = 0.104 \pm 0.017$ eV.

Lopez et.al.[143] reported the adsorption energy 0.08 eV as the adsorption energy of Cu monomer on a two-coordinated bridging oxygen (regular site) of the silica surface (figure 2.11) calculated by DFT (B3LYP) with the full counterpoise BSSE correction. However, without the BSSE correction, the energy increases to 0.56 eV and such conditions are important when geometry relaxation is large [143]. Since $\Delta E^{Cu/SiO_2} \sim 0.1$ eV [247], the energy calculation without BSSE correction is more reliable in this case.

On the other hand, the adsorption energy of silver E_{ad}^{Ag/SiO_2} seems to be lower than the energy of copper on SiO$_2$. According to the metal adsorption energy calculation on defect v-SiO$_2$ sites by Ferullo et al , the metal-oxide interaction follows the sequence $E_{ad}^{Cu/SiO_2} > E_{ad}^{Ag/SiO_2}$ [81]. Thus it is not so unrealistic that this order holds for the regular site. From this reference [81], the
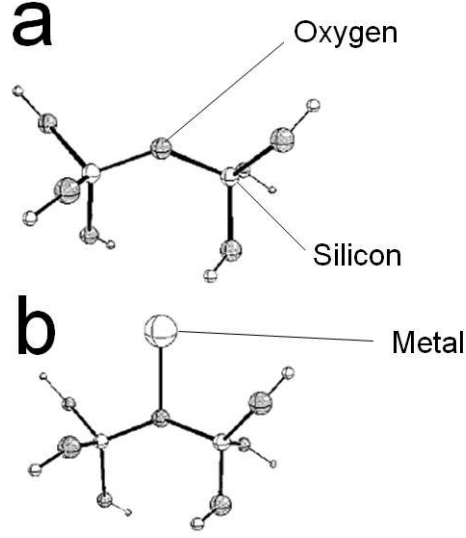
41

Figure 2.11: Molecular model of a two-coordinated bridging oxygen **a**, ≡Si-O-Si≡, on the nondefective SiO$_2$ surface cited by [143]. **b** is with a metal atom adsorbed on-top of the bridging oxygen.

ratio of adsorption energy between Ag and Cu is approximately 0.71~0.77:1.0. Thus the range of $\Delta E^{Ag/SiO_2}$ can be

$$\Delta E^{Ag/SiO_2} = 0.062 \sim 0.093. \tag{2.22}$$

From this observation, the parameter range $\Delta E^{Ag/SiO_2} = 0.06$ eV, 0.08 eV and 0.10 eV has been chosen for our model.

Reaction-diffusion equation

In the discussion of the Campbell model in section 2.1.3, a small diffusion area of Ag ad-monomers on v-SiO$_2$ surface is expected. Here we consider the average migration-reevaporation behavior of an ad-monomer deposited on the bare substrate surface without any further deposition. Let r_d be the desorption rate during one simulation time unit. If an ad-monomer is located at the origin at time $t = 0$, then the time dependent probability distribution of the ad-monomer $C = C(t, u, v)$ may follow the reaction-diffusion equation

$$\frac{\partial C}{\partial t} - D \left(\frac{\partial^2 C}{\partial u^2} + \frac{\partial^2 C}{\partial v^2} \right) = -r_d C \tag{2.23}$$

with the initial condition $C(0, u, v) = \delta(u)\delta(v)$, where δ is the Dirac delta function. Integrating eq. (2.23) with the initial condition yields the solution

$$C(t, u, v) = \frac{1}{4\pi Dt} exp\left(-\frac{u^2 + v^2}{4Dt} - r_d t \right). \tag{2.24}$$

Clearly,

$$\int_0^\infty \iint_{\Re^2} C(t, u, v) du dv dt = r_d^{-1}. \tag{2.25}$$

42

Now consider a discrete, atomistic diffusion model to exhibit this situation. The model considers the isotropic migration on rippled substrates in order to exclude the influence of surface steps as mentioned above.

The desorption probability of the adatom r_d follows the Boltzmann factor of the energy variation of the adsorption energy E_{ad}^{Ag/SiO_2} and the surface migration barrier E_m^{Ag/SiO_2}. For the variation

$$\Delta E := E_{ad}^{Ag/SiO_2} - E_m^{Ag/SiO_2} \tag{2.26}$$

the probability r_d of one atomic jump attempt on the discrete surface is given by

$$r_d = \frac{w_d}{w_{tot}} e^{-\Delta E/k_B T}, \tag{2.27}$$

where w_d and w_{tot} are the numbers of jump directions of desorption and total jump directions respectively, and T is the temperature of the substrate. Note that the number of desorption directions w_d depends on the local configuration of the jumping atom in the discrete cells. Clearly, the mean adatom lifetime T_{AL} is the inverse of this desorption rate, i.e.

$$T_{AL} \equiv \sum_{t=0}^{\infty} t(1 - r_d)^{t-1} r_d = r_d^{-1}. \tag{2.28}$$

The discrete simulation system is now constructed as a fcc lattice network embedded in simple cubic lattice sites. The lattice unit (lu) of the simulation is the one side length of this simple cubic lattice. Each unit pathway of this network corresponds to the diagonal of the unit square constructed by the simple cubic lattice sites. The depositions and migrations of atoms are considered on the fcc discrete surface oriented by the (100) symmetry.

For this fcc(100) surface network configuration, we have the diffusion coefficient

$$D = 1/6 \ [\text{lu}^2 \ \text{tu}^{-1}],$$

with the computational topography parameters $w_{tot} = 12$ and $w_d = 4$. The derivation of the discrete reaction-diffusion equation for this simulation system including the diffusion coefficient is written in appendix A. Substituting (2.27) into (2.24) with these parameters yields

$$C(t, u, v) = \frac{3}{2\pi t} exp\left(-\frac{3(u^2 + v^2)}{2t} - \frac{t}{3e^{\Delta E/kT}}\right). \tag{2.29}$$

Here the simulation time unit t corresponds to the iteration steps of single jump attempts for all atoms in the system.

Figure 2.12 shows this probability distribution $C(t, r)$ of the existence of a single adatom after deposition as a function of the distance r from the origin, where $C(t, r)$ represents the distribution C with plane polar coordinate system

$$r^2 = u^2 + v^2$$

in eq. (2.29). The symbols plot indicates statistics of the migration-adsorption simulation by lattice based KMC with various parameters. The length of a lattice unit is calculated as 0.204 nm (see below section 2.3.1). The KMC plots agree quite nicely with the analytical solution (2.29) from the continuum equation (2.23).

The surface migration of adatoms considered here arises from two dimensional random-walks on the fcc(100) surface. Due to the discrete transition symmetry, the area of the Wigner-Seitz primitive cell is $\sqrt{2}^2 = 2 \ \text{lu}^2$. Consider the mean two-dimensional propagation of adatom

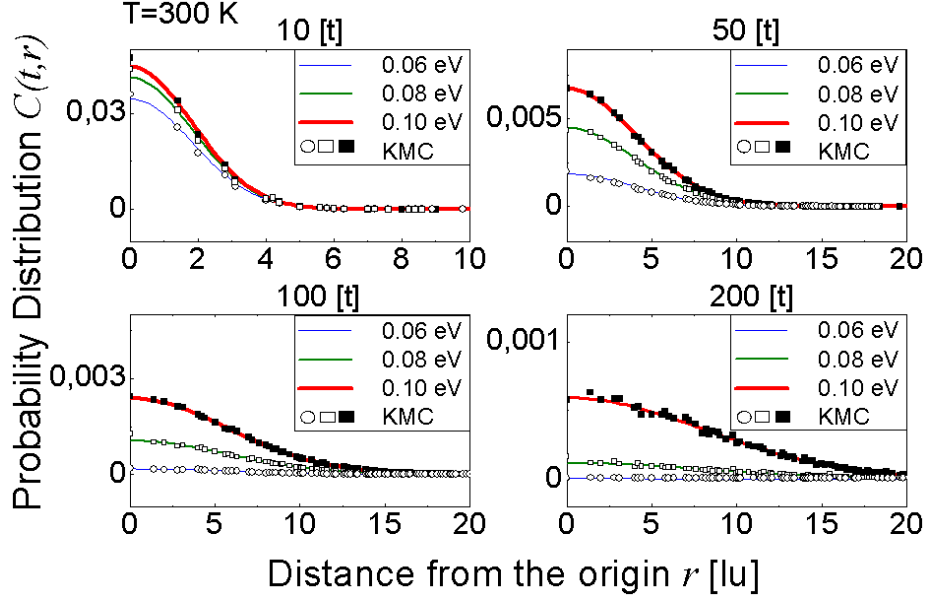$$S_{prop}(t) := \int_{\mathbb{R}^2} (u^2 + v^2)C(t, u, v)dudv$$

Figure 2.12: Probability distribution $C(t,r)$ of adatom existence as a function of distance from the origin in lu and the energy ΔE at 300 K. The analytical solution eq. (2.29) agrees with the KMC simulations at time $t = 10$, $t = 100$, $t = 200$ and $t = 500$.

as the second moment of distance from the origin after time step t. Then it follows

$$S_{prop}(t) = \frac{2}{3}te^{-r_d t}. \tag{2.30}$$

Here $e^{-r_d t}$ indicates the average decay of the existence probability of an adatom. Denote the mean adatom lifetime (AL) by T_{AL}. Then the propagation is given by $2T_{AL}/3e$ from (2.28). With the parameters for the simulation model, the size distribution of the mean adatom migration area is shown in figure 2.13. The orange solid line indicates the propagation function in the simulation system

$$A(T_{AL}) = 2S_{prop}(T_{AL}) + S_0 \ [\text{lu}^2]. \tag{2.31}$$

Since the shortest mean adatom lifetime is $T_{AL} = 3$ for $\Delta E = 0$, the graph indicates $3 \leq T_{AL}$. The initial propagation is $S_0 = 2$ lu^2. The circles are observed mean migration area distribution in simulations. $A(T_{AL})$ is an asymptote of the mean migration area of surface random-walks (dotted circles) with respect to the short-lifetime adatom migrations. However, the mean migration area is smaller than the propagation significantly with increasing AL since the overlapping area of the migration trace for a long AL is not negligible. This is because the overlapping area of a migration trace does not contribute to the enlargement of the migration area itself but to the existence probability. Therefore the difference between the mean propagation and migration area increases with increasing adatom lifetime, in which the overlapping migration occurs more frequently. A mathematical description is given in appendix C. Interestingly, the mean migration area is fitted by

$$A_{fit}(T_{AL}) = 2S_{prop}(T_{AL})^{0.9} + S_0$$

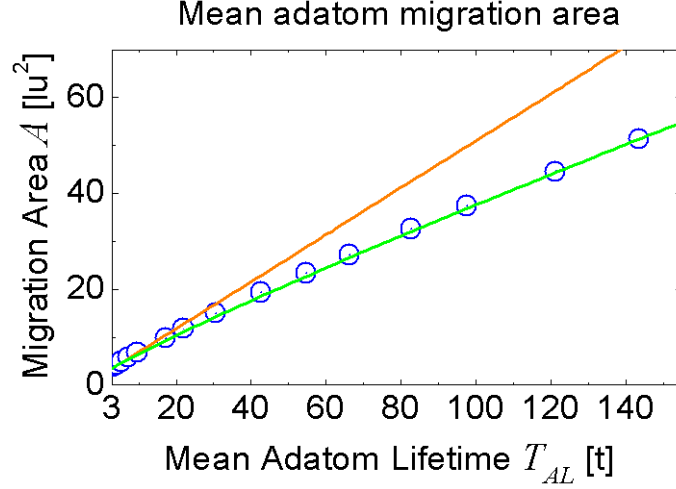with the exponential factor 0.9 nicely in this region (green curve).

Figure 2.13: Mean area of adatom surface migration as a function of simulation time. The circles ($\odot$) indicate observed data in simulations for the mean adatom lifetime $T_{AL} = $ 3-143.6 tu fitted by the green curve. The orange solid line indicates the second moment of the mean adatom displacement distance from eq. (2.30) and (2.31). The green curve is the power law of the propagation function with the scaling exponent 0.9 which is fitting the mean migration area of adatom quite nicely.

2.2.4   Simulation vs. experimental gauge

For the conversion from the simulated diffusion coefficient D_{sim} lu^{2}tu^{-1} to the surface diffusion coefficient of Ag on v-SiO$_2$ surface D_{Ag/SiO_2} m^{2}s^{-1}, the evaluation of the simulation time unit and lattice unit is required. Due to the nucleation process simulation discussed in the following section, it is convenient to chose the unit length of the fcc pathway as the inter-atomic distance of Ag, i.e. 1 lu= 0.204 nm. Since $D_{sim} = 1/6$ lu^{2}tu^{-1} for the fcc(100) surface diffusion, 1 tu should be consistent with

$$1[tu] \cong \frac{6.936 \times 10^{-21}}{D_{Ag/SiO_2}}[s].\tag{2.32}$$

On the other hand, by comparison with experimental observations of the initial nucleation distribution, the corresponding computational time scale can be estimated as

$$1[tu] \cong \frac{t_{exp}}{t_{sim}}[s],\tag{2.33}$$

where t_{exp} is the experimental time duration and t_{sim} is the corresponding total simulation time steps. From (2.32) and (2.33) the diffusion coefficient D_{Ag/SiO_2} is obtained as

$$D_{Ag/SiO_2} \cong \frac{t_{sim} \times 6.936 \times 10^{-21}}{t_{exp}} \ [\text{m}^2\text{s}^{-1}],\tag{2.34}$$

Espiau *et al* investigated Ag nanocluster nucleation in v-SiO$_2$ under ion beam irradiation [71]. In their work, a high mobility of Ag$^+$ in bulk oxide materials is mentioned referring to the bulk diffusivity $D_{Ag^+} \sim 10^{-12}$ m^{2}s^{-1} in soda lime glass at 773 K reported by Doremus [63]. However, even in bulk materials the diffusion of a non-ionized Ag monomer is difficult to measure because of the interference of Ag nanocluster precipitates [71]. Thus the experimental measurement of the intrinsic diffusion coefficient for the Ag monomer on a v-SiO$_2$ surface might be a quite challenging

task. For the bulk- and surface rate constants $D_\infty^{(b)}$ and $D_\infty^{(s)}$, the diffusion coefficients $D^{(b)}$, $D^{(s)}$ are

$$D^{(b)} = D_\infty^{(b)} e^{-E_m^{(b)}/k_B T'}, D^{(s)} = D_\infty^{(s)} e^{-E_m^{(s)}/k_B T}$$

where $E_m^{(b)}$ and $E_m^{(s)}$ are the migration energies of a monomer in the bulk and surface of the target material respectively. Accounting for the difference between bulk and surface Debye frequencies $D^{(b)} = \sqrt{2} D^{(s)}$ reported by van Delft [230], $T' = 773$ K and $D_{Ag-SiO_2}^{(b)} = 10^{-12}$ m^{2}s^{-1}, the surface diffusion coefficient at temperature T may be obtained from

$$D_{Ag/SiO_2}^{(s)} = \frac{10^{-12}}{\sqrt{2}} e^{\frac{1}{k_B} \left(\frac{E_m^{(b)}}{773} - \frac{E_m^{(s)}}{T} \right)} \ [\text{m}^2\text{s}^{-1}]. \tag{2.35}$$

In the following section, the initial Ag nucleation process by angular deposition on a pre-patterned surface is simulated by the KMC method with the consistent local varying flux distribution. It will be shown that the desorption rate introduced in this section plays a crucial role in the initial nucleation distribution observed in the angular PVD experiments onto pre-patterned v-SiO$_2$ templates [190].

2.3 Nucleation models: Surface gas condensation

Once the nucleation occurs on the surface, then the sticking probability and the inhomogeneous flux are no more constant on the surface due to a high cohesive energy of Ag-Ag interaction and the shadow effect of clusters. For the initial stage, the shadow effect of small clusters can be still neglected, but the enhancement of the sticking probability due to the Ag island distribution can be significant if the mean migration area of ad-monomer is sufficiently large. Thus the analytical model discussed in section 2.2.2 and 2.2.3 describes the further evolution not so accurately. Therefore the time evolution of deposited silver nucleation and the cluster growth process were studied with a KMC method based on a three dimensional lattice KMC simulation.

2.3.1 Simulation setup

The KMC simulation code is based on the code of Heinig *et al* [98], Strobel *et al* [219, 221], Müller *et al* [157], and Röntzsch *et al* [192]. In the simulation codes, the Ising-like potential model is utilized for the determination of the Hamiltonian of the system.

In order to exhibit more accurately the Ag cluster growth process, the code is developed by implementing a relatively simple many body inter-atomic potential, the Rosato-Guillopé-Legrand (RGL) potential [193]. The RGL potential is widely utilized in molecular dynamics simulations describing especially well the Ag facet properties [58, 79, 106, 107, 152, 156, 177, 194]. Some detailed description can be found in appendix D. Together with a look-up table constructed by the NN configuration and this potential, various migration barriers are estimated quickly. A similar approach was also reported by Voter in 1986 [239] to determined the migration barrier of rhodium cluster on Rh(100) using a Lennard-Jones 6-12 pair potential.

The model assumes that depositing and diffusing metal atoms are only allowed to occupy fcc sites within the perfect cubic overlayer with (100)-symmetry embedded in a simple cubic lattice of size 512×512×128 with periodic boundary conditions, so grain boundaries are excluded. The configuration of the substrate region is held fixed during simulations.

The unit length of the fcc grid is consistent with the inter-atomic distance of silver in the perfect fcc crystal structure, i.e. 1 lu corresponds to 0.204 nm as mentioned above. Various escape paths

in this fcc grid network and associated transition rate constants are estimated effectively as follows. The fcc grid is divided into a substrate and vacuum region. Ag atoms in the vacuum region are allowed to move only on the fcc lattice sites in the simulation cell and the substrate region is filled with pseudo atoms modeling amorphous SiO_2 atoms.

potential energy calculation

For simplicity, Ag and SiO_2 atoms are called the type-I and the type-II atoms respectively. The type-II atoms are held fixed during the simulation. For a type-I atom i, let n_i^I and n_i^{II} be the number of type-I, and type-II nearest neighbor (NN) atoms, respectively. The potential energy E_i can then be written with a simplification of the RGL functional as (see appendix D)

$$E_i = -\zeta \sqrt{n_i^I} + A n_i^I - E_i^{Ag-SiO_2}(n_i^{II}), \qquad (2.36)$$

where the first two terms are determined from the RGL-potential with parameters ζ=1.1663 eV, A=0.09982 eV [92] and $E_i^{Ag-SiO_2}(n_i^{II})$ is the Ag-SiO_2 interaction term which is given by

$$E_i^{Ag-SiO_2}(n_i^{II}) = \begin{cases} 0 & (n_i^{II} = 0) \\ E_b^{Ag-SiO_2} & (\text{otherwise}). \end{cases} \qquad (2.37)$$

The Hamiltonian $\mathcal{H}$ is defined as

$$\mathcal{H} = \sum_i E_i,$$

where i ranges all type-I atoms in the vacuum region. This Hamiltonian model can apply to other deposition materials by choosing appropriate parameters for the RGL potential and the expected interaction energy with the substrate materials.

The transition states of the simulation system are exhibited by the NN jump attempt of each type-I atom. The acceptance probability follows the Metropolis algorithm and the activation energy barrier E_a is simply calculated by the configuration energy difference before and after the jump attempt. For the transition attempt from the state Ω to Ω', the acceptance probability $P(\Omega, \Omega')$ is thus

$$P(\Omega, \Omega') = \begin{cases} 1 & (\mathcal{H}(\Omega) \geq \mathcal{H}(\Omega')) \\ e^{-[\mathcal{H}(\Omega') - \mathcal{H}(\Omega)]/k_B T} & (\mathcal{H}(\Omega) < \mathcal{H}(\Omega')). \end{cases} \qquad (2.38)$$

Local configuration approximation

Since the transition event modifies only the local configuration around the jumping atom, the potential energy change occurs only for the atoms neighboring the initial site and the final site of the jumping atom. These initial and final positions are surrounded by 18 NN sites and 52 other sites whose potential energy is affected by the transition. Hence the total number of possible configurations are 3^{70} (70 sites and three possibilities at each site, i.e. empty, type-I atom or type-II). However for the efficiency of the calculation, only the 18 NN positions surrounding the initial and the final sites are used to determine the migration energy.

Figure 2.14 shows u_{ini}, u_{fin} and the 18 NN positions that are divided into the sets

$$N_i := \{1, 2, 3, 4, 5, 6, 11\}, N_c := \{7, 9, 10, 12\}, \text{ and } N_f := \{8, 13, 14, 15, 16, 17, 18\}$$

with respect to the neighboring u_{ini} and u_{fin}. The positions belonging to N_i and N_f are NN sites of the initial site u_{ini} only, and of the final site u_{fin} only, respectively. The positions of N_c are the common NNs of the both sites. Since the configuration energy of each atom is calculated by (2.36),
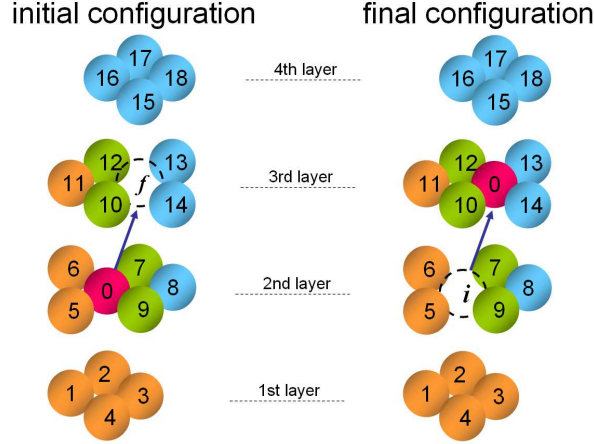
Figure 2.14: The local NN (fcc) configuration of an initial site u_{ini} and final site u_{fin} denoted by i and f. For this system, the NN sets for i and f can be seen to be $N_i := \{1, 2, 3, 4, 5, 6, 11\}$, $N_c := \{7, 9, 10, 12\}$ and $N_f := \{8, 13, 14, 15, 16, 17, 18\}$. The site 0 is occupied by a Type-I atom and other sites are either empty, or occupied by a type-I, or a type-II atom.

all local transition types are represented with the form $(|N_i^I|, |N_i^{II}|, |N_c^I|, |N_c^{II}|, |N_f^I|, |N_f^{II}|)$, where $|N_*^{I,II}|$ indicates the number of occupied NN sites by type-I, as well as type-II atoms belonging to the position index set N_*. These configurations account for the migration barrier estimation in all cases of jumps between unequal energy sites where the variation of the configuration energy is approximated by

$$\mathcal{H}(\Omega) - \mathcal{H}(\Omega') \approx E_{fin} - E_{ini}, \tag{2.39}$$

where E_{ini}, E_{fin} are the potential energies before and after a jump as determined by the 18 NN configurations and the expected NN configuration of each neighbor atom. The energy of the initial state E_{ini} is defined by

$$E_{ini} = \sum_{j=0}^{18} \epsilon_j E_j^{ini},$$

here ϵ_j indicates the occupation of the j-th site by the type-I atom. The configuration energy of each occupying atom is calculated as

$$E_j^{ini} = \begin{cases} E_0^{ini} & (j = 0) \\ E(\bar{n}) & (otherwise), \end{cases} \tag{2.40}$$

where E_0^{ini} is calculated by eq.(2.36) for the initial site 0 and $E(\bar{n})$ is the mean configuration energy

$$E(\bar{n}) := -\zeta\sqrt{\bar{n}} + A\bar{n}, \tag{2.41}$$

for the other atoms. Here, $\bar{n}$ is the average number of type-I NNs of all occupied sites by the type-I atoms possessing at least one empty NN site. This factor is influenced by the mean surface curvature of clusters growing in the system. The local configuration energy of the final state E_{fin} is defined similarly as

$$E_{fin} = \sum_{j=0}^{18} \epsilon_j E_j^{fin},$$

48

where the position $j = 0$ now implies the final site. Now each E_j^{fin} is given by:

$$E_j^{fin} = \begin{cases} E_0^{fin} & (j = 0) \\ E(\bar{n} - 1) & (j \in N_i^I) \\ E(\bar{n}) & (j \in N_c^I) \\ E(\bar{n} + 1) & (j \in N_f^I). \end{cases} \tag{2.42}$$

The average NN number $\bar{n}$ is updated every 12,000 time units.

2.3.2 Simulation parameters

Ag monomers are deposited on the (100)-oriented flat surface with the local flux f_{loc} calculated from the surface topography by eq. (2.11). The consistent surface topography is constructed by the parametric representation (2.10) with the asymmetric parameter $\epsilon = 0.7$, height, and wavelength parameters $h_0 = 4.5$ nm, and $l_0 = 47$ nm. The height to be chosen in the model is somewhat larger than a typical ripple height reported from low energy sputtering experiments in order to observe a clear difference between high- and low deposition area in the projected flat surface. The diffusion process and desorption probability are taken independent of the surface topography in this model. Ag atoms are deposited continuously until the total Ag accumulation reaches 6 ML for each parameter. The evolution of sticking probability of incident atoms, area fraction and distribution of modeled atomistic structure have been investigated.

In order to avoid undesired correlation between the adatom migration to the specified direction resulting from the (100)-symmetry of fcc grid and the local flux variation, the simulation surface is rotated anticlockwise to $\tan^{-1}(0.5)$ without breaking the PBC.

The temperature range was chosen to be consistent with the experiment carried out at room temperature. Since the surface temperature was not exactly monitored the simulations have been performed at $T = 300$ K, 350 K and 400 K. The range of the parameter ΔE has been chosen to be $0.06, 0.08$ and 0.10 as mentioned in section 2.2.3.

As shown in section 2.2.3, for Cu/SiO$_2$ the probability reported [247] is around 0.3 in the early stage (< 1 ML accumulation) of the vapor deposition on flat surface at room temperature (T=300 K). The cohesive energy between Ag and v-SiO$_2$ calculated by the density functional theory is generally weaker than of Cu [81]. Thus the expected sticking probability of Ag/SiO_2 is below 0.3 in the early stage of deposition.

Accounting for this point of low sticking, various preliminary calculations have been performed with changing the flux parameter. Figure 2.15 shows an Ag cluster distribution being quite similar to the experiment. The simulation parameter taken as $\Delta E/k_B T = 2.32$ refer to the range (2.22) with the final sticking probability 0.24 reproduces the experimentally observed structure remarkably well. The total simulation time was $t_{sim} = 3.0 \times 10^7$ tu and the effective average flux $\tilde{f} = 8.3 \times 10^{-6}$ atoms/nm^{-2}tu^{-1} (see eq. (2.18)) corresponding to 0.0046 ML s^{-1} calculated by the comparison with the total experimental deposition time 4500 s. The nucleation point distribution shown with yellow dots in figure 2.15(**a**) is quite similar to the expected distribution from the SEM image (**b**).

2.3.3 Evolution of sticking probability

In the model, the sticking probability of Ag monomer deposited is strongly influenced by the Ag island fraction on substrates due to a high cohesive energy of Ag-Ag and a high re-evaporation rate from the bare substrate. For the number of atoms remaining on the surface n_a and the mean fluence F_l, two types of sticking probabilities are considered.
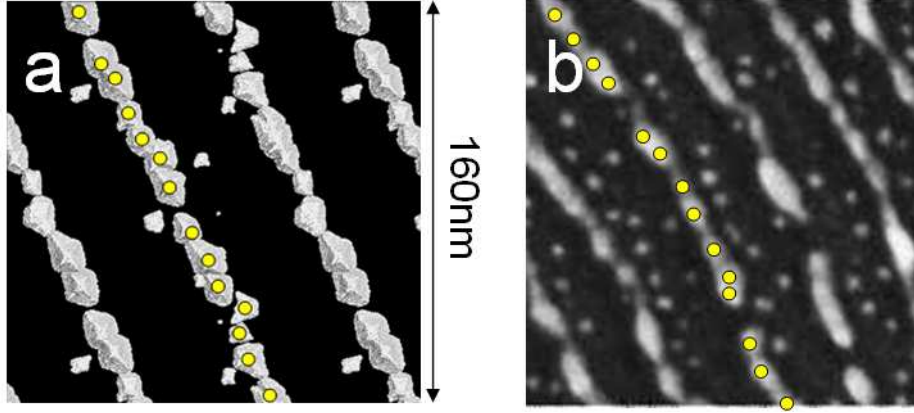
Figure 2.15: Top view of Ag clusters and initial nucleation points in the high flux region (yellow dots). **a** Simulation result: $\theta = 70°$, $\Delta E = 0.08$ eV, 209 nm× 209nm at 400K, total coverage 5 ML, total simulation time step 3.0×10^7t. **b** Experimental result: Silver rods created by 75 min. e-beam deposition with the beam flux 5.0 μA and the deposition angle $\theta = 70°$ on rippled SiO$_2$ surface 160 nm × 160 nm at room temperature. The mean Ag coverage is 5.8 ML.

The total sticking probability S_{tot} is simply represented by

$$S_{tot} = \frac{n_a}{F_l}. \tag{2.43}$$

Here, F_l is a function of deposition time and the mean flux (2.18), i.e., $F_l = tf\cos\theta$. Since the system evolves with this fluence F_l, all observed values are considered as functions of F_l. The instantaneous sticking probability S_{ins} is defined as the derivation of n_a with respect to F_l. I.e.

$$S_{ins} = \frac{d}{dF_l}n_a. \tag{2.44}$$

S_{ins} indicates the sticking probability of the atom arrived at the surface with the mean fluence F_l. Then the relation between S_{tot} and S_{ins} is

$$S_{ins} = S_{tot} + F_l\frac{d}{dF_l}S_{tot}.$$

Figure 2.16 shows the results of Ag PVD simulations for the corresponding deposition angle $\theta = 70°$. The evolutions of these types of sticking probability, mean Ag coverages and snap shots of substrates with 5ML Ag mean coverage are shown. Here, the mean coverage implies the total number of atoms on the substrates divided by the number of monolayer Ag atoms (~ 12 atoms nm^{-2}). In each diagram, the total- and instantaneous sticking probabilities $S_{tot}(F_l)$ and $S_{ins}(F_l)$ are indicated by the blue curve and the red curve respectively. The green curve indicates the evolution of mean coverage.

The relation between the incoming flux and the accumulative cluster distribution is investigated in detail.

Figure 2.17 shows the relative incoming flux distribution, Ag cluster distribution, i.e. the distribution of Ag atoms on the surface, and the projection of these Ag distributions. The color of the flux distribution and the Ag clusters in the left diagrams indicates the frequency of the relative flux rate and the height from the substrate, respectively. The flux distribution changes only uniaxially and the mean Ag cluster distribution has also the same tendency. In order to see this trend more clearly, the mean fluence- and Ag distributions on the surface are represented as the
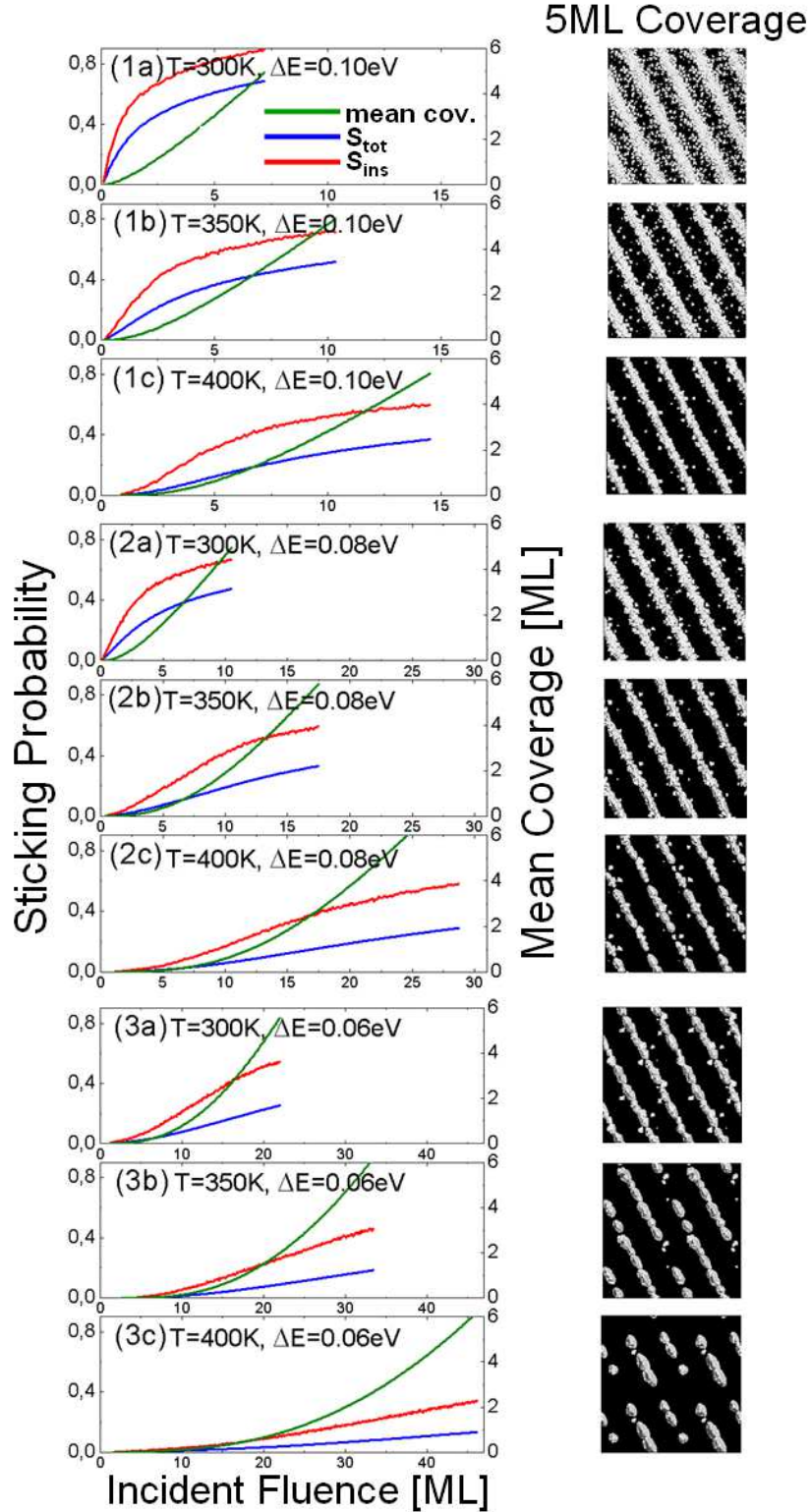
Figure 2.16: **Left** Evolution of total sticking probability S_{tot} (the blue curves, see eq. (2.43)) and instantaneous sticking probability S_{ins} (the red curves, see eq. (2.44)) and the mean coverage (the green curves) as functions of deposition fluence up to $\sim$ 5 ML mean Ag coverage. The inhomogeneous Ag deposition rate is calculated by eq. (2.11) for the corresponding rippled surface with $\epsilon = 0.7$, height 9 nm, and wavelength 47 nm. **right**: Snap shots of Ag clusters with the mean coverage 5 ML. Size of cells corresponds to 209 nm× 209 nm. Simulation parameters: $\Delta E^{Ag/SiO_2} = 0.06$ eV, 0.08 eV and 0.10 eV, T=300K, 350K, and 400K, $\theta = 70°$.

Projected mean Ag distribution

Figure 2.17: Schematic description of the projection of mean Ag distribution. The left diagrams show the relative, spatial distribution of incoming flux (upper) and Ag cluster accumulation with 5 ML mean coverage (lower). These distributions with one period of ripple and the PBC length are projected onto the surface indicated by the red dotted rectangle. The right diagram shows this projection. Black lines and green curves indicate total incidence atom distribution and 5ML Ag atoms on substrates, respectively. The number in the box represents the total incident fluence arising from the Ag deposition.
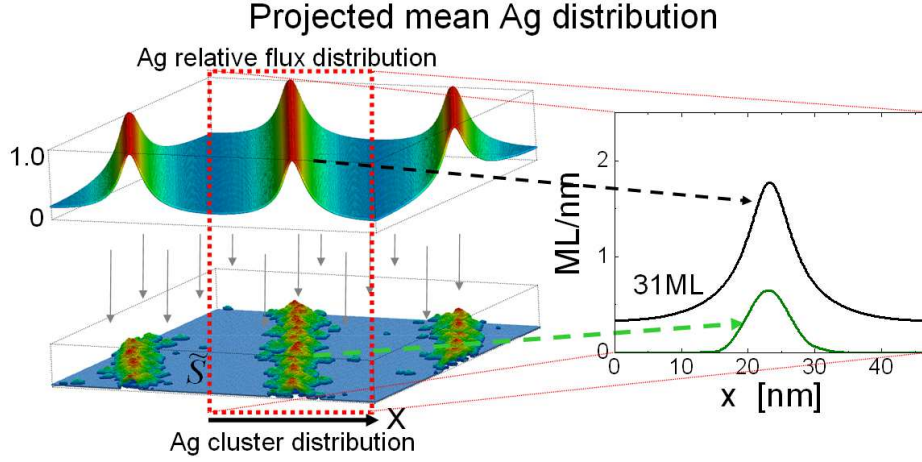
uniaxial graphs with respect to the direction of the flux variation in the right diagram. The dotted red rectangle in the left diagram indicates the corresponding frame of this projection. The length of the axis is one period of the local flux rate corresponding to the wavelength of the ripples. Totally 31 ML of incident fluence arises from 5 ML Ag mean coverage on the surface. This representation provides an interesting relation between the flux density and the Ag accumulation. Due to the small mean migration area, there exists a critical flux density for Ag nucleation. Below the critical flux density, Ag atoms do not remain on the substrate. This critical density depends also on the adhesive energy between Ag and the substrate. Figure 2.18 shows the projected distribution of all simulation models (1a)-(3c) for 5 ML mean coverage. In each diagram, the top view of the cluster distribution with PBC is shown and one period of simulation system is indicated by a red rectangle. The solid curves with color indicate 5 ML Ag distribution on the surface and the black curves are the total incident fluence distribution as shown in figure 2.17. The correlation between mean surface ad-monomer lifetime $T_{AL} = 3e^{\Delta E/k_B T}$, the local flux, and the mean cluster growth distributions can be seen. By a large $\Delta E/k_B T$, the cluster growth distribution is almost proportional to the flux distribution (1a). However, in the case of small $\Delta E/k_B T$ the growth distribution is significantly localized in the high flux region. The most efficient concentration range may be found between (1c), (2c), and (3a). Here, an efficient concentration means a high cluster concentration with a small re-evaporation rate.

The type of metal accumulation can be classified by the mean ad-monomer lifetime, or adatom lifetime (AL), on the substrate surface T_{AL}. The sticking probabilities increase depending mainly on this T_{AL} following the Boltzmann factor of ΔE by eq. (2.27). If AL is sufficiently long, then nucleation can occur even in the least flux region during a sufficiently long deposition time. This can be seen e.g. in (1a). In this case, most of all incident atoms remain on the surface at the final stage of the simulation ($S_{ins}(F_l = 7ML) \sim 0.9$). In contrast, for a short AL the nucleation occurs only in the highest flux region and atoms that arrive on the bare surface of the less flux region are re-evaporated (3c). Though small clusters might be generated in the initial deposition stage, they could not remain on the surface due to the high re-evaporation rate. Consequently,
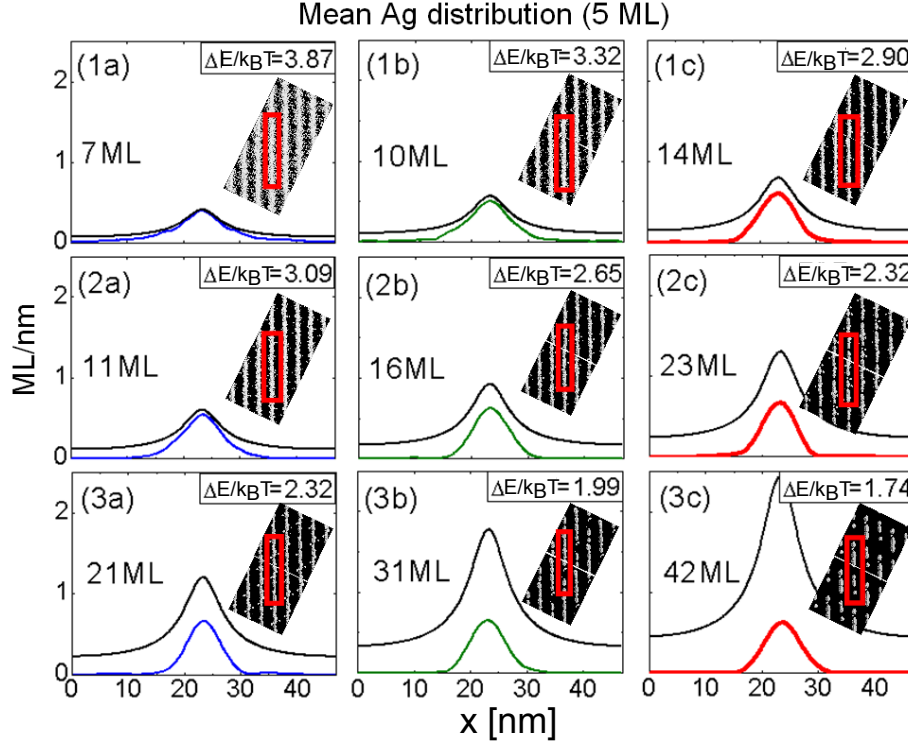
Figure 2.18: List of the mean cluster distribution of Ag 5 ML coverage defined in figure 2.17 (see also figure 2.16 right). Graphs show the uniaxial distributions of incoming flux as well as mean coverage 5ML Ag clusters. The red rectangle in each box indicates one period of ripple structure of each model. The corresponding simulation parameter $\Delta E/k_B T$

the instantaneous sticking probability S_{ins} is almost same as the effective surface area fraction of Ag clusters, i.e., the area fraction times the relative local flux density. In any case, the increase in the Ag area fraction leads to the enhancement of the sticking probability. On the other hand, the initial nucleation overcoming the critical size can be seen by the spontaneous enhancement of sticking probability. For example, in figure 2.16 (1c), the first effective cluster growth occurred after around 1 ML deposition in the high flux region.

Because of the low mobility of clusters, the nucleation process on the substrate is mainly triggered by impingements of ad-monomers during their surface migration. In most cases, dimers are stable enough on the substrate and grow to be large clusters. Since a concerted motion is excluded in the simulation model, the detachment of a dimer requires at least two steps of the atomic jump to a certain direction in the fcc network. In fact, the total number of dimer atoms detaching from the substrate is less than 0.02 % of the detaching monomers during the growth of 5 ML coverage in the simulation (3c) of figure 2.16. This is the largest case and numbers of removed dimers in other cases are even less.

The sticking probabilities are monotonously increasing and exhibit two different phases due to the cluster growth stage. In the early stage, small clusters in the high deposition region are often generated due to a sufficiently high adatom concentration (2.21). Once the coalescence of such clusters is saturated, i.e. the region with a sufficiently high local flux is fully covered by clusters, then this slows down since the sticking in this region is maximized and 2D islands growth in the lower flux region is much slower due to the small migration area of ad-monomers deposited. This

53

inflection point can be seen in (1a), (1b), (1c), (2a), (2b), (2c) and (3a) of figure2.16). On the other hand, the increasing of the probabilities of (3b) and (3c) is almost linear. In fact, the evolution of sticking probability is dominated by the growth of existing clusters and new dimer creation is quite rare under the condition of (3b) and (3c).

The effect of the temperature dependent cluster formation for the Ag accumulation can be seen by the comparison between (2c) and (3a) since T_{AL} is same in the both cases. The total sticking probability S_{tot} in (3a) is slightly higher than in (2c) since the Ag area fraction in (2c) is slightly smaller than in (3a). This difference results in the shape of the Ag clusters. The higher temperature, the smaller the surface area of Ag clusters due to the surface free energy minimization. This effect is however not so significant in these cases.

2.3.4 Evolution of Ag cluster growth

Since the Ag cluster growth is promoted by the direct deposition, nucleation and impingement of ad-monomers migrating on the surface, the evolution of the Ag area fraction indicates the contribution of these mechanisms. If the flux variation is critical, i.e. nucleation can occur only in a high flux region, then the contribution of nucleation and impingement will be disappear when the high flux region is fully covered.

Ag area fraction

First, consider the evolution of the Ag area fraction with respect to the total coverage. Figure 2.19 shows the area fraction of islands as a function of the total number of atoms on the simulation surfaces. Since the incoming flux is concentrated in a small region and the cluster growth is Volmer-Weber due to the small interface energy, two-dimensional growth is not favored in each case even with a large T_{AL}.

The blue dotted curve in the left diagram is the evolution with $T = 300$ K $\Delta E = 0.10$ eV and $\theta = 0$. In this case, the local deposition rate is induced by normal angle deposition onto rippled surfaces. Since the surface is only slightly patterned, the deposition rate is almost homogeneous everywhere. The spatial (2D) evolution of area fraction under this homogeneous metal deposition is much faster than other inhomogeneous deposition models.

The long dotted curve in the same graph shows the experimental result of homogeneous Au deposition onto $TiO_2(110)$ [178]. In this case the evolution of the metal area fraction in the early stage is more drastic since there seems to be many defect sites on $TiO_2(110)$ substrate chemisorbing Au monomers.

Area fraction vs. total coverage

Let $\phi_{loc} = \phi_{loc}(\chi, u, v)$ be the local area fraction density in (u, v) for the total coverage χ ML. In the discrete sense, ϕ_{loc} is the characteristic function for the site occupation by Ag atom, i.e. $\phi_{loc}(u, v) = 1$ for the case that Ag atom is in (u, v) and $\phi_{loc} = 0$ otherwise. Figure 2.20 is the double logarithmic representation of figure 2.19 for the total coverage for 0.01-0.5 ML as well as for 2-5 ML. The total Ag area fraction

$$\phi(\chi) := \int_{\tilde{S}} \phi_{loc}(\chi, u, v) du dv$$

evolves with the exponential factor of the total coverage χ. In the early stage of cluster growth, this exponential factor is generally larger than in the late stage. This inflection is resulting in the decay of Ag area fraction growth promoted by nucleation.
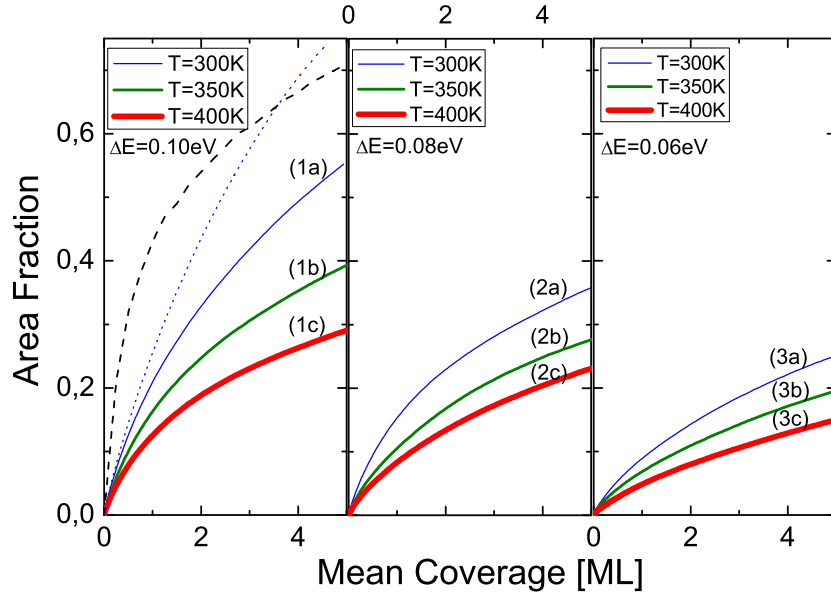
Figure 2.19: The area fraction of Ag islands on surfaces as a function of total Ag coverage for Ag deposition at 8.35 ML during 1.0×10^6 t at three different temperatures of substrates and adsorption energies ΔE. In left diagram, the dashed curve is from the experimental data of Au vapor deposition onto TiO_2 (110) at $\theta = 0°$ at $T = 293$ K [178] and the dotted curve is the simulation with $\theta = 0°$, $\Delta E = 0.10$ and $T = 300$ K. Except these two curves, all curves labeled by (1a)-(3c) are with the deposition angle $\theta = 70°$.

With the increasing number of clusters, namely, the cluster concentration, the sticking probability and area fraction of metal increase drastically since migrating atoms are caught by high concentrated clusters and enlarge the size of 2D islands. On the other hand, if the lifetime of adatoms is so short that the encounter with monomers is quite rare, then the cluster growth is only promoted by attachment of monomers and coalescence of clusters is also very rare due to the low cluster concentration. Hence, the increasing of area fractions and sticking probabilities are much slower than the former mechanism. An example of metal accumulation dominated mainly by the former case is (1a) of figure 2.16. There is much coalescence of small clusters and most of the high local flux area is covered by metal. In this case, a typical shape of an Ag cluster is rather than flat. The exponent coefficient for area fraction $\phi(\chi)$ is $\beta = 0.9$ in the early stage and $\beta = 0.6$ in the late stage (see figure 2.20). Since the high deposition region is saturated and only the region with low deposition rate is exposed, the growth speed of area fraction with total coverage slows down in the late stage. In contrast to (1a), the exponential factor of (3c) remains constant. Since the mean migration time is very short, there were only a few small clusters on the spot with the highest deposition rate at the beginning and they grew with the latter mechanism. The exponential factor $\beta = 0.7$ of (3c) is smallest in the early stage and the largest in the late stage since the region with the highest deposition rate is still far from the saturation. A typical shape of cluster in this example is smooth and tall. All other simulation samples are between these two extreme cases and the mixing rate of the two mechanisms is roughly characterized by T_{AL}. The sequence of Ag area fraction with total coverage (figure2.20) is exactly same as the sequence of T_{AL}, i.e. mean trace
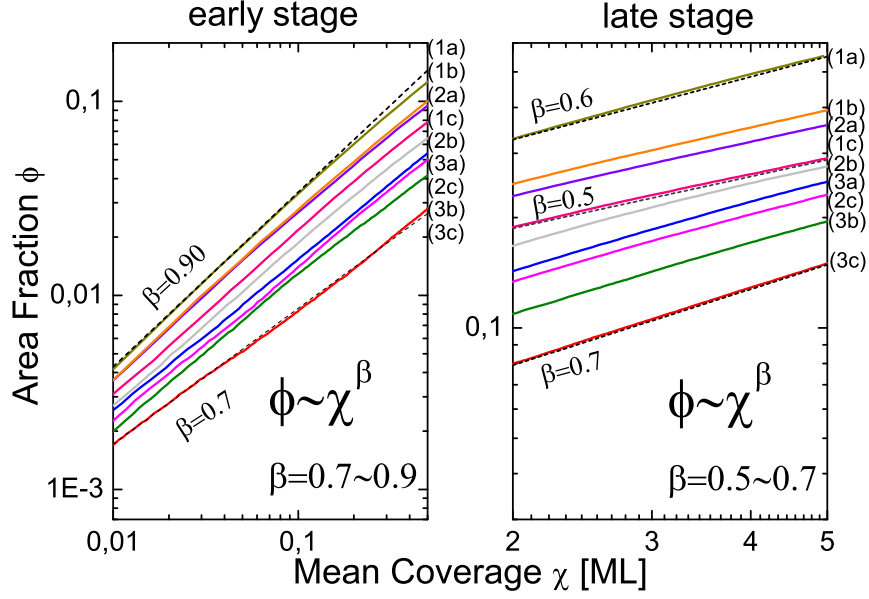
Figure 2.20: The area fraction ϕ of Ag islands on surfaces as a function of total Ag coverage χ. Labels in the upper right indicate the sequence of the simulation curves in the box.

area of surface random walks of adatoms.

Surface gas condensation

From the spontaneous evolution of S_{ins} as a function of the total Ag coverage at the initial stage, the condensation of Ag surface gas (ad-monomer) in the high flux region can be characterized. In order to evaluate the correlation between S_{ins} and the Ag area fraction accurately, ϕ_{loc} should be weighted by the relative local flux for the effective area fraction ϕ_{eff}. I.e.

$$\phi_{eff}(\chi) = \int_{\tilde{S}} \phi_{loc}(\chi, u, v) \frac{f_{loc}(u, v)}{f \cos\theta} du dv. \tag{2.45}$$

Figure 2.21 shows the difference between the instantaneous sticking probabilities S_{ins} and the effective surface area fraction

$$\Delta S = S_{ins} - \phi_{eff}.$$

This is shown in figure2.21 that the contribution of surface migration for the sticking probabilities has increased over (1c) and is not so significant under (2b). Since T_{AL} expected for (1c) and (2b) are $T_{AL} = 54.6$ t and $T_{AL} = 42.5$ t respectively, the critical mean access area of migrating ad-monomers is in the range of 19.3-23.4 lu^2 corresponding to 0.80-0.97 nm^2 in figure 2.13. This critical mean access area refers to the critical surface Ag gas concentration 1.03-1.25 atom/nm$^2 \sim 0.086$-0.104 ML in the early stage of metal deposition which gives the phase transition of the surface gas condensation. The weak adsorption of the v-SiO$_2$ substrate seems to act as a catalyst of selective metal nucleation resulting in a restricted surface migration of ad-monomers.

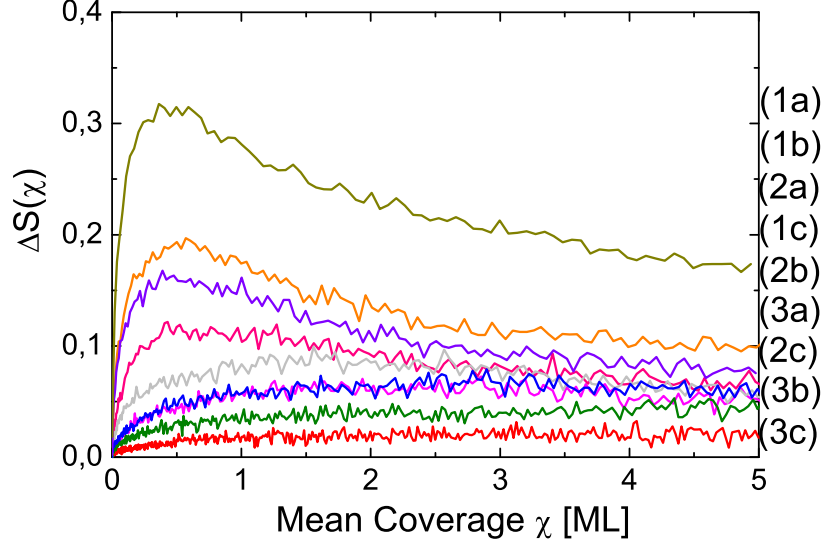**Effect of surface migrations for sticking probabilities**

Figure 2.21: Evolution of the difference between the instantaneous sticking probabilities and effective area fractions with total coverage.

2.3.5 Simulation time and system evolution

Now consider the interpretation of the simulation time step t for Ag atoms on silver clusters and for Ag adatoms on v-SiO$_2$ substrates. These two types of transition events are essentially different in the sense of their transition frequencies and minimum migration barriers mentioned in chapter 1.3.3. Let τ_{Ag} and τ_{ad} be the corresponding real time for one simulation time unit 1 tu. Then from eq. (1.47), τ_{Ag} and τ_{ad} are given by

$$\tau_{Ag} = \omega_{Ag}^{-1} e^{E_{min}^{Ag}/k_B T}, \text{ and } \tau_{Ag} = \omega_{ad}^{-1} e^{E_{min}^{ad}/k_B T},$$

where ω_* and E_{min}^* are the transition frequency and minimum migration barrier for $* = Ag, ad$ respectively. The delay rate of real time τ_{Ag}/τ_{ad} is

$$\frac{\tau_{Ag}}{\tau_{ad}} = \frac{\omega_{ad}}{\omega_{Ag}} \exp\left(\frac{E_{min}^{Ag} - E_{min}^{ad}}{kT}\right). \tag{2.46}$$

Moreover, for Ag atoms on various facets of Ag clusters, this kind of simulation time gap exists due to the algorithm defined by eq. (2.38) since the minimum migration barriers are different.

The dissimilarity of clusters obtained from the simulation model and the experimental finding may result from these gaps. In the following section, an extended model concerning this problem is introduced. The method is proposed in Ref. [172] by Numazawa *et al* .

2.4 Extended cluster growth model

The extended model is simply motivated by the correction of the different time correspondence for the events of Ag on Ag clusters and v-SiO$_2$ surface mentioned above. By assuming the overall
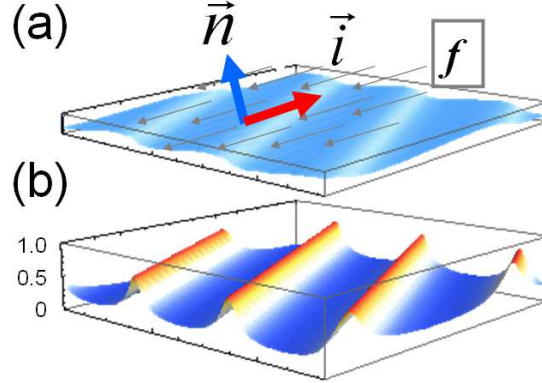
Figure 2.22: A schematic description of the PVD model and local flux. (a) The initial rippled surface and schematic description of metal deposition. Ag flux f, the incident angle vector $\vec{i}$, the surface normal vector $\vec{n}$ are shown. The angle of incidence in the simulations was fixed at $70°$ and perpendicular to the ripple direction. (b) The relative Ag arrival rate $f_{loc}/f = \vec{n} \cdot \vec{i}$.

frequency, the time gap results in various migration barriers for the events such that the Hamiltonian does not change before and after a transition. This concept is formulated as an effective transition event classification method. The mathematical formulation, detail and an application sample will be discussed in chapter 3. An advantage of this method is acceleration of computation time with a boost factor of several thousand compared to a traditional KMC approach, thus allowing experimental time scales to be modeled. The simulations give excellent reproduction of the experimentally observed nanocluster growth patterns. The simulation predicts a low sticking probability for the arriving atoms, millisecond order lifetimes for single Ag adatoms and ≈ 1 nm square surface migration ranges of Ag adatoms as discussed above.

2.4.1 Modified setup

The simulation setup is almost same as the previous model introduced in section 2.3.1. The extension is the following three points:
(1) Ripple like pre-patterned surface is directly introduced with a more suitable configuration for the consistent experiment.
(2) Migration barriers for Ag on Ag clusters are introduced.
(3) Atoms in unstable configurations can move continuously without the simulation time progression.
(4) All activation barriers are boosted by the same boost energy.

For (1), the saw-like asymmetric rippled substrate formed in the experiment is modeled by the fitting function (2.10) with periodicity $l_0 = 33$ nm, height 2.4 nm ($h_0 = 1.2$), and asymmetric parameter $\epsilon = 0.5$. Figure 2.22 (a) shows the consistent initial surface and schematic description of ion incidence angle as well as the surface normal vectors introduced. Because of the initial ripple structure and the $70°$ incidence angle, the local flux f_{loc} is a maximum of the slopes whose normals point toward the evaporation source and minimum on the slopes of the other side (figure 2.22 (b)). In fact f_{loc} ranges from 20% to 75% of the flux f from the evaporator. This strongly localized relative flux rate results in oblique angle deposition on a saw-like asymmetric rippled substrate. This topography of substrate region is held fixed during the simulation.

For (2), the migration barriers for transitions which conserve the number of NN's, migration

barriers taken from the literature are utilized. For example, the Ag ad-monomer (adatom) migration barriers on the (111), (100) and in-channel(110) oriented Ag surfaces are estimated as 0.10 eV, 0.38 eV, and 0.28 eV from the calculations in Ref. [69, 79, 177] respectively. For Ag adatom migration on the bare substrate, the barrier E_m^{Ag/SiO_2}=0.20 eV and the adsorption energy E_{ad}^{Ag/SiO_2}=0.245-0.300 eV are employed. The variation of these energies $\Delta E \equiv E_{ad}^{Ag/SiO_2} - E_m^{Ag/SiO_2}$, together with the Boltzmann factor $e^{-\Delta E/kT}$ determines the probability of desorption or adatom jump on the substrate. The simulation temperature is held fixed at 300 K.

The condition (3) is a small modification to the simulation algorithm, but may bring a significant difference in the results. The motivation for this correction is that the configuration appearing in the previous model is sometimes not so easily assumed in the sense of quasi-equilibrium atomic states in the discrete fcc grid. For example, if an atom hops to the position overcoming an ES barrier to go down the step, the atom stays in the intermediate position possessing less NNs than the previous position as well as any neighboring position in the down terrace. Although an atom in such a position does not stay even over the MD simulation time scale, it remains there until the next jumping term in the MC iteration. In order to avoid a statistical error accumulation resulting in such unlikely configurations, the position with less than three NNs are regarded as an unstable position. Obviously, this modification leads to the error for stable configurations with two NNs in the fcc grid, but this situation is quite rare.

A particular feature of this extended model is (4). All transition barriers are measured relative to the migration barrier E_m^{Ag/SiO_2}. Each jump attempt of an Ag atom is accepted with probability determined from the Boltzmann factor with this renormalized transition barrier. Every transition event is therefore classified from the level originating from this migration barrier. Each migration with a barrier under 0.2 eV is assumed as an unstable transition and exhibits free migration without any appropriation for the simulation time step. Thus, most of the simulation steps distinguish metastable level transitions with barriers above 0.2 eV. We term this the boost energy. A fuller description of the migration barrier estimation as well as details of the rate-based optimization method is presented in chapter3.

In this rate-based (RB) KMC model, the depositing atoms are set in the positions exposed to the trajectories and only the kinetics of Ag atoms are considered. The atoms detaching from Ag NCs or the substrate including desorbent ad-dimers are eliminated from the simulation immediately. Concerted motions, grain boundaries, reflection and surface drifting on impact are excluded. Under this scenario the migration barrier of Ag adatoms on the substrate is close to the desorption energy and arriving Ag adatoms are easily released to the vacuum and thus a short AL is expected. The boost energy 0.2 eV accelerates the simulation speed with a factor of $e^{0.2/kT} \sim 2290$. A typical growth process takes two or three CPU days on a modern single processor machine whereas a traditional KMC simulation might require some decades of computation time to obtain a similar surface coverage!

2.4.2   Simulation result

The result of this extended cluster growth simulation which is the most similar to the experimental observation is obtained with the parameter $\Delta E = E_{ad}^{Ag/SiO_2} - E_m^{Ag/SiO_2} = 0.06$ eV at $T = 300$ K. The factor $\Delta E/k_B T$ for AL is as same as the best fitting cases (3a) and (2c) of the previous simulation model. The total simulation time is 1.2×10^7 t for 6 ML Ag accumulation. In this case, Ag atoms equivalent to 17.1 ML of Ag atoms are deposited with 35% remaining on the surface in total. Comparing the experimental duration of 75 min with the total simulation time of 1.2×10^7 t yields 1 $t = 3.75 \times 10^{-4}$ s, giving a consistent simulation flux of f =0.0038 ML/s.
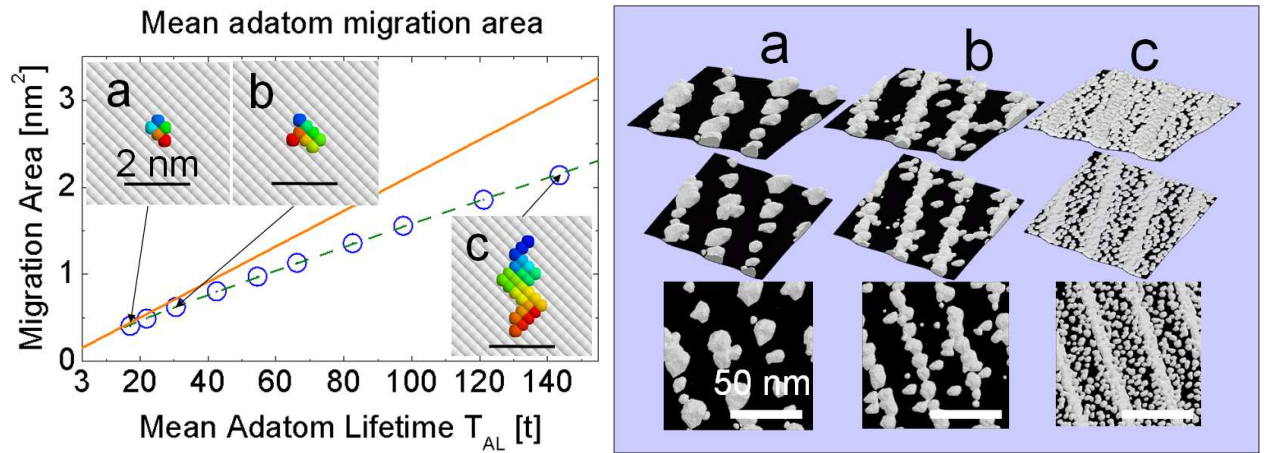
Figure 2.23: **Left**: The adatom lifetime as a function of the mean migration area of an Ag adatom and the Ag NC growth modes of three examples are shown (cf. figure 2.13). The circles (○) indicate data obtained from the simulations with parameters ΔE =0.045-0.100 eV at 300 K. The insets show typical traces of surface adatom random-walks with the color scale indicating the sequence of atomistic movements; **a**, **b** and **c** are with parameters ΔE=0.045 eV, 0.060 eV and 0.100 eV respectively. **Right**: The corresponding Ag surface morphology after a mean coverage 6 ML with three different viewpoints for each case.

The surface diffusion coefficient D for the (100) oriented surface is D =0.167 lu^2/t corresponding to 1.85×10^{-17} m^2/s. Figure 2.23 **left** shows again the diagram of the mean area of adatom surface surface migration with its expected residence time (figure 2.13). The insets in the left diagram of figure 2.23 show typical migration traces of adatom random-walks and the right diagram shows three dimensional views of a 6 ML Ag cluster distribution for $\Delta E = 0.045$ eV (**a**), 0.060 eV (**b**), and 0.100 eV (**c**) respectively.

a is the shortest AL sample with the binding energy $E_b^{Ag-SiO_2} = 0.245$ eV. The total sticking probability is only 18% (i.e. 82% of deposited atoms evaporate). Arriving atoms rarely stick at first, even in the relatively high local flux regions. Nucleation occurs by Ag atoms depositing directly onto preformed Ag clusters which remain in the system while atoms deposited onto the bare substrate are mainly evaporated. The mean AL is 17.1 t∼6.41×10^{-3} s and the mean migration area is 0.41 nm^2. This shows that a large number of Ag NCs with the VW growth mode is observed only in high deposition regions and that the NCs tend to grow in the direction of deposition. Ag accumulation therefore strongly enhances the small surface topography variation. **b** and **c** are the nucleation pattern when $E_b^{Ag-SiO_2} = 0.26$ eV and $E_b^{Ag-SiO_2} = 0.30$ eV respectively. Although these variations in binding energy are quite small, the adatom lifetime of metal monomers on the bare surface is prolonged exponentially with increasing binding energy. In the **b** diagram, nucleation occurs constantly in the high flux region of the surface and a coalescence of small Ag clusters is observed. A few clusters are also observed to grow in the low flux region. In total 35% of Ag atoms remain in the system. Experimentally observed Ag nanowires are quite close to this type of growth mode. The parameters corresponding to **b** give the best fitting to the SEM picture. The mean AL is 30.6 t∼1.15×10^{-2} s and the mean migration area is 0.62 nm^2. Nucleation occurs frequently in the peak deposition region and coalescence of NCs is promoted there. In the **c** diagram, the sticking probability is 82% and nucleation can occur overall on the substrate surface with the Ag accumulation following almost as same trend as the local flux distribution of figure 2.22(**b**). This is the longest AL sample and here the mean AL and migration area are 143.6 t∼ 5.39×10^{-2} s and 2.14 nm^2 respectively.

These results predict that the type of NC growth can be tuned by controlling the substrate
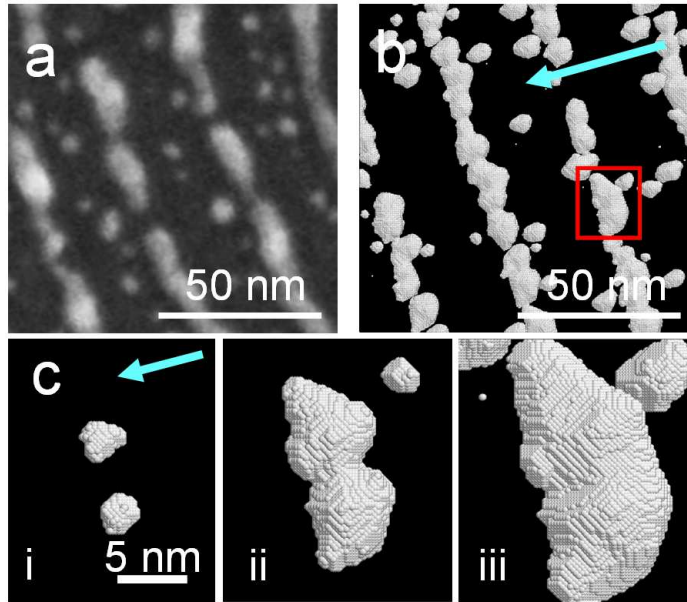
60

Figure 2.24: **a** Micrograph of the deposited Ag nanorods and NCs. **b** The simulation result from the Ag PVD model with a mean coverage of 4 ML. **c** Atomic scale NC growth process at the simulation time 10% (i), 50% (ii) and 100% (iii) of the growth stage indicated by the rectangle in **b**. Arrows in **b**, **c**-i exhibit the azimuthal direction of the incoming Ag flux.

temperature, the incident angle and flux to promote an effective coalescence along the surface topography due to the AL of metal adatoms. Indeed, for Co, which possesses a much higher adsorption energy to v-SiO$_2$ than of Ag, we observed selective nucleation of type **b** after heating pre-patterned substrates up to 1200 K, while overall nucleations similar to type **c** were observed at RT [191]. Under a high flux the tendency of nucleations shifts **a** $\rightarrow$ **b**, **b** $\rightarrow$ **c** and vice versa. From the graph of figure 2.23, a linear flux dependency of the nucleation pattern is expected for a long AL while a striking amplification of the underlying surface topography is observed for a short AL.

2.4.3 Comparison with experiment

In the experiment, nucleation is mostly observed in narrow stripe-like regions where the local flux is highest. Rapidly growing NCs in the high local flux region coalesce and become nanorods. The more slowly growing NCs located in the lower flux region remain as satellite clusters but there is some evidence of incomplete nanorod formation close to the well-formed nanorods where the flux is not quite so high. figure 2.24 (**a**) and (**b**) show the direct comparison (top views) between the magnified SEM image (**a**) and the model (**b**). A similar formation of Ag nanorods and satellite NCs is obtained from the RB-KMC simulations with E$_{ad}^{Ag/SiO_2}$=0.26 eV, i.e. $\Delta E = 0.06$ eV. The simulation result is the same as in figure 2.23 **b** with a different random number seed. This ΔE agrees nicely with the value expected by (2.22) and the adsorption energy is also closed to the DFT calculation of Ag adsorption energy on regular oxygen site 0.23 eV as well as regular Mg site 0.22 eV on MgO(100) [256] introduced in chapter 1.1.2.

Figure 2.24 (**c**) shows three different growth stages of NCs. In the early stages, nucleation is concentrated on the slopes facing the incoming atoms. Two small Ag particles with the diameter 2 nm and the height 1.2 nm (6 layers) are observed (i). Less nucleation occurs in low local flux regions due to a high re-emission rate. Further deposition promotes VW growth preferentially along the ripple due to NC coalescence (ii). The height is around 4.1 nm, the width and length are 5 nm and 12 nm respectively. Various growth stages of the Ag NCs can be seen due to the

time difference between nucleations. As more Ag is deposited, the KMC algorithm minimizes the surface free energy of the NCs and their shapes attain a form that would be expected from purely thermodynamic considerations (iii). The top of the NC is 5.4 nm high from the substrate; the width is 10 nm. A round shape appears typically on the deposition side of the NC whereas the other side is faceted.

Although ad-dimer desorption occurs in the simulation, this is less than for ad-monomers due to the model restriction of concerted motions. However, the adhesion energy of an Ag dimer on SiO_2, calculated by DFT, is lower than the Ag monomer even on a defect site [81]. Thus, ΔE can be a little larger than suggested here due to a high desorption rate of ad-dimers. Desorption of larger NCs is not observed and in any case a high adhesion energy of trimers is also predicted by DFT [81].

2.5 Summary

In summary, the Ag cluster growth mechanism on ripple-like pre-patterned v-SiO_2 is investigated by the continuum equation of reaction diffusion on slightly pre-patterned surfaces, the sticking probability, surface ad-monomer random walks, morphology- and incident angle dependent local flux rate, Ag area fraction growth, and the cluster formation process. The experimentally observed Ag NCs grown on rippled templates have been successfully reproduced by the introduction of a new type of KMC simulation method, the RB-KMC method. The coalescence of NCs is promoted mainly in high flux regions and less nucleation occurs in low flux regions due to re-evaporation from the substrate. This theoretical work predicts that millisecond order lifetimes, and ≈ 1 nm square surface migration ranges of Ag adatoms can trigger metal nucleations even on defect free surfaces. The nucleation density is influenced strongly by the AL of metal adatoms on templates as well as the flux, especially for a short AL and the amplification of the initial pre-patterned surface is highly enhanced in a certain low flux regime.

Chapter 3

A Markov chain model of transition states

In this chapter, a theoretical background for the rate-based KMC simulation scheme introduced in the previous chapter is more fundamentally discussed. The corresponding classical harmonic transition state theory applied in discrete lattice cells with hierarchical transition levels is considered [173].

The scheme used to determine transitions in the lattice-based KMC simulation model leads to an effective reduction of simulation steps by utilizing a classification scheme of transition levels for thermally activated atomistic diffusion processes. These atomistic movements are considered as local transition events constrained in potential energy wells over certain local time periods. These processes are mathematically formulated and represented by Markov chains of multi-dimensional Boolean valued functions in three dimensional lattice space. The events controlled by the barriers under a certain level are regarded as thermal fluctuations of the canonical ensemble and accepted freely. Consequently, the fluctuating system evolution process is implemented as a Markov chain of equivalence class objects. It is shown that the process can be characterized by the acceptance of metastable local transitions. The method is applied to a problem of Au and Ag cluster growth on a rippled surface. The simulation predicts the existence of a morphology dependent transition time limit from a local metastable to stable state for subsequent cluster growth by accretion. Excellent agreement with observed experimental results is obtained.

3.1 Acceleration of thin film growth simulation

Atomistic modeling of the growth of thin films or self assembled monolayers has attracted much attention over recent years due to the large number of technological applications in the field of nanotechnology [30, 124, 142]. Usually these models include a description of the interaction field between the atoms of the differing species in terms of a potential energy function. The deposition simulation then proceeds either by the addition of another species onto the surface or as a diffusive process where atoms rearrange themselves on the surface. Classical MD simulations to model the growth process have been carried out but usually these involve unrealistically fast deposition rates because the diffusive processes are dominated by rare events and would therefore require extremely long computing times beyond the scope of present computers. KMC simulations of the growth processes have also been performed but in many cases this has required a pre-knowledge of the likely transitions and their barriers since to calculate these *on-the-fly* has also been a computationally expensive process.

Recently however some progress has been made into the problem. For example Sprague *et al* [215] have shown by using TAD [214] that surface growth patterns of Cu deposited on Ag(001) are completely different than those that would arise without a proper description of surface diffusion. Henkelman and Jónsson proposed a method finding configuration energy saddle point using two different replicas of the system [99]. The coordinations of two replicas are slightly displaced by a fixed distance from each other like "dimer". The saddle point is explored by moving the dimer uphill on the potential energy surface from the vicinity of the potential energy minimum of the initial state up towards a saddle point. Combining this dimer method with KMC simultaneously, the algorithm calculates a long time scale system evolution on-the-fly, e.g., millisecond order Al(100) crystal growth [76, 101]. Other authors have also begun to study the growth process by KMC with calculating the transition barriers on-the-fly [195, 233]. There are however still many unsolved problems especially when the potential energy surface is such that there are lots of small transition barriers that only correspond to atomic vibration rather than a transition to a new state. In addition calculating barriers on-the-fly is computationally expensive.

However even when a traditional KMC process [165] is driven by a look-up table, simulations can be inordinately long when there are some transitions that are governed by very small energy barriers but where the main processes that drive the system have much higher barriers. A key aim of this work is therefore to develop a KMC method that will allow the main escape paths and rate constants to be determined quickly but at the same time will capture the essential physics.

To develop the methodology, the general concept of atomistic evolution induced by thermally activated kinetics in a discrete space is considered. A new calculation method including an alternative algorithm for a lattice-based KMC simulation is presented and applied to the problem of nanocluster growth on rippled surfaces. The basic idea of the simulation model is the classification of various transitions into unstable, metastable and stable (no) transition levels with their transition probabilities depending on local configurations. Under the assumption that metastable transitions dominate the entire system evolution, the optimization of their efficiency provides a method to predict the statistical behavior over an extremely long time. This approach can be represented with an oriented graph, considered as an extended percolation-model of Fortuin and Kasteleyn [86]. The transition states of cluster growth evolution induces oriented edges which essentially differ from atomistic interactions based on their application to the Ashkin-Teller-Potts model [11, 188].

This chapter is laid out as follows. In section 3.2, some terminologies of the mathematical description of the model utilized in this work are defined. In section 3.3 every transition event is classified into two types, the first caused by an external factor and the second by a thermal fluctuation. The evolution process induced by the latter type is then localized for the use with the KMC simulation. Section 3.4 discusses the efficiency of the local transition events to the entire system evolution by the introduction of the equivalence class of the fluctuation. The implementation of the modified KMC algorithm is also described. A concrete application to physical vapor deposition (PVD) experiments is presented in section 3.5, where the basic physical growth mechanisms and the stability of the formation process are also discussed. Finally, the effect of modified Metropolis algorithm to the convergence limit distribution of microstates is analyzed in section 3.6.

3.2 Definitions

In this section several basic terminologies are given.

Let $\mathbb{L} := \mathbb{Z}_{n_x} \times \mathbb{Z}_{n_y} \times \mathbb{Z}_{n_z}$ be a 3D lattice space with the spatial periodicity (n_x, n_y, n_z) for $n_x, n_y, n_z \in \mathbb{N} \cup \{\infty\}$. We define an *object* Ω on $\mathbb{L}$ as a Boolean-valued function. A *q-colored object* Ω is a $q + 1$-valued function on $\mathbb{L}$, i.e. all mappings of $\mathbb{L} \to \{0, 1, ..., q\}$. The total number of q-

colored objects is clearly $(q+1)^{n_{cell}}$, where $n_{cell} = n_x \times n_y \times n_z$. The number of colors q corresponds to the number of materials treated in the target simulation. The set of all objects on $\mathbb{L}$ is denoted by $\mathcal{O}(\mathbb{L})$. For $\Omega \in \mathcal{O}(\mathbb{L})$, $|\Omega|$ denotes the number of cells occupied by atoms. For the case of $q = 1$, $\mathcal{O}(\mathbb{L})$ is simply a Boolean representation of the simulation lattice system consistent with the bit encoding of the system [97].

A *functional* Φ *on* $\mathcal{O}(\mathbb{L})$ is defined as a mapping from $\mathcal{O}(\mathbb{L})$ to the real numbers $\mathbb{R}$, for example, the total potential energy of the system.

A *morphism* f of $\mathcal{O}(\mathbb{L})$ is a mapping from $\mathcal{O}(\mathbb{L})$ to itself. The total number of morphisms of $\mathcal{O}(\mathbb{L})$ is $(q+1)^{n_{cell}(q+1)^{n_{cell}}}$. The q'-*generator* $g_{q',u}$ and the *annihilator* a_u for each point $u \in \mathbb{L}$ and $q' = 1, ..., q$ are morphisms of $\mathcal{O}(\mathbb{L})$ defined as

$$g_{q',u} \circ \Omega(v) = \begin{cases} q' & (v = u \wedge \Omega(v) = 0) \\ \Omega(v) & (otherwise) \end{cases} \tag{3.1}$$

$$a_u \circ \Omega(v) = \begin{cases} 0 & (v = u) \\ \Omega(v) & (otherwise) \end{cases} \tag{3.2}$$

for all $v \in \mathbb{L}$ and objects $\Omega \in \mathcal{O}(\mathbb{L})$. Let $\wp := \{g_{q'u}, a_u : u \in \mathbb{L}, q' = 1, ..., q\}$ be the composition of all generators and annihilators. Define $\wp^*$ to be the set of minimal representations of those morphisms containing the null product as the identity morphism.

For $\Omega, \Omega' \in \mathcal{O}(\mathbb{L})$ an ordered pair (Ω, Ω') is called a *transition event from* Ω *to* Ω' and denoted also in the text by $\Omega \to \Omega'$.

The composition of morphisms $f_m \circ f_{m-1} \circ ... \circ f_0 \circ \Omega$ on $\mathbb{L}$ induces the Markov chain of objects $\Omega_0 \to \Omega_1 \to ... \to \Omega_m$, where $\Omega_{m'} = f_{m'} \circ ... \circ f_0 \circ \Omega_0$ for $m' = 0, ..., m$. For a Markov chain of objects $\mathcal{M} \equiv \Omega_0 \to ... \to \Omega_m$, $|\mathcal{M}|$ denotes the length m of the chain. The Markov chain $\mathcal{M}$ together with the potential energy functional Φ_p induces the sequence of real numbers $\Phi_p(\Omega_0) \to ... \to \Phi_p(\Omega_m)$ which indicates the evolution of the system's potential energy.

3.3 Transition states of Markov chains

3.3.1 Local transition events

In an atomistic simulation of a solid, the system evolves either through a modification induced by external factors e.g. a deposition event, through internal dynamical processes that occur more quickly than thermal fluctuations at a constant temperature T or by internal rare events which occur over longer time scales. It is these internal rare events that will be the focus of the work here, i.e. every internal transition event (Ω_l, Ω_{l+1}) is temporally well separated and each microstate of objects is regarded as a quasi-equilibrium state at T.

We assume that the transition $\Omega_l \to \Omega_{l+1}$ has the unique decomposition into the elementary transition states induced by an atomic jump attempt including exchange $\Omega_l = \nu_0 \to ... \to \nu_{s'} = \Omega_{l+1}$. These jump events are assumed to occur locally, i.e. the interaction distance is restricted so that an atomic jump occurs only to the nearest, or second nearest neighbor position. one of the morphisms $f_j(q', u, u') := g_{q'u'}a_u$ (jump) including the identity, **id** and $f_e(q', q'', u, u') := g_{q'u}g_{q''u'}a_{u'}a_u$ (exchange) for certain atomic types q', q'' and the positions $u, u' \in \mathbb{L}$. Note that if $u = u'$ then $f_j \equiv \textbf{id}$. From the sequence of transition events $(\nu_0, \nu_1^{at}), (\nu_1, \nu_2^{at}), ..., (\nu_{s'-1}, \nu_{s'}^{at})$, if an attempt (ν_j, ν_{j+1}^{at}) is accepted, then $\nu_{j+1} = \nu_{j+1}^{at}$, otherwise $\nu_{j+1} = \nu_j$. Set

$$\wp_{loc}^* := \bigcup_{u \in \mathbb{L}} \{f_j, f_e : |u' - u|_{\mathbb{L}} \leq r; q', q'' = 0, ..., q\}.$$

The transition events $\nu \to \mu$ of the objects $\nu, \mu \in \mathcal{O}(\mathbb{L})$ induced by $f \in \wp_{loc}^*$ will be termed *local transition events* and the decomposition of the transition event (Ω, Ω') into the local transition event together with the sequence of jump attempts will be called the *local decomposition of* (Ω, Ω').

From the quantum physical point of view mentioned in chapter 1.3.4, the local transition events can be generalized easily into the Markov chain indexed by complex numbers in order to handle the diffusion of particles with the imaginary time evolution. In this case, $\wp_{loc}^*$ is simply extended with the addition of the generator and the annihilator as the transition operators from the current real time step to the next real time step. The statistics of transition sequence connecting two complex times with different real time components can indicate all possible transition pathways consistent with the path integral of Feynman [82].

3.3.2 The Monte-Carlo method

Let $\Omega_l \to \dots \to \Omega_{l'}$ be a sub-chain of events lying between two external modification events. Consider its local decomposition $\Omega_l = \nu_0 \to \nu_1 \to \dots \to \nu_s = \Omega_{l'}$ and set this Markov chain as $\mathcal{M}$. The total length of the decomposition is

$$s = \sum_{t=l}^{l'-1} |\Omega_t|. \tag{3.3}$$

Now consider simulating this Markov process $\mathcal{M}$ with a Monte-Carlo (MC) method. In order to follow the process $\mathcal{M}$ the algorithm is constructed as follows:
(i) for every object ν_j choose an arbitrary morphism $f^j \in \wp_{loc}^*$,
(ii) each local transition event $(\nu_j, f^j \circ \nu_j)$ is considered as a jump attempt and accepted with probability $P(\nu_j, f^j)$.
(iii) after each local transition event a local time consumption, e.g. for an atom i, $\tau_j(i) = 1/|\nu_j|$ is added to the MC simulation time. If the atom i jumps to a non-equilibrium state, then the jump attempt continues until it reaches a position considered as an equilibrium state without adding τ_j.

The process (iii) implies that every transition is considered as the transition between two equilibrium states that are not always consistent with the nearest lattice positions. Note that one iteration of the simulation step (i)-(iii) advances the MC simulation time only τ_j time units and it continues for $j = 0, \dots, s-1$.

Let n be the number of total types of events and for $k = 1, \dots, n$, let α_k be the acceptance number of the type-k local transition event in $\mathcal{M}$. Then the n-events acceptance distribution $(\alpha_k) := (\alpha_1, \dots, \alpha_n)$ models the evolution of the system. Since the local transition probability $P(\nu_j, f^j)$ is a functional of the object ν_j and the morphism f^j that decide the migration barrier; P is also a function of the migration barrier and categorized into n-types $P_1, \dots, P_n$. Without loss of generality, it is assumed that $P_1 \geq P_2 \geq \dots \geq P_n$. Then the length s of the Markov chain $\mathcal{M}$ is approximately

$$s \approx \sum_{k=1}^{n} \alpha_k P_k^{-1} \tag{3.4}$$

and the total MC simulation time unit $t_{MCT}^{\mathcal{M}}$ is

$$t_{MCT}^{\mathcal{M}} = l' - l. \tag{3.5}$$

The process of $\mathcal{M}$ corresponds to the experimental evolution time and can be extremely long and impractical to evaluate within reasonable computation time. In the following section we consider the effective reduction of this process.

3.4   Effective transitions of objects

In this section, the relation between the accepted event distribution (α_k) defined in 3.3.2 and the fluctuation of the potential energy sequence is considered. This leads to a method to reduce the number of simulation steps. The effect of this in terms of the thermal fluctuations is discussed.

3.4.1   Convergence of the local fluctuation

The evolution of the system $\Omega_l \to ... \to \Omega_{l'}$ can be monitored through the potential energy sequence $\Phi_p(\Omega_l), ..., \Phi_p(\Omega_{l'})$. Denote by $\mathcal{M}_\iota$ the local decomposition of the sub-chain $\Omega_l \to ... \to \Omega_{l+\iota}$ for $\iota = 0, ..., l' - l$ and $\mathcal{M} = \mathcal{M}_{l'-l}$ as in 3.3.2. and set the variation mapping $\phi : \mathcal{M}_\iota \mapsto \mathbb{R}$ as $\phi(\mathcal{M}_\iota) = \Phi_p(\Omega_{l+\iota}) - \Phi_p(\Omega_l)$. Then the potential energy sequence is also given by $\phi(\mathcal{M}_0), ..., \phi(\mathcal{M}_{l'-l}) = \phi(\mathcal{M})$. Now consider the sequence of the local decomposition $\Phi_p(\nu_0), ..., \Phi_p(\nu_s)$. In this case, the potential energy gain (or lost) for the jump attempt (ν_i, ν_{i+1}^{at}) is $\Phi_p(\nu_{i+1}^{at}) - \Phi_p(\nu_i)$ and it gives a *weight* to the local transition event (ν_i, ν_{i+1}^{at}). If the local transition event (ν_i, ν_{i+1}^{at}) is a proper event of type-k, then denote $E_k^{pot} := \Phi_p(\nu_{i+1}^{at}) - \Phi_p(\nu_i)$. Consequently, for the partial distributions $(\alpha_k^\iota), \iota = 0, ..., l' - l$ of the accepted events distribution in $\mathcal{M}_\iota$, $\phi(\mathcal{M}_\iota) - \phi(\mathcal{M}_0) = (\alpha_k^\iota) \cdot (E_k^{pot})$. Now the union

$$\mathcal{M}_\Sigma := \bigcup_{\iota=1}^{l'-l} \{\mathcal{M}_\iota\},$$

$\mathbb{N}_0^n$, and $\mathbb{R}$ with three mappings, the potential energy difference ϕ, the accepted events distributions $g : \mathcal{M}_\iota \mapsto (\alpha_k^\iota)$ and the weight sum $h : (\alpha_k^\iota) \mapsto \sum_{k=1}^n \alpha_k^\iota E_k^{pot}$ can be written in terms of a commutative diagram :

$$
\begin{array}{ccc}
\mathcal{M}_\Sigma & \xrightarrow{g} & \mathbb{N}_0^n \\
\phi \downarrow & \swarrow & h \\
\mathbb{R}. &
\end{array}
\tag{3.6}
$$

Since the n-dimensional vector (E_k^{pot}) is constant, one can observe the temporal fluctuations through the sequence of $(\alpha_k^1), ..., (\alpha_k^{l'-l})$. The fluctuations lower the energy with some irreversible transitions and the system reaches a quasi-equilibrium state. Consider the behavior of the thermal fluctuations of the micro-canonical ensemble. Set

$$\Delta t := l' - l \tag{3.7}$$

the time interval of the external modification which is preset in the model, e.g. from experimental data so that

$$\Delta t = t_{exp}^{\mathcal{M}} \omega_{\mathbf{eff}} \tag{3.8}$$

for an experimental time interval $t_{exp}^{\mathcal{M}}$ and the average effective transition frequency $\omega_{\mathbf{eff}}$ of the system. Note that the corresponding time interval of every event $(\Omega_{\iota'}, \Omega_{\iota'+1})$ is thus $\omega_{\mathbf{eff}}^{-1}$. Let (α_k^ι) be the partial distributions of the accepted events distribution in $\mathcal{M}_\iota$. If Δt is long compared to the recovery time from an *unusual* fluctuation induced by the last external modification to a *usual* fluctuation (quasi-equilibrium state), then the convergence of the acceptance of each event $\alpha_k^\iota \to \alpha_k$ for $\iota \to \Delta t$ is also to be considered. Let ε be the range of the usual fluctuation of the potential

energy of the system at a temperature T. Then one finds the minimal value $\iota_0 = \iota_0(\varepsilon)$ with the property that

$$|\Phi_p(\Omega_{\iota'}) - \Phi_p(\Omega_{\iota''})| < \varepsilon$$

for all $\iota', \iota'' \in [\iota_0, \Delta t]$, where $\Phi_p(\Omega)$ indicates the potential energy of Ω. Denote

$$\theta(\iota) := \frac{\iota}{\Delta t}, \tag{3.9}$$

the *convergence factor* of the subchain $\Omega_l \to ... \to \Omega_{l'}$ in the sense of the potential energy transition within the fluctuation range ε. $\theta(\iota_0) =: \theta_0$ is the minimum convergence factor in this sense. The Boltzmann's entropy S (see chapter 1.3.1 eq. (1.31)) of the system for this quasi-equilibrium state is therefore given by

$$S = k_B \ln |\{\Omega_\iota : \iota \in [\iota_0, \Delta t]\}|. \tag{3.10}$$

Now consider the contribution of $(\alpha_k^\iota), \iota = 0, ..., \Delta t$ for the entropy calculation. Let (α_k^t) be the continuum extension with respect to the time parameter ι of (α_k^ι). Then the dissipation of unusual fluctuations implies $\partial_t \alpha_k^t = 0$ for $t > \iota_0$ and for usual fluctuations the derivation $\partial_t \alpha_k^t$ remain. These types of events compose the thermal fluctuation. The set of microstates consistent with the fluctuating system is the set of all accessible states with the screened transition types, i.e.

$$\{\Omega_\iota : \iota \in [\iota_0, \Delta t]\} = [\Omega_{\iota_0}]$$

where $[\Omega_{\iota_0}]$ is the equivalence class of objects connected by the pathways consisting of type-k transitions with $\partial_t \alpha_k^t \neq 0$ for $t > \iota_0$. These transitions are small barriers and the introduction of an equivalence class for the whole process is the core idea of the modified MC algorithm described in section 3.4.3. Due to the principle of equal *a priori* probabilities, every microstate belonging to the class $[\Omega_{\iota_0}]$ appears with same probability in the sequence $\Omega_{\iota_0} \to ... \to \Omega_{l'}$. Consequently, it is enough to consider the Markov chain $\mathcal{M}_{\iota_0}$ to follow the essential system evolution. The convergence factor (3.9) indicates how the physical process is shortened.

Since the number of transition attempts, i.e. the effective jump frequency, is independent of the system evolution, the length of the local decomposition $\mathcal{M}_\iota$ is approximately

$$|\mathcal{M}_\iota| \approx \theta(\iota)s = \frac{\iota s}{t_{MCT}^{\mathcal{M}}}. \tag{3.11}$$

from eq.(3.5), (3.7) and (3.9)

3.4.2 The importance of individual local transitions

The contribution of each local transition event to the entire system evolution is not straightforward. Clearly, for a high transition probability P_k a large number of α_k is expected. However, the number of accepted jumps also depends on the frequency of occurrence of the configuration. The frequency of occurrence distribution can be represented as

$$(\beta_k) := (\alpha_1/P_1, ..., \alpha_n/P_n). \tag{3.12}$$

The quantity β_k is called the *attempt frequency* of the type-k event. The relation $\beta_k < \beta_{k'}$ implies that the configuration giving the type-k' transition is more preferred than the type-k transition event. An excessive acceptance of certain types of event does not always mean a change. For example, an adatom deposited on a flat crystal surface can diffuse around until it reaches a defect or a step edge. During diffusion, the correlation between the deposition point and the current

position is lost and only when the adatom finally reaches a binding site does the system evolution proceed further. The crucial evolution of the system occurs with a metastable state transition such as overcoming a step-edge barrier. The model should ensure that the total potential energy does not change substantially through the reduction in the number of α_ks that the evolution of system is misdirected.

The activation energy barrier border between the unstable (usual fluctuations) and metastable states is defined to be as the *boost energy* E_{bst} and all activation energies above E_{bst} are considered as *effective* migration barriers contributing to unusual fluctuations. The boost energy is a parameter that needs to be carefully set for each simulation so that the dynamics is not distorted by choice of too high a factor. Let P_{n_0} be the transition probability induced by the smallest effective migration barrier. Now consider the identification of transitions with small fluctuations. From the mathematical point of view, this coarse graining introduces the equivalence relation in the set of all objects $\nu, \mu \in \mathcal{O}(\mathbb{L})$ as follows:

$$\nu \sim \mu \Leftrightarrow \qquad \exists a \in \mathbb{N}, \exists f_1, ..., f_a \in \wp_{loc}^*;$$
$$\mu = f_a...f_0 \circ \nu$$
$$\text{with } P(f_{a'-1}...f_0 \circ \nu, f_{a'}) > P_{n_0}$$
$$\text{for } a' = 1, ..., a.$$

The corresponding equivalence class of objects is $[\nu]$ in $\mathcal{O}(\mathbb{L})$. In the worst case, namely for a system with a high entropy, each equivalence class retains all possible configurations consisting of identical atoms. However, if high potential barriers separate the states, then this enhances the effect of the metastable transitions.

The potential energy of the class $[\Omega]$ is defined as the following interval of the energy range

$$\inf_{\tilde{\Omega} \in [\Omega]} \Phi_p(\tilde{\Omega}) \leq \Phi_p(\Omega) \leq \sup_{\tilde{\Omega} \in [\Omega]} \Phi_p(\tilde{\Omega}),$$

which represents the usual fluctuation range of the microstate Ω denoted by $\Phi_p([\Omega])$. The transition probability $\mathcal{P}([\nu], [\mu])$ of the equivalence classes $[\nu] \to [\mu]$ may be defined as the expected value of all transition paths

$$\mathcal{P}([\nu], [\mu]) = \begin{cases} 1 & ([\nu] = [\mu]) \\ \displaystyle\sum_{\nu' \xrightarrow{f} \mu'} \frac{P(\nu', \mu')}{w_{loc}([\nu], [\mu])} & ([\nu] \neq [\mu]), \end{cases} \tag{3.13}$$

where $w_{loc}([\nu], [\mu])$ is the number of all such local transition pathways and the summation ranges over all local transition events from $\nu' \in [\nu]$ to $\mu' \in [\mu]$ induced by local translation morphisms $f \in \wp_{loc}^*$. The Markov chain of the equivalence classes of objects $[\Omega_0] \to ... \to [\Omega_l]$ induces the sequence of fluctuating potential energies $\Phi_p([\Omega_0]) \to ... \to \Phi_p([\Omega_l])$. Note that if E_{bst} is smaller than the minimum migration barrier, i.e. $n_0 = 1$, then $[\Omega] = \{\Omega\}$ and $\Phi_p([\Omega_l]) = \{\Phi_p(\Omega_l)\}$.

By introducing this classification method the acceptance of the local transition probability with small barriers is maximized and the time spent to distinguish the local transition events with small barriers is considerably reduced.

3.4.3 The modified algorithm for effective transition states

The modification P_k' of the transition probability P_k for the type-k local jump attempt described in 3.4.2 is implemented as:

$$P_k' = \begin{cases} 1 & (\ k < n_0) \\ P_k/P_{bst} & (\ otherwise) \end{cases} \tag{3.14}$$

for the boost probability P_{bst} corresponding to the acceptance of the highest barrier E_{bst} within the usual fluctuations, The local time consumption $\tau'(i)$ of this type-k transition attempt of atom i is set as

$$\tau'(i) = \begin{cases} 0 & (\ k < n_0) \\ \tau(i) & (\ otherwise). \end{cases} \tag{3.15}$$

So every simulation step which is spent for the transition with barrier less than E_{bst} does not advance the time step.

Now consider a KMC simulation with the algorithm mentioned above. Let $\mathcal{M}' \equiv \Omega_l = \nu_0 \to \nu_1' \to ... \to \nu_{s'}'$ be the Markov chain describing the simulation consisting of the local transition events with the modified acceptance probability (3.14). Assume $\mathcal{M}'$ reproduces the experimentally observed evolution process and let $(\alpha_k') = (\alpha_{n_0}', ..., \alpha_n')$ be the corresponding accepted event distribution. If the system evolution excludes this probability translation, then the number of accepted events for the effective transitions should be approximately the same as the number of those transitions in $\mathcal{M}_\iota$ for some $\iota \geq \iota_0$, i.e.

$$\alpha_k^\iota \approx \alpha_k' \text{ for } k = n_0, ..., n. \tag{3.16}$$

It is important that the system evolution proceeds according to the property (3.16).

The translation mapping (3.14) enhances the acceptance of effective transitions linearly while one might expect a continuous dynamical evolution would induce a nonlinear enhancement. This also affects the attempt frequency (3.12) of effective transitions, from preferred local configurations. If various metastable transition events determine the system evolution, then the relative acceptance ratio plays a crucial role in the formation of local configurations and a nonlinear translation of (P_k) would therefore have a high risk of losing the correct evolution of the system since it does not keep the same relative acceptance ratio.

For the Markov chain $\mathcal{M}_\iota$, the length is $\theta(\iota)s$ from eq.(3.11) and can be represented as

$$\theta(\iota)s = \delta_{bst} + \sum_{k=n_0}^{n} \alpha_k^\iota P_k^{-1} \tag{3.17}$$

from the same argument by (3.4), where δ_{bst} is the number of simulation steps spent for local transition events with small barriers $\leq E_{bst}$. Since the translation mapping for the effective transition events is linear, a reduction in the time required for the Monte Carlo simulation with the boost factor P_{bst}^{-1} is expected. The total length of $\mathcal{M}'$, describing the simulation system evolution is

$$s' := \delta_{bst}' + P_{bst} \sum_{k=n_0}^{n} \alpha_k^\iota P_k^{-1}. \tag{3.18}$$

Hence, if the Markov chain $\mathcal{M}'$, i.e. the KMC simulation, reproduces the experimentally observed evolution process with the reduced simulation steps s', then the reduction expectancy in the number of simulation steps $|\mathcal{M}'|/|\mathcal{M}|(= s'/s)$ is given by the relation

$$\frac{s'}{s} = \frac{\delta_{bst}'}{s} + P_{bst}\left(\theta - \frac{\delta_{bst}}{s}\right), \tag{3.19}$$

from eq.(3.17) and eq.(3.18). Additionally, if the number of total atoms in the system is relatively stable during the original Markov process $\mathcal{M}$, one can estimate the length $|\mathcal{M}|$ as

$$s \approx t_{exp}^{\mathcal{M}} \omega_{\mathbf{eff}} |\Omega_l|, \tag{3.20}$$

from eq.(3.3) and eq.(3.8). Similarly, since the MC simulation time counts the number of the effective transitions with (3.15), it follows that

$$s' - \delta'_{bst} \approx t^{\mathcal{M}'}_{MCT} |\Omega_l| \tag{3.21}$$

for the MC simulation time $t^{\mathcal{M}'}_{MCT}$ of $\mathcal{M}'$. Moreover, the maximization of the small barrier transition acceptance (3.14) implies

$$\frac{\delta_{bst}}{s} < \theta(\iota)\frac{\delta'_{bst}}{s'}. \tag{3.22}$$

Thus one can evaluate the convergence factor θ with eq.(3.19)-(3.22) and the simulation value s', δ'_{bst} as

$$\frac{t^{\mathcal{M}'}_{MCT}}{t^{\mathcal{M}}_{exp}\omega_{\mathbf{eff}}P_{bst}} < \theta(\iota) < \frac{t^{\mathcal{M}'}_{MCT}}{t^{\mathcal{M}}_{exp}\omega_{\mathbf{eff}}P_{bst}}\left(1 - \frac{\delta'_{bst}}{s'}\right)^{-1}. \tag{3.23}$$

The relation (3.23) indicates the stability range in the sense of the evolution speed of the system which can be reproduced by the consistent modified KMC simulation $\mathcal{M}'$. In other words, a success of reproduction by $\mathcal{M}'$ guarantees the existence of the convergence factor $\theta(\iota) > \theta_0$ in this range. For the minimum Markov chain $\mathcal{M}_{\iota_0}$ and the convergence factor θ_0, the minimum KMC time range required is from (3.23)

$$t^{\mathcal{M}}_{exp}\omega_{\mathbf{eff}}P_{bst}\theta_0\left(1 - \frac{\delta'_{bst}}{s'}\right) < t^{\mathcal{M}'}_{MCT} < t^{\mathcal{M}}_{exp}\omega_{\mathbf{eff}}P_{bst}\theta_0.$$

Thus the possible reduction rate of simulation time is from (3.5), (3.7), (3.8) and this argument

$$\frac{t^{\mathcal{M}'}_{MCT}}{t^{\mathcal{M}}_{MCT}} \sim P_{bst}\theta_0. \tag{3.24}$$

Note that if P_{bst} is chosen so small that E_{bst} exceeds the usual fluctuation range of the system, the simulation can not follow the evolution process accurately.

3.5 Cluster growth simulation models

Although the method described in the previous sections is general to many lattice-based systems, a strong motivating factor for its development was an understanding of experimental work of Ranjan *et al* [190], concerned with the deposition of Ag clusters on silica surfaces where ripple structures had been pre-patterned using an ion beam described in the previous chapter. In this section, the detail of the extended model mentioned in chapter 2.4 together with Au PVD and the application to this problem are described.

The initial surface is shown in Figure 3.1 with three clearly defined ripple peaks along with the direction at which the Ag atoms deposit. The ripple shape is an excellent approximation to the cross-sectional transmission electron microscope image of the SiO_2 substrate (figure 2.6 (a)). The asymmetrical ripple surface shown in figure 3.1 is set as Ω_0 and held fixed during the simulations. This substrate is also chosen to be commensurate with the metal crystal overlayer. Ag atoms are deposited homogeneously with the incident angle $\theta = 70°$ to the mean surface normal and perpendicular to the ripple direction. The local flux, f_{loc}, ranges from 20% to 75% of the flux f from the evaporator due to the surface slope and the deposition angle in this case. SiO_2 is regarded
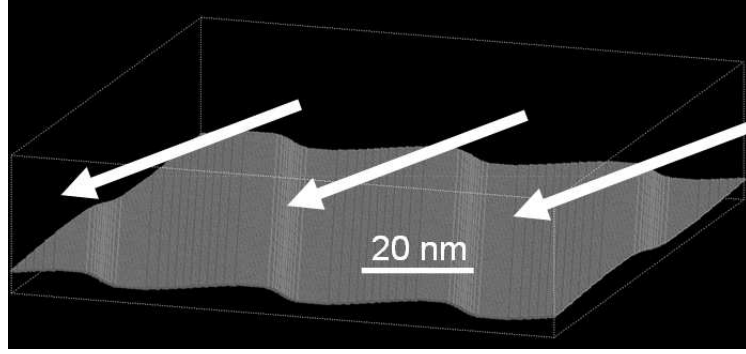
Figure 3.1: The initial surface of the simulation model, together with the direction of the arriving flux from the evaporation source (perpendicular to the ripple structures). The asymmetrical ripple shape is fitted to represent the rippled v-SiO$_2$ surface shown in figure (2.6)(a).

as an homogeneous material and therefore $q = 2$ in $\mathcal{O}(\mathbb{L})$, namely, the metallic atoms are regarded as the type-I atoms while every SiO$_2$ component is type-II.

The internal modification of the system (local transition morphisms $\wp_{loc}^*$) is handled by single atomistic jumps of type-I atoms to the NN empty positions as the local transition. Concerted motions are not allowed. The external modification to the system occurs through the deposition of metal monomers. The depositing atoms are simply set in the positions exposed to the incident trajectories and neither reflection nor surface drifting on impact is considered. The atoms detaching from metallic clusters or the substrate are regarded as re-evaporated atoms and eliminated from the simulation. Thus there is no effect of re-deposition of atoms returning to the gas phase.

The KMC simulation proceeds either by a single deposition event on to the surface or through the jump of a surface atom. The relative frequency of a deposition event is chosen to match experimental flux rates but the acceptance or otherwise of a candidate jump event is determined from energies obtained from the geometrical arrangements and types of the neighboring sites. The way in which these energies are determined is given in the next section.

3.5.1 The configuration energy and migration barriers

For a type-I atom i, let n_i^I and n_i^{II} be the number of type-I, and type-II NN atoms, respectively. The potential energy E_i of i is defined from eq. (2.36) as $E_i = -\zeta\sqrt{n_i^I} + An_i^I - E_i^{M-SiO_2}(n_i^{II})$, with parameters ζ=1.8352 eV (M→Au), 1.1663 eV (M→Ag), A=0.2179 eV (M→Au), 0.09982 eV (M→Ag) [92] and $E_i^{M-SiO_2}(n_i^{II})$ is the metal-SiO$_2$ interaction term given by eq. (2.37) for each metal. The potential functional Φ_p is defined as

$$\Phi_p(\Omega) = \sum_i E_i,$$

where i ranges all type-I atoms in $\Omega \in \mathcal{O}(\mathbb{L})$.

Let $\nu \in \mathcal{O}[\mathbb{L}]$ be an object. For two sites $u_{ini}, u_{fin} \in \mathbb{L}$, let u_{ini} be the positions where the atom i is located and u_{fin} be an empty NN position of u_{ini} represented by ν, i.e. $|u_{ini} - u_{fin}| = \sqrt{2}$ [l.u.], $\nu(u_{ini}) = 1$ and $\nu(u_{fin}) = 0$. For a local transition morphism $f := f_j(1, u_{ini}, u_{fin})$, set $\nu' := f \circ \nu$. Then the migration barrier $E_m(\nu, f)$ is given by

$$E_m(\nu, f) = \begin{cases} 0 & (\Phi_p(\nu) > \Phi_p(\nu')) \\ \Phi_p(\nu') - \Phi_p(\nu) & (\Phi_p(\nu) < \Phi_p(\nu')) \\ E_{mig}(\nu, \nu') & (\Phi_p(\nu) = \Phi_p(\nu')) \end{cases} \tag{3.25}$$

$|N_i^I|_{(=|NN_f^I|)}$	0	1	2	3	4	5	6	7
$|N_c^I|=0$	0	0	0	$E_{mig}^{(111)}$	$E_{mig}^{(100)}$	$E_{mig}^{(110)}$	0	0
$|N_c^I|=1$	0	0	$E_{mig}^{(111)}$	$E_{mig}^{(100)}$	$E_{mig}^{(110)}$	0	0	0
$|N_c^I|=2$	0	$E_{mig}^{(111)}$	$E_{mig}^{(100)}$	$E_{mig}^{(110)}$	0	0	0	0
$|N_c^I|=3$	$E_{mig}^{(111)}$	$E_{mig}^{(100)}$	$E_{mig}^{(110)}$	0	0	0	0	0
$|N_c^I|=4$	$E_{mig}^{(100)}$	$E_{mig}^{(110)}$	0	0	0	0	0	0

Table 3.1: Migration energy list $E_{mig}(\nu, \nu')$ for type-I interactions. $|N_*^{II}| = 0$ for every case. The barriers in the table are estimated from the literature adatom migration barriers on the (111), (100) and in-channel (110) oriented surfaces with the same neighbor configurations. $E_{mig}^{(111)}$=0.04-0.10, 0.07 eV (Ag [69, 177],Au [69]), $E_{mig}^{(100)}$=0.38, 0.51 eV (Ag [69],Au [69]), $E_{mig}^{(110)}$=0.28, 0.23 eV (Ag [79],Au [69]). The zero barriers correspond to transitions and configurations which have been tested by numerical experiment to be so unimportant that an accurate determination is unnecessary.

where E_{mig} is the migration barrier list for potential energy conservative transitions determined from literature values and described in more detail below. The advantage of this functional (3.25) is to give a quick estimation of the migration barriers such as the ES barrier (see chapter 2.1.2) and various surface migration barriers during the atomistic movement along the network of fcc sites. In the first case of (3.25), the model assumes that the transition barrier is negligible if the final configuration ν' is more stable than the initial configuration ν. Particularly it allows atoms overcoming the ES barrier to move freely until they reach stable positions. This could cause however an error if the initial configuration ν is already a quasi-equilibrium state.

For the case of the symmetric configurations due to the NN environment of the initial and the final states where the RGL potential does not change, the migration barrier list $E_{mig}(\nu, \nu')$ shown in Table 3.1 is utilized. The cases shown with the zero barriers refer to transitions that are either rare or whose contribution is negligible. The other cases where the initial, final and common number of nearest neighbours are the same as in the cases of adatom transitions on surfaces, data from the literature corresponding to these values are used. The transition barriers for the type-I atoms are estimated from the adatom migration barriers on (111), (100) and in-channel (110) oriented surfaces calculated in Ref.[69, 79]. Although these values are the best estimates for the surface transitions they may be less accurate for some other configurations possessing the same number of $|N_i^I|$, $|N_f^I|$ and $|N_c^I|$. The migration barrier for the case of the symmetric configurations including type-II atoms is assumed as the constant E_m^{Ag/SiO_2} (see chapter 2.2.3).

Figure 3.2 shows examples of some configuration energies of atoms located in various positions and a step-edge barrier. Each E_i is calculated by eq.(2.36) and the step-edge barrier $E_m = 0.39$ eV for the transition indicated is derived for the transition of type $(|N_i^I|, |N_c^I|, |N_f^I|) = (2, 1, 1)$, with the average NN site occupation $\bar{n} = 8.5$ (∗ in figure 3.2).

In figure 3.2, the atom i has been deposited on the part of the surface which appears to be an island with a (111) surface orientation whereas the atom with $E_i = -1.93$ eV is located on an island with a (100) surface. Compared to all other atoms belonging to the (111) island, the configuration energy of i is quite high. Even for the relatively high energy atom located along the edge of the island, the reverse migration barrier climbing up to the island top is at least $E_m = 0.98$ eV with the transition type $(3, 2, 0)$. Such an event is unlikely to happen and thus the adatom i will be constrained to the island (see also figure 3.6). The migration barrier of i on Ag(111) is 0.04-0.10 eV by Table 3.1. Since this barrier is quite small in any case, following the scheme outlined in the previous section is regarded as a usual fluctuation.
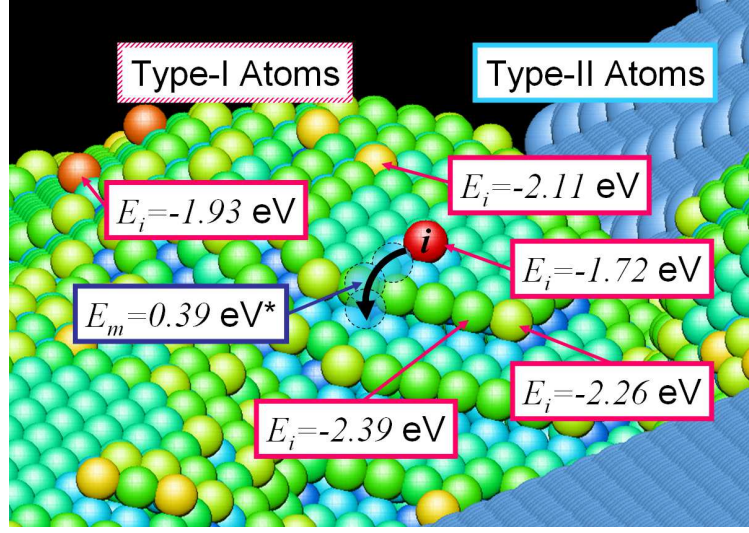
Figure 3.2: The atomistic landscape during an Ag PVD simulation: the E_i values indicate the configuration energy change for an atom depositing at the arrowed site, calculated from eq.(2.36).

The transition probability P for the migration barrier $E_m(\nu, f)$ is assumed to follow the Arrhenius law with a constant prefactor for all transitions

$$P(\nu, f) = \exp\{-E_m(\nu, f)/k_B T\}, \tag{3.26}$$

where the local time consumption for atom i is

$$\tau(i) = \frac{1}{|\nu|}.$$

All the sites possessing at least 3 occupied NN sites are considered as equilibrium configurations and the atom i continues jumping until it gains such a configuration with local time consumption $1/|\nu|$.

For the initial nucleation distribution, the optimal values $E_b^{Ag-SiO_2} = 0.26$ eV, $E_b^{Au-SiO_2} = 0.24$ eV are found during simulations and it is these energies that are used to determine the lifetime of metal adatoms on the SiO_2 surface by (2.37). A similar adhesion energy range of Ag, 0.23 eV, on regular oxide site of MgO(100) surface is also predicted by DFT calculation [256] whereas a bit higher energy is expected for Ag/SiO_2. Each transition probability is determined by the primary local configuration with (3.25) and (3.26).

Sequential evolution of a cellular system determined automatically by the precursory local configuration is called a cellular automaton [245]. Wolfram classified the cellular automata into four classes with respect to the type of time evolution. A class 1 object is the type such that all initial patterns evolve quickly into a stable, homogeneous state. If the system evolves quickly into a stable or periodically oscillating structure with remaining some initial randomness, it is categorized as class 2. A class 3 object evolves in a preudo-random or chaotic manner from any initial patterns. If the randomness and a stable or oscillating structure are outcome for relatively long time period, it is in class 4. Local changes to the initial pattern may spread indefinitely. Due to the probabilistic determination[1] and the complex transition process along the local topography with the deterministic potential field, the entire system evolution between the external modification can be regarded as a class 4 object of a three dimensional (3D)-cellular automaton.

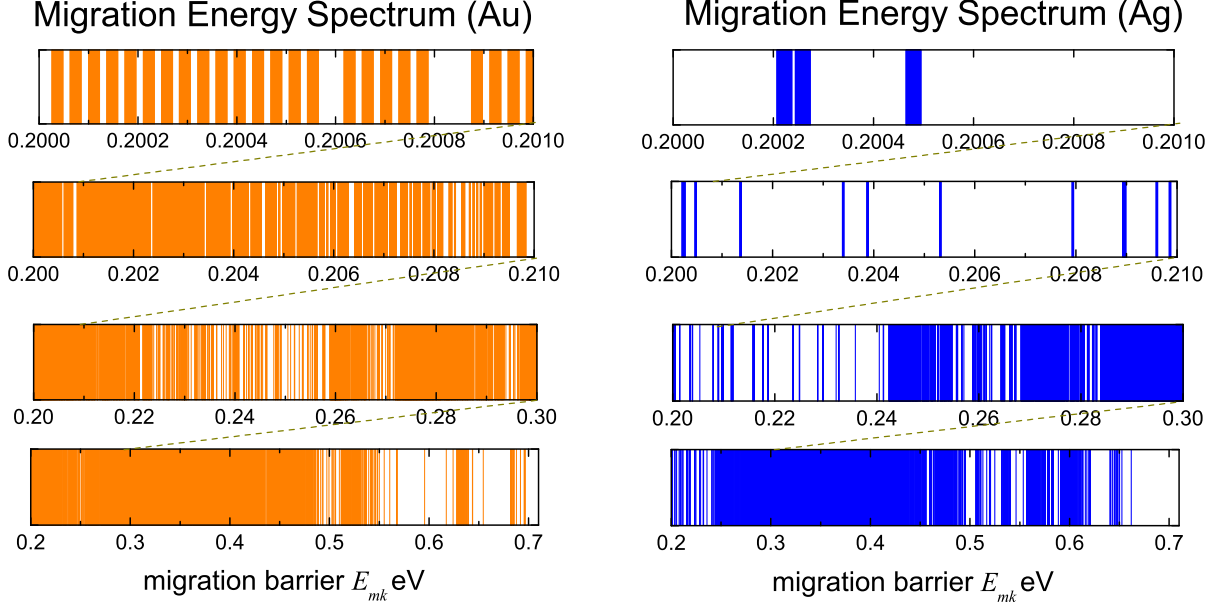[1]Usually a cellular automaton is deterministic and not statistical.

Figure 3.3: The effective migration barriers estimated by the RGL potential with the parameters [92] for Au and Ag. Totally 4039-types (Au) and 4712-types (Ag) of effective transition events are accepted during a MC simulation time of 1.2×10^7 units.

3.5.2 Transition events

For all positive migration barriers determined by (2.39) let $E_{m_1}, ..., E_{m_n}$ be the barriers with $E_{m_1} < ... < E_{m_n}$. Set $P_k := \exp\{-E_{m_k}/k_B T\}$. For the both PVD simulations the surface transitions

$$P'_k := \exp\{-\vartheta(E_{m_k} - E_{bst})/k_B T\} \qquad (3.27)$$

is considered with $E_{bst} = 0.20$ eV. In arriving at this number some simulations were carried out at different E_{bst} values. With $E_{bst} = 0.30$ eV, the simulations ran even quicker but the system evolution is distorted because of the barriers associated with the dominant processes of the migration of metal monomers in the in-channel direction on the (110) oriented surface. These are 0.28 eV for Ag and 0.23 eV for Au. For a value of $E_{bst} = 0.10$ eV, the nanostructures showed no observable difference to those formed with $E_{bst} = 0.20$ eV. ϑ is the temperature factor which should be close to 1 by the argument in section 3.4.3. Since the PVD experiments were carried out at the room temperature, the temperature parameters are set as $\vartheta = 1$ and $T = 300$K during the simulation.

As a result of the choice of E_{bst}, all transition events under a barrier 0.20 eV possess the same acceptance ratio 1. Thus the number of the acceptances for every such event depends only on the frequency of its configuration occurrence. The boost probability P_{bst}, defined in 3.4.3, is thus $P_{bst} = \exp(-0.2/k_B T) = 4.37 \times 10^{-4}$ and the boost factor is $P_{bst}^{-1} = 2.29 \times 10^3$. Figure 3.3 shows the list of accepted migration barrier distribution for type-I atoms interaction. Every activation barrier is calculated by eq.(3.27) and listed in the look-up table. A total of 4,039 types (Au) and 4,712-types (Ag) local transition events are accepted during 1.2×10^7 time units corresponding to
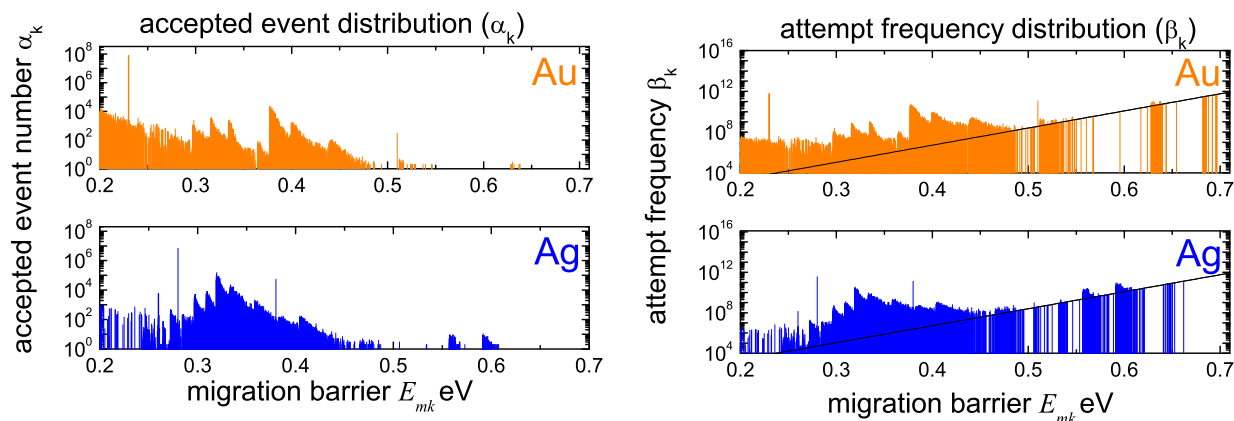
Figure 3.4: The distribution of accepted events, and the attempt frequencies for the Au and Ag growth simulations. Migrations with barriers lying between 0.2 eV and 0.7 eV are regarded as metastable transition states. The barriers shown are for the interactions of type-I atoms only. The solid lines in the (β_k)-distribution indicate the inverse probability P_k^{-1}, i.e. the average number of attempts for one acceptance.

3 CPU days calculation on a typical single processor desktop machine. However, most of these transition barriers rely on the mean configuration energy term (2.41) and by fixing the average number $\bar{n}$, the number of accepted event types is reduced to around 100. This implies that most transition events have a low probability of acceptance and only around 100 events represent the metastable transitions. Figure 3.4 shows the total accepted effective event distribution and its attempt frequency (3.12) during the simulation of Au and Ag PVD deposition. The distributions (α_k) and (β_k) include all local transition events considered as the internal modification activity.

In the (α_k)-distribution, the solitary peaks located at 0.23 eV, 0.51 eV (Au) and 0.28 eV, 0.38 eV (Ag) correspond to adatom migration attempts on the metal (110) in-channel and (100) surfaces, respectively. The saw-like peaks in the graphs mainly indicate the acceptance of various types of step-edge barriers due to the mean NN configuration. As an Ag cluster grows, its mean surface curvature decreases. Thus the mean value of the NN occupied positions increases and consequently, each local transition event reduces the barrier slowly by decreasing the configuration energy difference E_j^{ini}-E_j^{fin} for $j > 0$ from eq. (2.40), eq.(2.41) and eq.(2.42).

In the (β_k)-distribution, the attempt frequency for barriers other than the (110) and (100) type transitions slightly increases with increasing barrier height. This indicates that the acceptance of small metastable transitions is already saturated and the system is waiting for a rarer transition with a higher barrier. The solid lines exhibit the average attempt frequency for one acceptance, i.e. P_k^{-1}, and it can be seen that this average arises from only 1 transition for the high barrier events. Hence, as the graph of (α_k) also shows, the acceptance of such high barrier event is so small as to have hardly any influence on the system evolution and thus the practical metastable transition range is anticipated only in the range 0.2-0.6 eV.
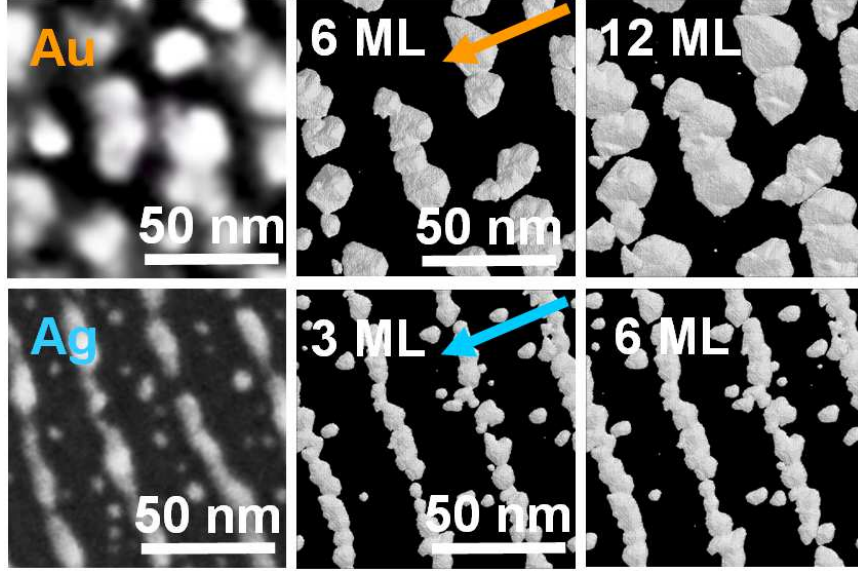
Figure 3.5:   A comparison between the experimental results for Au and Ag PVD with the simulation model. SEM images of the rippled v-SiO$_2$ surfaces after Au and Ag deposition (**left**) for 30 and 75 minutes respectively. A top view of the rippled simulation surfaces after Au ($E_b^{Au-SiO_2} = 0.24$ eV) and Ag ($E_b^{Ag-SiO_2} = 0.26$ eV) simulations (**middle, right**) are shown. The total metal accumulation is equivalent to 6 ML (**middle**), 12 ML (**right**) for Au and 3 ML (**middle**), 6 ML (**right**) for Ag. Arrows indicate the direction of incident metal atoms.

3.5.3   Comparison with Experiment

As discussed in the previous chapter, the aggregation of clusters is observed mainly where the local flux is a maximum, namely on the slopes facing the evaporator in experiment. A similar tendency is also observed in the simulations. Nucleation occurs when two adatoms migrating on the substrate come together. Due to the strong binding energy (2.36) the detachment of a dimer from the surface is unlikely at the simulation temperature of 300 K. However, despite their lower mobility than monomers, a small proportion of dimers still detach from the substrate. The mobility of trimers including detachment is almost negligible. Thus the nucleation probability is strongly influenced by the migration of monomers during the adatom lifetime and the local flux.

Figure 3.5 gives a direct comparison of the simulation results with the SEM images [172][2]. With the chosen binding energy parameters ($E_b^{Au-SiO_2} = 0.24$ eV and $E_b^{Ag-SiO_2} = 0.26$ eV), the simulated metal clusters are very similar to the SEM images. Especially the shape of the cluster edges and sizes agree nicely with the experimental observations. The adhesion energy of Au-SiO$_2$ is generally less than of Ag-SiO$_2$ [81]. From the DFT calculation (B3LYP, with BSSE correction) by Ferullo *et al* [81] the adhesion energy of Au and Ag monomer on reduced SiO$_2$ site is -1.90 eV and -2,13 eV respectively. If one applies this rate Au-SiO$_2$/Ag-SiO$_2 \sim 0.9$ to the Ag monomer binding energy $E_b^{Ag-SiO_2} = 0.26$ on a regular site, then the energy of an Au monomer is approximately $E_b^{Au-SiO_2} = 0.23$. Thus the simulation results agrees nicely with this estimation if the surface migration barriers $E_m^{Au-SiO_2}$ and $E_m^{Ag-SiO_2}$ are in same range. The similarity of the cluster shapes suggests the validity of the chosen parameters for Au and Ag and helps validate the unusual fluctuation convergence model considered above. The size and coalescence of clusters result in the nucleation probability on the substrate which is strongly influenced by the adatom lifetime and local flux.

---

[2]STM images are provided by Dr. Mukesh Ranjan (private communication).

In the early stages of growth, nucleation occurs mainly on the slopes facing the incoming metal atoms where the local flux is high but some small Ag clusters are also observed in the lower flux regions where there is also a higher relative detachment rate. Further deposition promotes the Volmer-Weber growth of Ag as well as Au clusters and their coalescence. The Au cluster shape observed in the early stage (6ML, figure 3.5 **middle**) is similar to the Ag PVD simulation with $\Delta E = 0.245$ (figure 2.23 **c**) but the cluster distribution is more concentrated in the high flux region than Ag. This fact suggest that under a certainly higher flux, Au clusters can be aligned solely in the high flux region with a high concentration so that their coalescence leads to a long nanowire along the ripple slope. Indeed, quite well-defined Au nanowires were obtained experimentally[3].

On a (100)-oriented flat substrate, the mean adatom lifetimes of metal monomers T_{AL}^M with the simulation time unit tu is given by eqs. (2.27) and (2.28) as $T_{AL}^M = 3 \exp{(E_b^{M-SiO_2} - E_{bst})}/kT$ tu. In the simulation model, $E_b^{Au-SiO_2} = 0.24$ eV and $E_b^{Ag-SiO_2} = 0.26$ eV are employed and therefore the mean adatom lifetime of two metals on a flat surface is $T_{AL}^{Au} = 14.1$ tu and $T_{AL}^{Ag} = 30.6$ tu. The total MC simulation time and the experimental deposition time are $t_{MCT}^{tot,Au} = 2.7 \times 10^7$ tu, $t_{MCT}^{tot,Ag} = 1.2 \times 10^7$ tu and $t_{exp}^{tot,Au} = 1800$ s, $t_{exp}^{tot,Ag} = 4500$ s respectively. Thus to be consistent with experiment, the adatom lifetime of metals is $T_{AL}^{Au} = 9.40 \times 10^{-4}$ s and $T_{AL}^{Ag} = 1.15 \times 10^{-2}$ s for Au and Ag respectively. Hence the simulation model predicts an adatom lifetime of Au monomers which is one tenth that of Ag on the bare surface. The consistent MC simulation time units are 1 tu$\cong 6.67 \times 10^{-5}$ s for Au and 1 tu$\cong= 3.75 \times 10^{-4}$ s for Ag, respectively. By assuming the same reaction rate constant the difference of migration barriers $\Delta E_m = E_m^{Ag-SiO_2} - E_m^{Au-SiO_2}$ is estimated as

$$\Delta E_m = k_B T \log(\frac{3.75 \times 10^{-4}}{6.67 \times 10^{-5}}) \sim 0.045 \text{ [eV]}$$

with $T = 300$ K. Thus from the observation of the nucleation point distribution by KMC simulations, one can evaluate the energies relating to the metal-SiO$_2$ interaction as $E_m^{Ag-SiO_2} = 0.20$ eV, $E_b^{Ag-SiO_2} = 0.26$ eV,$E_m^{Au-SiO_2} = 0.16$ eV, $E_b^{Au-SiO_2} = 0.20$ eV and the effective transition frequency $\omega^{M-SiO_2} = 6.1 \times 10^6$ s^{-1}. Note that these values are based on the migration barrier of Ag/SiO$_2$ in the case of $f^{Ag} = 0.0038$ ML s^{-1}. These film growth rates, assuming unit sticking probability, give flux parameters of $f^{Au} = 0.020$ ML s^{-1} and $f^{Ag} = 0.0038$ ML s^{-1} and are less than those of Petersen and Mayr [184] by a factor of O(10-10^2). Taking into account the incident angle $\cos(70°) \sim 0.34$ and allowing for a reflection rate of 0.4 [247], the Ag flux is still low by factor of O(10). This could be understood by a small deviation from the target of the e-beam[4] (see figure 2.1).

3.5.4 Cluster growth stability evaluation

In order to estimate the stability range (3.22) of the evolution speed discussed in section 3.4.3, recall the simulation- and experimental parameters required. In the simulations shown in figure 3.5, 6 ML Ag nanocluster growth has been obtained after a MC simulation time of 1.2×10^7 units with a boost factor of 2.3×10^3. The experimentally observed Ag nanostructure was grown after 75 minutes of PVD.

The effective transition frequency $\omega_{\textbf{eff}}$ depends both on the material and the temperature. According to Ref.[214], its range is generally in the region of O(10^{12}-10^{13}) s^{-1}. Now assume that the effective transition frequency is the Debye-frequency $\omega_{\textbf{eff}} = \omega_D^M$ of the metal to derive the consistent convergence factor evaluated in (3.23) and (3.9) with the simulation. The total deposition time

---

[3]Unpublished result by Mukesh Ranjan in 2010.

[4]"That is possible." by Mukesh Ranjan (private communication).

Figure 3.6: Schematic description of local flux for Ag deposition on an Ag(111) island. The area of the island is $S_{mig} \sim 3.06$ nm^2. $\vec{n}$ and $\vec{i}$ are as defined in figure 2.22.

of an Ag PVD experiment is $t_{exp}^{tot} =$4500 s. The total simulation fluence is $F =$175 atoms nm^{-2} corresponding to 15 ML of Ag deposition. The total MC simulation time is $t_{MCT}^{tot} = 1.2 \times 10^7$ tu with 3 % of all the transition events belonging to those described as usual fluctuations. The Debye-frequency of Ag is $\omega_D^{Ag} =$2.95$\times 10^{13}$ s^{-1}.

Let $\mathcal{M}, \mathcal{M}'$ be the original and modified simulation process in a typical interval between two Ag depositions in a small region, respectively. Let $t_{exp}^{\mathcal{M}}, t_{MCT}^{\mathcal{M}'}$ be the experimental, and MC simulation time as defined in 3.3.2 and 3.4.1. Assume the uniform reduction

$$\frac{t_{MCT}^{\mathcal{M}'}}{t_{exp}^{\mathcal{M}}} \approx \frac{t_{MCT}^{tot}}{t_{exp}^{tot}},$$

then the relation (3.23) is given by

$$\frac{t_{MCT}^{tot}}{t_{exp}^{tot}\omega_D^{Ag}P_{bst}} < \theta(\iota) < \frac{t_{MCT}^{tot}0.97^{-1}}{t_{exp}^{tot}\omega_D^{Ag}P_{bst}}. \tag{3.28}$$

Thus $\theta(\iota)$ is in the range $2.07 \times 10^{-7} < \theta(\iota) < 2.13 \times 10^{-7}$ and the mean acceleration of the simulation time is $P_{bst}^{-1}\theta(\iota)^{-1} \sim 1.09 \times 10^{10}$ from (3.24). To see the situation more clearly, consider a concrete example. Figure 3.6 shows the deposition of an Ag adatom i on an Ag(111) island with area S_{mig} nm^2. This scene is same as in figure 3.2. For the unit vectors of the incident atoms $\vec{i}$ and the surface normal $\vec{n}$ the local flux is given by

$$f_{loc} = FS_{mig}\vec{i} \cdot \vec{n}/t_{exp}^{tot} \text{ [atoms/s]}. \tag{3.29}$$

As shown in 3.5.1, most transition events relating to the island are only (i) migration on the (111) island itself, (ii) a transition over the step edge by the atom i and (iii) a transition along the island edge by i and i' since the other transitions are blocked by high potential barriers. The non-dimensional time interval between two external modifications (Ag deposition) in this region is

$$\Delta t = f_{loc}^{-1}\omega_D^{Ag}. \tag{3.30}$$

The consistent numerator of the convergence factor ι for this situation can be estimate from (3.9), (3.28), (3.29), (3.30) and the local parameters as

$$\frac{5.32 \times 10^{-6}}{S_{mig}\vec{i} \cdot \vec{n}} < \frac{\iota}{\omega_D^{Ag}} < \frac{5.48 \times 10^{-6}}{S_{mig}\vec{i} \cdot \vec{n}} \text{ [s]}.$$

The simulation would therefore predict a convergence time for local metastable states of the order of microseconds for the situation shown in figure 3.6. In other words, the deposited atom i which might arrive at a neighbor position of the atom i' would reach a stable local configuration at the latest 1.80μs for $S_{mig} \sim 3.06$ nm^2 after the deposition with a high probability when the surface is facing the evaporation source $(\vec{i} \cdot \vec{n} = 1)$.

For the region, which is not exposed to the largest flux, the surface is barer due to more re-evaporation occurring before the next deposition event.

3.6 Stability of modified convergence limit

The method discussed in this chapter is tested on some simple 1D diffusion models where a full KMC simulation without a time boost was also undertaken to confirm that the results of the full and boosted method were almost equivalent within a certain threshold of the boost factor.

3.6.1 Acceleration of convergence to Gibbs field

First, recall the statistical convergence of microstates probability distribution simulated by Metropolis algorithm due to the limit theorem mentioned in chapter 1.3.2. The sequence of probability distributions of finite atomistic states from an arbitrary initial distribution ϕ_0, ϕ_1,... under the Metropolis algorithm after n simulation time step follows the Chapman-Kolmogorov equation

$$\phi_n = \phi_0 M^n,$$

where M is the Markov kernel of the specific Metropolis algorithm applying to the simulation system. For atomistic states i, j and the corresponding configuration energy $E_c(i), E_c(j)$, the Boltzmann constant k, and temperature T, the transition probability is given by

$$M(i,j) = \begin{cases} \min\{1, \exp[(E_c(i) - E_c(j))/kT]\} & (i \to j \text{ is considerable}) \\ 0 & (\text{otherwise}) \end{cases} \tag{3.31}$$

and the Gibbs distribution Π is

$$\begin{aligned} \Pi(i) &= \exp(-E_c(i)/kT)/Z, \\ Z &= \sum_i \exp(-E_c(i))/kT. \end{aligned} \tag{3.32}$$

Since Π is the unique invariant of M, the sequence ϕ_n converges to the Gibbs distribution Π uniformly when the Markov kernel is primitive (see chapter 1.3.2, Limit theorem). Hence the acceleration of the simulation process implies essentially the speed up of this convergence. Here, the practical convergence speed of the boosted system is investigated with a simple 1D cyclic diffusion model.

The Markov kernel $M'(i,j)$ of the boosted system is given by

$$M'(i,j) = \begin{cases} \min\{1, e^{\vartheta(E_c(i) - E_c(j) - E_{bst})/kT}\} & (j = i \pm 1 \text{ mod } 10) \\ 0 & (\text{otherwise}). \end{cases} \tag{3.33}$$

Here, ϑ is the temperature factor and E_{bst} is the boost energy. Let ϕ'_0, ϕ'_1,... be the sequence of probability distributions with the translated Markov kernel M'. In order to evaluate the *quality* of the translated system evolution process, the root mean square (RMS) deviation of the difference between the original Gibbs distribution and the probability distribution (ϕ'_n) observed is employed. The RMS deviation is given by

$$R(n) = \sqrt{\sum_i [\phi'_n(i) - \Pi(i)]^2 / N}, \qquad (3.34)$$

where $N = 10$ is the number of states.
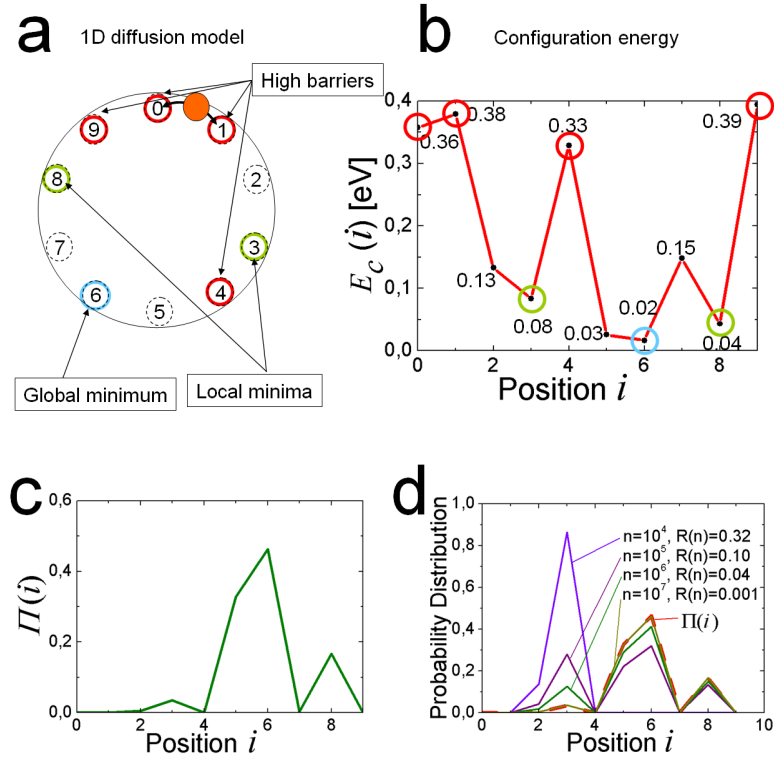
Figure 3.7: **a** Schematic description of the 1D diffusion model. **b** The distribution of configuration energy at each position. **c** The corresponding Gibbs field Π with **b** describing the occupation probability distribution from (3.32) with $T = 300$ K. **d** The convergence of the probability distribution ϕ_n with the simulation time step n. The global minimum, local minima, and high barriers are indicated in **a** and **b**.

3.6.2 Relative convergence speed

In order to verify the acceleration of the convergence speed, a small 1D atomic migration model is considered. In this model an atom is deposited in a circular system with ten configuration energies. Figure 3.7 exhibits a schematic description of this model (**a**), the configuration energy landscape (**b**) and the theoretical limit distribution consistent with the Gibbs distribution Π (**c**). The configuration energies are randomly chosen between 0.0 and 0.4 eV (**b**, list in box) and held fixed during all relevant simulations. Note that the convergence property depends strongly on the system configuration and thus every convergence speed discussed below is the relative speed with respect to this fixed system. The atom jumps to the next position in the circle consisting of these

10 states (**a**). The minimum positive migration barrier is state $6\rightarrow$ state 5 with 0.09 eV. **c** shows the corresponding Gibbs distribution (3.32) with the temperature $T = 300$ K. Figure 3.8 **a** exhibits
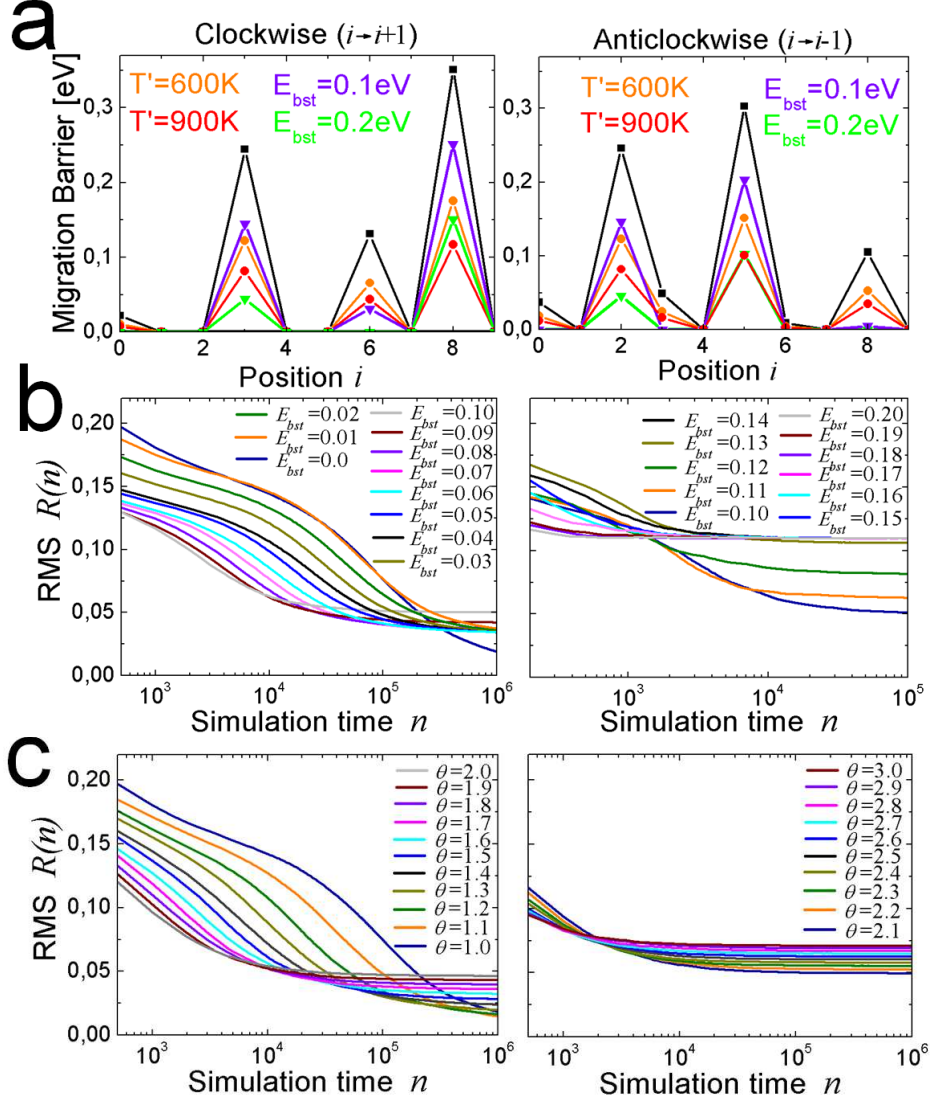

Figure 3.8: **a** Migration barriers with respect to the jump direction. **b,c** The convergence of the RMS deviation (3.34) for the boosted system. The boost parameter range: **b** $E_{bst} = 0.01\text{-}0.20$ eV, T=300 K; **c** $\vartheta = 1.0\text{-}3.0$, $E_{bst} = 0$ eV, The enhanced temperature T' is given by eq. (3.35) with $T = 300$ K.

the line charts of configuration energy difference for the jump to NN position with various boost factors. The barrier $E_m(i, j)$ is given by

$$E_m(i,j) = \begin{cases} \vartheta(E_c(i) - E_c(j) - E_{bst}) \} & (j = i \pm 1 \bmod 10) \\ 0 & \text{(otherwise)}. \end{cases}$$

In the case of $j = i + 1$, or $j = i - 1$ mod 10 the atom hops clockwise (**left**), or anticlockwise (**right**) respectively. The black solid line in figure 3.8 **a** indicates $E_m = 0$ eV. The barriers under the line are practically zero and those that are above the line determine the transitivity of states due to the probability (3.31). For simplicity, the translation parameter ϑ is represented by the corresponding
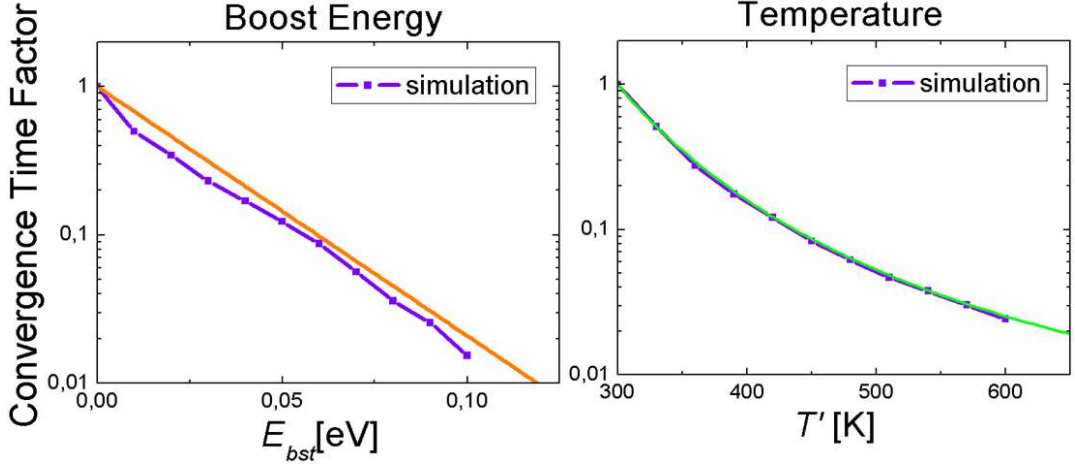
Figure 3.9: Logarithmic line charts of convergence factor with respect to E_{bst} (**left**) and T' (**right**). The orange line and the green curve in the diagrams indicate the acceleration profile expected from eq. (3.36) and eq. (3.37) respectively.

temperature enhancement factor T' with

$$T' = T\vartheta \text{ [K]}. \tag{3.35}$$

Some barriers disappear with increasing the boost energy E_{bst} while every barrier is reduced but still remains in the cases of the temperature enhancement T'.

Figure 3.8 **b** display the evolution of $R(n)$ with the boost parameter range $E_{bst} = 0.0$ eV - 0.10 eV (**right**) and $E_{bst} = 0.10$ eV - 0.20 eV (**b left**). **c** is with the temperature factor $T' = 300\text{-}600$ K (**left**) and $T' = 630 - 900$ K (**c right**). In the both cases, the blue curves indicate the convergence of the non boosted system. The evolution profile is investigated through the average evolution of 10,000 samples for each boost parameter. In each sample case, an atom is deposited at a random position and the occupation probability during 5,000,000 iteration steps noted for various boost parameters. In each case, $R(n)$ converges to a certain limiting value which indicates the distance from the probability distribution of the non boosted system, i.e. the Boltzmann distribution. In this sense, the inaccuracy of the convergence limit $R(\infty)$ increases irregularly with the boost energy due to the loss of migration barriers as displayed in figure 3.8 **a** and regularly with temperature enhancement. As shown in chapter 1.3.2, the probability distribution of microstates transited by the Markov kernel consistent with a modified Metropolis algorithm converges to a certain limit distribution. This can be seen by the convergence of $R(n)$ to the constant asymptotic line. The convergence speed is however quite different in the different cases.

Figure 3.9 displays the convergence factor with respect to the boost parameters. The convergence time of the system is determined by the iteration time step n_c such that the mean fluctuation range $|R(n) - R(n')| < 0.01$ for $n_c < n, n' \leq n_{max}$ with $n_{max} = 5.0 \times 10^6$ being the maximal simulation time step. Each convergence time with a boost parameter is divided by the convergence time for the non-boosted system n_0. The factor for the system with the kinetic energy boost E_{bst} is fitted by

$$n_c \sim n_0 \exp(-E_{bst}/k_B T). \tag{3.36}$$

Since every acceptance probability of positive activation barrier higher than E_{bst} is boosted by $P_{bst}^{-1} = e^{E_{bst}/k_B T}$ and other transitions have no waiting time, this is clear from the discussion by eq.

(3.18). The orange line indicate this relative convergence factor in figure 3.9 **left**. Note that this factor does not depend on the system configuration. On the other hand, the convergence factor for the system with enhanced temperature T' is more complicated. Each acceptance ratio for a jump attempt with positive migration barrier E_m is boosted by the factor $e^{E_m(1/T - 1/T')/k_B}$ and therefore it depends on the configuration of the system. In this case, the convergence time for the temperature enhanced system can be quite nicely fitted by

$$n_c = n_0 \exp\left\{ \frac{\bar{E}_m}{k_B} \left(\frac{1}{T'} - \frac{1}{T} \right) \right\}, \tag{3.37}$$

where the factor n_c/n_0 is indicated by the green curve in figure 3.9 **right** with $\bar{E}_m = 0.19$ eV. This $\bar{E}_m$ is neither the mean migration barrier $\bar{E}_m \neq \frac{1}{10} \sum_i [E_m(i, i+1) + E_m(i, i-1)] \sim 0.15$ nor the expected migration barrier $\bar{E}_m \neq \frac{1}{Z} \sum_i e^{-E_c(i)/k_B T} [E_m(i, i+1) + E_m(i, i-1)]/2 \sim 0.13$. The expected migration barrier in the boosted system with T' varies from 0.130-0.136 eV for T'=300-600 K, but the curve can not be fitted by any case.

3.6.3 1D Ag models

On the surface of metal clusters described in the previous section, some situations can be approximated by the 1D diffusion model introduced above using the same migration barrier calculation (3.25). Three typical sample cases describing a single ad-monomer migration on various facets and certain types of step edge barrier are selected and discussed below. In all cases, the global minimum is quite stable and therefore the convergence of the probability distribution implies simply the probability that the atom is found at the minimum position converges to 1. In order to see this situation clearly, the weighted root mean square function

$$R_w(n) = \sqrt{[\phi_n'(i_{min}) - \Pi(i_{min})]^2} \tag{3.38}$$

is considered with the global minimum position i_{min} instead of the regular RMS (3.34). This indicates approximately the probability that the atom is migrating on the facet and not caught by the global minimum position until n-th iteration step.

First, consider the situation of an Ag ad-monomer deposited on an Ag(111) island in the simulation system with the discrete RGL potential field as discussed in the previous section. Since every atomic movement except this ad-monomer migration is blocked by high activation barriers, the event expected in this local system is only the surface migration of the ad-monomer until it hops down to the layer below. This situation is approximated by a 1D diffusion model illustrated in figure 3.10. The corresponding configuration energies as well as migration barriers are set as shown in **a left**. The situation assumed is illustrated in **a right**. The migration barrier is 0.04 eV and the ES barrier to the B-step terrace is calculated as 0.39 eV with $\bar{n} = 8.5$ from eq. (3.25). The ES barrier for the A-step terrace is 0.87 eV with $\bar{n} = 8.5$ and this scale of migration barrier was rarely observed during the simulation (see figure 3.4). The barrier of the ascending movement is 0.98 eV and therefore the convergence of the probability distribution is practically determined by the overcoming of the ES barrier. **b** shows the evolution of the RMS with respect to the boost parameters. In this diffusion model, an Ag atom is deposited at position 0 at $n = 0$ and the occupation probability during 1,000,000 steps is monitored through the evolution of $R_w(n)$. The total number of samples is 1000 for each boost parameter and the parameter range is the same as in the random configuration model. In each simulation within the total iteration steps, the influence of the ascending jump is negligible since the acceptance probabilities with the reduced barrier are at most $e^{-0.68/k_B T} \sim 3.8 \times 10^{-12}$ for $T = 300$ K and $E_{bst} = 0.3$ eV, and $e^{-0.98/k_B T'} \sim 3.3 \times 10^{-6}$ for
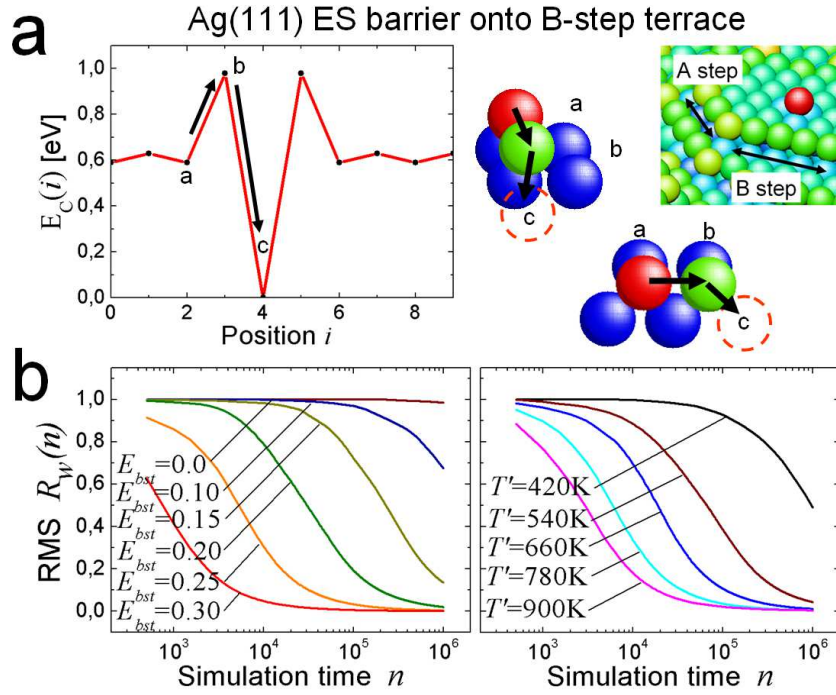
Figure 3.10: 1D model of Ag/Ag(111) migration. **a**: Configuration energy landscape modeling the Ag/Ag(111) migration (**left**) and the schematic description of the step edge barrier with respect to the jump onto the B-step terrace (**right**). In the small rectangle figure (**a right**) the relevant situation of Ag monomer on Ag(111) in the cluster growth model is illustrated. A-step and B-step terraces are also shown. Arrows indicate the corresponding jumps in the 1D model and the illustration. **b**: The evolution of the RMS deviation (3.34) for the boosted system. The boost parameter ranges are (E_{bst} =0.0-0.30 eV at 300K (**b left**) and T' = 300-900 K with E_{bst} =0 eV (**b right**).

$T' = 900$ K, respectively. For each case, $R_w(n)$ converges to 0 with various speed and this implies that the most of atoms can overcome the ES barrier within the simulation process accelerated by the various boost factors.

The model described in figure 3.11 is for Ag migration on Ag(100) with certain type of down step jump. If the ad-monomer on the Ag(100) surface falls into the corner of the (100) island (**a right**), then the situation of atomistic movement can be approximated by this model. In this case, the monomer at each position on the (100) island is rather stable due to the high migration barrier 0.38 eV and the barrier of the jump to the down step is even slightly smaller (0.33 eV) than of the normal diffusion. The convergence speed of the boosted systems shown in **b** are slightly faster than the case of Ag(111) since these barriers playing the crucial role are in the same range. The barrier for the ascending jump is 0.86 eV and this is also a quite high barrier so that almost no reverse action is expected in each boosted system.

Another example is shown in figure 3.12. In this case, Ag monomer migration along the in-channel of Ag(110) surface and falling into the corner of the channel is modeled (**a left**). This situation is similar to the case of monomer migration along the B-step terrace of the (111) island and transition to the A-step side. Thus it is an important process for the enlargement of the (111) island which affects the shape stability [151]. In this case, the migration barrier (0.28 eV) and the step edge barrier (0.31 eV) are almost identical and the barrier for the ascending jump is 0.56 eV. This barrier is still high in the energy boosted system (the acceptance probability $e^{-0.26/k_B T} \sim 4.3 \times 10^{-5}$ for $T = 300$ K and $E_{bst} = 0.3$ eV) but not so high any more in the
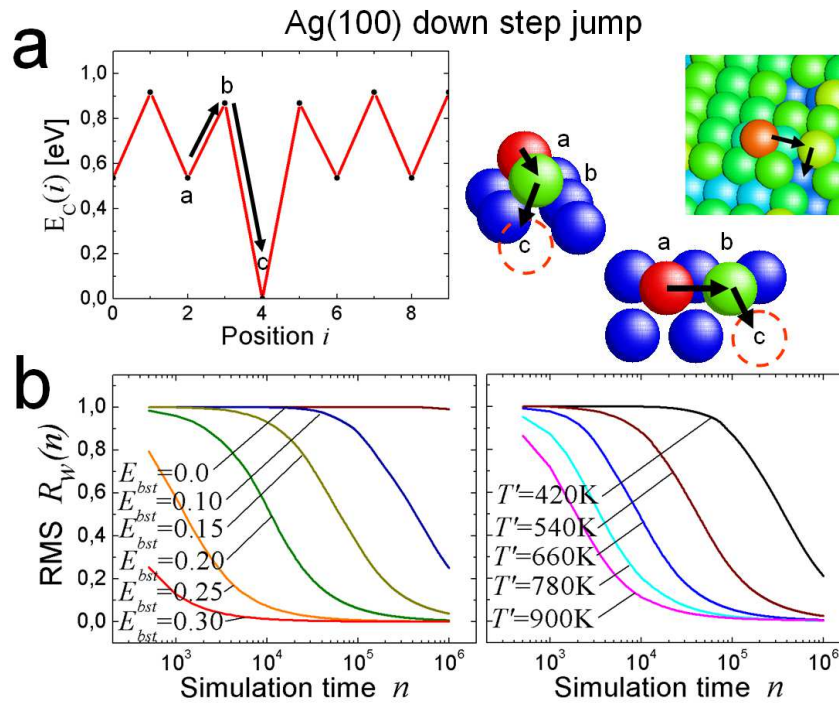
Figure 3.11: Configuration energies modeling Ag/Ag(100) migration and the step edge barrier with respect to the jump onto the lower (100) layer **a**. The convergence of the RMS deviation (3.34) for the boosted system (**b**,**c**). The boost parameter range and configuration energy calculation are the same as for Ag(111) (figure 3.10).
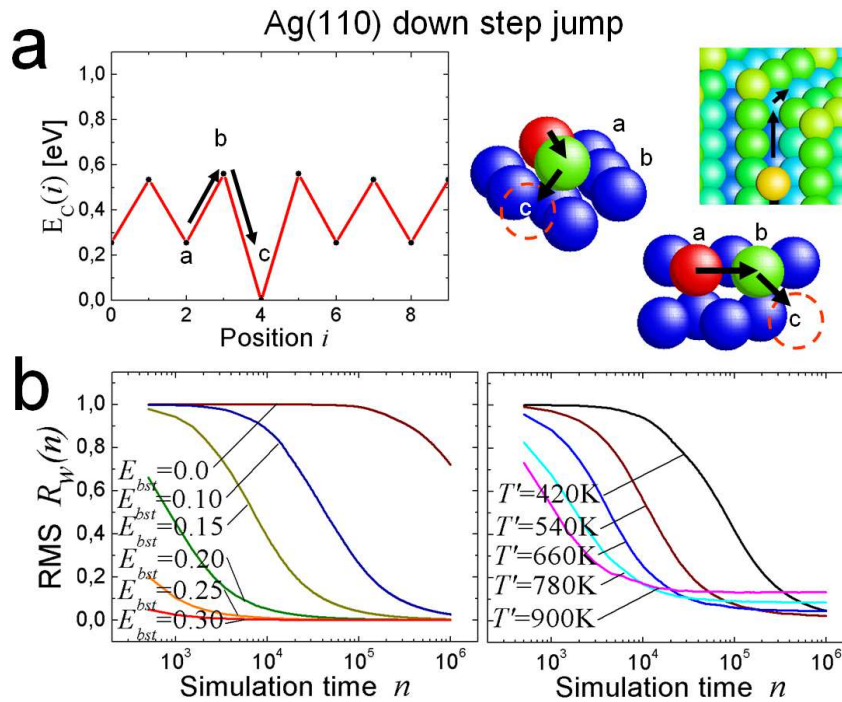

Figure 3.12: Configuration energies modeling Ag/Ag(110) migration and the step edge barrier with respect to the jump onto the in-channel (110) terrace **a**. The convergence of the RMS deviation (3.34) for the boosted system (**b**,**c**). The boost parameter range is the same as for Ag(111) (figure 3.10)

86

maximal temperature enhanced system (the acceptance probability $e^{-0.56/k_B T'} \sim 7.3 \times 10^{-4}$ for $T' = 900$ K). Moreover, the migration barrier remains in every temperature enhanced system whereas it is reduced significantly in the kinetic energy boosted system, e.g., for E_{bst} =0.25 eV the barrier is reduced to 0.03 eV while it is still 0.09 eV for T' =900 K. In these cases, the acceptance ratios of the migration barrier as well as the ascending jump boosted by the boost energy have the same factor $e^{0.25/k_B T} \sim 1.6 \times 10^4$ while by the temperature enhancement they are $e^{0.26(1/T-1-T')/k_B} \sim 8.2 \times 10^2$ and $e^{0.56(1/T-1/T')/k_B} \sim 1.9 \times 10^6$ respectively. Due to this higher ascending probability and slow mobility on the (110) in-channel region, the convergence limit of this system in the temperature enhanced system is worse than that of the kinetic energy boosted system. This fact gives evidence for the risk of misleading results from temperature enhancement for the system evolution as mentioned in section 3.4.3.

3.6.4 Stability theorem

The eigenvector ϕ of the Markov kernel M with respect to the eigenvalue 1 is uniquely determined as mentioned chapter 1.3.2. Thus this correspondence induces a mapping from the set of all primitive Markov kernels to the vector space affecting to the set of all microstates as probability distributions. Now consider the variation of the eigenvector with modifying the original Markov kernel. As observed above, if the magnitude of modification is sufficiently small, then the corresponding Boltzmann distribution remains close to the original distribution with respect to the variation norm. The limit of the probability distribution ϕ' for the modified Markov kernel M' is bounded by the norm of two Markov kernels as follows:

Theorem 1. *Let ϕ, ϕ' be the limit distribution of the original and translated Markov kernels M and M' respectively. Let M be primitive with $c(M^k) < 1$ for $\exists k \in \mathbb{N}$. Then the norm $||\phi - \phi'||$ is bounded by*

$$||\phi - \phi'|| \leq \frac{k}{1 - c(M^k)}||M - M'||_\infty,$$

where $||M - M'||_\infty$ is the maximum norm of linear operators on the probability space defined by

$$||M - M'||_\infty := \sup_{||\psi||=1} ||\psi M - \psi M'||.$$

Proof. It follows that

$$
\begin{aligned}
||\phi - \phi'|| &= ||\phi M^k - \phi' M^k + \phi' M^k - \phi' M'^k|| \\
&\leq c(M^k)||\phi - \phi'|| + ||\phi' M^k - \phi' M'^k||.
\end{aligned}
\tag{3.39}
$$

Now the second term of (3.39) is

$$
\begin{aligned}
||\phi' M^k - \phi' M'^k|| &\leq ||\phi' M^k - \phi' M^{k-1} M'|| + ||\phi' M^{k-1} M' - \phi' M'^k|| \\
&\leq ||M - M'||_\infty + ||\phi' M^{k-1} - \phi' M'^{k-1}||c(M') \\
&\leq ||M - M'||_\infty + ||\phi' M^{k-1} - \phi' M'^{k-1}||.
\end{aligned}
$$

Inductively one can see that

$$||\phi' M^k - \phi' M'^k|| \leq k||M - M'||_\infty.
\tag{3.40}$$

From (3.39) and (3.40) the variation norm $||\phi - \phi'||$ is bounded as

$$||\phi - \phi'|| \leq \frac{k}{1 - c(M^k)}||M - M'||_\infty.$$

$\square$

This convergence property indicates the stability of the system evolution with respect to the perturbation of the original algorithm. As shown above, the distance between two limit distributions depends on the modification size, i.e. the maximum norm of Markov kernels $||M - M'||_\infty$, and the contraction property $c(M^k)$ relating to the transitivity of the original system.

3.7 Summary

An atomistic, KMC simulation method has been proposed and successfully applied to metal cluster growth processes on surfaces with pre-patterned ripple structures. The method consists of two essential ideas. One is the discretization of the entire process into local transition events and the other is the classification of the transition levels with respect to the thermal fluctuation of the system. By allowing free transitions with small barriers to be considered as fluctuations, the entire system evolves as a Markov chain of 'equal entropy' equivalence class objects. The evolution dynamics of the system is promoted by the metastable level transitions. The effect of parameters chosen in the method is investigated with 1D atomic diffusion models and the acceleration effect is verified with the convergence speed of the probability distribution of microstates to the Boltzmann distribution.

Also, contrary to some previous accelerated dynamics methods [45, 153, 214], where there are many small migration barriers, an acceleration of the system evolution can still be achieved, when the system does not require too many transition events to reach the quasi-equilibrium state. In the metallic PVD example, the model predicts a convergence time of metastable states, after each metal deposition onto the surface, of $< \mu$s-order. The model can also predict the metal cluster growth patterns accurately with detailed atomistic transition event statistics.

An application limit of the transition level classification method may exist, due to the inability of the small transition effect to model the physics at high temperatures, but so long as the system does not require too many transition events to reach the usual fluctuation, the model provides a relatively fast (3-9 CPU days on a modern single processor machine) estimation of the metal cluster growth process of 6-12 ML accumulation. Since a typical boost factor is 2290, a traditional KMC simulation, i.e. without a boost, might require 18-54 CPU years to obtain a similar surface coverage.

These simulations can be developed further by utilizing more data from experimental measurements together with/or more accurate barrier calculations such as those provided by density functional theory or improved inter atomic potentials. The method can also be extended to more complex systems such as multicomponent materials and grain boundaries, provided a good description of the relevant transition barriers is available.

Other modifications could include, for example, use of the nudged elastic band method [36, 100] to calculate accurate energy barriers together with a systematic storage of data [62], either on-the-fly or not, a more accurate and complicated event table can be constructed so that local transition events can be more systematically determined. In addition, the aesthetic algebraical structure of the Markov chain [20] itself is also a subject of interest to study, especially as an extended class 4 object of a cellular automaton [245]. As shown in the end of chapter 1.3.4, such Markovian process can be extended for the representation of wave functions through the integration of all pathways connecting states at two complex times. Since the Hamiltonian is in principle determined by the inter atomic potential resulting in the electrons and nuclei interactions, such a classification method can be applicable for describing various levels of physics. The cutoff of small barriers for the long term evolution process is essentially the renormalization of time scale with respect to the target phenomenon.

Chapter 4

Ion beam inducing surface pattern formation

In this chapter, the mechanism of surface pattern formation induced by ion beam irradiation is considered. As mentioned in chapter 2, although pattern formation on semiconductor surfaces under ion beam erosion is an established technique in nanotechnology, the basic formation mechanism is still under hot discussion. Here a "simple" and "essential" mechanism is explored. Especially, the importance of surface mass current induced by the ion beam for pattern formation is examined. Is sputtering of surface materials necessary to obtain the nanostructure? If self-organized surface nanostructure, such as ripples and dots with nm order periodicity, can be formulated in the absence of sputtering, then it could lead to the expansion of the application range and be more economical.

The contents are laid out as follows. In section 4.1, an overview of ion-induced surface modification is introduced from both the theoretical and experimental point of view in order to illustrate the development of the subject. In section 4.2, surface as well as bulk modification of Si induced by single low-energy ion beam is investigated by MD simulation. From the observation of the results, mainly the surface modification, some simple models are constructed and performed by KMC simulations. In these models, especially, by accounting for the surface viscosity and short time temperature enhancement a very clear, self-organized ripple pattern formation is observed. In section 4.3, a mathematical model based on these observations is constructed. The model considers the surface modification resulting from infinitesimal atomic flow induced by ion bombardment. The equation of motion, the basic physical mechanisms, the mathematical derivation process and model parameters are discussed. A traveling wave solution for the equation of motion with the specific incident angle is considered and the Lyapunov stability of this solution is shown. A quantitative comparison with the experiment of Carter and Vishnyakov [35] is presented. The contributions of thermally activated surface diffusion and sputter effect for the atomic flow based pattern formations are discussed in section 4.4. With appropriate contributions of these factors depending on the temperature and ion beam energy range, the periodical pattern formation predicted by this theory agrees with various experimental observations quite nicely.

4.1   Ion-inducing pattern formation

4.1.1   Bradley-Harper equation

Self-organized semiconductor surface nanostructures induced by ion beam erosion such as corrugations and dots have been well known phenomena since the 1960's [72, 164]. Smith and Walls

considered the 3D development of surface topography during ion beam erosion in 1980 [209, 211]. For the target surface $h = h(t, x, y)$, the substrate atomic density ρ_0, the mean ion flux ϕ in the direction of the ion beam, the ion incident angle φ with respect to the local surface normal, and the angular dependent sputtering yield $Y_0(\varphi)$, the surface evolution is described as (see also figure 4.7 **a** and **c**)

$$\frac{\partial h}{\partial t} = -\sqrt{1 + (\nabla h)^2} \frac{\phi}{\rho_0} Y_0(\varphi) \cos \varphi. \tag{4.1}$$

This non-linear model could also be applied to the case of a spatially and time varying flux $\phi(x, y, t)$ and also the case where the sputtering yield could depend on the azimuthal angle such as in crystals. The model was applied to show how smooth surfaces could develop edges under erosion and some example structures evaluated using the method of characteristics. However for typical experimentally measured sputtering yields the net effect was that surface features were smoothed out as a result of the erosion process and the formation of ripple structures was not possible. In 1988, Bradley and Harper proposed a surface evolution model with a curvature dependent ion energy deposition from Sigmund's sputter theory [201, 202, 203], and Mullins-Herring diffusion [160], known as the Bradley-Harper (BH) theory [27]. According to Sigmund's approach to sputtering, the ion energy deposition distribution in the bulk follows the Gaussian distribution

$$F_D(x, y, z) = \frac{E}{(2\pi)^{3/2} \sigma_p \sigma_l^2} \exp\left(-\frac{z - h_0 - a}{2\sigma_p^2} - \frac{x^2 + y^2}{2\sigma_l^2}\right), \tag{4.2}$$

where E is the total energy deposited, a is the mean depth of energy deposition, and σ_p and σ_l are the widths of the distribution parallel and lateral to the ion beam direction which is assumed as the negative direction of z-axis here. This distribution is independent from the surface configuration but the effect of energy deposition is dependent on topography since the atomic displacement near the surface induces the emission of the bulk atoms, i.e. the sputtering. They considered the local surface erosion velocity $v_s(\varphi, \kappa)$ as a function of the local incident angle θ and local curvature κ. Under the slow varying surface assumption compared to a, i.e. $|a\kappa| << 1$, the first order Taylor expansion of v_s is considered. Together with the smoothening effect resulting in surface diffusion [160], the equation of motion for the surface height is

$$\frac{\partial}{\partial t} h(t, x, y) \cong -v_0(\theta) + v_0'(\theta) \frac{\partial h}{\partial x} + \frac{\phi a}{\rho_0} Y_0(\theta) \left[\Gamma_1(\theta) \frac{\partial^2 h}{\partial x^2} + \Gamma_2(\theta) \frac{\partial^2 h}{\partial y^2}\right] - B\nabla^2(\nabla^2 h), \tag{4.3}$$

where θ is the ion incident angle θ with respect to the positive direction of z-axis, $v_0(\theta)$ is the erosion velocity of the unperturbed planar surface, $\Gamma_i(\theta)$ is the angular dependent erosion coefficient (< 0) with respect to components $i = x, y$, and B is the coefficient for the curvature dependent diffusion term. This is the first order Taylor expansion of the curvature- and incident angle dependent surface erosion velocity. The mean energy deposition depth a is a function of ion energy E and the relevant species. For the low ion energy region where elastic ion stopping dominates, the mean depth of the stopped ion from the entering point, which is called the mean projected range R_p, is given in power-law approximation by [141, 163]

$$R_p = \frac{1 - m}{2m} \left(\frac{4M_1 M_2}{(M_1 + M_2)^2}\right)^{m-1} \frac{E^{2m}}{\rho_0 C_m} \left(1 + \frac{M_2}{3M_1}\right)^{-1}, \tag{4.4}$$

where M_1, M_2 are the mass of ion and substrate with $M_1 > M_2$, m is a numerical constant with $m = 1, 1/2, 1/3, ...$, and C_m is another constant relating to the potential energy transfer. The

fitting parameter m can be chosen either $1/3$ or $1/2$ depending on the ion energy range E [163] and consequently the energy dependency of the projected range is approximately given by

$$R_p \propto \begin{cases} E^{2/3} & \text{for } \tilde{E} \leq 0.2 \\ E & \text{for } 0.05 < \tilde{E} < 10, \end{cases} \tag{4.5}$$

where $\tilde{E}$ is the reduced energy relating to the Thomas-Fermi screening function a_{TF} given by

$$\tilde{E} = \frac{4\pi\varepsilon_0 a_{TF}}{Z_1 Z_2 e^2} \frac{M_2}{M_1 + M_2} E$$

where Z_1, Z_2 are the atomic numbers of ion and substrate respectively, ε_0 is the vacuum permittivity, and e is the elementary charge. a_{TF} is given by

$$a_{TF} = \frac{0.4692}{\sqrt{Z_1^{2/3} + Z_2^{2/3}}} \; [\text{Å}].$$

The accuracy of this approximation is 20-40 %. Especially at very low ion energies, this range is seriously underestimated [163]. The mean energy deposition depth a has then the same magnitude as R_p. The angular dependence of the sputter yield $Y_0(\theta)$ can be fitted by Yamamura formula [249] given by

$$Y_0(\theta) = \frac{Y_0(0)}{\cos^f \theta} \exp\left[-f \cos\theta_{opt}(\frac{1}{\cos\theta} - 1)\right], \tag{4.6}$$

where f is an adjustable parameter and θ_{opt} is the incident angle at the maximum yield. The fitting parameter f is given by

$$f = 1.85 \left(1 + \frac{1.25}{\sqrt{E/E_{th}} - 1}\right), \tag{4.7}$$

where E_{th} is the sputtering threshold energy. The curvature dependent surface diffusion term is derived by Mullins in 1957 [160] from some physical relations concerning the local curvature dependent chemical potential variation by Herring [102] as well as the average velocity of drifting surface atoms varying with the change of chemical potential along the arc length (the *Nernst-Einstein relation* [112]). The coefficient B is given by

$$B = \frac{D_s \gamma \nu}{\rho_0^2 k_B T}.$$

for the surface diffusion coefficient $D_s > 0$, surface free energy per unit area $\gamma > 0$, and the areal density of diffusing atom $\nu > 0$. The derivation detail is given below in the context of a relevant ripple simulation model (section 4.2.2). The driving force for ripple formation is assumed to be the combination of the energetic sputter process and thermally activated surface smoothing in these theories. By setting $h = h - v_0 t$ in eq. (4.3) it is reformulated as

$$\frac{\partial}{\partial t} h(t,x,y) = v'(\theta)\frac{\partial h}{\partial x} + S_x(\theta)\frac{\partial^2 h}{\partial x^2} + S_y(\theta)\frac{\partial^2 h}{\partial y^2} - B\nabla^2(\nabla^2 h) \tag{4.8}$$

with consistent coefficients $S_{x,y} := \frac{\phi a}{\rho_0} Y_0 \Gamma_{1,2}$. Solving this linear PDE (4.8) by using the Fourier transformation $\mathcal{F}((t,x,y)) = \hat{h}_k(t,k_x,k_y)$ yields

$$\begin{aligned} \hat{h}_k(t,k_x,k_y) &= \hat{h}_k(0,k_x,k_y) \exp[\{-S_x(\theta)k_x^2 - S_y(\theta)k_y^2 - B(k_x^2 + k_y^2)^2\}t]e^{-iv_0't} \tag{4.9} \\ &=: \hat{h}_k(0,k_x,k_y) \exp[\omega(k_x,k_y)t]e^{-iv_0't}, \end{aligned}$$

where $\omega(k_x, k_y)$ indicates the growth (> 0) or decay (< 0) of the amplitude of the Fourier component $\hat{h}_k(0, k_x, k_y)$ with the periodicity being proportional to (k_x, k_y) in the 2D frequency domain. The relation

$$\omega(k_x, k_y) = -S_x(\theta)k_x^2 - S_y(\theta)k_y^2 - B(k_x^2 + k_y^2)^2 \tag{4.10}$$

is the *dispersion relation* between the growth speed and wave number. Thus the periodic pattern formation may be dominated by the Fourier component $\hat{h}_k(0, k_x, k_y)$ providing the maximum growth speed. Since $B > 0$ the growth rate $\omega(k_x, k_y)$, takes the maximum

$$R_{max} := \frac{\max\{S_x^2, S_y^2\}}{4B}$$

with $(k_x^2, k_y^2) = (\sqrt{R_{max}/B}, 0)$ for $S_x^2 > S_y^2$ and $(k_x^2, k_y^2) = (0, \sqrt{R_{max}/B})$ for $S_x^2 < S_y^2$. Linear instability analysis explains also the angular dependent ripple rotation due to the change of the inequality involving S_x and S_y. Accounting for $\phi \propto S_x, S_y$ and the temperature dependent diffusion coefficient $B \propto e^{-E_d/k_B T}$, the dominating ripple wavelength $\lambda \propto k_x$ or k_y is then predicted as

$$\lambda^{-1} \propto \sqrt{R_{max}/B} \propto (\phi T)^{1/2} e^{E_d/2k_B T},$$

where E_d is the activation energy of the surface self-diffusion reported as $\sim 1.2 \pm 0.1$ eV for Si by Erlebacher *et al* [70]. These formulations are valid under the assumption of slowly varying surface topography as mentioned above and thus if the surface roughening reaches a certain level, then this description is no longer accurate. Moreover this theory predicts the continuous evolution of ripple amplitude but in reality there is a saturation of the height of ripples [44, 70, 118]. In order to obtain the pattern evolution and stabilize this roughening process, the positive coefficient, i.e. negative $S_{x,y}$, of the second order term the fourth order term resulting in the erosion and the diffusion are necessary in (4.10). However, under low energy (≤ 1 keV) ion bombardment [44, 118], and also at low temperatures, 100 K [35], 140 K [146], ripple-like nanostructures are observed. Especially for covalent materials such as Si where amorphization occurs after ion bombardment and where, low sputter yields and few diffusion processes are expected, a model, different from those considered previously, would provide more reasonable explanation of ripple formation.

4.1.2 Nonlinear continuum models

In the past two decades, much effort was dedicated to deriving nonlinear extensions of the BH equation in order to overcome these problems with the sputter-diffusion mechanisms [35, 37, 43, 53, 73, 162]. Cuerno and Barabasí considered the surface topography evolution due to ion beam erosion assuming a local curvature dependent energy deposition as [53]

$$\frac{\partial}{\partial t} h(t, x, y) = -v_s(\varphi, R_x, R_y)\sqrt{1 + (\nabla h)^2}, \tag{4.11}$$

where v_s is the same velocity of height evolution as in the BH model represented as a function of the local angle φ and the radii of surface curvature R_x, R_y. Neglecting the third or higher order terms of the Taylor expansion and adding a diffusion term and a Gaussian noise term $\eta(t, x, y)$ with mean zero and variance proportional to the flux ϕ yields

$$\frac{\partial}{\partial t} h(t, x, y) = -v_0 + v_0'\frac{\partial h}{\partial x} + \nu_x\frac{\partial^2 h}{\partial x^2} + \nu_y\frac{\partial^2 h}{\partial y^2} + \frac{\lambda_x}{2}\left(\frac{\partial h}{\partial x}\right)^2 + \frac{\lambda_y}{2}\left(\frac{\partial h}{\partial y}\right)^2 - B\nabla^2(\nabla^2 h) + \eta, \tag{4.12}$$

with the coefficients $\nu_{x,y}$ and $\lambda_{x,y}$ consistent with the expansion of eq. (4.11). This equation is called a Kuramoto-Sivashinsky type equation which originated in a similar equation derived by

Kuramoto [131] and Sivashinski [205] for chemical wave and the propagation of disturbed spherical flame fronts respectively. This nonlinear PDE is further extended e.g. adding a damping term $-\alpha h$ with a damping coefficient α in order to suppress spatiotemporal chaos [73], reforming the nonlinear terms accounting for aeolian sand dune like kinetic process with the excavation and addition of surface atoms [37]. Especially, this "hydrodynamic" description of surface atomic flow formulated by Castro *et al* [37] and Muñoz-García *et al* [161] reproduces various experimental observations by numerical calculations [162]. The additional factors, excluding those from the BH theory, contributing to the coefficients of each term are the redeposition rate of sputtered atoms, the thickness and the fraction of mobile surface atoms and the diffusion constant with respect to these mobile atoms, the mean nucleation rate for the flat surface and their curvature dependency denoted by symbols $\bar{\phi}, R, R_{eq}, D, \gamma_0$ and $\gamma_{x,y}$ in original papers [37, 161, 162] respectively. The factors relating to the nucleation rate are due to the assumption that the mobile atoms aggregate preferentially in surface protrusions.

4.1.3 Other approaches

Recently, MD simulations showed that a low energy, single ion impact induces a small crater-like Si surface modification [113, 114, 170]. Kalyanasundaram *et al* reported that a ripple formation appears in the numerical calculation of the ion beam inducing surface modification utilizing MD data [114]. In their calculation, an angular dependent crater formation function fitted by interpolation to MD data modifies the surface over a region of a few nm^2 [113] after each ion impact. Together with the surface diffusion term, a ripple formation with around 100 nm periodicity was obtained. A correlation between crater formation and ripple formation obtained by the combination of a binary collision approximation MD [261] and KMC simulation is investigated in the thesis of Liedke [139].

Other MD simulations [154, 222, 226] and theoretical analysis [149] suggest that the ballistic phase of a cascade induced by low energy ion bombardment, is over very quickly (a few ps) and affects the substrate only locally. In particular MD simulation by Süle *et al* [224] showed that ripples of a large periodicity (>35 nm) seem to be stable against continuous ion bombardment, without the contribution of Mullins-Herring diffusion. Concerning the surface property, the crucial effect of metal contamination for Si surface nanostructure formation is also reported by Macko *et al* [145].

Carter and Vishnyakov showed that ripple patterns can be produced at 100K by Xe$^+$ 40 keV bombardment [35]. They also considered ion bombardment inducing atomistic displacement and added the gradient of the atomic flux term to the BH model. For the 1+1 dimension system, it is formulated as

$$\frac{\partial}{\partial t}h(t,x) = -v_0(\theta) + v_0'(\theta)\frac{\partial h}{\partial x} + \frac{\gamma}{\mu}\left|\frac{\partial h}{\partial x}\right| + \frac{\phi a}{\rho_0}Y_0(\theta)\left[\Gamma_1(\theta)\frac{\partial^2 h}{\partial x^2}\right] + \frac{1}{\rho_0}\frac{\partial}{\partial x}\Phi(u) - B\nabla^2(\nabla^2 h) + \eta(x,t),$$
(4.13)

where μ is the viscosity, $\Phi(u)$ is the atomic flux along the local coordinate u, and η is the noise term. The term $\gamma/\mu|\partial h/\partial x|$ is due to the viscous relaxation in the frequency space suggested by Chason *et al* [43]. The atomic flux Φ is given by

$$\Phi(u) = \phi\frac{k(E)\epsilon}{4E_d}\sin 2\left[\theta - \tan^{-1}\left(\frac{\partial h}{\partial x}\right)\right]$$
(4.14)

with the effective energy deposition $k(E)$, the mean displacement distance ϵ, and the displacement energy E_d. However, in contrast to eqs. (4.13) and (4.14), Keller *et al* [118, 120] reported that the ripple pattern does not depend on the ion flux ϕ but the ion fluence under 300-500 eV Ar$^+$

irradiation at room temperature whereas the flux dependency is also reported at 800-900 K as predicted by the BH theory [44, 70].

From these results one could suppose that the main driving force of ripple formation on Si is likely to be the accumulation of locally affecting spontaneous surface modification induced by ion irradiation rather than any contribution of the global surface atomic diffusion. Thus, from this point of view, a MD simulation of low energy ion impact and KMC simulations of several surface defect creation types are performed in the following section.

4.2 Simulation of surface defects induced by ion beams

4.2.1 MD simulation of single ion impact

Classical constant volume MD simulations utilizing the PARCAS code [166] have been performed to investigate the statistical behavior of surface defects induced by a single ion impact. The surface of (001) oriented crystalline Si (c-Si) consisting of 9000 atoms in an 81.45 [Å]×81.45 [Å]×27.15 [Å] simulation box was bombarded by a single Xe^+ ion (500 eV). The incident angle was chosen to be 67° from the surface normal since an instability of surface pattern formation is reported at this angle in the sense of spontaneous change from parallel to perpendicular mode ripples [118]. For Si-Si and Xe-Si interactions, the Tersoff potential [228] joined to the Ziegler-Biersack-Littemark (ZBL)like repulsive potential is employed. Accounting for the weak bonding potential of Si-Xe calculated by GAUSSIAN (see chapter 1.1.2), the parameters of Tersoff potential are fitted to this *ab initio* calculation. The details of fitting method is given in Ref. [223].

The system temperature is 300 K controlled by a Berendsen heat bath [19] at the bottom of the cells and the simulation time is 5 ps for each impact. The system temperature is sufficiently cooled down within the simulation time regime and no more significant displacement resulting from the impact is observed after this time. Generally, under low energy ($\leq$ 1 keV) ion bombardment, the temperature of impact region decreases immediately after the impact and the thermal spike takes place over only a few ps [149, 222, 226]. Further simulation details are given in Ref.[224]. Figure 4.1 shows the initial state and an example of the final state for single ion impact. The initial positions and ion trajectory are illustrated in the left diagrams. **a** is the lateral view and **b** is the top view of the simulation system, respectively. The atoms displaced more than 1 Åfrom their equilibrium position are shown in the right diagrams. The color of atoms indicates the distance from their original positions. The range of displacement distance from the initial position and the final position observed in this case is 1-12 Å. One can see that most are located near the surface and displaced along the surface to positions not so far from their initial positions except for several atoms above the mean surface height. Here three types of atomic displacement relating to the surface modification can be investigated from the ion impact simulation results that are surface drifting, shifting, and sputtering. Especially for atomic shifting, it can be imagined that atoms near the surface are molten for a short time and flow along the topography infinitesimally. Such kind of atomic flow near a surface has also been calculated by MD simulation reported by Norris *et al* [171].

Figure 4.2 shows the statistical atomic density variation induced by single ion impact within the various height ranges where the mean surface height is 12.9 Å(see figure 4.1). The simulation samples are 489 individual ion impacts. Every starting point and the azimuth angle of the ion trajectory are chosen arbitrary at each ion impact. The simulation system is shifted and rotated with respect to these parameters after each impact simulation in order to normalize the starting point and the impact point. The simulation system near the impact point is divided into $40 \times 40 \times 16$ cubes with a volume of 1 $Å^3$ and the statistical atomic density variation for a single ion impact in
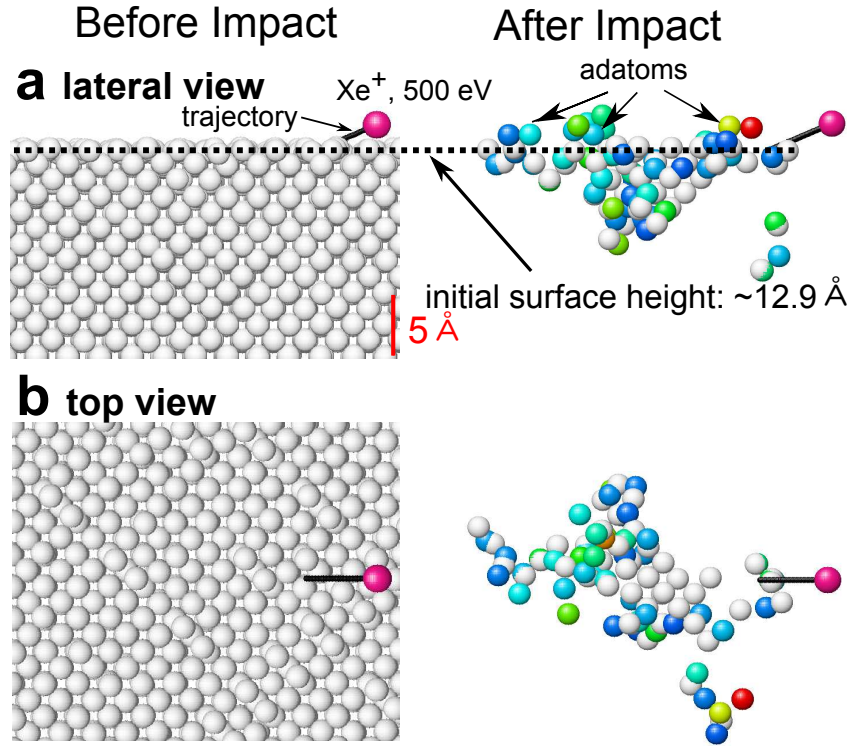
Figure 4.1: Illustration of an MD simulation for an ion bombarded Si surface. **a** Lateral view of the initial positions of the Si atoms and the Xe ion (**left**) and the final state after single ion impact (**right**). The trace of the ion, the initial mean surface height, adatoms generated after the impact are also indicated. **b** Top view of the initial and the final states. The mean surface height is 12.9 Å in the simulation system and a scale of 5 nm is shown (see also figure 4.2). Color indicates the distance 1-12 Å from the original position. The red atom is the atom moved the longest distance (11.7 Å). The atoms with white color are the original positions of atoms displaced more than 1Å.

these unit cells is considered. In order to avoid the deviation of this atomic density resulting in the crystal (diamond) structure and the representation cells by the computation, the target region is shifted with an arbitrary distance within the size of the unit cell before the discretization and the average density of 100 times shifts is computed for each ion impact. The average atomic density shown in each diagram consists of 40×40 unit cells. The scale of mean atomic density variation in the figure is thus atoms/Å^3 where the normal density of crystal silicon at $T = 300$ K is $\rho_0 = 0.05$ atoms/Å^3. The atomic density is decreased near the impact point and increased in the small region above the mean initial surface. This indicate the excavation and the mass redistribution of the planar surface in the sense of Ref. [37, 161, 162]. In this case, the effective depth from the mean surface height contributing to the mass current is 4-5 Å. The mean sputtering yield Y_{sp} is 7.6 atoms and the mean number Y_{ad} of adatoms, that are displaced above the initial overlayer, is 7.7 atoms. The distributions of these quantities Y_{sp} and Y_{ad} can be fitted by the positive part of normal distributions with the medians $\mu_{sp} = 3.6$ Å and $\mu_{ad} = 8.6$ Å as well as the variances $\sigma_{sp}^2 = 2.5$ Å^2 and $\sigma_{ad}^2 = 19.2$ Å^2. The variance of adatom creation is much higher than that of sputtering. This is due to the surface channeling events along the dimer rows. A higher adatom creation rate is expected for the ion incident angle parallel to the rows than that of perpendicular to them. On average, atoms near the surface are displaced preferentially in the direction of ion incidence along the surface and two symmetrical peaks of adatom creation as well as one peak of vacancy creation have been
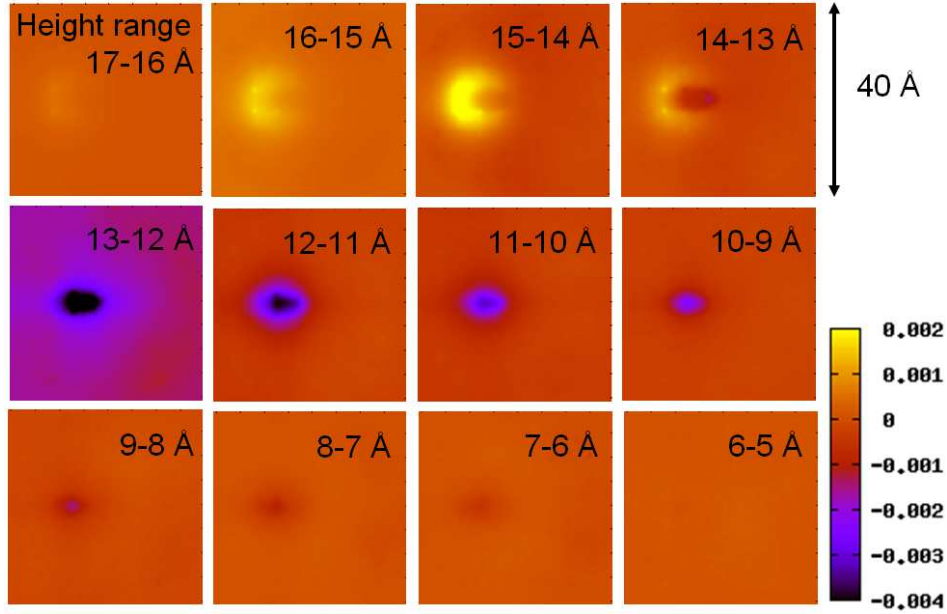
Figure 4.2: 3D defect statistics induced by single ion impact: the color scale indicates the mean atomic density variation within the height range before and after ion impact. The scale is atom/Å^3.

observed. There are no interstitials in bulk Si in the sense of atomic density enhancement. The shape of the mass current region can be fitted by an ellipsoid (prolate spheroid) with the long axis being parallel to the surface including the ion incident direction.

4.2.2 Monte-Carlo simulations of surface modification

In the previous MD simulation, an ion induced mass transport has been observed. This event leads to surface defect generation consisting of vacancies and adatoms. This event is implemented in the KMC simulations with an Ising-like potential field in fcc lattice system.

Yewande *et al* [251, 252] reported the sputter induced surface pattern formation by KMC simulations. In their model, the incident angle θ and the mean energy deposition depth a are fixed typically at $\theta = 50°$ and $a = 6$. The appearing ripple modes are investigated with varying mainly the variances of ion energy deposition rate with respect to the energy distribution σ_p, and σ_l in eq. (4.2). Clear parallel mode ripples are observed for $\sigma_p < \sigma_l$. Accounting for the surface diffusion process at the effective temperature 1200 K they obtained a clear periodic structure formation whereas no ripples were observed at room temperature. The temperature enhancement is interpreted as an ion beam induced thermal spike [149]. Their KMC model is constructed as 2+1 D solid-on-solid model with sc lattice structure [208] and therefore the atomic mobility is restricted to 6-1 directions at most where -1 is for the mean surface normal direction. Thus the number of atomic jumps to find a minimum energy configuration is necessarily larger than of those in the fcc structure where the possible number of atomic jump directions is 12. Since a bombarded Si surface is amorphized, a complex mobility of an adatom is expected on the surface. Because the fcc structure has more NN positions than that of the sc structure, the NN configuration dependency of a single atomic jump attempt is more complex in the fcc network. This is an advantage to model the responsible situation of an amorphized Si surface with the fcc structure. Although a diamond structure can better model this situation, the problems with the complexity of the local configuration dependency utilizing an

appropriate potential and the number restriction of atoms are still difficult to overcome. Hence we use the pseudo atoms with the NN interaction in the fcc structure as approximated amorphous Si atoms in this work. The corresponding inter atomic distance and the cohesive energy are discussed below.

Here, the sputter effect is one of the three factors observed in the previous MD model. However, surface mass redistribution suppressing the sputter effect with the full 3D-fcc KMC model has been performed in order to examine this effect in isolation.

Simulation parameters

The corresponding inter atomic distance and the cohesive energy of the pseudo atoms are calculated to fit to the energy- as well as atomic density of crystal Si (c-Si). The difference of these properties between crystal- and amorphous Si is ignored here. Since a silicon atom in a crystal has a cohesive energy of 4.63 eV [1] and a accounting for the difference of diamond and the fcc lattice structure, one bond energy E_b is calculated as $E_b = 0.39$ eV in the model. Since an atomic jump with breaking bonds leads to the bond lost of the jumping atom as well as of the NN atoms, the acceptance probability $P_{i \to f}$ of this jump attempt is calculated to be

$$P_{i \to f} = \exp(-2n_b E_b / k_B T), \tag{4.15}$$

with n_b being the number of breaking bonds. The inter atomic distance d^{fcc} of these pseudo atoms is calculated from the corresponding atomic density of c-Si as

$$d^{fcc} = d_{Si} \times (\rho_{fcc}/\rho_{dia})^{1/3} \sim 0.30 \text{ [nm]}$$

where ρ_{fcc} and ρ_{dia} are the atomic density arranged in fcc cells as well as in diamond cells respectively, and $d_{Si} = 2.35$ Åis the inter atomic distance of Si. Thus the corresponding length of lattice unit is

$$1 \text{ [lu]} \cong \frac{d^{fcc}}{\sqrt{2}} \sim 0.21 \text{ [nm]}.$$

The factor $\sqrt{2}$ is due to the arrangement of atoms in the fcc lattice system. The system size is 512 $\times$ 512 $\times$ 128 corresponding to 107 nm $\times$ 107 nm $\times$ 27 nm. All KMC simulations are performed under the standard condition of 3D lattice KMC [219]. Thus the simulation system is not boosted and migration barriers for the same NN configuration are assumed to be zero.

Ellipsoid displacement models

The shape of the region where atoms are displaced in the MD simulation is approximately a rugby ball (prolate spheroid). Thus a simple ballistic surface atom displacement together with the thermal diffusion process is modeled. The substrate surface is irradiated by artificial ions with no energy consideration with incident angle 67° from the surface normal. The surface atom hit by an ion is simply displaced within a certain displacement region on the surface. Figure 4.3 shows a schematic description of two patterns of this model. **a** is a prolate spheroid model (model A) that is similar to the MD result. The long axis is 1.02 nm and the short axis is 0.83 nm. The displacement region is the intersection of this ellipsoid and the surface is indicated by the green color. **b** is the sphere model (model B) with the diameter 0.83 nm. The flux ϕ varies from 0.1-0.001 ions nm^{-2} tu^{-1} and the total fluence is 6×10^{18} ions nm^{-2} in each case. The surface temperature is held fixed at $T = 300$ K during the simulation. Figure 4.4 shows the evolution of both models with flux

---

[1]This is calculated with the Tersoff potential. Calculating with the Stillinger-Weber potential yields 4.33 eV.
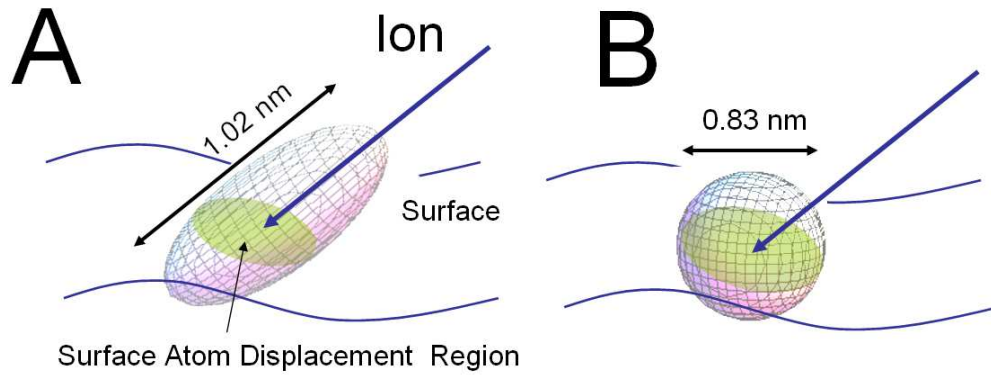
Figure 4.3: A schematic description of the shape dependent surface mass current model. (**A**) The surface atom displacement region is shown by the green color. The tips of the blue arrows represent the impact points and their direction, that of the ion beam.
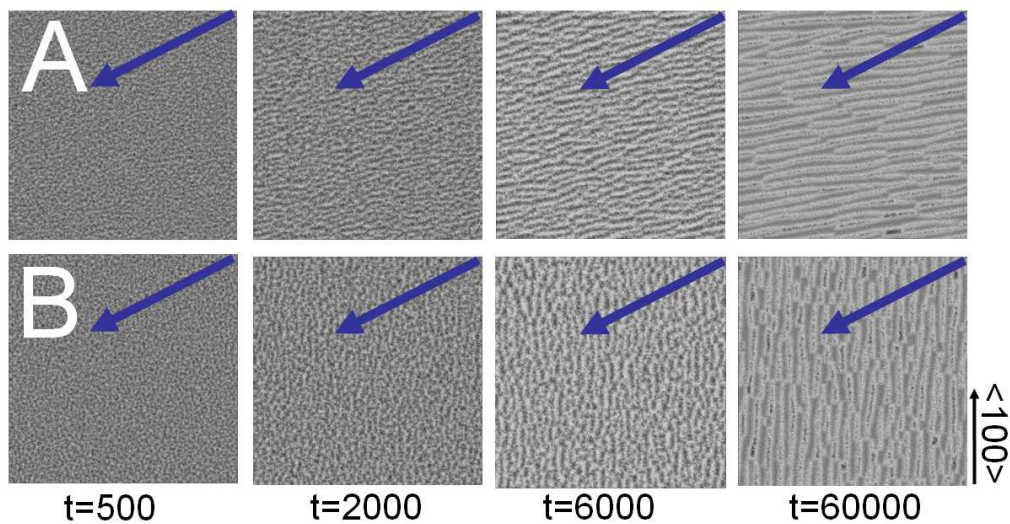

Figure 4.4: Simulation results for the displacement shape dependent ripple formation model A and B. Blue arrows indicate the direction of the ion beam and black arrow indicates $< 100 >$ direction in the fcc lattice. Simulation parameters for the both cases are $T = 300$ K, flux 0.1 ions nm^{-1} tu^{-1}, and $t = 500, 2000, 6000, 60000$ tu.

ϕ =0.1. In the initial stage, the surface is simply roughened ($t = 500$) and no significant difference is observed between model A and B. At $t = 2000$, small structures with slightly different patterns appear. At $t = 6000$, the difference between the two surface patterns becomes clear. Finally, clear ripples with periodicity ~5 nm appear at $t = 60000$ in each case. The direction of the periodicity tends to the perpendicular and parallel direction with respect to the ion azimuth angle for model A and B respectively. Such a small asymmetry results in the drastic change of pattern with respect to the correlation direction.

In the both cases, the direction of the ripple periodicity is tilted to $< 100 >$ direction. This is due to the influence from the surface orientation of the fcc structure since the structure observed is small in magnitude compared to the discretization of the atomic system modeling the amorphous structure.

Remarkably, no significant difference is observed by reducing the flux parameter ϕ by a factor 10-100 ($\phi = 0.01$-0.001). The modification process depends mainly on the fluence. The diffusion process with bond breaking hardly occurs at room temperature ($T = 300$ K) since the minimum barrier for such event is 0.78 eV by eq. (4.15) and the acceptance ratio is only $P_{i \to f} = 7.87 \times 10^{-14}$. The mobility of surface atoms are thus restricted to migration to positions possessing the same number or more NN atoms. Once the surface is roughened, such migration pathways are only possible over a local region and reach a local minimum energy configuration immediately. Hence, in this model, the diffusivity, in the sense of long range ($\geq \lambda$), plays a minor role and a spontaneous local condensation as well as the local atomic flow distribution shape may contribute more for the ripple formation.

Quasi-liquid surface atomic flow model

In contrast to the previous model, the effect of thermal diffusion and ion direction dependent anisotropic displacement is considered in the absence of the sputter effect and introduction of a high viscosity of surface atoms. This model is based on model B introduced above. The surface atom hit by an ion is shifted on the surface within the certain radius centered at the impact point. The difference from the previous model is that the displacement direction is restricted to the forward direction with respect to the ion trajectory. The radius of the displacement sphere is chosen to be a minimum, i.e. the NN distance. The normal and azimuthal incident angles are fixed at 67° and 45°. Due to the lattice orientation of the fcc simulation system, three NN positions are regarded as the backward displacement positions. Thus the 9 NN positions of the atom impinged are considered as the ballistic displacement positions. This anisotropic ballistic displacement leads to a statistical surface atomic flow along the topography and the flow speed is associated with the local flux.

For the diffusion process, the temperature is enhanced to be $T' = 15,269$ K which corresponds to $2E_b/k_B T' = 1.0$. The kinetic energy given is $(T' - T)k_B \sim 1.3$ eV per atom. In order to avoid evaporation, detachment from the surface is entirely suppressed. The surface atoms possess consequently a high liquidity. The flux chosen is 0.01 ions nm^{-2} tu^{-1}. This means atoms in a surface area with 1 nm^2 can move only 100 times at most before the area is bombarded again. Again, by calculating with the Debye frequency $\omega_{Si} = 8.45 \times 10^{13}$ s^{-1}, this time range corresponds to 1.2 picoseconds. A temperature enhancement above 10,000 K for ~0.1 ps is observed in the MD simulation of 1 keV Ar$^+$ bombardment on Ti/Pt multilayer [222]. Another MD simulation shows that liquid Si atoms are observed until ~1 ps after single 10 keV Si-Si bombardment [168]. Thus a local temperature enhancement over this time range is practically possible for ion bombardment with ~10 keV order around the center of the kinetic energy deposition , i.e. in the bulk region near the surface. Note that this temperature is induced solely by ion impacts and therefore independent from the equilibrium surface temperature in the laboratory.
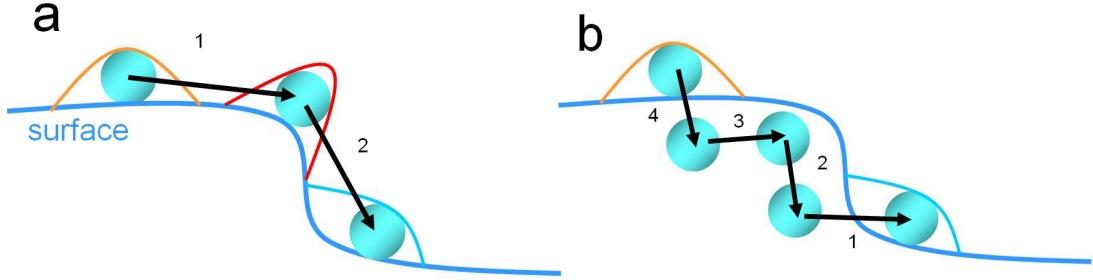
Figure 4.5: Schematic description of atomistic transition processes with a small curvature intermediate position (**a**) and quasi-bulk diffusion process avoiding the significant curvature reduction (**b**). Numbers indicate the transition step of atomic jump.

Accounting for the viscosity of surface, the movement with a high local curvature is suppressed. According to the Nernst-Einstein relation, the velocity v_{surf} of surface atoms is derived as [112]

$$v_{surf} = -\frac{D_s}{k_B T}\frac{\partial \mu_c^{(\kappa)}}{\partial s},\tag{4.16}$$

where $\mu_c^{(\kappa)}$ is the increase of chemical potential per atom at a point of curvature κ on the surface compared to a flat surface, and s is the arc length measured along the curve. Here, the curvature κ at a point p on the surface is the reciprocal of the radius of the osculating circle and taken as positive for a convex bulge of the profile. Moreover, from Herring's diffusional viscosity theory [102], this increase of chemical potential associated with the curvature κ is

$$\mu_c^{(\kappa)} = \frac{\gamma}{\rho_0}\kappa.\tag{4.17}$$

For the surface diffusion atomic density per unit area ν, the surface atomic current J_{surf} is calculated from eq. (4.16) and (4.17) as

$$J_{surf} = v_{surf}\nu = -\frac{D_s\gamma\nu}{\rho_0 k_B T}\frac{\partial \kappa}{\partial s}.\tag{4.18}$$

This implies that the atom cannot move in the direction in which the curvature decreases. In a fcc lattice network system, this situation corresponds to the ES barrier. Figure 4.5 gives a schematic description of two types of surface atomic movement leading to the same configuration change with different kinetic pathways. The type **a** path is a typical process overcoming an ES barrier. The numbers indicate the transition step. Surface curvature is reduced at the intermediate position after the step 1 indicated by a red curve. The type **b** path is a quasi-bulk diffusion process yielding the same final configuration but avoids the significant local curvature reduction seen in **a**. By step 1, an atom hops to the next position on the same layer and the atom above this moving atom goes down by step 2, and so on. Such a migration process is expected by the inward relaxation of vacancies in Si [9]. In this case, the diffusion is rather complicated and requires more transition steps resulting in a discrete viscous diffusion process deduced from eq. (4.18). For **a**, most of the ES barriers in an fcc system are formed at intermediate positions with NN number 1 or 2. Thus all transition pathways that go through the position with the NN number smaller than 3 are blocked in the thermally activated transition process. The jump to such a position is thus only possible by a ballistic displacement process. Evaporation is also suppressed from this condition.

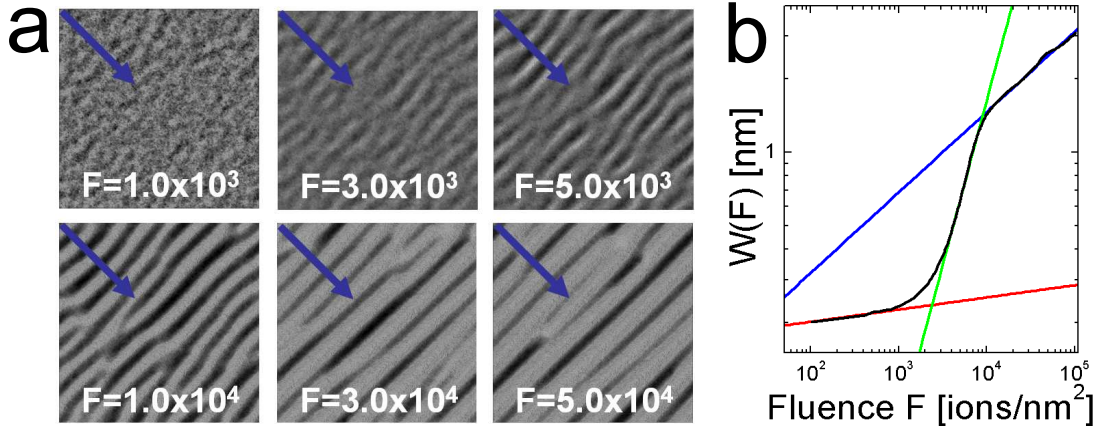Under these conditions a KMC simulation has been performed. Figure 4.6 shows the top view

Figure 4.6: Top view of the simulation surface (**a**) and the width evolution with total fluence (**b**). The lines in **b** indicate the asymptotic lines with growth exponents: green $\beta =1.35$; blue $\beta =0.33$; red $\beta =0.05$ in eq. (4.20).

of the surface evolution process (**a**) and the *width* of the surface height as a function of ion fluence F (**b**). A very clear ripple formation process is observed in **a** with increasing the fluence F. The interface width $W(S, F)$ of the simulation surface S with respect to fluence F is defined as the root mean square of the surface height, i.e.,

$$W(S,F) := \left(\frac{1}{|S|} \int_S [h(F) - \bar{h}(F)]^2 dxdy \right)^{1/2} , \qquad (4.19)$$

where S is the domain of h in the xy-plane and $|S|$ is the area of S. This describes the fluctuation of the simulation surface height around the mean height.

The simulation system size is however restricted in a certain area with PBC. When the structure is still small enough compared to the system size, then the evolution may be independent from the system periodicity whereas it will be dominated by the PBC in the late stage. From this point of view, the early- and late stage of the width may be fit by the so-called finite-size scaling expression

$$W(S,F) \propto \begin{cases} |S|^\alpha & (|S|^\alpha << F^\beta) \\ F^\beta & (F^\beta << |S|^\alpha) \end{cases} \qquad (4.20)$$

for some positive constants $\alpha, \beta > 0$. This *Ansatz*, or scaling assumption, was originally introduced by Vicsek and Family for the height analysis for cluster growth simulation [74, 234]. In this case, the power exponent β of the fluence F indicates the behavior of the evolution process in the early stage independent from the system size. On the other hand, the growth saturates in the late stage and the width is asymptotically constant determined by $|S|^\alpha$. These constants α, β are called the roughness- and the growth exponent respectively. System evolution dominated by a similar dynamics that can be characterized by equations of motion with different scale factors behaves with similar exponents α, β. Especially, the quantity $W(S, F)/|S|^\alpha$ against $F/|S|^\alpha$ is a scaling invariant [74].

Concerning the surface roughness evolution $W(F)$ (figure 4.6 **b**), the simulation system seems not yet to have reached a steady state. There are three clear phases observed in this fluence regime. The turning points are around $F = 1.0 \times 10^3$-2.0×10^3 ions nm^{-2} as well as $F \sim 1.0 \times 10^4$.

In the first phase, the surface coarsening is rather homogeneous since the surface is still flat and almost every wave is growing stably due to surface diffusion as shown in the linear stability analysis of the BH theory. Various small hillocks are constructed because of the homogeneous propagation

of small waves in the linear regime. The structures have the periodicity $\sim$10 nm at the end of the first phase.

Due to the ballistic displacement with respect to the surface topography, i.e. small hillocks, as well as the consequent local flux variation, waves propagate preferentially in the lateral direction of the ion beam when the structure grows to a sufficient level. This is because the flow speed slows down in the low flux region behind the hills. This fact results in the aggregation of small structures in the lateral direction resulting in the ripple formation observed. This aggregation further promotes topography change leading to a more significant local flux variation. This is a nonlinear effect and the BH theory may be not valid any more. During this phase, as shown in the width evolution (figure 4.6 **b**), the growth of structures is quite fast due to this synergy effect of the aggregation and the local flux change. This may be the reason of spontaneous ripple formation observed in experiment [70]. In contrast to the lateral direction, the prolongation of the wavelength with respect to the parallel direction of ion beam is slow and no significant growth is observed during the second phase since the contribution of surface diffusion may be required.

In the third phase, the coalescence of ripples with respect to the lateral direction of the ion beam are almost saturated and the wavelength starts to extend. The ripple waves are moving along the ion beam direction with almost same velocity. The surface self-organization process tries to minimize the number of branches and the extension of the wavelength seems to be from this action.

Such a transition with the three phases of the width with the time evolution is also observed qualitatively in the numerical integration of the 3D hydrodynamic model [162] with the form

$$\frac{\partial h}{\partial t} = -h_{xx} + 0.1(-h_{yy} + h_x^2 + h_y^2) - \sum_{i,j=x,y} [h_{iijj} + 0.1r(h_j^2)_{ii}]$$

for each parameter r =0.25-100 whereas the third phase is not observed in their 2D model.

4.2.3 Curvature dependent surface diffusion

In the temperature range of the KMC simulation performed above, thermal diffusion may play an important role. From the surface current equation (4.18), the atomic current depends on the surface gradient of the curvature κ. In the case of a 2D Cartesian system $(x, h(x))$, the curvature κ is given by

$$\kappa = -\frac{h_{xx}}{(1 + h_x^2)^{3/2}}. \tag{4.21}$$

In a 3D system, each point p on the surface possesses two orthogonal directions giving the minimum and maximum curvature known as *principal directions* (Euler, 1760). These minimum- and maximum curvatures denoted by κ_m and κ_M are called the *principal curvatures* at p.

The evolution of atomic concentration c_{surf} follows Fick's second law

$$c_{surf} = -\frac{\partial}{\partial s} J_{surf}.$$

The velocity of surface evolution with respect to the normal direction r_n is then given by the conservation of atomic density as

$$r_n = \frac{c_{surf}}{\rho_0} = B\frac{\partial^2 \kappa}{\partial s^2}. \tag{4.22}$$

In contrast to the derivation by Mullins [160], we avoid the low-corrugation approximation here. Accounting for the direction of the surface normal by the factor $\sqrt{1 + (\nabla h)^2}$, the evolution of the

surface height h resulting in the atomic current is

$$\frac{\partial h}{\partial t} = \sqrt{1 + (\nabla h)^2} r_n = B\sqrt{1 + (\nabla h)^2}\frac{\partial^2 \kappa}{\partial s^2}. \tag{4.23}$$

In a 3D Cartesian system, the velocity (4.16) is a vector along the gradient with respect to the principal directions. Consequently, the concentration is given by the divergence with respect to the direction coordinate. Thus the evolution $r_n^{(3D)}$ at p is given by

$$r_n^{(3D)} = B\nabla_s^2 \kappa = B\left(\frac{\partial^2}{\partial s_m^2} + \frac{\partial^2}{\partial s_M^2}\right)K, \tag{4.24}$$

where s_m, s_M are the arc lengths along the curves crossover orthogonally at p and giving the principal directions with respect to the minimum- and maximum curvature respectively, and $K = \kappa_m + \kappa_M$. Choose the coordinate system (x, y) parallel to the principal directions. Then, for $(i, u) = (m, x), (M, y)$, the differential 1-forms satisfy the relation $ds_i = du\sqrt{1 + h_u^2}$ and therefore the partial derivatives are

$$\frac{\partial}{\partial s_i} = \frac{\partial u}{\partial s_i}\frac{\partial}{\partial u} = \frac{1}{\sqrt{1 + h_u^2}}\frac{\partial}{\partial u}, \tag{4.25}$$

respectively. From eqs. (4.21), (4.24) and (4.25) together with the height direction factor the height evolution is derived as

$$\frac{\partial h}{\partial t} = B\sqrt{1 + (\nabla h)^2} \sum_{u=x,y} \frac{1}{\sqrt{1 + h_u^2}}\frac{\partial}{\partial u}\left(\frac{1}{\sqrt{1 + h_u^2}}\frac{\partial K}{\partial u}\right), \tag{4.26}$$

with

$$K = -\frac{h_{xx}}{(1 + h_x^2)^{3/2}} - \frac{h_{yy}}{(1 + h_y^2)^{3/2}}. \tag{4.27}$$

By assuming a slow surface variation $|h_x|, |h_y| << 1$, and ignoring second and higher degree terms in eqs. (4.26) and (4.27) yields

$$\frac{\partial h}{\partial t} \cong -B\nabla^2(\nabla^2 h),$$

which gives the diffusion term of the BH equation (4.3). Note that the time scale corresponds to the scale of the velocity of surface atoms introduced by the Nernst-Einstein relation (4.16). Hence in the viscous surface KMC model, the time unit is dependent on the quenching time of the local temperature enhancement of order ~ 1 ps.

4.3   Continuum model

From the fundamental observation of the MD simulation, it is assumed that defects such as vacancies and interstitials during ion bombardment are created with some relaxation between impact events. The KMC simulation models established the atomics current induced ripple formation process together with quite short temperature enhancement due to the ion energy deposition.

In this section, a mathematical model is considered in which these processes are merged. Assume that each ion bombardment induces infinitesimal atomic flow as in a pseudo-compressible media. This temporary density change in the near surface region leads to the surface evolution locally driven by mass conservation. The mathematical model is essentially independent from the surface topography changes induced by both of sputtering and surface diffusion.

First, a nonlinear equation of motion will be derived. Then it will be shown that it possesses a travelling wave solution for a specific incident angle, which agrees excellently with the experimental observation [35]. By applying the model to different systems it is anticipated that induced ripple structure shapes (periodicity and aspect ratio) can be predicted and used to guide experimental nanostructure fabrication.
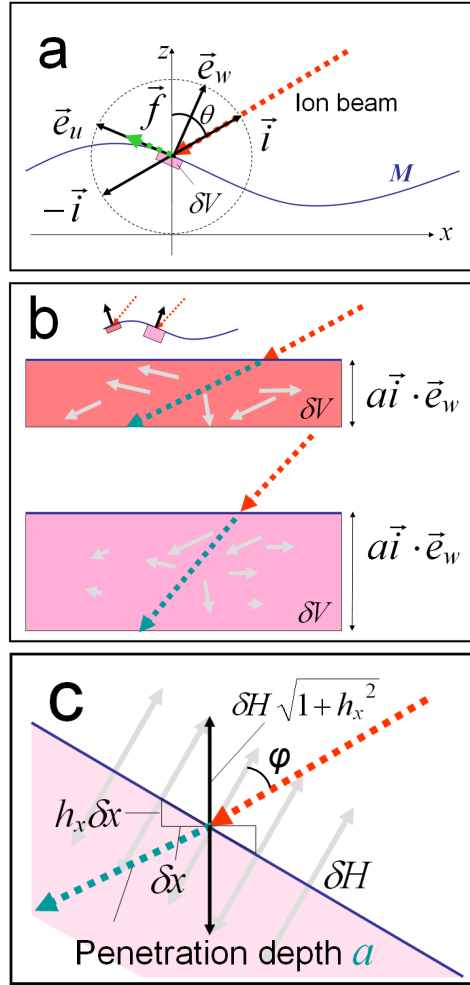
4.3.1 Equation of motion

Figure 4.7: A schematic description of single ion impact. **a** Vectors describing the ion incidence $\vec{i}$, surface normal $\vec{e_w}$, surface tangent $\vec{e_u}$, surface atomic flow $\vec{f}$ and the ion incidence angle θ are defined. **b** The local angle dependence of the flow in the affected region δV. **c** The (two-dimensional) surface swelling process around the impact point.

Let (u, v, w) be the local coordination system with (u, v) spanning the tangent space of the surface manifold $M := \{(x, y, h(t, x, y)) : x, y \in \mathbb{R}\}$. Moreover, let $\vec{e_u}, \vec{e_v}, \vec{e_w}$ be the corresponding unit vectors associated with these directions, i.e. $\vec{e_w}$ defines the outward surface normal vector; the unit vector oriented to the mean direction of incoming ions is denoted by $-\vec{i}$. Here, the directions of the components u and v of the coordinate system are defined by $\vec{i}$ and the normal vector $\vec{e_w}$ as

$$\vec{e_u} = \frac{\vec{i} \times \vec{e_w}}{|\vec{i} \times \vec{e_w}|} \times \vec{e_w}, \quad \vec{e_v} = \vec{e_w} \times \vec{e_u}. \tag{4.28}$$

The flow of atoms in the small region δV around the impact point is now considered. Figure 4.7 **a** illustrates this condition for the case when $\vec{i}$ is parallel to the (x, z)-plane.

Let $N = N(E, a)$ be the total number of displaced atoms due to the collision cascade [35, 202, 203] for a effective penetration depth a and ion energy E. Note that this effective penetration depth a is related to the mobile atom region, considered in the hydrodynamic model [37, 161, 162], and the penetration depth itself depends on both the energy E and the type of ion [257] (see eq. (4.4)). Assume that this N is independent from the local angle of incidence so long as the angle is not too glancing. Now consider an effective flow of atoms displaced in a small region δV near the impact point. The model assumes an atomic motion induced by ion impact in δV, considered as a fast Eulerian-like flow. This δV may depend on the local angle of ion incidence due to the flow invoking the surface modification. It is also assumed that the number of atoms set in an effective motion depends on the volume of δV and the rate of these atoms flowing is constant. Let N^{eff} be this rate of atoms contributing to the effective flow in δV. The energy density deposited may depend on the number of atoms in δV (figure 4.7 **b**). Set

$$N_{loc}^{eff} := N^{eff} \rho_0 |\delta V|, \tag{4.29}$$

where $|\delta V|$ indicates the volume of δV. Let $\vec{v}_i$ be the flow vector of atoms $i = 1, ..., N_{loc}^{eff}$. Let Δv be the magnitude of the velocity loss during the effective collision process evoking the flow. Here, M_1 and M_2 are the mass of ion and surface atoms as defined in section 4.1, respectively. Then due to elastic collisions

$$M_1 \sum_{i=1}^{N_{loc}^{eff}} \vec{v}_i = M_2 \Delta v(-\vec{i}).$$

Thus the average velocity $\vec{v}$ of atoms is

$$\vec{v} = \frac{M_2 \Delta v}{M_1 N_{loc}^{eff}}(-\vec{i}). \tag{4.30}$$

For the effective quenching time t_q, let $\epsilon := |\vec{v}| t_q$ be the mean displacement distance. Then from (4.30) we have

$$M_1(\epsilon/t_q) = \frac{M_2 \Delta v}{N_{loc}^{eff}}. \tag{4.31}$$

The quenching time t_q of the effective flow is effectively the ballistic phase of a collision cascade predicted as a few ps by MD simulations of low energy ion impact [213]. The displacement distances ϵ_u, ϵ_v and ϵ_w projected in the direction of (u, v, w) are thus $\epsilon_j = \epsilon(-\vec{i} \cdot \vec{e}_j)$, for $j = u, v, w$ respectively. The local atomic flow vector $\vec{f}_{loc}$ is now represented by

$$\vec{f}_{loc} = \rho_0 \sum_{j=u,v,w} (\epsilon_j/t_q)\vec{e}_j = -\frac{\rho_0 \epsilon}{t_q}\vec{i}. \tag{4.32}$$

For a typical ion flux ϕ, the mean time interval between two ion impacts per unit square is much longer than the quenching time t_q. Let

$$S_f = \frac{|\delta V|}{a\vec{i} \cdot \vec{e}_w}$$

be the surface area where the atomic flow occurs. Then this time interval t_d is given by

$$t_d = \frac{1}{S_f \phi} = \frac{a\vec{i} \cdot \vec{e}_w}{|\delta V|\phi}. \tag{4.33}$$

105

Denote

$$r_t := \frac{t_q}{t_d} = \frac{t_q |\delta V| \phi}{a \vec{i} \cdot \vec{e}_w} \tag{4.34}$$

the ratio of these two times. Note that the time interval t_d decreases with increasing flux. From (4.29), (4.31), (4.32) and (4.33) the global flow function $\vec{f}$ is then given by

$$\vec{f} = (\vec{i} \cdot \vec{e}_w) r_t \vec{f}_{loc} = -\rho_0 u \vec{i},$$

where

$$u = \frac{\phi t_q M_2 \Delta v}{a \rho_0 M_1 N^{eff}} \tag{4.35}$$

is a positive constant with the dimension of velocity independent from the local topography.

Now, the mass current $\vec{f}$ and the atomic density ρ satisfy the conservation of mass equation

$$\int_{\delta v} \frac{\partial \rho}{\partial t} dV + \int_{\partial \delta v} \vec{f} \cdot \vec{n}_s dS = 0. \tag{4.36}$$

This describes the fast defect creation process. The volume of δV is approximately $|\delta V| \approx \delta u \delta v a (\vec{i} \cdot \vec{e}_w)$. The mean height evolution due to the relaxation of defects can be evaluated as (figure 4.7 **c**)

$$\langle \frac{\partial h}{\partial t} \rangle \approx \frac{< \sqrt{1 + (\nabla h)^2} >}{\rho_0 \delta u \delta v} \int_{\delta v} \frac{\partial \rho}{\partial t} dV. \tag{4.37}$$

In the model, surface swelling, or shrinking is allowed only in the surface normal direction where the resistance is considered to be least. Thus the volume variation $\delta \rho$ is proportional to the variation of local surface height relaxation δH (figure 4.7 **c**).
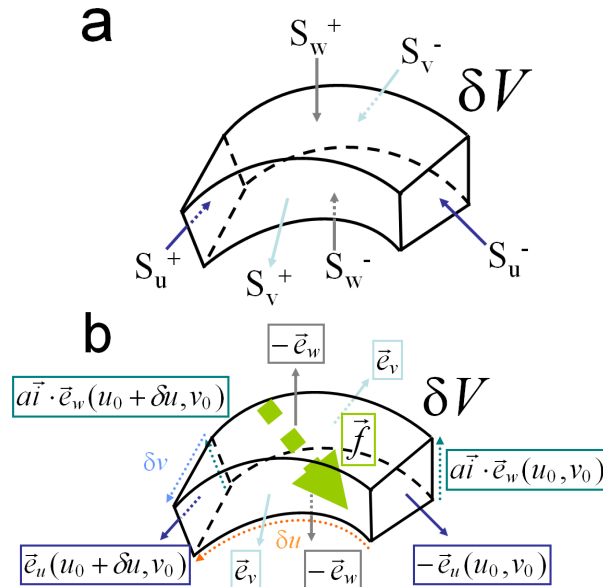

Figure 4.8: Schematic description of δV with respect to the local coordinate system (u, v, w) and relevant vectors.

Let $S_u^{\pm}$, $S_v^{\pm}$ and $S_w^{\pm}$ be the surfaces of δV (see figure4.8 **a**). Since $\vec{f}$ is parallel to $\vec{i}$ by (4.35), it follows from (4.28)

$$\vec{f} \cdot \vec{e}_v \propto \vec{i} \cdot \vec{e}_v = \vec{i} \cdot (\vec{e}_w \times \vec{e}_u) = \vec{e}_u \cdot (\vec{i} \times \vec{e}_w) = 0.$$

Thus from eq.(4.36) (see also figure4.8 **b**)

$$
\begin{aligned}
&- \int_{\delta V} \frac{\partial \rho}{\partial t} dV \\
&= \int_{\partial \delta V} \vec{f} \cdot \vec{n}_s dS \\
&= \int_{S_u^+} \vec{f} \cdot \vec{e}_u dS - \int_{S_u^-} \vec{f} \cdot \vec{e}_u dS \\
&\quad + \int_{S_w^+} \vec{f} \cdot \vec{e}_w dS - \int_{S_w^-} \vec{f} \cdot \vec{e}_w dS \\
&= \int_{-a\vec{i} \cdot \vec{e}_w (u_0 + \delta u, v_0)}^{0} \int_{v_0}^{v_0 + \delta v} \vec{f} \cdot \vec{e}_u (u_0 + \delta u, v_0) dv dw \\
&\quad - \int_{-a\vec{i} \cdot \vec{e}_w (u_0, v_0)}^{0} \int_{v_0}^{v_0 + \delta v} \vec{f} \cdot \vec{e}_u (u_0, v_0) dv dw \\
&\quad + \int_{S_w^+} \vec{f} \cdot \vec{e}_w dS - \int_{S_w^-} \vec{f} \cdot \vec{e}_w dS \\
&= a\vec{i} \cdot \vec{e}_w (u_0 + \delta u, v_0) \delta v \vec{f} \cdot \vec{e}_u (u_0 + \delta u, v_0) \\
&\quad - a(\vec{i} \cdot \vec{e}_w (u_0, v_0)) \delta v \vec{f} \cdot \vec{e}_u (u_0, v_0) \\
&\quad + \int_{S_w^+} \vec{f} \cdot \vec{e}_w dS - \int_{S_w^-} \vec{f} \cdot \vec{e}_w dS.
\end{aligned}
\tag{4.38}
$$

The third and the fourth term give the flow components oriented to the surface normal. The third term is negative, since $\vec{i} \cdot \vec{e}_w > 0$ but there are no atoms flowing into the surface from the vacuum region, hence

$$
\int_{S_w^+} \vec{f} \cdot \vec{e}_w dS = 0.
\tag{4.39}
$$

The fourth term giving the normal flow into the bulk is offset by the swelling process. It follows that

$$
\int_{S_w^-} \vec{f} \cdot \vec{e}_w dS = 0.
\tag{4.40}
$$

Accounting for the recoil flow in the normal direction, we assume a constant sputtering rate Y in the direction of the w, for the atoms flowing out from S_w^+ proportional to the energy deposition $\propto |\vec{f} \cdot \vec{e}_w|$. This rate Y may also depend on the surface curvature as well as the incident angle. Here, however, we ignore these dependencies and simply eliminate atoms from this impact region corresponding to a loss of material given by

$$
\int_{S_w^+} Y |\vec{f} \cdot \vec{e}_w| dS.
$$

For small δu and δv, this term is approximately

$$
\int_{S_w^+} Y |\vec{f} \cdot \vec{e}_w| dS \approx Y \delta u \delta v |\vec{f} \cdot \vec{e}_w|.
\tag{4.41}
$$

Hence, for the macroscopic view, as $\delta u, \delta v \to 0$, it follows from eq. (4.36)-(4.41)

$$
\begin{aligned}
\frac{\partial h}{\partial t} &= \lim_{\delta u, \delta v \to 0} \frac{< \sqrt{1 + (\nabla h)^2} >}{\rho_0 \delta u \delta v} \int_{\delta V} \frac{\partial \rho}{\partial t} dV \\
&= -\lim_{\delta u, \delta v \to 0} \frac{< \sqrt{1 + (\nabla h)^2} >}{\rho_0 \delta u \delta v} \\
&\quad \times \left\{ \int_{S_u^+} \vec{f} \cdot \vec{e}_u dS - \int_{S_u^-} \vec{f} \cdot \vec{e}_u dS + Y \delta u \delta v |\vec{f} \cdot \vec{e}_w| \right\} \\
&= \frac{\sqrt{1 + (\nabla h)^2}}{\rho_0} \left\{ a \mathrm{u} \rho_0 \frac{\partial}{\partial u} (\vec{i} \cdot \vec{e}_w)(\vec{i} \cdot \vec{e}_u) - \mathrm{u} Y \rho_0 (\vec{i} \cdot \vec{e}_w) \right\} \\
&= \mathrm{u} \sqrt{1 + (\nabla h)^2} \left(a \frac{\partial}{\partial u} \{(\vec{i} \cdot \vec{e}_w)(\vec{i} \cdot \vec{e}_u)\} - Y \vec{i} \cdot \vec{e}_w \right).
\end{aligned}
\tag{4.42}
$$

The sputtering term of (4.42) is consistent with eq. (4.1) when the beam is incident in the z direction and Y varies with incidence angle. Here Y is the rate of sputtered atoms flowing perpendicular to the surface of δV and Y_0 is simply the mean number of atoms sputtered by single ion impact. A more accurate description accounting for the angular dependency of Y will be discussed in section 4.4.2. Similar forms to (4.37) as well as for the derivative along the local coordinates in (4.42) appear in the calculation of Cuerno and Barabási [53] as well as the model of Carter and Vishnyakov [35], respectively. Our fluid model differs from these due to the direction of surface elevation resulting in the pseudo-compressibility of the fluid atoms. Consequently, the derived equation of motion (4.42) can be thought of as lying somewhere between those in the models of [35] and [53]. The partial derivative of the inner product with respect to the local coordinate u in eq. (4.42) delivers the second derivative along the direction parallel to the ion track as well as the surface normal. Thus, in our model the evolution is influenced by both this second derivative [35] and the gradient [53] of the surface height. In the initial stage, at least, this equation may require the diffusion term in order to avoid the instability of surface roughening inherent in the linear dispersion relation of the BH theory.

4.3.2 A travelling wave solution

Once the total ion fluence reaches a certain level, it has been observed experimentally that surface roughening is saturated and the ripple periodicity is stable [118]. This fact suggests that there may exist a travelling wave solution satisfying the continuum equation (4.42). Now assume the surface height varies only with x ($h_y \equiv 0$) and ignore the y-component as observed in experiments. For the counter vector $\vec{i}$ of the radiation direction, let θ be the angle between z-axis and $\vec{i}$ (see figure 4.7 **a**). Then $\vec{i} = \begin{pmatrix} \sin\theta \\ \cos\theta \end{pmatrix}$ and the surface tangent vector is $\vec{e}_u = \frac{-1}{\sqrt{1+h_x^2}} \begin{pmatrix} 1 \\ h_x \end{pmatrix}$. The outward normal vector is $\vec{e}_w = \frac{1}{\sqrt{1+h_x^2}} \begin{pmatrix} -h_x \\ 1 \end{pmatrix}$. After a straightforward calculation the time evolution of h from (4.42) is

$$
\begin{aligned}
\frac{\partial h}{\partial t} &= \mathrm{u} a \frac{h_{xx}}{(1 + h_x^2)^2} \{-2h_x \sin 2\theta + (1 - h_x^2) \cos 2\theta\} \\
&\quad + \mathrm{u} Y (h_x \sin\theta - \cos\theta).
\end{aligned}
\tag{4.43}
$$

Thus for the specific incident angle $\theta = 45°$, eq. (4.43) is simply

$$
\frac{\partial h}{\partial t} = \mathrm{u} \left[-2a \frac{h_{xx} h_x}{(1 + h_x^2)^2} + \frac{Y}{\sqrt{2}} (h_x - 1) \right].
\tag{4.44}
$$

Set $h = \tilde{h} - (\mathrm{u}Y/\sqrt{2})t$, then eq. (4.44) is equivalent to

$$\frac{\partial \tilde{h}}{\partial t} = \mathrm{u}\left[-2a\frac{\tilde{h}_{xx}\tilde{h}_x}{(1+h_x^2)^2} + \frac{Y}{\sqrt{2}}\tilde{h}_x\right]. \tag{4.45}$$

Set the travelling wave assumption $\tau \equiv x + \sigma t$ for the wave velocity σ. Then (4.45) is

$$\sigma\tilde{h}_\tau = \mathrm{u}\left[-2a\frac{\tilde{h}_{\tau\tau}\tilde{h}_\tau}{(1+\tilde{h}_\tau^2)^2} + \frac{\mathrm{u}Y}{\sqrt{2}}\tilde{h}_\tau\right]. \tag{4.46}$$

A solution to this equation exists in the form of a parametric representation $\tilde{h} = \tilde{h}(\tau)$ as

$$\tau = a(p + \sin p), \tilde{h} = a\cos p \tag{4.47}$$

The function $\tilde{h}(\tau)$ is simply a cycloid function and is differentiable almost everywhere. Calculating with the chain rule yields

$$\tilde{h}_{\tau\tau} = -\frac{1}{4a}(1+\tilde{h}_\tau^2)^2. \tag{4.48}$$

Hence, from (4.46), (4.47) and (4.48), the function

$$h(t,x) = \tilde{h}(x+\sigma t) - \frac{\mathrm{u}Y}{\sqrt{2}}t \tag{4.49}$$

satisfies the equation of motion (4.44) with the specific wave velocity σ given by

$$\sigma = \mathrm{u}\left(\frac{1}{2} + \frac{Y}{\sqrt{2}}\right).$$

The wave moves in the negative x direction and the velocity increases with the sputtering rate. Thus the direction of wave movement agrees with experimental observations [93] in contrast to the BH prediction induced by the angular dependent sputtering rate [40]. From eq. (4.35), the velocity of the ripple wave is proportional to the flux ϕ, the quenching time t_q, the mass of ion M_1, and the velocity loss of ion Δv during the effective collision process evoking the flow and in inverse proportion to the effective penetration depth a, the density of substrate ρ_0, the mass of target atoms M_2, and the effective number of those atoms flowing in the impact region. The sputtering rate Y contributes to the acceleration of the wave velocity. One remarkable point is that this wave solution requires neither sputtering nor diffusion. In addition, the shape of the specific solution given above is not of small variation since the height and the wavelength can be of the same magnitude so the linear theory is invalid.

Recently, Macko *et al* reported ripple formation on an Fe co-deposited Si surface by 2 keV Kr$^+$ irradiation at 140 K - 440 K [146]. A typical incident angle where ripples appeared was around $\theta_{loc} \approx 50$, close to the angle given in our solution. Note that this solution predicts the final stage of ripple formation and does not describe the growth of process. In the initial stage, a contribution from surface diffusion is necessary to stabilise the growth of the structures. This will be discussed further in section 4.4.1.

4.3.3 Lyapunov stability

Now consider the Lyapunov stability of the solution. Let $g(x) \in C_b^2(\mathbb{R})$ be an arbitrary disturbance and $\tilde{g} = g + h$ be the perturbed solution. Here, $C_b^n(\mathbb{R})$ denotes the class of all functions defined on

the real space $\mathbb{R}$ that are n times continuously differentiable and bounded. Then from (4.44)

$$\left| \tilde{g}_t - \mathrm{u}\left[-2a\frac{\tilde{g}_{xx}\tilde{g}_x}{(1+\tilde{g}_x^2)^2} + \frac{Y}{\sqrt{2}}(\tilde{g}_x - 1) \right] \right|$$
$$\leq \quad \frac{\mathrm{u}}{2}\left| \tilde{h}_\tau + \frac{4a\tilde{g}_{xx}\tilde{g}_x}{(1+\tilde{g}_x^2)^2} \right| + \frac{\mathrm{u}Y}{\sqrt{2}}|g_x|.$$

Thus the stability of

$$\left| \tilde{h}_\tau + \frac{4a\tilde{g}_{xx}\tilde{g}_x}{(1+\tilde{g}_x^2)^2} \right| \qquad (*)$$

has to be shown. In fact, $(*)$ is bounded by a polynomial function of $\|g\|$ converging to 0 for $\|g\| \to 0$ in $C_b^2(\mathbb{R})$. It can be seen, for example, the bound of $(*)$ is

$$(*) \leq \frac{32}{9}(|g_x|^4 + 5|g_x|^3 + 6|g_x|^2 + 10|g_x| + 8a|g_x||g_{xx}| + 4a|g_{xx}|). \qquad (4.50)$$

Hence the solution satisfies Lyapunov stability. The derivation detail of (4.50) is given in appendix E. Interestingly, the solution itself is not in C_b^1, but the perturbed solution is still bounded. This stability implies that if the perturbation term of the original solution is small enough, then the solution perturbed is still stable and does not diverge with the time evolution. Especially, all terms appearing in (4.50) are derivatives of the disturbance g and therefore, if the disturbance is slow changing, then the solution perturbed is quite stable.

4.3.4   Comparison with experiment

Figure 4.9 displays a comparison between the analytical solution obtained in (4.49) (**a**) and the experimental result for Si [35] (**b**). **a** shows the cross-section which has an equivalent aspect ratio as the experiment (**right**) and the direct 3 dimensional (3D) visualisation (**left**) of the travelling wave solution (4.47) with the original aspect ratio for $a = 0.06$ μm. **b** gives the cross-section (**left**) and the top view (**right**) of an atomic force micrograph (AFM) image of a Si surface after 40 keV Xe$^+$ at $\theta = 45°$, ion fluence 1×10^{18} ions cm^{-2} at 100 K. The analytical solution contains singularities in the valley region and this tendency is also observed in the experimental height profile with the same trend of a convex, symmetric periodic shape as predicted by the stable travelling wave solution. The superimposed incidence directions show that the bottoms of the valleys are not directly exposed to ion irradiation (figure 4.9 **a**) and therefore the solution is likely to give an inaccurate description in this region. Certainly the troughs of the ripples in the experiment are exposed to the beam and seem to be much smoother, (figure 4.9 **b,left**) possibly also due to ion reflection as well as diffusion.

However the Lyapunov stability shown above should guarantee the stability of the analytical solution against any small perturbation in the shadowed region (figure 4.9 **a,left**). The height profile of the experiment exhibits surface roughening in the initial stage but eventually a ripple formation converges to the shape predicted by the analytical model. The mean ripple wavelength from the experiment is [35] $\lambda = 0.4$ μm and the solution would then predict a stable wave height of $2 \times \lambda/2\pi \sim 0.13$ μm. This agrees also nicely with the average height of the experimental result 0.12 μm (**b, left**). The effective penetration depth a in this case is thus $\lambda/2\pi \sim 0.06$ μm which is consistent with the mean penetration depth R_p of 40 keV Ar$^+$ ions, calculated as 0.05 μm using the SRIM code [261].

4.3.5   Approximate solutions for other angles

The highest order term of eq. (4.43) is $h_{xx}h_x^2$. If this term can be ignored, then the equation is

$$\frac{\partial h}{\partial t} \approx \mathrm{u}a\frac{h_{xx}}{(1+h_x^2)^2}\{-2h_x\sin 2\theta + \cos 2\theta\} + \mathrm{u}Y(h_x\sin\theta - \cos\theta). \qquad (4.51)$$
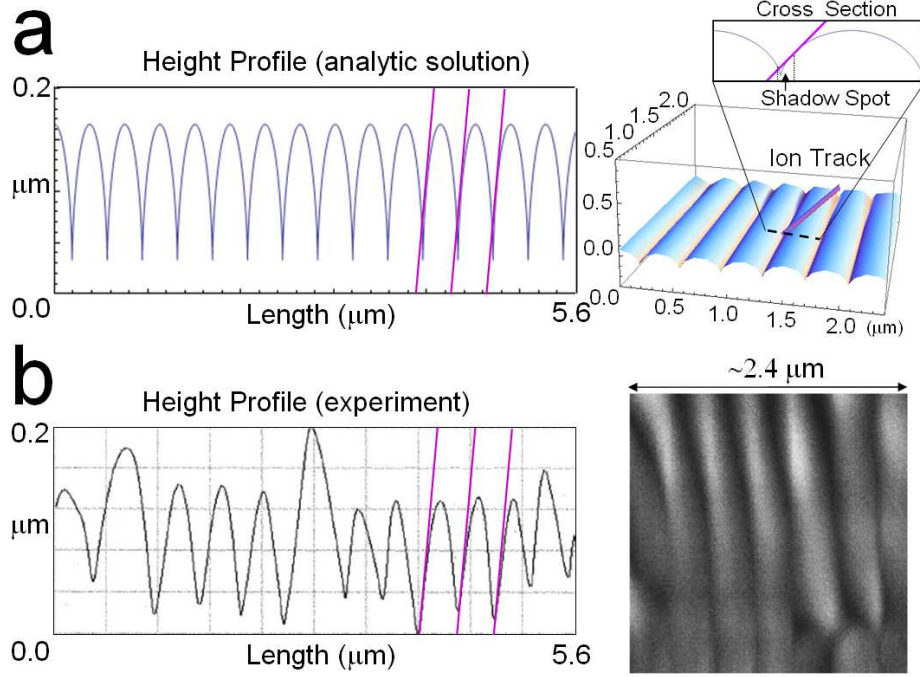
Figure 4.9:   Comparison between the analytical solution and experiment. **a** The analytical travelling wave solution $h = h(\tau)$, $a = 0.06$ μm for $\theta = 45°$ with the consistent aspect ratio (**left**) and the direct 3D image of the travelling wave solution (4.47) (**right**). The bars in the the height profile and the 3D diagram indicate the trace of incident ion at 45°. The magnified cross section along the dotted line is shown. **b** AFM image of rippled Si surface produced by 40 keV Xe$^+$ at $\theta = 45°$ (courtesy V. Vishnyakov, [35]). The height profile with ion traces (bars) (**left**) and top view (**right**).

This also possesses a travelling wave solution given by

$$h(t, x) = \tilde{h}(x + \sigma t) - u \left(\frac{\cos 2\theta}{4} + Y \cos \theta \right) t$$

with

$$\tilde{h} = a \cos p, \, x + \sigma t = a(p + \sin p), \text{ and } \sigma = u \left(\frac{\sin 2\theta}{2} + Y \sin \theta \right).$$

Since the height is of order a, this approximation is valid when the effective energy deposition depth a is relatively small in magnitude compared to other terms. However, the contribution of other factors, such as thermally activated diffusion and topography dependent sputtering, should be taken into account for more accuracy.

4.4   Contribution of other effects

4.4.1   Surface diffusion

In the initial stages of ion bombardment, so long as the linear approximation is still valid, the model described above is unstable for every wave component at $\theta \neq 45°$ in the linear dispersion relation. For small structure formation in the initial stage, the periodic structure growth is stabilised by the contribution of the diffusion term [27]. On the other hand, under an enhanced temperature environment the correlation length is extended due to the high mobility of atoms. In these cases, the

contribution of the diffusion term should be taken into account since the surface curvature is large compared to the size of any surface structure and the range of mobility of the atoms. Incorporating the diffusion term from eq. (4.8) yields

$$
\begin{aligned}
\frac{\partial h}{\partial t} &= \sqrt{1 + (\nabla h)^2} \\
&\times \left(\mathrm{u}a \frac{\partial}{\partial u} \{ (\vec{i} \cdot \vec{e}_w)(\vec{i} \cdot \vec{e}_u) \} - \mathrm{u}Y \vec{i} \cdot \vec{e}_w + \tilde{B} \nabla_s^2 \kappa \right),
\end{aligned} \tag{4.52}
$$

where $\tilde{B}$ is the temperature dependent diffusion coefficient given by

$$
\tilde{B} = \frac{D_s \gamma \nu}{\rho_0^2 k_B} \left(\frac{e^{-E_d/k_B T}}{T} + r_t \frac{e^{-E_d/k_B T'}}{T'} \right) \tag{4.53}
$$

where the substrate temperature is T and the locally enhanced temperature from each ion impact, T'. With a high substrate temperature T, the diffusion term is dominated by the first term when the quenching time is small enough, i.e. if

$$
\frac{T' e^{E_d/k_B T'}}{T e^{E_d/k_B T}} >> r_t \tag{4.54}
$$

holds. Indeed, for a typical quenching time $t_q \sim 10^{-12}$ s [168], flux $\phi \sim 1$ ions nm^{-2}s^{-1} [118], migration barrier $E_d \sim 1.2$ eV [44], melting temperature of Si $T' \sim 1700$ K, and surface area of atomic flow, $S_f \sim 1$ nm^2 [168], the ratio r_t is

$$
r_t = t_q S_f \phi = 10^{-12}
$$

from (4.34) and the critical temperature T_c for

$$
\frac{T' e^{E_d/k_B T'}}{T_c e^{E_d/k_B T_c}} \sim r_t
$$

is $T_c \sim 380$ K. Thus in experiments at a temperature of $T > 800$ K reported by Erlebacher *et al* and Chason *et al*, the substrate temperature based diffusion term plays a crucial role; at low and moderate temperatures diffusion is restricted to the short time local temperature enhancement induced by the ion impact. Note that this critical temperature is highly dependent on the displacement barrier E_d.

In the linear regime, ignoring the constant term, eq. (4.52) in a 2D Cartesian system reduces to

$$
\frac{\partial h}{\partial t} \cong \mathrm{u}a \cos 2\theta h_{xx} + \mathrm{u}Y \sin \theta h_x - \tilde{B} h_{xxxx}.
$$

The height evolution obeying this equation of motion behaves like the BH model for $\theta > 45°$ due to the negative sign of the second order derivative term. The incident angle dependence is in agreement with the smoothing term of the Carter and Vishnyakov model [35]. For $\theta \le 45°$, every wave component decays with time evolution and the surface is simply eroded since the coefficients of these terms are positive. This prediction is close to the critical angle $\sim 50°$ reported by the low energy ion sputtering of pure silicon surface by Madi *et al* [147]. Since u $\propto \phi$, the wavelength λ giving the maximum initial structure growth speed is

$$
\lambda^{-1} \propto \sqrt{\mathrm{u}a/\tilde{B}} \propto (\phi T)^{1/2} e^{E_d/2k_B T},
$$

which is the same prediction of the BH theory with respect to the ripple wavelength of parallel mode. Moreover, in this case the wavelength follows a negative power law of the ion energy

$$\lambda^{-1} \propto \sqrt{ua} \propto E^{7/12}$$

since $u \propto \Delta v \propto E^{1/2}$ from eq. (4.35) and $a \sim$ projected range $\propto E^{2/3}$ from the Sigmund theory. This prediction $\lambda \propto E^{-0.58}$ is close to that reported by Brown *et al* [28] $\lambda \propto E^{-0.45}$ at 930 K found experimentally. On the other hand, at lower temperatures, the contribution of the diffusion term for the final configuration is not so significant and the wavelength follows a positive power law relationship

$$\lambda \propto a \propto E^{2/3}$$

as predicted by the travelling wave solution (4.47). Such positive power law dependencies are also reported by Chini *et al* [46] $\lambda \propto E^{0.45}$ for Ar^+ 50-140 keV, as well as Ziberi *et al* [257] $\lambda \propto E^{0.44}$ for Ar^+ 0.5-2 keV at room temperature.

4.4.2 Surface Sputtering

Now consider a more detailed description of the contribution of sputtering in the case of ion beams with energies in the range (≤ 5 keV). By assuming a small penetration depth $a << \kappa^{-1}$, the erosion velocity v_s depends on the local topography as [27]

$$v_s(\varphi, \kappa) = v_0(\varphi) - v_c(\varphi)a\kappa, \tag{4.55}$$

for a fixed incident angle θ and a constant ion energy. By accounting for the surface normal factor [53] as in eq. (4.11), the time evolution of h is given by

$$\begin{aligned} \frac{\partial h}{\partial t} &= \sqrt{1 + (\nabla h)^2} \\ &\times \left(ua\frac{\partial}{\partial u}\{(\vec{i} \cdot \vec{e}_w)(\vec{i} \cdot \vec{e}_u)\} - v_0 + v_c a\kappa + \tilde{B}\nabla_s^2\kappa \right), \end{aligned} \tag{4.56}$$

where v_0 and v_c are functions of φ where φ is given by $\varphi = \theta - \tan^{-1}(h_x)$. Note that the magnitudes of the wave velocity coefficient u and the erosion velocities v_0, v_c are considered as of the same order of magnitude. We can also assume that the magnitude of the diffusion term $\tilde{B}$ is at most as same as of other coefficients at room temperature. From the corresponding term in eq. (4.43) we have

$$\begin{aligned} &\sqrt{1 + (\nabla h)^2}\frac{\partial}{\partial u}\{(\vec{i} \cdot \vec{e}_w)(\vec{i} \cdot \vec{e}_u)\} \\ &= \frac{h_{xx}\{-2h_x \sin 2\theta + (1 - h_x^2)\cos 2\theta\}}{(1 + h_x^2)^2}, \end{aligned}$$

in 2D Cartesian system and the curvature κ is

$$\kappa = -\frac{h_{xx}}{(1 + h_x^2)^{3/2}}.$$

Thus eq. (4.56) can be written as

$$\begin{aligned} \frac{\partial h}{\partial t} &= ua\frac{h_{xx}\{-2h_x \sin 2\theta + (1 - h_x^2)\cos 2\theta\}}{(1 + h_x^2)^2} \\ &- v_c(\varphi)a\frac{h_{xx}}{1 + h_x^2} + \sqrt{1 + h_x^2}(-v_0(\varphi) + \tilde{B}\nabla_s^2\kappa) \end{aligned} \tag{4.57}$$

Under the assumption of a small variation [27] in h with $a << \kappa^{-1} \sim x$, the spacial variation can be scaled $\tilde{x} := \varepsilon x$ with a small number $\varepsilon \sim a$. so that $\tilde{x} \approx O(1)$. Then eq. (4.57) is

$$\frac{\partial h}{\partial t} = -\sqrt{1 + \varepsilon^2 h_{\tilde{x}}^2} \, v_0(\varphi) + O(\varepsilon^3, a\varepsilon^2). \tag{4.58}$$

and the local angle is

$$\varphi = \theta - \varepsilon h_{\tilde{x}} + O(\varepsilon^3).$$

Thus

$$v_0(\varphi) = v_0(\theta) - v_0'(\theta)\varepsilon h_{\tilde{x}} + \frac{v_0''(\theta)}{2}\varepsilon^2 h_{\tilde{x}}^2 + O(\varepsilon^3).$$

The prefactor of eq. (4.56) in 2D system becomes

$$\sqrt{1 + h_x^2} = 1 + \frac{\varepsilon^2 h_{\tilde{x}}^2}{2} + O(\varepsilon^4).$$

By ignoring third order terms i.e. $\varepsilon^3 \sim a\varepsilon^2 \sim 0$ and rewriting in terms of the original unscaled variables eq. (4.58) becomes

$$\frac{\partial h}{\partial t} \cong -\frac{v_0(\theta) + v_0''(\theta)}{2}h_x^2 + v_0'(\theta)h_x - v_0(\theta). \tag{4.59}$$

The diffusion term disappears at low and moderate temperatures since it is of 4th order. Here, we are not considering the local quick recovery process from the damage of every ion impact but the global surface dynamics with the order of wavelength ($\sim \kappa^{-1}$) observed. Furthermore, the curvature dependence also disappears from the equation. The difference from the sputtering term in eq. (4.52) is essentially the existence of the nonlinear term h_x^2.

The surface erosion velocity v_0 is proportional to the angular dependent sputter rate $Y_0(\theta)$, a good model of which is given by eqs. (4.6) and (4.7), the Yamamura formula [249], i.e.

$$v_0(\theta) \propto Y_0(\theta). \tag{4.60}$$

For $Ar^+ \rightarrow Si$, $\theta_{opt} = 69.5°$ [148, 250] and $E_{th}^{Ar} = 32.8$ eV [66]. Figure 4.10 shows the sputtering yield and its derivative, Y_0, Y_0' and the function $Y_0 + Y_0''$. **a, b,** and **c** are for 1 keV Ar^+, and **d** is for 2 keV Kr^+ irradiation. One can see that for the specific angle $\theta_s \sim 60°$ the coefficient of h_x^2, i.e. $v_0(\theta_s) + v_0''(\theta_s)$ vanishes. The vanishing angle for 2 keV Kr^+ with $\theta_{opt} = 70°$, $E = 2$ keV and $E_{th}^{Kr} = 39.6$ eV [66] is almost the same (see **d**). This angle is agreement with the incident angle at which the clearest ripples are observed in the experiment of Macko *et al* [145] ($*$ in **d**) for the same Kr^+ ion beam energy of 2 keV. From the Yamamura formula, the specific angle θ_s is not especially sensitive to E and E_{th} but is highly dependent on θ_{opt}.

For the specific angle θ_s, eq. (4.59) is simply

$$\frac{\partial h}{\partial t} = v_0'(\theta_s)h_x - v_0(\theta_s). \tag{4.61}$$

This also possesses a periodic travelling wave solution

$$h(t, x) = c_0 \cos(x + v_0'(\theta_s)t + c_1) - v_0(\theta_s)t,$$

where c_0 and c_1 are constants. As before there also exists a cycloid solution for eq. (4.61) given by

$$h = c_0 \cos(p + c_1) - v_0(\theta_s)t, \quad x + v_0'(\theta_s)t = p + c_2 \sin p, \tag{4.62}$$
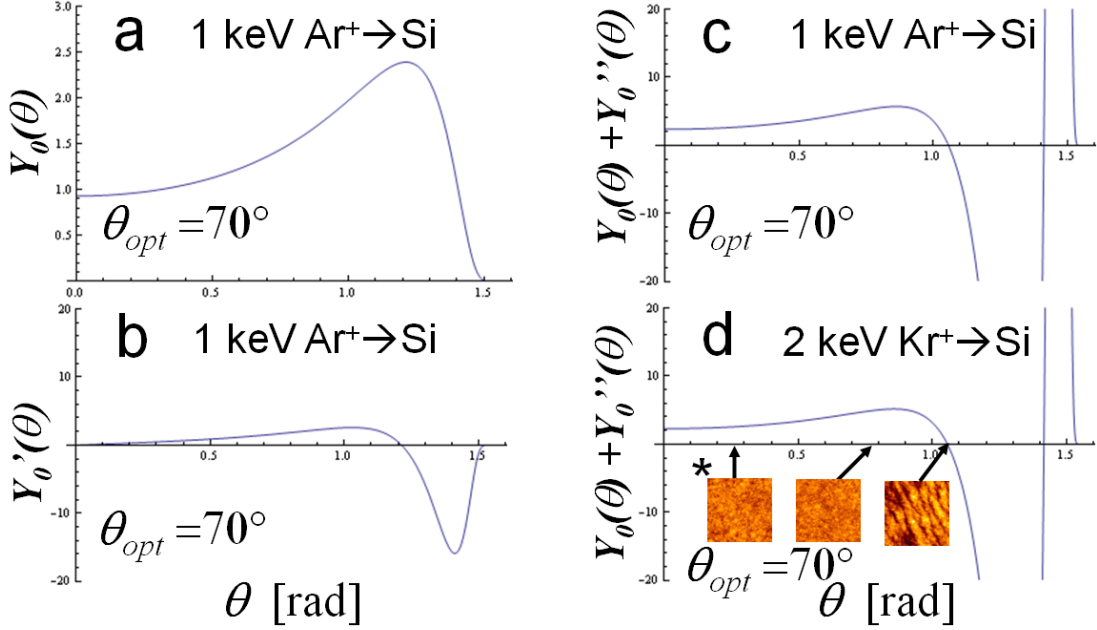
Figure 4.10: The angle dependent sputtering yields and their derivatives. **a**: The sputtering yield given by eqs. (4.6) and (4.7) with $Y_0(0) = 0.93$ [253], $\theta_{opt} = 70°$, $E = 1000$ eV and $E_{th}^{Ar} = 32.8$ eV. **b**: The first derivative of $Y_0(\theta)$. The sign of this term is related to the direction of the travelling wave solution. **c**: The term being proportional to the coefficient of h_x^2 in eq. (4.59). **d**: The same expression as **c** with different energy parameters $E = 2000$ eV and $E_{th}^{Kr} = 39.6$ eV. *: STM images of the surface topography of Si after $E = 2000$ eV Kr ion irradiation at 300 K (courtesy Sven Macko and Thomas Michely [145]).

where c_2 is a constant with $|c_2| < 1$. Indeed, figure 2.6 in chapter 2 gives an evidence that the cycloid solution describes the experimentally observed surface pattern formation quite nicely. For $c_0 = 0.22$, $c_1 = \pi/2$ and $c_2 = 0.7$ with the scale factor 7.4 nm, the cycloid solution fits the experimental observation extremely well(see figure 2.6 and the discussion there).

It is known experimentally that there exists a "magic angle" where clear pattern formation is observed. This angular dependence is however strongly influenced by the substrate properties and various preferential angles are reported e.g. $\theta_s = 5°\text{-}20°$ [258], $\theta_s = 60°\text{-}75°$ [145], and $\theta_s \sim 67°$ [119].

These differences can be understood by the vanishing angle of the nonlinear term in eq. (4.59) which depends on the parameters in eq. (4.6). For example, for $\theta_{opt} = 10°$ and $75°$, the vanishing angle changes from $\theta_s \sim 26°$ to $\theta_s \sim 67°$. Figure 4.11 gives some examples of the effect of varying the maximum erosion angle. It can be seen that for $\theta_{opt} = 10°$, there is little increase in sputtering yield with θ (**a**) with an almost constant value for $\theta < 0.6$ rad $\sim 34°$. This shape is more or less similar for $0° < \theta_{opt} < 45°$. Because of this the velocity of the travelling wave as shown in **b** is almost zero. The term $Y_0 + Y_0''$ for $\theta < 0.6$ is much smaller than that for $\theta_{opt} > 60°$ (**c** and **d**, see also Fig. 4.10 **c** and **d**) and almost vanishes for small θ. Note that all terms are proportional to the normal yield $Y_0(0)$ by the relation (4.60) and eq. (4.6). For this situation, the nonlinear term is small over wide range angles so that a travelling wave solution is possible at these angles as reported by Ziberi *et al* [257]. Experimentally, ripple formation at these small angles is more well-defined than with higher angles (see 1 and 3 in **c**).

Additionally, in **c** there also exists a second vanishing angle at $\theta \sim 1.1$ rad $\sim 63°$. Thus a reappearance of some periodic pattern formation at this angle is also expected. Indeed, the prediction of this reappearance agrees with the experimental observations of the ripple formation at $\theta = 65°$ by Cornejo *et al* [52] (**c** 1,2,3) and the dot formation at $\theta = 75°$ by Ziberi *et al* [259]

115

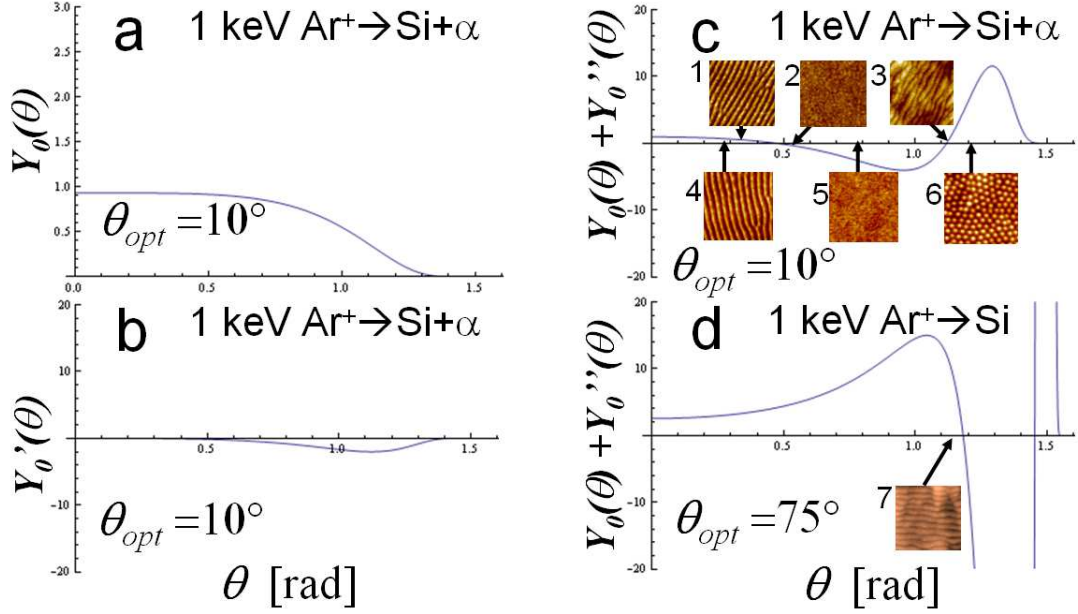Figure 4.11: Examples of varying θ_{opt}. **a**: The sputtering yield given by eqs. (4.6) and (4.7) with $\theta_{opt} = 10°$ and other parameters are same as in Fig. 4.10 **a**. **b**: The first derivative of $Y_0(\theta)$. The sign of this term is entirely negative and the travelling wave solution moves slightly against the ion beam. **c**: The coefficient of the non-linear term term in eq. (4.59). **d**: The same term as in **c** but with $\theta_{opt} = 75°$. The corresponding vanishing angle is 1.18 rad $\sim 67.6°$. The insets in **c** and **d** are surface patterns on Si with some metal impurity incorporation with Kr^+ 2 keV (1,2) and 1.5 keV (3), with Ar^+ 1.5 keV (4,5) and 0.5 keV (6) (courtesy Frank Frost (3) [52], (6) [259]), and with Ar^+ 0.5 keV (7) (courtesy Adrian Keller [119]) respectively. All experiments were done at room temperature and all ripples shown here were with the periodicity being parallel to the ion beam direction.

(**c** 4,5,6). However the dot formation is so far not explained by this approach. In the case of the observations of Cornejo *et al* , the first vanishing angle is lower than 0.5 rad, but the second vanishing angle is in the same regime of **c**. In the cases of Ziberi *et al* , the second vanishing angle is around 1.2 rad. Without any significant contribution of sputtering suppression, pattern formation appears preferentially at 60°-70° as reported by Macko *et al* [145] (Fig. 4.10 **d** ∗) and by Keller *et al* [119] (**d** 7).

4.5 Summary

Previous models of surface pattern formation under ion bombardment have been examined and a new kinetic model of surface modification based on the atomic flow induced by an ion beam has been constructed within a similar framework. In the initial stage of pattern formation, thermal diffusion is necessary to stabilise the initial evolution of wave components within the linear stability regime but away from this regime the model gives a cycloid function as a stable travelling wave solution in Lyapunov sense for a specific incident angle. The atomic flow based pattern formation can explain ripple formation induced by ion beams at low and moderate temperatures, namely without a significant contribution of thermally activated surface diffusion. The solution agrees with the a corresponding experimental observation of Carter and Vishnyakov.

Once the size of periodic patterns exceeds a certain size, the contribution of surface diffusion disappears because of a 4th order topography dependency. Then the topography converges to the shape of a travelling wave which appears most clearly at the specific angles where a nonlinear

term in the approximated equations of motion disappears due to the contribution of the angular dependency of the sputtering yield $Y_0(\theta) + Y_0''(\theta)$.

From this point of view, the similarity between the hexagonal dot structures of semiconducter surfaces reported Facsko *et al* [72] as well as Ziberi *et al* [259] and the Bérnard cells could be understood as the local Rayleigh-Bérnard convection induced by the discrete atomic flow process promoted by the accumulation of the quick atomic flow process under low energy ion beam irradiation. Although surface erosion occurs under ion beam irradiation, this theory predicts that a local fast flow process due to disordering induced by the irradiation significantly contributes toward the essential driving force for the surface nanostructuring. Suppressing the sputtering can also promote well-defined ripple formation. In contrast, where recrystallisation occurs between ion impacts, such as in most metals under low energy bombardment or where the sputter effect is large enough to dominate the relaxation process, this type of nanostructure formation is unlikely to occur.

Chapter 5

Summary

In this thesis, three topics, the metal nanocluster growth mechanism on prepatterned substrates, the acceleration of the KMC simulation model, and ion-beam inducing surface pattern formation mechanism have been studied. The main results and the outlook of each topic are summarized here.

Metallic cluster growth model

The Ag cluster growth mechanism on ripple-like pre-patterned v-SiO$_2$ has been investigated by a reaction diffusion model on slightly pre-patterned surfaces with an weak interaction, the sticking probability evolution, surface ad-monomer random walks, morphology- and incident angle dependent local flux rate, Ag area fraction growth, and the cluster formation process with atomistic simulation and continuum theory. For the atomistic simulation model, a lattice-based kinetic Monte-Carlo (KMC) method was used. In this model, a combination of a simplified inter-atomic potential and experimental transition barriers taken from the literature was employed. The main results relating to the metal cluster growth mechanism are as follows:

- The experimentally observed Ag NCs grown on rippled templates were successfully reproduced by a new type of KMC simulation method with a weak interaction between Ag and v-SiO$_2$ of the bond energy $E_b^{Ag/SiO_2} = 0,26$ eV and the migration barrier $E_m^{Ag/SiO_2} = 0.20$ eV that are relatively in good agreement with the DFT calculations.

- It was revealed that the observed coalescence of NCs promoted mainly in high flux regions and less nucleation occurs in low flux regions is due to a high re-evaporation rate from the substrate.

- It is predicted that millisecond order lifetimes, and $\approx$1 nm square surface migration ranges of Ag adatoms can trigger metal nucleations even on defect free surfaces.

- The nucleation density is strongly influenced by the AL of metal adatoms on templates as well as the flux, especially for a short AL and the amplification of the initial pre-patterned surface is highly enhanced in a certain low flux regime.

Further development of this work is e.g.

- Application of other deposition materials such as Co, CdTe, Si, Ge from experimental- and industrial importance.

○ Development of 3D cluster growth simulation model accounting for some other effects such as the ballistic detachment-redeposition process, the cohesive energy profile of metal atoms connecting with the substrate, the annealing process, multicomponent materials and grain boundaries, a more accurate and complicated event table in order to determined local transition events more systematically.

Markov chain model

A new type of accelerated KMC simulation method has been developed in order to model a cluster formation process comparable with experiment. The acceleration method consists of two essential ideas that are the discretization of the entire process into local transition events and the classification of the transition levels with respect to the thermal fluctuation of the system. The main results from this topic are summarized below:

- By allowing free transitions with small barriers to be considered as fluctuations, the entire system evolves as a Markov chain of 'equal entropy' equivalence class objects.

- The evolution dynamics of the system is promoted by the metastable level transitions.

- Contrary to some previous accelerated dynamics methods [214, 153, 45] accounting for many small migration barriers, an acceleration of the system evolution can still be achieved, when the system does not require too many transition events to reach the quasi-equilibrium state and a typical acceleration factor for the metallic PVD example is 2000-3000.

- The model predicts a convergence time of metastable states, after each metal deposition onto the surface, of $< \mu$s-order.

- The model can predict the metal cluster growth patterns accurately with detailed atomistic transition event statistics.

- The effect of parameters chosen in the method is investigated with 1D atomic diffusion models and the acceleration effect is verified with the convergence speed of the probability distribution of microstates to the thermodynamical limit (the Boltzmann distribution).

- The perturbation of the limit distribution of microstates is bounded by the characteristic number of the original Markov kernel and the maximum norm of this kernel and perturbed Markov kernel (Theorem 1).

For further development:

○ A systematical study of the application limit of the transition level classification method with respect to the inability of the small transition effect of individual simulation system under various temperatures.

○ More accurate barrier calculations such as those provided by DFT or improved inter atomic potentials.

○ Extension for the representation of wave functions through the integration of all pathways connecting states at two complex times for describing various levels of physics.

Ripple formation theory

Surface pattern formation under ion bombardment has been studied by examining previous models and through the formulation of a new non-linear kinetic model based on the local atomic flow and associated density change in the near surface region. The main results of this theory are enumerated below:

- A nonlinear equation of motion describing surface evolution by ion beam inducing atomic flow was derived and a cycloid function as a stable traveling wave solution in Lyapunov sense was found for the specific angle.

- Under the slowly varying surface assumption, the same equation possesses a similar traveling wave solution for any incident angle.

- In the initial stage of pattern formation, thermal diffusion and an incident angle $\theta > 45°$ are necessary to stabilise the initial evolution of wave components within the linear stability regime which agrees with the recent report of Madi *et al* [147].

- Away from the initial regime, the model gives this stable travelling wave solution and the positive power law ion energy dependency of the wavelength $\lambda \propto E^{2/3}$ predicted, agrees with the experimental reports by Chini *et al* [46] $\lambda \propto E^{0.45}$ and Ziberi *et al* [257] $\lambda \propto E^{0.44}$.

- The atomic flow based pattern formation can explain ripple formation induced by ion beams at low and moderate temperatures, namely without a significant contribution of thermally activated surface diffusion.

- The solution agrees with the a corresponding experimental observation of Carter and Vishnyakov [35].

- Once the size of periodic patterns exceeds a certain size, the contribution of surface diffusion disappears because of a 4th order topography dependency.

- In the final stage, the topography converges to the shape of a traveling wave which appears most clearly at the specific angles where a nonlinear term in the approximated equations of motion disappears due to the contribution of the angular dependency of the sputtering yield $Y_0(\theta) + Y_0''(\theta)$.

- This prediction can explain various experimental observations of ripple formation under irradiation at 'magic angles' reported by Macko *et al* [145], Cornejo *et al* [52], Ziberi *et al* [259] and Keller *et al* [119].

This theory predicts that a local fast flow process due to disordering induced by the irradiation significantly contributes toward the essential driving force for the surface nanostructuring. In contrast, where recrystallisation occurs between ion impacts, such as in most metals under low energy bombardment or where the sputter effect is large enough to dominate the relaxation process, this type of nanostructure formation is unlikely to occur. As outlook, there are some topics to be investigated in order to extend this atomic flow based pattern formation theory.

- A more accurate description of the statistical distribution of atomic flow directions especially for the sideways motion.

○ It is predicted that the change of angular dependency of the sputtering yield results in the ripple formation. Thus an accurate contribution analysis of impurity species for the sputtering feature should be examine by e.g. combination of MD- and experimental approaches, especially an appropriate material assisting the clear ripple formation without any disturbance of the electric property of the semiconductor would be explored if exist.

○ Further property of the nonlinear solution found in this work and its application to the similar type of dynamical systems.

○ The application of the continuum models to cluster growth processes such as metal whiskering.

The consideration of another intriguing ion inducing pattern formation, the hexagonally ordered dot structures, reported by e.g. Facsko *et al* [72] as well as Ziberi *et al* [259] are excluded in this work. Thus the applicability of the model to this phenomenon is an interesting and challenging topic. For the industrial application, the second point is quite important. Concerning the third point, the solution found in this work satisfies a nonlinear PDE essentially due to the multiplication of another nonlinear term which is 1 under the second order approximation. A further study of such property could also be an interesting mathematical subject bringing a new light on the general solution of nonlinear dynamical systems such as the Navier-Stokes equation [91].

The aim of this study was to develop a theoretical understanding of experimentally observed ion-inducing ripple-like surface pattern formation of semiconductors and its application of the metallic nanocluster growth by PVD. It is concluded that this aim has been successfully accomplished through an rigorous reexamination of the previous models and a new, atomic flow based kinetic model including the full consideration of the nonlinear equations of motion and the discovery of their analytical solutions, and a new type of atomistic simulation model with an extremely effective acceleration method respectively.

Appendices

A The discrete reaction diffusion equation

The reaction-diffusion equation (2.23) for the simulation cell of the fcc structure can be derived from the second and the third order approximation for time- and space variables respectively. Let $C(t, u, v)$ be the existence probability of an atom in the discrete lattice site (u, v) on the fcc(100) surface at time t. There are totally 12 jump directions in the fcc grid and four of them are directions of detachment where the probability of the detachment is $e^{-\Delta E/kT}$. Thus C is represented by

$$
\begin{aligned}
C(t+1, u, v) = \frac{1}{12}\Big\{ & C(t, u-1, v-1) \\
& + C(t, u+1, v-1) \\
& + C(t, u-1, v+1) \\
& + C(t, u+1, v+1)\Big\} \\
+ \frac{1}{3}\Big\{1 + (1 - & e^{-\Delta E/kT})\Big\}C(t, u, v).
\end{aligned}
$$

Then,

$$
\begin{aligned}
C(t+1, u, v) - C(t, u, v) = \frac{1}{12}\Big\{ & C(t, u-1, v-1) \\
+ C(t, u+1, v-1) + & C(t, u-1, v+1) \\
+ C(t, u+1, v+1) - & 4C(t, u, v)\Big\} \\
& - \frac{e^{-\Delta E/kT}}{3}C(t, u, v).
\end{aligned}
\tag{A.1}
$$

The formal expansion of eq. (A.1) yields

$$
\begin{aligned}
C_t(t, u, v) = \frac{1}{6}\Big\{ & C_{uu}(t, u, v) + C_{vv}(t, u, v)\Big\} \\
& - \frac{e^{-\Delta E/kT}}{3}C(t, u, v) + O(\partial_t^2, \partial_{u,v}^3),
\end{aligned}
$$

where subscripts imply the partial derivatives with respect to variables. With this approximation the reaction-diffusion equation models nicely the behavior of adatom random-walks on the fcc(100) surfaces. Similarly, one can derive the diffusion coefficient $D = 1/4$ for the adatom migration on the fcc(111) surface in the same simulation cell. The derivation of other diffusion constants is also analogous.

B The derivation of the solution (2.20)

Let $I = I(t, u, v)$ be a solution of the inhomogeneous diffusion equation

$$\partial_t I - D \; \nabla^2 \; I = g(t, u, v), \tag{B.1}$$

with the initial condition

$$I(0, u, v) \equiv 0. \tag{B.2}$$

Then the solution is given by the convolutions of 0, g and the 2D Green's function G_2 as mentioned in chapter 1.3.3, i.e.,

$$
\begin{aligned}
I(t, u, v) & \equiv \; G * 0 + \int_0^t G_2(t - s) * g(s) ds \\
& = \; \frac{1}{4\pi D} \int_0^t \int_{\mathbb{R}^2} \frac{1}{t - s} \\
& \times \; exp\Big(-\frac{(u - u')^2 + (v - v')^2}{4D(t - s)} \Big) g(s, u', v') du' dv' ds.
\end{aligned} \tag{B.3}
$$

Set $I =: \tilde{g}(t) \cdot \tilde{I}(t, u, v)$ (*quasi solution Ansatz*). Since I satisfies (B.1), it follows

$$
\begin{aligned}
\tilde{g}' \tilde{I} + \tilde{g} \partial_t \tilde{I} - \tilde{g} D \; \nabla^2 \; \tilde{I} & = \; g, \\
\partial_t \tilde{I} - D \; \nabla^2 \; \tilde{I} & = \; \frac{g}{\tilde{g}} - \frac{\tilde{g}'}{\tilde{g}} \tilde{I}.
\end{aligned} \tag{B.4}
$$

By the comparison of eq. (B.4) with eq. (2.14), $g/\tilde{g}$ and $\tilde{g}'/\tilde{g}$ satisfy

$$\frac{g}{\tilde{g}} = \tilde{f}_{loc}, \; \frac{\tilde{g}'}{\tilde{g}} = r_d.$$

Thus $\tilde{g}(t) = c_0 e^{r_d t}$ with the integral constant c_0 and therefore

$$g(t, u, v) = c_0 e^{r_d t} \tilde{f}_{loc}(u, v) \approx c_0 e^{r_d t} f_{loc}(u, v) = c_0 e^{r_d t} \cos\Big(\theta + \frac{dh}{du} \Big).$$

Hence $\tilde{C} \equiv \tilde{g}^{-1} \cdot I$ satisfies eq. (2.14) with the plane surface initial condition (B.2). From (B.3) it follows that

$$
\begin{aligned}
\tilde{C}(t, u, v) & \equiv \; \frac{1}{4\pi D} \int_0^t \int_{\mathbb{R}^2} \frac{1}{t - s} \\
& \times \; exp\Big[-\frac{(u - u')^2 + (v - v')^2}{4D(t - s)} - r_d(t - s) \Big] \cos\Big(\theta + \frac{dh(u')}{du'} \Big) du' dv' ds \\
& = \; \frac{1}{4\pi D} \int_0^t \int_{\mathbb{R}^2} \frac{1}{s'} \\
& \times \; exp\Big[-\frac{(u - u')^2 + (v - v')^2}{4Ds} - r_d s' \Big] \cos\Big(\theta + \frac{dh(u')}{du'} \Big) du' dv' ds'.
\end{aligned}
$$

C   Contribution of overlapping migration area

Here, a generalised situation described in section 2.2.1 is discussed. The idea is extended to a general m-dimensional case for an arbitrary natural number $m \in \mathbb{N}$. Now, consider the time dependent existence probability distribution of an element in m-dimensional lattice space $\mathbb{Z}^m$. The element is generated at the origin at time $t = 0$ and migrates with a certain annihilation rate in the discrete cells. E.g., an adatom on a 2D system is considered as the element in section 2.2.1. For each lattice point $\mathbf{x} \in \mathbb{Z}^{\mathbf{m}}$, let $C(t, \mathbf{x})$ be the desired distribution at $\mathbf{x}$. Let $N_n(t, \mathbf{x})$ be the number of occupation times of the lattice point $\mathbf{x}$ at time t in n-th iteration process. Then the existence probability is obtained by

$$C(t, \mathbf{x}) = \lim_{n \to \infty} \frac{\sum_{j=1}^{n} N_j(t, \mathbf{x})}{n}. \tag{C.1}$$

Now the migration region, i.e. the number of occupation sites $V_n(t)$ at time t after n-th iteration process, is defined by

$$V_n(t) := \sum_{\mathbf{x} \in \mathbb{Z}} \mathrm{sgn}\Big[\sum_{i=0}^{t} N_n(i, \mathbf{x}) \Big]. \tag{C.2}$$

Note that $N_n(i, \mathbf{x})$ is non negative and takes a positive value at most in a finite number of lattice points $\mathbf{x} \in \mathbb{Z}$ for every iteration step $n < \infty$. This value indicates the proper number of lattice sites occupied at least once by the migrating element. The mean intermediate migration volume $V(t)$ of the element until the simulation time t is then defined by

$$V(t) = \lim_{n \to \infty} \frac{\sum_{j=1}^{n} S_j(t)}{n}.$$

Thus, from (C.1) and (C.2)

$$V(t) = \sum_{\mathbf{x} \in \mathbb{Z}} \lim_{n \to \infty} \frac{\sum_{j=1}^{n} \mathrm{sgn}\Big[\sum_{i=0}^{t} N_j(i, \mathbf{x}) \Big]}{n} \leq \sum_{\mathbf{x} \in \mathbb{Z}} \sum_{i=0}^{t} C(i, \mathbf{x}). \tag{C.3}$$

The maximum simulation time step t_{max} is effectively the longest lifetime of the element during the iterations. Thus t_{max} increases monotonically with increasing the iteration number n. Hence the limit of the mean migration volume V can be defined as $V := \lim_{n \to \infty} V(t_{max}(n))$ which satisfies the relation

$$V \leq \sum_{\mathbf{x} \in \mathbb{Z}} \sum_{t=0}^{\infty} C(t, \mathbf{x}) = r_{ann}^{-1}, \tag{C.4}$$

where r_{ann} is the annihilation rate of the element at each transition step. As seen in section 2.2.1, one can easily see that the rate r_{ann}^{-1} is the limit of the summation in (C.3) and corresponds to the mean lifetime of the element in the system. The inequality of (C.3) arises from the sign function. The difference increases when the sum of the occupation number $\sum_j N_j(i, \mathbf{x})$ is much larger than 1. The rate of overlapping migration occurrence is therefore higher for a long lifetime migration than for a short lifetime. Nevertheless, when the lifetime is long enough compared to the scale of discrete sites, the probability of overlapping occupation is ignorable since the most of occupation number of sites are 1 or 0 as seen in chapter 1.3.3.

metal	cohesive energy		repulsive energy		lattice parameter
	ζ (eV)	q	A (eV)	p	a (Å)
Cu	1.2603	2.43	0.09334	10.55	3.61
Ag	1.1663	3.05	0.09982	10.84	4.09
Au	1.8352	4.30	0.2179	10.525	4.08

Table D.1: Parameters for Cu, Ag and Au used in eq. (D.2) and (D.3), given in Ref [92].

D   The RGL potential

The RGL potential function describes thermodynamic properties of fcc transition metals proposed by Rosato, Guillope and Legrand in 1989 [193]. This potential function is a semi-empirical model introducing the second-moment approximation of the tight-binding scheme [65] for the attractive energy and a Born-Mayer type pairwise interaction for the repulsive energy. The interaction between two atoms depends not only on the length of bonds but also on the local environment around the atom, i.e. the number of neighboring atoms within the cutoff radius. The total cohesive energy E_c is represented as

$$E_c = -\sum_i (E_b^i + E_r^i), \tag{D.1}$$

where i ranges all atoms in the system, E_b^i is the band energy and E_r^i is the repulsive energy. Here the band energy is written with parameters ζ, q and the first neighbor distance r_0 as

$$E_b^i = -\left\{ \sum_j \zeta^2 \exp\left[-2q(\frac{r_{ij}}{r_0} - 1) \right] \right\}^{1/2}, \tag{D.2}$$

where r_{ij} is the bond length between atoms i and j. The parameters ζ and q are an effective hopping integral and the distance dependence of the hopping integral, respectively. The repulsive energy E_r^i is a Born-Mayer type, i.e., $\propto \exp -r$, pairwise interaction

$$E_r^i = \sum_j A \exp\left[-p(\frac{r_{ij}}{r_0} - 1) \right]. \tag{D.3}$$

The parameters A, p, ζ and q are empirically optimized by fitting the cohesive energy, lattice parameter, bulk modulus and shear elastic constants. The equilibrium condition is also taken into account. Table D.1 shows the parameters for noble metals. Because of the fcc structure the lattice parameter a is given by

$$a = \sqrt{2}r_0.$$

It is suggested by the original paper of Rosato et al [193] that the summation j ranges all atoms located in the first neighbor positions for each atom i. This restriction is extended up to the third neighbors by Guillope and Legrand [92]. Note that the rate of the first, second and third neighbor distances of fcc structure is $1 : \sqrt{2} : \sqrt{3}$. For the fcc grid based KMC simulation system treated in this work, the inter-atomic distance corresponds to the diagonal length of the square lattice and the first NN interaction is considered. Thus from eq. (D.1) the cohesive energy E_i of a single atom i in the lattice KMC simulation system is simply given by

$$E_i = -\zeta\sqrt{n} + An,$$

where n is the number of atoms locating in the NN sites of i. Note that for the potential energy calculation the sign of the energy changes.

E Stability of the traveling wave solution

Concerning the nonlinear stability of the solution, it will be shown that the solution (4.49) satisfies the Lyapunov stability criterion. We define Lyapunov stability in the following sense in this work.

Definition 1. *A weak solution $h \in C_b([0,\infty)\times\mathbb{R})$ of the partial differential equation $F(\frac{\partial h}{\partial t}, \frac{\partial h}{\partial x}, \frac{\partial^2 h}{\partial x^2}) \equiv 0$ satisfies **Lyapunov stability** if for an arbitrary function $g \in C_b^2(\mathbb{R})$ and positive number $\varepsilon > 0$, there exists $\delta > 0$ such that*

$$\|g\| < \delta \Rightarrow \left| F(\frac{\partial h}{\partial t}, \frac{\partial(h+g)}{\partial x}, \frac{\partial^2(h+g)}{\partial x^2}) \right| < \varepsilon,$$

where $\|\cdot\|$ and $|\cdot|$ is the maximal norm in $C_b^2(\mathbb{R})$ and $C_b([0,\infty)\times\mathbb{R})$ respectively. Here, the weak solution implies that the solution function is defined in $[0,\infty)\times\mathbb{R}$ except a null set in the sense of the Lebesgue measure.

Let $g(x) \in C_b^2(\mathbb{R})$ be an arbitrary disturbance and $\tilde{g} = g + h$ be the perturbed solution. Then from (4.44)

$$
\begin{aligned}
(*) : \quad &= \left| \tilde{g}_t - \mathrm{u}\left[-2a\frac{\tilde{g}_{xx}\tilde{g}_x}{(1+\tilde{g}_x^2)^2} + \frac{Y}{\sqrt{2}}(\tilde{g}_x - 1) \right] \right| \\
&= \left| h_t + \mathrm{u}\left[\frac{2a\tilde{g}_{xx}\tilde{g}_x}{(1+\tilde{g}_x^2)^2} - \frac{Y}{\sqrt{2}}(g_x + h_x - 1) \right] \right| \\
&= \left| \tilde{h}_\tau \sigma - \frac{\mathrm{u}Y}{\sqrt{2}} + \mathrm{u}\left[\frac{2a\tilde{g}_{xx}\tilde{g}_x}{(1+\tilde{g}_x^2)^2} - \frac{Y}{\sqrt{2}}(g_x + \tilde{h}_\tau - 1) \right] \right| \\
&= \left| \tilde{h}_\tau \mathrm{u}\left(\frac{1}{2} + \frac{Y}{\sqrt{2}}\right) - \frac{\mathrm{u}Y}{\sqrt{2}} + \mathrm{u}\left[\frac{2a\tilde{g}_{xx}\tilde{g}_x}{(1+\tilde{g}_x^2)^2} - \frac{Y}{\sqrt{2}}(g_x + \tilde{h}_\tau - 1) \right] \right| \\
&= \mathrm{u}\left| \frac{1}{2}\tilde{h}_\tau + \frac{2a\tilde{g}_{xx}\tilde{g}_x}{(1+\tilde{g}_x^2)^2} - \frac{Y}{\sqrt{2}}g_x \right| \\
&\leq \frac{\mathrm{u}}{2}\left| \tilde{h}_\tau + \frac{4a\tilde{g}_{xx}\tilde{g}_x}{(1+\tilde{g}_x^2)^2} \right| + \frac{\mathrm{u}Y}{\sqrt{2}}|g_x|.
\end{aligned}
$$

Here, $|\cdot|$ implies the maximum norm.

Remark 1. *For*

$$\left| \tilde{h}_\tau + \frac{4a\tilde{g}_{xx}\tilde{g}_x}{(1+\tilde{g}_x^2)^2} \right| =: (**),$$

it follows

$$\frac{\mathrm{u}}{2}(**) - \frac{\mathrm{u}Y}{\sqrt{2}}|g_x| \leq (*) \leq \frac{\mathrm{u}}{2}(**) + \frac{\mathrm{u}Y}{\sqrt{2}}|g_x|.$$

Thus the stability of $(*)$ is equivalent to the stability of $(**)$.

Proposition 1. *The traveling wave solution (4.49) satisfies Lyapunov stability.*

Proof. Since $\tilde{h}(p) = a\cos p,\ \tau = a(p + \sin p)$,

$$\tilde{h}_\tau = \frac{d\tilde{h}}{dp}\frac{dp}{d\tau} = -\frac{\sin p}{1 + \cos p}, \tag{E.1}$$

$$\tilde{h}_\tau^2 + 1 = \frac{\sin^2 p + (1+\cos p)^2}{(1+\cos p)^2} = \frac{2}{1+\cos p}, \tag{E.2}$$

$$\tilde{g}_x = g_x + h_x = g_x + \tilde{h}_x = g_x + \tilde{h}_\tau, \tag{E.3}$$

$$\tilde{g}_{xx} = g_{xx} + \tilde{h}_{\tau\tau} = g_{xx} - \frac{1}{a(1+\cos p)^2}. \tag{E.4}$$

Set $\alpha = g_x^2 + 2\tilde{h}_\tau g_x, \beta = 1 + \cos p$, then from (E.1)-(E.4) we have

$$
\begin{aligned}
1 + \tilde{g}_x^2 &= 1 + (g_x + \tilde{h}_\tau)^2 \\
&= g_x^2 + 2\tilde{h}_\tau g_x + \frac{2}{1 + \cos p} \\
&= \alpha + \frac{2}{\beta}.
\end{aligned}
$$

Now $(**)$ is

$$
\begin{aligned}
(**) &= \left| -\frac{\sin p}{\beta} + \frac{4(ag_{xx}\beta^2 - 1)(g_x - \frac{\sin p}{\beta})}{(\alpha\beta + 2)^2} \right| \\
&\leq \left| \frac{\sin p}{\beta} \left(1 - \frac{4}{(\alpha\beta + 2)^2} \right) \right| \\
&\quad + 4 \left| \frac{|g_x|(a|g_{xx}\beta^2| + 1) + |ag_{xx}\beta \sin p|}{(\alpha\beta + 2)^2} \right|.
\end{aligned} \tag{E.5}
$$

We claim that these upper bound terms of (E.5) are bounded by a polynomial function of $\|g\|$ converging to 0 for $\|g\| \to 0$ in $C_b^2(\mathbb{R})$ with the help of the following two arguments.

Claim 1. *The ranges of parameters $\alpha\beta$ and $\alpha \sin p$ are*

$$
\begin{aligned}
i. &\quad -|g_x|^2 - 1 \leq \alpha\beta \leq 2(|g_x|^2 + |g_x|), \\
ii. &\quad \alpha \sin p \leq |g_x|^2 + 4|g_x|.
\end{aligned}
$$

Proof of claim 1. i: from the definition

$$
\alpha\beta = (g_x^2 - \frac{2\sin p}{\beta}g_x)\beta = \beta g_x^2 - 2g_x \sin p \leq |\beta||g_x^2| + 2|g_x \sin p|.
$$

Since $0 \leq \beta \leq 2$ and $-1 \leq \sin p \leq 1$, the upper bound is clear. The lower bound is

$$
\begin{aligned}
\alpha\beta &= (1 + \cos p)g_x^2 - 2g_x \sin p \\
&= (g_x - \sin p)^2 + g_x^2 \cos p - \sin^2 p \\
&\geq -|g_x|^2 - 1.
\end{aligned}
$$

ii: it follows

$$
\begin{aligned}
\alpha \sin p &= g_x^2 \sin p - 2g_x \frac{\sin^2 p}{1 + \cos p} \\
&\leq |g_x|^2 + 2|g_x|(1 - \cos p) \\
&\leq |g_x|^2 + 4|g_x|.
\end{aligned}
$$

Q.E.D. of claim 1.

From claim 1 and (E.5), it follows

Claim 2. *For $|g_x| \leq 1/2$, $(**)$ is bounded by*

$$
\frac{32}{9}(|g_x|^4 + 5|g_x|^3 + 6|g_x|^2 + 10|g_x| + 8a|g_x||g_{xx}| + 4a|g_{xx}|).
$$

Proof of claim 2. By the assumption and prop.1,

$$-5/4 \leq \alpha\beta \leq 2(|g_x|^2 + |g_x|).$$

Thus the first term of (E.5) is

$$
\begin{aligned}
\left| \frac{\sin p}{\beta} \left(1 - \frac{4}{(\alpha\beta+2)^2} \right) \right| &= \left| \frac{\sin p}{\beta} \left(\frac{(\alpha\beta)^2 + 4\alpha\beta}{(\alpha\beta+2)^2} \right) \right| \\
&= \left| \frac{(\alpha\beta)\alpha\sin p + 4\alpha\sin p}{(\alpha\beta+2)^2} \right| \\
&= \left| \frac{(\alpha\beta+4)\alpha\sin p}{(\alpha\beta+2)^2} \right| \\
&\leq \frac{\{2(|g_x|^2 + |g_x|) + 4\}(|g_x|^2 + 4|g_x|)}{(2 - 5/4)^2} \\
&= \frac{32}{9}(|g_x|^2 + |g_x| + 2)(|g_x|^2 + 4|g_x|) := A.
\end{aligned}
$$

Similarly, the second term of (E.5) is bounded by

$$
\begin{aligned}
4\left| \frac{|g_x|(a|g_{xx}\beta^2| + 1) + |ag_{xx}\beta\sin p|}{(\alpha\beta+2)^2} \right| & \\
\leq 4\left| \frac{|g_x|(a|g_{xx}2^2| + 1) + |ag_{xx}2|}{(2 - 5/4)^2} \right| & \\
= \frac{64}{9}\{|g_x|(4a|g_{xx}| + 1) + 2a|g_{xx}|\} := B. &
\end{aligned}
$$

Thus

$$
\begin{aligned}
(**) \leq\ =\ & A + B \\
=\ & \frac{32}{9}(|g_x|^2 + |g_x| + 2)(|g_x|^2 + 4|g_x|) + \frac{64}{9}\{|g_x|(4a|g_{xx}| + 1) + 2a|g_{xx}|\} \\
=\ & \frac{32}{9}(|g_x|^4 + 5|g_x|^3 + 6|g_x|^2 + 10|g_x| + 8a|g_x||g_{xx}| + 4a|g_{xx}|).
\end{aligned}
$$

Q.E.D. of claim 2.

Clearly, the polynomial function bounding (**) converges to 0 for $\|g\| \to 0$ in $C_b^2(\mathbb{R})$. Hence, from remark 1 the solution (4.49) satisfies Lyapunov stability.

$\square$

Bibliography

[1] Ackland, G. J., Tichy, G., Vitek, V. and Finnis, M. W. Simple N-body potentials for the noble metals and nickel. *Philos. Mag. A* **56**(6): 735-756 (1987).

[2] Alder, B. J. and Wainwright, T. E. Studies in molecular dynamics. I. General method. *J. Chem. Phys.* **31**(2): 459 (1959).

[3] Amar, J. G, and Family, F. Step-adatom attraction as a new mechanism for instability in epitaxial growth. *Phys. Rev. Lett.* **77**(22): 4584 (1996).

[4] Amera, P., Hsu, D. and Straub, J. E. lobal energy minimum searches using an approximate solution of the imaginary time Schrödinger equation. *J. Chem. Phys.* **97**: 6715-6721 (1993).

[5] Anderson, J. B. A random-walk simulation of the Schrödinger equation: H_3^+. *J. Chem. Phys.* **63**(4): 1499 (1975).

[6] Anderson, J. B. Quantum chemistry by random-walk. H ^2P, H_3^+ $D_{3h}^1 A_1$, $H_2 {}^3\Sigma_u^+$, $H_4 {}^1\Sigma_g^+$, Be ^1S. *J. Chem. Phys.* **65**(10): 4121 (1976).

[7] Anderson, J. B. Quantum chemistry by random-walk. H_4 Square. *Int. J. Quantum Chem.* **15**: 109 (1979).

[8] Anderson, J. B. Predicting rare events in molecular dynamics. *Adv. Chem. Phys.* **91**: 381 (1995).

[9] Antonelli, A., Kaxiras, E. and Chadi, D. J. Vacancy in silicon revisited: Structure and pressure effects. *Phys. Rev. Lett.* **81**(10): 2088 (1998).

[10] Aoki, T., Seki, T., Ninomiya, S., Ichiki, K. and Matsuo, J. Study of crater formation and sputtering process with large gas cluster impact by molecular dynamics simulations. *Nucl. Instr. and Meth. B* **267**: 1424-1427 (2009).

[11] Ashkin, J. and Teller, E. Statistics of two-dimensional lattices with four components. *Phys. Rev.* **64**: 178-184 (1943).

[12] Becke, A. D. Density functional calculations of molecular bond energies. *J. Chem. Phys.* **84**(8): 4524 (1986).

[13] Becke, A. D. Density-functional exchange-energy approximation with correct asymptotic behavior. *Phys. Rev. A* **38**(6): 3098 (1988).

[14] Becke, A. D. Density-functional thermochemistry. I. The effect of the exchange-only gradient correction. *J. Chem. Phys.* **96**(3): 2155 (1992).

[15] Becke, A. D. Density-functional thermochemistry. II. The effect of the Perdew-Wang generalized-gradient correlation correction. *J. Chem. Phys.* **97**(12): 9173 (1992).

[16] Becke, A. D. A new mixing of Hartree-Fock and local density-functional theories. *J. Chem. Phys.* **98**(2): 1372 (1993).

[17] Becke, A. D. Density-functional thermochemistry. III. The role of exact exchange. *J. Chem. Phys.* **98**(7): 5648 (1993).

[18] Becker, R. and Döring, W. Kinetische Behandlung der Keimbildung in übersättigen Dämpfen. *Annalen der Physik* **24**: 719 (1935).

[19] Berendsen, H. J. C., Postma, J. P. M., van Gunsteren, W. F., DiNola, A. and Haak, J. R. Molecular dynamics with couplong to an external bath. *J. Chem. Phys.* **81**(8): 3684 (1984).

[20] Bidigare, P., Hanlon, P. and Rockmore, D. A combinatorial description of the spectrum for the Tsetlin library and its generalization to hyperplane arrangements.. *Duke Math. J.* **99**: 135-174 (1999).

[21] Binder, K. and Stauffer, D. Statistical theory of nucleation, condensation and coagulation. *Adv. Phys.* **25**(4): 343-396 (1976).

[22] Bohm, D. A suggested interpretation of the quantum theory in terms of "hidden" variables. I *Phys. Rev.* **85**(2): 166 (1952).

[23] Bohm, D. A suggested interpretation of the quantum theory in terms of "hidden" variables. II *Phys. Rev.* **85**(2): 180 (1952).

[24] Bortz, A. B., Kalos, M. H. and Lebowitz, J. L. A new algorithm for Monte Carlo simulation of Ising spin systems. *J. Comput. Phys.* **17**: 10-18 (1975).

[25] Boys, S. F. Electronic wave functions I. A general method of calculation for the stationary states of any molecular system. *Proc. R. Soc. London Ser. A* **200**: 542-554 (1950).

[26] Boys, S. F. and Bernardi, F. The calculation of small molecular interactions by the differences of separate total energies. Some procedures with reduced errors. *Mol. Phys.* **19**(4): 553-566 (1970).

[27] Bradley, R.M. and Harper, J.M.E. Theory of ripple topography induced by ion bombardment. *J. Vac. Sci. Technol. A* **6** 2390 (1988).

[28] Brown, A.-D. and Erlebacher, J. Temperature and fluence effects on the evolution of regular surface morphologies on ion-induced Si(111). *Phys. Rev. B* **72**: 075350 (2005).

[29] Burke, K., Werschnik, J. and Gross, E. K. U. Time-dependent density functional theory: Past, present, and future. *J. Chem. Phys.* **123**(6): 062206 (2005).

[30] Braun, G., Lee, S.-J., Dante, M., Nguyen, T.-Q., Moskovits, M. and Reich, N Surface-enhanced Raman spectroscopy for DNA detection by nanoparticle assembly onto smooth metal films. *J. Am. Chem. Soc.* **129**: 6378-6379 (2007).

[31] Cahn, J. W. and Hilliard, J. E. Free energy of a nonuniform system. I. Interfacial free energy. *J. Chem. Phys.* **28**(2): 258 (1958).

[32] Cahn, J. W. and Hilliard, J. E. Free energy of a nonuniform system. III. Nucleation in a two-component incompressible fluid. *J. Chem. Phys.* **31**(3): 688 (1959).

[33] Camelio, S., Babonneau, D., Simonot, L. and Pailloux, F. Anisotropic optical properties of silver nanoparticle arrays on rippled dielectric surfaces produced by low-energy ion erosion. *Phys. Rev. B* **80**: 155434 (2009).

[34] Campbell, C. T. Ultrathin metal films and particles on cxide surfaces: structural, electronic and chemisorptive properties. *Surf. Sci. Rep.* **27**: 1-111 (1997).

[35] Carter, G. and Vishnyakov, V. Roughening and ripple instabilities on ion-bombarded Si. *Phys. Rev. B* **54**: 17647 (1996).

[36] Castin, N. and Malerba, L. Calculation of proper energy barriers for atomistic kinetic Monte Carlo simulations on rigid lattice with chemical and strain field long-range effects using artificial neural networks. *J. Chem. Phys.* **132**: 074507 (2010).

[37] Castro, M., Cuerno, R., Vazquez, L. and Gago, R. Self-organized ordering of nanostructures produced by ion-beam sputtering. *Phys. Rev. Lett.* **94**: 016102 (2005).

[38] Chałasiński, G. and Szcęśniak, M. M. Origins of structure and energetics of van der Waals clusters from ab initio calculations. *Chem. Rev.* **94**: 1723-1765 (1994).

[39] Chamberlain, J. W. and Hunten, D. M. Theory of planetary atmospheres: An introduction to their physics and chemistry. 2nd ed. *Academic press, San Diego* (1987).

[40] Chan, W.-L. and Chason, E. Making waves: Kinetic processes controlling surface evolution during low energy ion sputtering. *J. Appl. Phys.* **101**: 121301 (2007).

[41] Chandler, D. Statistical mechanics of isomerization dynamics in liquids and the transition state approximation. *J. Chem. Phys.* **68**(6): 2959 (1978).

[42] Chang, K. J. and Cohen, M. L. *Ab initio* speudopotential study of structual and high-pressure properties of SiC. *Phys. Rev. B* **35**(15): 8196 (1987).

[43] Chason, E., Mayer, T. M., Kellerman, B. K., Mcllroy, D. T. and Howward, A. Roughening instability and evolution of the Ge(001) surface durinf ion sputtering. *Phys. Rev. Lett.* **72**: 3040 (1994).

[44] Chason, E., Erlebacher, J., Aziz, M. J., Floro, J. A. and Sinclair, M. B. Dynamics of pattern formation during low-energy ion bombardment of Si(001). *Nucl. Instr. and Meth. B* **178**: 55 (2001).

[45] Chatterjee, A. and Voter, A. F. Accurate acceleration of kinetic Monte Carlo simulations through the modification of rate constants. *J. Chem. Phys.* **132**: 194101 (2010).

[46] Chini, T. K., Sanyal, M. K. and Bhattacharyya, S. R. Energy-dependent wavelength of the ion-induced nanoscale ripple. *Phys. Rev. B* **66**: 153404 (2002).

[47] Cho, A. Y. and Arthur, J. R. Molecular beam epitaxy. *J. Chem. Phys.* **62**(5): 1847 (1975).

[48] Chodera, J. D., Singhal, N., Pande, V. S., Dill, K. A. and Swope, W. C. Automatic discovery of metastable states for the construction of Markov models of macromolecular conformational dynamics. *J. Chem. Phys.* **126**: 155101 (2007).

[49] Christov, I. P. Correlated electron dynamics with time-dependent quantum Monte Carlo: Three-dimensional helium. *J. Chem. Phys.* **135**: 044120 (2011).

[50] Christov, I. P. Time-dependent quantum Monte Carlo and the stochastic quantization. *J. Chem. Phys.* **127**: 134110 (2007).

[51] Colle, R. and Salvetti, O. Approximate calculation of the correlation energy for the closed shells. *Theorer. Chim. Acta (Berl.)* **37**: 329-334 (1975).

[52] Cornejo, M., Ziberi, B., Meinecke, C., Hirsch, D., Gerlach, J. W., Höche, T., Frost, F. and Rauschenbach, B. Self-organized patterning on Si(001) by ion sputtering with simultaneous metal incorporation. *Appl. Phys. A* **102**: 593-599 (2011).

[53] Cuerno, R and Barabási, A. L. Dynamic scaling of ion-sputtered surfaces. *Phys. Rev. Lett.* **74**: 4746 (1995).

[54] Dahlquist, G. and Björck, A. Numerical Methods. *Prentice-Hall, Englewood Cliffs* P. 353 (1974).

[55] Dew, M. S. and Baskes, M. I. Embedded-atom method: Derivation and application to impurities, surfaces, and other defects in metals. *Phys. Rev. B* **29**(12): 6443 (1984).

[56] de Bliglie, L. Recherches sur la théorie des quanta. *Thesis, Paris* (1924).

[57] Debye, P. Zur Theorie der spezifischen Wärme. *Annalen der Physik* **39**(4): 789 (1912).

[58] De Giorgi, C., Aihemaiti, P., Buatier de Mongeot, F., Boragno, C., Ferrando, R. and Valbusa, U. Submonolayer homoepitaxial growth on Ag(110). *Surf. Sci.* **487**: 49-54 (2001).

[59] Ding, K. and Andersen, H. C. Molecular-Dynamics simulation of amorphous germanium. *Phys. Rev. B* **34**(10): 6987 (1986).

[60] Dirac, P. A. M. The quantum theory of the electron. *Proc. R. Soc. Lond. A* **117**: 610-624 (1928).

[61] Dirac, P. A. M. The quantum theory of the electron. Part II. *Proc. R. Soc. Lond. A* **118**: 351-361 (1928).

[62] Djurabekova, F. G., Domingos, R., Cerchiara, G., Castin, N., Vincent, E. and Malerba, L. Aitificial intelligence applied to atomistic kinetic Monte Carlo simulations in Fe-Cu alloys. *Nucl. Instr. and Meth. B* **225**: 8-12 (2007).

[63] Doremus, R. H. "Diffusion in noncrystalline silicates" in *Modern Aspects of the Vitreous State*, edited by Mackenzie, J. D. *Butterworths, London* (1962).

[64] Dovesi, R., Saunders, V. R., Roetti, C., Causà, M., Harrison, N.M., Orlando, R. and Aprá, E. CRYSTAL-95 User Manual. *University of Turin, Turin* (1996).

[65] Ducastelle, F. and Cyrot-Lackmann, F. Moments developements and their application to the electronic charge distribution of *d* bands. *J. Phys. Chem. Solids* **31**: 1295-1306 (1970).

[66] Eckstein, W. "Sputtering Yields", in *Sputtering by Particle Bombardment: Experiments and Computer Calculations from Threshold to MeV Energies*, edited by Behrisch, R. and Eckstein, W. *Springer, Berlin* (2007).

[67] Ehrlich, G. and Hudda, F. G. Atomic view of surface self-diffusion: Tungsten on tungsten. *J. Chem. Phys.* **44**(3): 1039 (1966).

[68] El-Sayed, M., A. Some interesting properties of metals confined in time and nanometer space of different shapes. *Accounts Chem. Res.* **34**(4): 257-264 (2001).

[69] Eremeev, S. V., Lipnitskii, A. G., Potekaev, A. I. and Chulkov, E. V. Activation energy for diffusion of point defects at the surfaces of f.c.c. metals. *Russ. Phys. J.* **40**(6): 584 (1997).

[70] Erlebacher, J., Aziz, M. J., Chason, E., Sinclair, M. B. and Floro, J. A. Spontaneous pattern formation on ion bombarded Si(001). *Phys. Rev. Lett.* **82**(11): 2330 (1999).

[71] Espiau de Lamaestre, R., Béa, H., Bernas, H., Belloni, J. and Marignier, J. L. Irradiation-induced Ag nanocluster in silicate glasses: Analogy with photography. *Phys. Rev. B* **76**: 205431 (2007).

[72] Facsko, S., *et al* Formation of ordered nanoscale semiconductor dots by ion sputtering *Science* **285**: 1551 (1999).

[73] Facsko, S., Bobek, T., Stahl, A., Kurz, H. and Dekorsy, T. Dissipative continuum model for self-organized pattern formation during ion-beam erosion. *Phys. Rev. B* **69**: 153412 (2004).

[74] Family, F. and Vicsek, T. Scaling of the active zone in the Eden process on percoration networks and ballistic deposition model. *J. Phys. A: Math. Gen.* **18**: L75-L81 (1985).

[75] Faraday, M. The Bakerian lecture: experimental relations of gold (and other metals) to light. *Philosophical Transactions of the Royal Society of London* **147**(145-181): 159 (1847).

[76] Feibelman, P. J. Diffusion path for an AL adatom on Al(001). *Phys. Rev. Lett.* **65**: 730 (1990).

[77] Fermi, E. Un Metodo Statistico per la Determinazione di alcune Prioprietá dell'Atomo. *Rend. Accad. Naz. Lincei* **6**: 602607 (1927).

[78] Ferrando, R. and Tréglia, G. Anisotropy of diffusion along steps on the (111) faces of gold and silver. *Phys. Rev. B* **50**(16): 12104 (1994).

[79] Ferrando, R. Correlated jump-exchange processes in the diffusion of Ag on Ag(110). *Phys. Rev. Lett.* **76**(22): 4195 (1996).

[80] Ferrando, R., Hontinfinde, F. and Levi, A. C. Morphologies in anisotropic cluster growth: A Monte Carlo study of Ag(110). *Phys. Rev. B* **56**(8): R4406 (1997).

[81] Ferullo, R. M., Garda, G. R., Belelli, P. G., Brada, M. M. and Castellani, N. J. Deposition of small Cu, Ag, and Au particles on reduced SiO_2. *J. Mol. Struct. TEOCHEM* **769**: 217-223 (2006).

[82] Feynman, R. Space-time approach to non-relativistic quantum mechanics. *Rev. Mod. Phys.* **20**(2): 367 (1948).

[83] Fisher, M. E. The theory of condensation and the critical point. *Physics* **3**: 255 (1967).

[84] Fisher, M. E. The theory of equilibrium critical phenomena. *Rept. Progr. Phys.* **30**: 615 (1967).

[85] Foiles, S. M. ,Baskes, M. I. and Dew, M. S. Embedded-atom method functions for fcc metals Cu, Ag, Au, Ni, Pd, and their alloys. *Phys. Rev. B* **33**(12): 7983 (1986).

[86] Fortuin, C. M. and Kasteleyn, P. W. On the random-cluster model. I. Introduction and relation to their models. *Physica* **57**: 536-564 (1972).

[87] Foulkes, W. M. C., Mitas, L., Needs, R. J. and Rajagopal, G. Quantum Monte Carlo simulation in solids. *Rev. Mod. Phys.* **73**(1): 33 (2001).

[88] Gabriel, A.-A. Atomistic simulation of solid-phase epitaxial regrowth of amorphous germanium. *Diplomarbeit, TU Dresden* (2008).

[89] Gear, C. W. Numerical Initial Value Problems in Ordinary Differential Equations. *Prentice-Hall, Englewood Cliffs* (1971).

[90] Gibbs, J. W. Elementally principles in statistical mechanics. *Ox Bow Press, Woodridge* (1902, reprinted 1981).

[91] Giga, M.-H., Giga, Y. and Saal, J. Nonlinear partial differential equations: Asymptotic behavior of solutions and self-similar solutions. *Springer, New York Dordrecht Heidelberg London* (2010).

[92] Guillopé, M. and Legrand, B. (110) surface stability in noble metals. *Surf. Sci.* **215**: 577-595 (1989).

[93] Habenicht, S., Lieb, K. P., Koch, J. and Wieck, A. D. Ripple propargation and velocity dispersion on ion-beam-eroded silicon surfaces. *Phys. Rev. B* **65**: 115327 (2002).

[94] Hamill, P., Kiang, C. S. and Stauffer, D. Nucleation theory: Fisher's droplet picture and microscopic surface tension. *Chem. Phys. Lett.* **28**(2): 209 (1974).

[95] Harrison Jr., D. E. Application of molecular dynamics simulations to the study of ion-bombarded metal surfaces. *Crit. Rev. Solid State* **14**(S1): s1-s78 (1988).

[96] Heady, R. B. and Cahn, J. W. Experimental test of classical nucleation theory in a liquid-liquid miscibility gap system. *J. Chem. Phys.* **58**(3): 896 (1973).

[97] Heinig, K.-H. Efficient cellular automaton algorithm based on low-level bit manipulations. (unpublished, 1994).

[98] Heinig, K.-H., Schmidt, B., Markwitz, A., Grötzschel, R., Strobel, M. and Oswald, S. Precipitation, ripening and chemical effects during annealing of Ge^+ implanted SiO_2 layers. *Nucl. Instr. and Meth. in Phys. Res. B* **148**: 969-974 (1999).

[99] Henkelman, G. and Jónsson, H. A dimer method for finding saddle points on high dimensional potential surface using only first derivatives. *J. Chem. Phys.* **111**(15): 7010 (1999).

[100] Henkelman, G., Uberuaga, B. P. and Jónsson, H. A climbing image nudged elastic band method for finding saddle points and minimum energy paths. *J. Chem. Phys.* **113**(22): 9901 (2000).

[101] Henkelman, G. and Jónsson, H. Long time scale kinetic Monte Carlo simulations without lattice approximation and predefined event table. *J. Chem. Phys.* **115**(21): 9657 (2001).

[102] Herring, C. Diffusional viscosity of a polycrystalline solid. *J. Appl. Phys.* **21**: 437 (1950).

[103] Hertz, H. Über einen Einfluss des ultravioletten Lichtes auf die electrische Entladung. *Annalen der Physik* **267**(8): 983 (1887).

[104] Hiep, H. M., Endo, T., Kerman, K., Chikae, M., Kim, D.-K., Yamamura, S., Takamura, Y. and Tamya, E. A localized surface plasmon resornance based immunosensor for the detection of casein in milk. *Sci. Thechnol. Adv. Mater.* **8**: 331-338 (2007).

[105] Hohenberg, P. and Kohn, W. Inhomogeneous electron gas. *Phys. Rev.* **136**(3B): 864 (1964).

[106] Hontinfinde, F., Ferrando, R. and Levi, A. C. Diffusion processes relevant to the epitaxial growth of Ag on Ag(110). *Surf. Sci.* **366**: 306-316 (1996).

[107] Hontinfinde, F. and Ferrando, R. Ripple formation and rotation in the growth of Ag/Ag(110). *Phys. Rev. B* **63**: R121403 (2001).

[108] Huang, J. S., Vernon, S. and Wong, N. C. Homogeneous nucleation in a critical binary fluid mixture. *Phys. Rev. Lett.* **33**(3): 140 (1974).

[109] Huang, J. S., Goldburg, W. I. and Moldover, M. R. Observation of anomalously large supercooling in carbon dioxide. *Phys. Rev. Lett.* **34**(11): 639 (1975).

[110] Ising, E. Beitrag zur Theorie des Ferromagnetismus. *Z. Physik* **31**: 253 (1925).

[111] Jansen, A. P. J. Monte Carlo study of temperature-programmed desorption spectra with attractive lateral interactions. *Phys. Rev. B* **52**(7): 5400 (1995).

[112] Jost, W. Diffusion in solids, Liquids, Gases *Academic Press, Inc. New York* (1952).

[113] Kalyanasundaram, N., Ghazisaeidi, M., Freund, J. B. and Johnson, H. T. Single impact crater functions for ion bombardment of silicon. *Appl. Phys. Lett.* **92**: 131909 (2008).

[114] Kalyanasundaram, N., Freund, J. B. and Johnson, H. T. A multiscale crater function model for ion-induced pattern formation in silicon. *J. Phys.: Condens. Matter* **21**: 224018 (2009).

[115] Kawasaki, K. Diffusion constants near the critical point for time-dependent Ising models I. *Phys. Rev.* **145**: 224 (1966).

[116] Kawasaki, K. Diffusion constants near the critical point for time-dependent Ising models II. *Phys. Rev.* **148**: 375 (1966).

[117] Kawasaki, K. Diffusion constants near the critical point for time-dependent Ising models III. Self-diffusion constant. *Phys. Rev.* **150**(1): 285 (1966).

[118] Keller, A., Rossbach, S., Facsko, S., and Möller, W. Simultaneous formation of two ripple modes on ion sputtered silicon. *Nanotechnology* **19**: 135303 (2008).

[119] Keller, A., Facsko, S., and Möller, W. Minimization of topological defects in ion-induced ripple patterns on silicon. *New J. Phys.* **10**: 063004 (2011).

[120] Keller, A. Evolution of Ion-Induced Ripple Patterns. -Anisotropy, nonlinearity, and scaling. *Thesis, TU Dresden* (2009).

[121] Kellogg, G. L. Field ion microscope studies of single-atom surface diffusion and cluster nucleation on metal surfaces. *Surf. Sci. Rep.* **21**: 1-88 (1994).

[122] Kelly, K. L., Coronado, E., Zhao, L.-L. and Schatz, G. C. The optical properties of metal nanoparticles: The influence of size, shape, and dielectric environment. *J. Phys. Chem. B* **107**: 668-677 (2003).

[123] Kiang, C. S. Use of liquid-droplet model in calculations of the critical exponent δ. *Phys. Rev. Lett.* **24**(2): 47 (1970).

[124] Klein, M. L. and Shinoda, W. Large-scale molecular dynamics simulations of self-assembling system. *Science* **321**: 798 (2008).

[125] Kohn, W. and Sham, L. J. Quantum density oscillations in inhomogeneous electron gas. *Phys. Rev.* **137**(6A): 1697 (1965).

[126] Kohn, W. and Sham, L. J. Self-consistent equations including exchange and correlation effects. *Phys. Rev.* **140**(4A): 1133 (1965).

[127] Kostrowicki, J., Piela, L., Cherayil, B. J. and Sheraga, H. A. Performance of the diffusion equation method in searches for optimum structures of clusters of Lennard-Jones atoms. *J. Phys. Chem.* **95**: 4113-4119 (1990).

[128] Kramers, H. A. and Wannier, G. H. Statistics of two-dimensional ferromagnet Part I. *Phys. Rev.* **60**: 252-262 (1941).

[129] Kramers, H. A. and Wannier,G. H. Statistics of two-dimensional ferromagnet Part II. *Phys. Rev.* **60**: 263-276 (1941).

[130] Kumar, A. and Zhou, C. The race to replace tin-doped indium oxide: Which material will win? *ACS. Nano* **4**: 11 (2010).

[131] Kuramoto, Y. and Tsuzuki, T. Persistent propergation of concentration waves in dissipative media far from thermal equilibrium. *Prog. Theor. Phys.* **55**: 356 (1976).

[132] Lang, C. B. and Pucker, N. Mathematische Methoden in der Physik. *Spektrum Akademischer Verlag, Heidelberg Berlin*: (1998).

[133] Langer, J. S. Metastable states. *Physica* **73**: 61-72 (1974).

[134] Leal, F. F., Ferreira, S. C. and Ferreira, S. O. Modelling of epitaxial film growth with an Ehrlich-Schwoebel barrier dependent on the step height. *J. Phys.: Condens. Matter* **23**: 292201 (2011).

[135] Lee, C., Yang, W. and Parr, R. G. Development of the Colle-Salvetti correlation-energy formula into a functional of the electron density. *Phys. Rev. B* **37**(2): 785 (1988).

[136] Lee, D. H. and Joannopoulos, J. D. Simple scheme for deriving atomic force constants: Application to SiC. *Phys. Rev. Lett.* **48**(26): 1846 (1982).

[137] Lee, J.-Y., Connor, S. T., Cui, Y. and Peumans, P. Solution-processed metal nanowire mesh transparent electrodes. *Nano lett.* **8**(2): 689-692 (2008).

[138] Lehovec, K. A mechanism causing supersaturation of impurities during semiconductor crystal growth. *Surf. Sci.* **1**: 165-170 (1964).

[139] Liedke, B. Ion beam processing of surfaces and interfaces. -Modeling and atomistic simulations-. *Thesis, TU Dresden* (2010).

[140] Liedke, M. O., Liedke, B., Keller, A., Hillebrands, B., Mücklich, A., Facsko, S. and Fassbender, J. Induced anisotropies in exchange-coupled systems on rippled substrates. *Phys. Rev. B* **75**: 220407 (2007).

[141] Lindhard, J., Scharff, M. and Schiott, H. E. Range concepts and heavy ion ranges (Notes on Atomic Collision II). *Mat. Fys. Medd. Dan Vid. Selsk.* **33**(14): 3 (1963).

[142] Liu, N., Guo, H.-C., Fu, L.-W., Kaiser, S., Schweizer, H. and Giessen, H. Three-dimensional photonic metamaterials as optical frequencies. *Nat. Mater.* **7**: 31-37 (2008).

[143] Lopez, N., Illas, F. and Pacchioni, G. Adsorption of Cu, Pd, and Cs atoms on regular and defect sites of the SiO_2 surface. *J. Am. Chem. Soc.* **121**: 813-821 (1999).

[144] Lothe, J. and Pound, G. M. Reconsideration of nucleation theory. *J. Chem. Phys.* **36**(8): 2080 (1962).

[145] Macko, S., Frost, F., Ziberi, B., Förrster, D. F. and Michely, T. Is keV ion-induced pattern formation on Si(001) caused by metal impurities? *Nanotechnology* **21**: 085301 (2010).

[146] Macko, S., Frost, F., Engler, M., Hirsch, D., Höche, T., Grenzer, J. and Michely, T. Phenomenology of iron-assisted ion beam pattern formation on Si(001). *New J. Phys.* **13**: 073017 (2011).

[147] Madi, C. S., Davidovitch, B., George, H. B., Norris, S. A., Brenner, M. P. and Aziz, M. J. Multiple bifurcation types and linear dynamics of ion sputtered surfaces. *Phys. Rev. Lett.* **101**: 246102 (2008).

[148] Madi, C. S., Anzenberg, E., Ludwig Jr., K. and Aziz, M. J. Supplementary materials to Mass redistribution causes the structural rechness of ion-irradiated surfaces. *Phys. Rev. Lett.* **106**: 066101 (2011), http://link.aps.org/supplemental/10.1103/PhysRevLett.106.066101.

[149] Marks, N. A. Evidence for subpicosecond thermal spikes in the formation of tetrahedral amorphous carbon. *Phys. Rev. B* **51**: 2441 (1997).

[150] Metropolis, N., Rosenbluth, A. W., Rosenbluth, M. N., Teller, A. H. and Teller, E. Equation of state calculations by fast computing machines. *J. Chem. Phys.* **21**(6): 1087-1092 (1953).

[151] Michely, T. and Krug, J. Islands, Mounds and Atoms: Patterns and Processes in Crystal Growth Far from Equilibrium. *Springer, Berlin* (2003).

[152] Montalenti, F. and Ferrando, R. Jumps and concerted moves in Cu, Ag and Au(110) adatom self-diffusion. *Phys. Rev. B* **59**(8): 5881 (1999).

[153] Montalenti, F., Voter, A. F. and Ferrando, R. Spontaneous atomic shuffle in flat terraces: Ag(100). *Phys. Rev. B* **66**: 205404 (2002).

[154] Moore, M. C., Kalyanasundaram, N., and Johnson, H. T. Structural and sputtering effects of medium energy ion bombardment of silicon. *Nucl. Instr. and Meth. B* **225**: 241 (2004).

[155] Morgenstern, K., Rosenfeld, G., Lagsgaard, E., Besenbacher, F. and Comsa, G. Measurement of energies controlling ripening and annealing on metal surfaces. *Phys. Rev. Lett.* **80**(3): 556 (1998).

[156] Mottet, C., Ferrando, R., Hontinfinde, F. and Levi, A. C. A Monte Carlo simulation of submonolayer homoepitaxial growth on Ag(110) and Cu(110). *Surf. Sci.* **417**: 220-237 (1998).

[157] Müller, T., Heinig, K.-H. and Schmidt, B. Formation of Ge nanowires in oxidized silicon V-grooves by ion beam synthesis. *Nucl. Instr. and Meth. in Phys. Res. B* **175-177**: 468-473 (2001).

[158] Müller, T., Heinig, K.-H., Möller, W. Bonafos, C., Coffin, N., Cherkashin, N., Ben Assayag, G., Schamm, S., Zanchi, G., Claverie, A., Tencé, M. and Colliex, C. Multi-dot floating-gates for nonvolatile semiconductor memories: Their ion beam synthesis and morphology. *Appl-Phys, Lett.* **85**(12): 2373 (2004).

[159] Müller, T. Low energy ion beam synthesis of Si nanocrystals for nonvolatile memories -kinetic Monte Carlo studies on phase separation. *Thesis, TU Dresden* (2005).

[160] Mullins, W. W. Theory of thermal grooving. *J. Appl. Phys.* **28** 333 (1957).

[161] Muñoz-García, J., Castro, M. and Cuerno, R. Nonlinear ripple dynamics on amorphous surfaces patterned by ion beam sputtering. *Phys. Rev. Lett.* **96**: 086101 (2006).

[162] Muñoz-García, J., Cuerno, R. and Castro, M. Coupling of morphology to surface transport in ion-beam irradiated surfaces: Oblique incidence. *Phys. Rev. B* **78** 205408 (2008).

[163] Nastasi, M., Mayer, J. W. and Hirvonen, J. K. Ion-Solid Interactions. Fundamentals and applications. *Cambridge University Press, Cambridge* (1996).

[164] Navez, M., Sella, C., and Chaperot, D. Microscopie electronique - etude de lattaque du verre par bombardement ionique. *C. R. Acad. Sci. Paris* **254**: 240 (1962).

[165] Newman, M. E. J. and Barkema, G. T. Monte Carlo methods in statistical physics. *Oxford University Press, Oxford New York* (1999).

[166] Nordlund, K. Molecular dynamics simulation of ion ranges in the 1-100 keV energy range. *Comp. Mater. Sci.* **3**: 448-456 (1995).

[167] Nordlund, K. Point defect movement and annealing in collision cascades. *Phys. Rev. B* **56**(5): 2421 (1996).

[168] Nordlund, K., Ghaly, M., Averbackand, R. S., Caturla, M., Diaz de la Rubia, T. and Tarus, J. Defect production in collision cascades in elemental semiconductors and fcc metals. *Phys. Rev. B* **57**(13): 7556 (1998).

[169] Nordlund, K. Lecture note; "Basics of Monte Carlo simulations", chapter 8. *http://beam.acclab.helsinki.fi/∼knordlun/mc/* (2006).

[170] Norris, S. A., Brenner, M. P. and Aziz, M. J. From crater functions to partial differential equations: a new approach to ion bombardment induced nonequilibrium pattern formation. *J. Phys.: Condens Matter* **21**: 224017 (2009).

[171] Norris, S. A., Samera, J., Bukonte, L., Backman, M., Djurabekova, F., Nordlund, K., Madi, C., S., Brenner, M. P. and Aziz, M. J. Molecular dynamics of single-particle impacts predicts phase diagrams for large scale pattern formation. *Nature Comm.* **2**(276): 1 (2011).

[172] Numazawa, S., Ranjan, M., Heinig, K. H., Facsko, S. and Smith, R. Ordered Ag nanocluster structures by vapor deposition on pre-patterned SiO$_2$. *J. Phys.: Condens. Matter* **23**: 222203 (2011).

[173] Numazawa, S. and Smith, R. Markov-chain model of classified atomistic transition states for discrete kinetic Monte Carlo simulations. *Phys. Rev. E* **84**: 046714 (2011).

[174] Nurminen, L., Kuronen, A. and Kaski, K. Kinetic Monte Carlo simulation of nucleation on pattern substrates. *Phys. Rev. B* **63**: 035407 (2000).

[175] Oates, T. W. H., Keller, A., Noda, S. and Facsko, S. Self-organized metallic nanoparticle and nanowire array from ion-sputtered silicon templates. *Appl. Phys. Lett.* **93**: 063106 (2008).

[176] Owens, J. D., Luebke, D., Govindaraju, N., Harris, M., Krüger, J., Lefohn, A. E. and Purcell, J. T. A survey of general-purpose computation on graphics hardware. *Computer Graphics Forum* **26**(1): 80-113 (2007).

[177] Papanicolaou, N. I., Evangelakis, G. A. and Kallinteris, G. C. Molecular dynamics description of silver adatom diffusion on Ag(100) and Ag(111) surfaces. *Comp. Mater. Sci.* **10**: 105-110 (1998).

[178] Parker, S. C., Grant, A. W., Bondzie, V. A. and Campbell, C. T. Island growth kinetics during the vapor deposition of gold onto TiO$_2$(110). *Surf. Sci.* **441**: 10-20 (1999).

[179] Perdew, J. P. and Wang, Y. Accurate and simple analytic representation of the electron-gas correlation energy. *Phys. Rev. B* **45**(23): 13 244 (1992).

[180] Perdew, J. P., Chevary, J. A., Vosko, S. H., Jackson, K. A., Pederson, M. R. and Singh, D. J. Atoms, molecules, solids, and surfaces: Applications of the generalized gradient approximation for exchange and correlation. *Phys. Rev. B* **46**(11): 6671 (1992).

[181] Perdew, J. P., Burke, K. and Ernzerhof, M. Generalized gradient approximation made simple. *Phys. Rev. Lett* **77**(18): 3865 (1996).

[182] Perdew, J. P., Ernzerhof, M. and Burke, K. Rationale for mixing exact exchange with density functional approximations. *J. Chem. Phys.* **105**(22): 9982 (1996).

[183] Perdew, J. P., Ruzsinszky, A., Tao, J., Staroverov, V. N., Scuseria, G. E. and Csonka, G. I. Prescription for the design and selection of density functional approximations: More constraint satisfaction with fewer fits. *J. Chem. Phys.* **123**(6): 062201 (2005).

[184] Petersen, J. and Mayr, S. G. Dewetting of Ni and NiAg solid thin films and formation of nanowires on ripple patterned substrates. *J. Appl. Phys.* **103**: 023520 (2008).

[185] Philibert, J. Atom movements, diffusion and mass transport in solids. *Les Editions de Physique, Les Ulis* (1991).

[186] Pierre-Louis, O., D'Orsogna, M. R. and Einstein, T. L. Edge diffusion during growth: The kink Ehrlich-Schwoebel effect and resulting instabilities. *Phys. Rev. Lett.* **82**(18): 3661 (1999).

[187] Posselt, M. and Gabriel, A. Atomistic simulation of amorphous germanium and its solid phase epitaxial recrystallization. *Phys. Rev. B* **80**: 045202 (2009).

[188] Potts R. B. Some generalized order-disorder transformations. *Proc. Camb. Phil. Soc.* **48**: 106 (1952).

[189] Preis, T., Virnau, P., Paul, W. and Schneider, J. J. GPU accelerated Monte Carlo simulation of the 2D and 3D Ising model. *J. Comput. Phys.* **228**: 4468-4477 (2009).

[190] Ranjan, M., Oates, T. W. H., Facsko, S. and Möller, W. Optical properties of silver nanowire arrays with 35 nm periodicity. *Opt. Lett.* **35**(15): 2576 (2010).

[191] Ranjan, M. Metal nanoparticles/nanowires self-assembly on ripple patterned substrate. - Mechanism, properties, and applications. *Thesis, TU Dresden* (2010).

[192] Röntzsch, L., Heinig, K.-H., Schmidt, B., Mücklich, A., Möller, W., Thomas, J. and Gemming, T. Direct evidence of self-aligned Si nanocrystals formed by ion irradiation of Si/SiO_2 interfaces. *Phys. Status Solid A* **202**(15): R170-R172 (2005).

[193] Rosato, V., Guillope, M. and Legrand, B. Thermodynamical and structural properties of f.c.c. transition metals using a simple tight-binding model. *Phil. Mag. A* **59**(2): 321-336 (1989).

[194] Rusponi, S., Boragno, C., Ferrando, R., Hontinfinde, F. and Valbusa, U. Time evolution of adatom and vacancy clusters on Ag(110). *Surf. Sci.* **440**: 451-459 (1999).

[195] Sanville, E. J., Vernon, L. J., Kenny, S. D., Smith, R., Moghaddam, Y., Browne, C. and Mulheran, P. Surface and interstitial transition barriers in rutile (110) surface growth. *Phys. Rev. B* **80**: 235308 (2009).

[196] Schrödinger, E. Der stetige Übergang von der Mikro- zur Makromechanik. *Die Naturwissenshaften*: 664 (1926).

[197] Schrödinger, E. An undulatory theory of the mechanics of atoms and melecules. *Phys. Rev.* **28**(6): 1049 (1926).

[198] Schwartz, A. J., Huang, J. S. and Goldburg, W. I. Spinodal decomposition in a binary liquid mixture near the critical point. *J. Chem. Phys.* **62**(5): 1847 (1975).

[199] Schwoebel, R. and Shipsey, E. J. Step motion on crystal surfaces. *J. Appl. Phys.* **37**(10): 3682 (1966).

[200] Segall, M. D., Lindan, P. J. D., Probert, M. J., Pickard, C. J., Hasnip, P. J., Clark, S. J. and Payne, M. C. First-principles simulation: ideas, illustrations and the CASTEP code. *J. Phys.: Condence. Matter.* **14**: 2717-2744 (2002).

[201] Sigmund, P. Theory of sputtering. I. Sputtering yield of amorphous and polycrystalline targets. *Phys. Rev.* **184**: 383-416 (1969).

[202] Sigmund, P. On the number of atoms displaced by implanted ions or energetic recoil atoms. *Appl. Phys. Lett.* **14**: 114 (1969).

[203] Sigmund, P. A mechanism of surface micro-roughening by ion bombardment. *J. Mater. Sci.* **8**: 1545 (1973).

[204] Singh-Boparai, S. P., Bowker, M. and King, D. A. Crystallographic anisotropy in chemisorption: Nitrogen on tungsten single crystal planes. *Surf. Sci.* **53**: 55-73 (1975).

[205] Sivashinsky, G. I. On self-turbulization of a laminar flame. *Acta Astronaut.* **6**(5-6): 569-591 (1979).

[206] Slater, J. C. The theory of complex spectra. *Phys. Rev.* **34**(10): 1293 (1929).

[207] Šmilauer, P., Wilby, M. R. and Vvedensky, D. D. Reentrant layer-by-layer growth: A numerical study. *Phys. Rev. B* **47**(7): 4119 (1993).

[208] Šmilauer, P. and Vvedensky, D. D. Step-edge barriers on GaAs(001). *Phys. Rev. B* **48**(23): 17603 (1993).

[209] Smith, R. and Walls, J. M. The development of a general three-dimensional surface under ion bombardment. *Phil. Mag. A* **42**(2): 235-248 (1980).

[210] Smith, R., Valkering, T. P. and Walls, J. M. The erosion of amorphous and crystalline surface by ion bombardment. *Phil. Mag. A* **44**(4): 879-893 (1981).

[211] Smith, R., Carter, G. and Nobes, M.J. The theory of surface erosion by ion bombardment. *Proc. Roy. Soc. London. A* **407**(4): 405-425 (1986).

[212] Smith, R., Harrison Jr., D. E. and Garrison, B. J. KeV particle bombardment of semiconductors: A molecular-dynamics simulation. *Phys. Rev. B* **40**(1): 93 (1989).

[213] Smith, R. Harrison, D.E. and Garrison, B.J. keV particle bombardment of semiconductors: A molecular-dynamics simulation. *Phys. Rev. B* **40**: 93-101 (1989).

[214] Sørensen, M. R. and Voter, A. Temperature-accelerated dynamics for simulation of infrequent events. *J. Chem. Phys.* **112**(21): 9599 (2000).

[215] Sprague, J. A., Montalenti, F., Uberuaga, B. J., Kress, J. D. and Voter, A. F. Simulation of growth of Cu on Ag(001) at experimental deposition rates. *Phys. Rev. B* **66**: 205415 (2002).

[216] Stephens, P.- J., Devlin, F. J., Chabalowski, C. F. and Frisch, M. J. Ab Initio calculation of vibrational adsorption and circular dichroism spectra using density functional force fields. *J. Phys. Chem.* **98**(45): 11623 (1994).

[217] Steurer, W., Apfolter, A., Koch, M., Ernst, W. E., Søndergård, E., Manson, J. R., and Holst, B. Surface dynamics measurements of silica glass. *Phys. Rev. B* **78**: 045427 (2008).

[218] Stillinger, F. H. and Weber, T. A. Computer simulation of local order in condensed phases of silicon. *Phys. Rev. B* **31**(8): 5262 (1985).

[219] Strobel, M., Heinig, K.-H. and Möller, W. A combination of atomic and continuum models describing the evolution of nanoclusters. *Comp. Mater. Sci.* **10**: 447-462 (1998).

[220] Strobel, M. Modeling and computer simulation of ion beam synthesis of nanostructures. *Thesis*: Technische Universität Dresden (1999).

[221] Strobel, M., Heinig, K. H. and Möller, W. Three-dimensional domain growth on the size scale of the capillary length: Effective growth exponent and comparative atomistic and mean-field simulation. *Phys. Rev. B* **64**: 245422 (2001).

[222] Süle, P., Menyhárd, M. and Nordlund, K. Does the thermal spike affect low energy ion-induced interfacial mixing? *Nucl. Instrum. Methods B* **211**: 524 (2003).

[223] Süle, P. Anisotropy driven ultrafast nanocluster burrowing. *J. Phys. Chem.* **129**: 084707 (2008).

[224] Süle, P. and Heinig, K. H. The molecular dynamics simulation of ion-induced ripple growth. *J. Phys. Chem.* **131**: 204704 (2009).

[225] Swope, W. C., Andersen, H. C., Berens, P. H. and Wilson, K. R. A computer simulation method for the calculation of equilibrium constants for the formation of physical clusters of molecules: Application to small water clusters. *J. Chem. Phys.* **76**(1): 637 (1982).

[226] Tarus, J., Nordlund, K., Kuronen, A. and Keinonen, J. Effect of surface on defect creation by self-ion bombardment of Si(001). *Phys. Rev. B* **58**: 9907 (1998).

[227] Teller, E. On the stability of molecules in the Thomas-Fermi theory. *Rev. Mod. Phys.* **34**(4): 627 (1962).

[228] Tersoff, J. Modeling of solid-state chemistry: Interatomic potentials for multicomponent systems. *Phys. Rev. B* **39**(8): 5566 (1989).

[229] Thomas, L. H. The calculation of atomic fields. *Proc. Cambridge Phil. Soc.* **23**(5): 542-548 (1927).

[230] van Delft, F. C. M. J. M. Bulk and surface Debye temperatures in relation to cohesive energy and Lennard-Jones potentials. *Surf. Sci.* **251-252**: 690-695 (1991).

[231] Verlet, L. Computer "Experiments" on classical fluids. I. Thermodynamical properties of Lennard-Jones molecules. *Phys. Rev.* **159**(1): 98 (1967).

[232] Verlet, L. Computer "Experiments" on classical fluids. II. Equilibrium correlation functions. *Phys. Rev.* **165**(1): 201 (1968).

[233] Vernon, L., Kenny, D. and Smith, R. Growth of TiO_2 surfaces following low energy ($<$ 40 eV) atom and small cluster bombardment. *Nucl. Instr. and Meth. B* **268**: 2942-2946 (2010).

[234] Vicsek, T. and Family, F. Dynamic scaling for aggregation of clusters. *Phys. Rev. Lett.* **52**(19): 1669 (1984).

[235] Videcoq, A., Hontinfinde, F. and Ferrando, R. Multilayer growth of Ag(110): a simulation study. *Surf. Sci.* **515**: 575-587 (2002).

[236] Vincent, R. A theoretical analysis and computer simulation of the growth of epitaxial films. *Proc. Roy. Soc. Lond. A.* **321**: 53-68 (1971).

[237] Vineyard, G. H. Frequency factors and isotope effects in solid state processes. *J. Phys. Chem. Solids* **3**: 121-127 (1957).

[238] Vosko, S. H., Wilk, L. and Nusair, M. Accurate spin-dependent electron liquid correlation energies for local spin density calculations: a critical analysis. *Canad. J. Phys.* **58**(8): 12001211 (19

[239] Voter, A. Classically exact overlayer dynamics: Diffusion of rhodium clusters on Rh(100). *Phys. Rev. B* **34**(10): 6819 (1986).

[240] Voter, A. Hyperdynamics: Accelerated molecular dynamics of infrequent events. *Phys. Rev. Lett.* **78**(20): 3908 (1997).

[241] Voter, A. A method for accelerating the molecular dynamics simulation of infrequent events. *J. Chem. Phys.* **106**(11): 4665 (1997).

[242] Wen, J.-M., Chang, S.-L., Burnett, J. W., Evans, J. W. and Thiel, P. A. Diffusion of large two-dimensional Ag clusters on Ag(100). *Phys. Rev. Lett.* **73**(19): 2591 (1994).

[243] Wen, J.-M., Evans, J. W. , Bartelt, M. C., Burnett, J. W.and Thiel, P. A. Coarsening mechanisms in a metal film: From cluster diffusion to vacancy ripening. *Phys. Rev. Lett.* **76**(4): 652 (1996).

[244] Winkler, G. Image analysis, random fields and Markov chain Monte Carlo methods. *Springer-Verlag, Berlin Heidelberg New York* (2003).

[245] Wolfram, S. A New Kind of Science. *Wolfram Media, Champaign* (2002).

[246] Xantheas, S. S. On the importance of the fragment relaxation energy terms in the estimation of the basis set superposition error correction to the intermolecular interaction energy. *J. Chem. Phys.* **104**(21): 8821 (1996).

[247] Xu, X. and Goodman, D. W. Metal deposition onto oxides: An unusual low initial sticking probability for copper on SiO_2. *Appl. Phys. Lett.* **61**(15): 1799 (1992).

[248] Xu, X., He, J.-W. and Goodman, D. W. A surface spectroscopic study of metal-support interactions: model studies of copper on thin on SiO_2 films. *Surf. Sci.* **284**: 103-108 (1993).

[249] Yamamura, Y., Itikawa, Y. and Itoh, N. Angular dependence of sputtering yields of monatomic solids. *Institute of Plasma Physicd, Nagoya University* Report No. IPPJ-AM-26 (1983).

[250] Yamamura, Y., Mössner, C. and Oechsner, H. The bombarding-angle dependence of sputtering yields under various surface conditions. *Radiat. Eff.* **103**: 25 (1987).

[251] Yewande, E. O., Hartmann, A. K. and Kree, R. Propagation of ripples in Monte Carlo models of sputter-induced surface morphology. *Phys. Rev. B* **71**: 195401 (2005).

[252] Yewande, E. O., Kree, R. and Hartmann, A. K. Morphological regions and oblique-incidence dot formation in a model of surface sputtering. *Phys. Rev. B* **73**: 115434 (2006).

[253] Zalm, P. C. Energy dependence of the sputtering yield of silicon bombardment with neon, argon, krypton, and xenon ions. *J. Appl. Phys.* **54**(5): 2660 (1983).

[254] Zhang, T. C., Mei, Z. X., Guo, Y., Xue, Q. K. and Du, X. L. Influence of growth temperature on formation of continuous Ag thin film on ZnO surface by ultra-high vacuum deposition. *J. Phys. D: Appl. Phys.* **42**: 065303 (2009).

[255] Zhu, W.-G., Buatier de Mongeot, F., Valbusa, U., Wang, E. G. and Zhang, Z.-Y. Adatom ascending at step edges and faceting on fcc metal (110) surfaces. *Phys. Rev. Lett.* **92**(10): 106102 (2004).

[256] Zhukovskii, Y. F., Kotomin, E. A., Jacobs, P. W. M. and Stoneham, A. M. *Ab initio* modeling of metal adhesion on oxide surfaces with defects. *Phys. Rev. Lett* **84**(6): 1256 (2000).

[257] Ziberi, B., Frost, F., Höche, Th. and Rauschenbach, B. Ripple pattern formation on silicon surface by low-energy ion-beam erosion: Experiment and theory. *Phys. Rev. B* **72**: 235310 (2005).

[258] Ziberi, B., Frost, F., Tarz, M., Neumann, H. and Rauschenbach, B. Ripple rotation, pattern transitions, and long range ordered dots on silicon by ion beam erosion. *Appl. Phys. Lett.* **92**: 063102 (2008).

[259] Ziberi, B., Cornejo, M., Frost, F. and Rauschenbach, B. Highly ordered nanopatterns on Ge and Si surfaces by ion beam sputtering. *J. Phys.: Condens Matter* **21**: 224003 (2009).

[260] Ziegler, T. Approximate density functional theory as a practical tool in molecular energetics and dynamics. *Chem. Rev.* **91**: 651667 (1991).

[261] Ziegler, J. F., Biersack, J. P. and Littmark, U. The Stopping and Range of Ions in Solids. *Pergamon, New York* (1985).

Acknowledgments

for the useful discussions, the helpful advices in various situations, and the relaxed conversations. Particularly, Tim is my grate c/c++ programing teacher, Bartosz helped me very much during the stay in Budapest for the collaboration project and guided the beautiful catholic church in Krakow during the COSIRES 2010 conference, and the critical discussion with Dr. Posselt strongly motivated me to improve the mathematical description related to the physical phenomenon.

I also appreciate the Hungarian collaborators in KFKI Budapest so much. Dr. Péter Süle gave me many valuable comments on molecular dynamics simulation with the simulation package PARCAS. Especially, his intuition about the diffusivity of molecules stimulated me to enhance the theoretical description of the surface property. Dr. Géza Ódor kindly organized and arranged the comfortable stay in Budapest during the DAAD-MÖB project.

Many thanks to Sabine Zybell, Bo Li and her family, Dr. Gintautas Abrasonis and his family for supporting my family.

List of Publications

Peer-reviewed journals

Publications related to this work:

Chapter 2

Numazawa, S., Ranjan, M., Heinig, K.-H., Facsko, S. and Smith, R.
"Ordered Ag nanocluster structures by vapor deposition on pre-patterned SiO_2." J. Phys.:Condens.
Matter 23 222203 (2011).
(IOP select article, a short introduction is found in *Lab-talk article*:
http://nanotechweb.org/cws/article/lab/47681, http://iopscience.iop.org/0953-8984/labtalk-article/46254)

Chapter 3

Numazawa, S. and Smith, R.
"Markov-chain model of classified atomistic transition states for discrete kinetic Monte Carlo simulations." Phys. Rev. E 84 046712 (2011).

Other publications:

Kunze, T., Gemming, S., Numazawa, S. and Schreiber, M.
"Low-temperature modeling for degenerate and frustrated Heisenberg systems with anisotropy."
Comp. Phys. Comm. 181 806-812 (2010).

Conference contributions

Talks:

DPG Spring meeting 2010, Regensburg, Germany "Mechanism of metal nanostructure self-ordering
-during oblique deposition on pre-patterned surfaces."
COSIRES 2010, Krakow, Poland "Mechanism of selective nanostructures on pre-patterned surfaces."
Seminar of DFG FOR-845 Project Meeting, Muenster, Germany "Atomistic simulation of ion-erosion-induced surface patterning."

Posters:

IBMM 2010, Montréal, Canada "Ion patterning of Si studied by kinetic Monte Carlo using ion
damage from Molecular Dynamics calculations."
International workshop: Nanoscale Modification of Surfaces and Thin Films, 2009, Rathen, Germany "Mechanisms of metal self-ordering at grazing PVD on ion-erosion-induced surface pattern."
International Workshop: Nanoscale Modification of Surfaces and Thin Films, 2009, Rathen, Germany "Prediction of surface pattern formation by surface defect generation"
MRS Fall meeting 2009, Boston, USA "Prediction of surface pattern formation by surface defect
generation and diffusion."
MRS Fall meeting 2009, Boston, USA "Mechanisms of metal self-ordering at oblique PVD on
nanopatterned surfaces."
IUMRS-ICA 2008, Nagoya, Japan "Ion bombardment induced self-organization of nanopattern

149

studied by 3D lattice kinetic MC simulations."

Erklärung

Hiermit versichere ich, dass ich die vorliegende Arbeit ohne unzulässige Hilfe Dritter und ohne Benutzung anderer als der angegebenen Hilfsmittel angefertigt habe, die aus fremden Quellen direkt oder indirekt übernommenen Gedanken sind als solche kenntlich gemacht. Diese Arbeit wurde bisher weder im Inland noch im Ausland in gleicher oder ähnlicher Form einer anderen Prüfungsbehörde vorgelegt. Ich erkenne die Promotionsordnung der Technischen Universität Dresden an.

Dresden, den